Road traffic flow reconstruction and prediction with macroscopic models enhanced by data-based statistical approaches

Alexandra Würth

UNIVERSITÉ CÔTE D'AZUR

ÉCOLE DOCTORALE
SCIENCES FONDAMENTALES ET APPLIQUÉES

Reconstruction et prévision des flux de trafic routier au moyen de modèles macroscopiques renforcées par des approches statistiques basées sur des données

Alexandra Würth

Université Côte d'Azur, Inria équipe Acumes, CNRS, LJAD

Présentée en vue de l'obtention du grade de docteur en Mathématiques **d'**Université Côte d'Azur

Dirigée par: Paola Goatin
Co-dirigée par: Mickaël Binois

Soutenue le: 6 Décembre 2023

Devant le jury, composé de:
Mickaël Binois, Chargé de Recherche, Inria
Charles Bouveyron, Professeur des Universités, Inria
Fabrice Gamboa, Professeur des Universités, IMT Toulouse
Paola Goatin, Directrice de Recherche, Inria
Simone Göttlich, Professeure, Universität Mannheim
Carolina Osorio, Professeure, HEC Montréal
Benedetto Piccoli, Professeur, Rutgers University

Inria

UNIVERSITÉ CÔTE D'AZUR | 3iA Côte d'Azur Institut interdisciplinaire d'intelligence artificielle

Reconstruction et prévision des flux de trafic routier au moyen de modèles macroscopiques renforcées par des approches statistiques basées sur des données

Road traffic flow reconstruction and prediction with macroscopic models enhanced by data-based statistical approaches

Jury:

Président du Jury
Charles Bouveyron, Professeur des Universités, Inria

Rapporteurs
Fabrice Gamboa, Professeur des Universités, IMT Toulouse
Carolina Osorio, Professeure, HEC Montréal
Benedetto Piccoli, Professeur, Rutgers University

Examinateurs
Mickaël Binois, Chargé de Recherche, Inria
Paola Goatin, Directrice de Recherche, Inria
Simone Göttlich, Professeure, Universität Mannheim

Acknowledgements

My PhD time is coming to an end and I would like to take the opportunity to thank all the people who supported me during the past three years.

First of all, I would like to thank my two PhD supervisors, Mickaël Binois and Paola Goatin. Our scientific journey already started with an internship before the PhD where they invested such a great amount of time in our daily and fruitful phone discussions. I would like to thank them for their belief in me and also for the encouragement to continue with a PhD which was indeed the best decision I could have ever made. I have really enjoyed working with them, they always gave me the impression that I was on the right track. Moreover, I am so grateful to have had the chance to get to know two different fields of mathematical research which enabled me also to participate in various conferences, workshops and seminars. It has been a great honor for me to work with them and I would finally like to thank them very much for all their kind advice.
Special thanks also go to the members of the Acumes team at Inria who have integrated me so nicely from the beginning. I have learned so many things from them in this short time, they have made my "séjour" in France unforgettable. Thanks to them and their patience, I have had the chance to learn a new language that has broadened my horizon and has offered me so many great possibilities, both in my academic but also private life.

For reviewing this manuscript, I would also like to express my gratitude to Fabrice Gamboa, Carolina Osorio and Benedetto Piccoli. Additionally, I would like to thank Charles Bouveyron and Stéphane Junca for their helpful advice in our "Comité de Suivi de Thèse" meetings and Charles Bouveyron for also being part of the jury.
I am also very grateful to Simone Göttlich, without her I would have never found out this unique chance of doing my master thesis abroad. I would like to thank her for all her helpful advice, our inspiring scientific collaboration and for being a member of my PhD jury.
Moreover, I would like to thank Olivier Hermant whose opinion and suggestions I have always appreciated. Thanks to him and his fantastic teaching skills, I have developed my passion for programming. I thank him for his encouragement, suggestions and all the time that he invested in our discussions.

Finally, a heartfelt thanks goes to my family who has always supported me: thanks to you, your belief in me and your constant support, I was able to enjoy this time to the fullest.

Abstract

In this thesis, we focus on the modeling of traffic flow by means of hyperbolic conservation laws and statistical approaches. The presented results belong to two different areas of mathematical research: the analytical and numerical study presented in the first part builds the theoretical foundation for the second part, which is devoted to traffic model calibration, traffic reconstruction and prediction based on data.

First of all, we study the initial boundary value problem for generalized second order models, which consist in non-strictly hyperbolic 2×2 systems of conservation laws on an interval with characteristic boundaries, modeling traffic dynamics including vacuum states on a road stretch. After giving a detailed characterization of the admissible states at the boundary in terms of Riemann solver and entropy conditions, we prove existence of entropy weak solutions for data of bounded variation in the Riemann invariant coordinates by convergence of wave-front tracking approximations.
For computing numerically the solutions, we extend an upwind type finite volume scheme to second order traffic flow models. The scheme is shown to satisfy some maximum principle properties on the density. We provide numerical tests illustrating the behavior at vacuum, which coincides in the density component with the considered Riemann solution.

We then present different calibration approaches for parameter identification and traffic speed reconstruction, comparing the performances of first order models, consisting in the sole mass conservation equation, and second order ones, including a second equation accounting for speed evolution. All the approaches use aggregate measurements of vehicles moving on a highway, provided by magnetic loop detectors at fixed locations. In addition, they include a bias term, modeled as a Gaussian process, in order to account for the traffic flow models limitations.
Once the calibration parameters are obtained, our analysis distinguishes between travel time estimation and prediction, where the former is related to already realized traffic scenarios. For the second one, we integrate the partial differential equations of the hyperbolic system into the Gaussian process modeling in order to predict future traffic conditions at boundary loop detector locations and sparse time points. These serve as boundary data to simulate the traffic conditions at a finer scale, which enables travel time prediction. Thus, our approach combines physical and statistical knowledge, supporting the thesis that the physics provide useful information helping to improve the prediction results.
Finally, we compare the reconstructed traffic speeds and travel times between the ground truth and simulated data. Due to limited access to both trajectory and average loop detector data, we perform our analysis not only on real world traffic scenarios but also on synthetic data generated by a microscopic simulator. In general, we observe that the combination of a

physical model and a Gaussian process delivers the most reliable results compared to other tested methods.

Keywords: *Macroscopic traffic flow models; hyperbolic systems of conservation laws; weak boundary conditions; wave-front tracking; Godunov scheme; parameter calibration; Gaussian process modeling; loop detector and trajectory traffic data; travel time prediction.*

Résumé

Dans cette thèse, nous nous concentrons sur la modélisation du flux de trafic au moyen des lois de conservation hyperboliques et d'approches statistiques. Les résultats présentés appartiennent à deux domaines différents de la recherche mathématique: l'étude analytique et numérique présentée dans la première partie constitue la base théorique pour la deuxième partie, qui est consacrée à la calibration, la reconstruction et la prédiction de modèles de trafic basées sur des données.

Tout d'abord, nous étudions le problème aux limites pour des modèles généralisés du second ordre, qui consistent en des systèmes de lois de conservation non strictement hyperboliques de dimension 2×2 sur un intervalle avec des frontières caractéristiques, modélisant la dynamique du trafic, y compris les zones de vide. Après avoir donné une caractérisation détaillée des conditions aux limites en termes de solveur de Riemann ou d'entropie, nous prouvons par la méthode de suivi de fronts l'existence de solutions faibles entropiques pour des données de variation totale bornée dans les coordonnées des invariants de Riemann.
Pour calculer numériquement les solutions, nous étendons un schéma de volume fini de type "upwind" aux modèles de flux de trafic du second ordre. Le schéma satisfait un principe du maximum sur la densité. Nous effectuons des tests numériques illustrant le comportement près du vide, qui coincide dans la composante de densité avec la solution de Riemann considérée.

Ensuite, nous présentons différentes approches de calibration pour l'identification des paramètres et la reconstruction de la vitesse du trafic, en comparant les performances des modèles du premier ordre, consistant en la seule équation de conservation de la masse, et des modèles du second ordre, comprenant une deuxième équation tenant compte de l'évolution de la vitesse. Toutes les approches utilisent des mesures agrégées des véhicules circulant sur une autoroute, fournies par des détecteurs à boucle électromagnétique placés en des lieux fixes. De plus, elles incluent un terme de biais, modélisé par un processus gaussien, afin de pallier les limites des modèles de flux de trafic.
Une fois les paramètres de calibration obtenus, notre analyse distingue entre l'estimation et la prédiction des temps de trajet, où le premier cas étudie des scénarios de trafic déjà réalisés. Pour le second, nous prenons en compte les équations aux dérivées partielles du système hyperbolique dans le modèle du processus gaussien afin de prédire les conditions de trafic futures au niveau des boucles aux bords de la section considérée, ainsi qu'à différents temps fixés. Ceux-ci servent de données aux bords pour simuler l'évolution du trafic à une échelle plus fine, ce qui nous permet de prédire les temps de trajet. Ainsi, notre approche combine des connaissances physiques avec des statistiques, appuiant la thèse que la physique fournit des informations utiles pour améliorer les prédictions.

Enfin, nous comparons les vitesses de circulation et les temps de trajet reconstruits entre les données réelles et simulées. En absence de données de trajectoire et donnée boucle sur le même secteur d'étude, nous effectuons notre analyse non seulement sur des scénarios de trafic réels, mais aussi sur des données synthétiques générées par un simulateur microscopique. En général, nous constatons que la combinaison d'un modèle physique et d'un processus gaussien produit les résultats les plus fiables par rapport aux autres méthodes testées.

Mots clés: *Modèles de trafic macroscopiques; systèmes de conservation hyperboliques; conditions aux limites faibles; méthode de suivi de fronts; schéma de Godunov; calibration des paramètres; modélisation par processus gaussiens; données de détecteur de boucles électromagnétiques et de trajectoires; prédiction des temps de trajet.*

Contents

Acknowledgements **i**

Abstract **iii**

Résumé **v**

Contents **vii**

List of acronyms **ix**

List of symbols **xi**

Introduction **1**

1 The initial boundary value problem for second order traffic flow models with vacuum: existence of entropy weak solutions **9**
1.1 The Riemann solver for the GSOM model 9
1.2 Admissible boundary sets 15
1.2.1 Riemann boundary sets 15
1.2.2 Entropy boundary sets 17
1.3 Existence of entropy weak solutions 25
1.3.1 Wave-front tracking (WFT) algorithm 27
1.3.2 Convergence to an entropy weak solution 39
Appendix A 45

2 Numerical methods **47**
2.1 Godunov scheme 47
2.1.1 Ramp implementation 48
2.2 Harten-Lax-van-Leer scheme 49
2.3 Hilliges-Weidlich scheme 50
2.4 Boundary cell implementation 52
2.5 Data projection 52
2.6 Numerical tests 53
2.6.1 Solutions without vacuum states 54
2.6.2 Solutions involving vacuum states 57

3 Calibration approaches **63**
3.1 Preliminaries . . . 64
3.2 Gaussian process modeling . . . 65
3.2.1 Reduction of computational costs using Kronecker structure . . . 69
3.2.2 Supporting average observations in the correlation . . . 70
3.2.3 Modeling change in the traffic regime . . . 72
3.3 Fundamental fit approach for calibration . . . 75
3.4 Model-driven approaches for calibration . . . 77
3.4.1 $\mathbf{L^2}$ approach . . . 77
3.4.2 Kennedy O'Hagan approach . . . 77
3.4.3 Plumlee approach . . . 78
3.4.4 Bayesian parameter identification by MCMC . . . 79

4 Prediction approaches **81**
4.1 Reference travel times . . . 82
4.1.1 A method for trajectory data . . . 82
4.1.2 Methods for aggregated data . . . 82
4.2 Reconstructed travel times . . . 83
4.2.1 Loop detector data prediction from historical data . . . 84
4.2.2 Loop detector data prediction without historical data . . . 87

5 Description of traffic data sets **91**
5.1 Synthetic microscopic traffic data . . . 92
5.1.1 SUMO scenarios . . . 93
5.2 Real traffic data . . . 98
5.2.1 Data pre-processing . . . 98
5.2.2 Data clustering . . . 99
5.2.3 RTMC scenarios . . . 100

6 Validation of calibration and prediction approaches **105**
6.1 Traffic calibration results . . . 105
6.2 Traffic estimation results . . . 121
6.3 Traffic prediction results . . . 124
Appendix B . . . 132

Conclusion and perspectives **133**

Bibliography **135**

List of acronyms

ARZ	Aw-Rascle-Zhang
BV	Bounded variation
CFL	Courant-Friedrichs-Lewy
CTM	Cell Transmission Model
DTW	Dynamic time warping
ESS	Effective sample size
FF	Fundamental fit
GP	Gaussian process
GPS	Global Positioning System
GSOM	Generic Second Order (traffic flow) Model
HLL	Harten, Lax and van Leer
HW	Hilliges-Weidlich
IBVP	Initial boundary value problem
KOH	Kennedy-O'Hagan
LSTM	Long short-term memory
LWR	Lighthill-Whitham-Richards
MCMC	Markov chain Monte Carlo
ML	Machine learning
MnDOT	Minnesota Department Of Transportation
MOO	Multi-objective optimization
MVN	Multivariate normal
PC	Piece-wise constant
PDE	Partial differential equation
PINNs	Physics-informed neural network
PW	Payne-Whitham
RNN	Recurrent neural network
$\mathcal{RS}$	Riemann solver
RMSE	Root mean square error
SUMO	Simulation of Urban MObility
TS	Time series
TV	Total variation
WFT	Wave-front tracking

List of symbols

b	Discrepancy (or bias) term
$\mathbf{b}_N$	Observed biases at $\mathcal{X}_N$
$\beta(\cdot,\cdot)$	Entropy boundary condition
$\hat{\boldsymbol{\beta}}$	2-dimensional regression parameter, used in the DTW approach
$\mathcal{B}_L^{\text{Ent}}$	Set of entropy admissible values at the left boundary consisting in (ρ, w)-tuples
$\mathcal{B}_R^{\text{Ent}}$	Set of entropy admissible values at the right boundary consisting in (ρ, w)-tuples
$\mathcal{B}_L^{\text{Rie}}$	Riemann admissible left boundary set consisting in (ρ, w)-tuples
$\mathcal{B}_R^{\text{Rie}}$	Riemann admissible right boundary set consisting in (ρ, w)-tuples
$c(\cdot,\cdot)$	Positive definite kernel function, used for computing the correlation matrix $\mathbf{C}_N$
$c^{plum}(\cdot,\cdot)$	Positive definite kernel function, used for computing the correlation matrix $\mathbf{C}_N^{plum}$
C	Wave propagation speed in congestion (calibration parameter)
$C(\theta)$	Cost function in the $\mathbf{L^2}$ approach, dependent on θ
$\mathbf{C}_N$	Correlation matrix of size $N \times N$
$\mathbf{C}_N^{plum}$	Correlation matrix of size $N \times N$ in the Plumlee approach
d^{test}	Test time series
d^{train}	Train time series
dist	Euclidean DTW-distance
$\mathbf{D}$	Demand function, used in the Godunov scheme
$\vec{e}_j$	Unit vector containing 1 on its j-th row entry
$\text{erf}(\cdot)$	Error function
$\exp(\cdot)$	Exponential function
$\mathbf{E}$	Speed RMSE between field and simulated data
$\mathbf{E}_c$	Speed RMSE between field and corrected simulated data
$\mathbf{E}_{GP}$	Speed RMSE between field and GP modeled data
$\hat{\mathbf{E}}$	Predicted speed RMSE between field and simulated data
$\hat{\mathbf{E}}_c$	Predicted speed RMSE between field and corrected simulated data
$\hat{\mathbf{E}}_B^{\rho}$	Predicted density RMSE between field and approximated data at boundary loop detector positions
$\mathbf{E}^{\tau}$	Total travel time error between reference and simulated data

$\mathbf{E}_c^\tau$	Total travel time error between reference and corrected simulated data
$\mathbf{E}_k^\tau$	Total travel time error between reference data and data constructed by the $k \in \{GP, \text{N-curve}, \text{baseline}, \text{bench}\}$ approach
$\mathcal{E}$	Entropy
$f = f(u)$	Vector of fluxes, i.e. $(\rho v, \rho w v)$-tuple
$f_i^{obj}(l_1, l_2, g)$	Objective function in the MOO approach, $i \in \{1, 2\}$
$\mathbf{F}_j^n$	Vector of numerical fluxes at space position x_j and in the time interval $[t^n, t^{n+1}[$
g	Noise parameter (hyper-parameter)
g^C	Congestion noise parameter (hyper-parameter)
g^F	Free flow noise parameter (hyper-parameter)
$\gamma(\Delta x)$	Numerical order of accuracy for the mesh size Δx
θ	Calibration parameter
θ^m	Mode calibration parameter, used in the MCMC approach
θ^*	Optimal calibration parameter
θ^*_{plum}	Optimal calibration parameter in the Plumlee approach
$\mathbf{I}_N$	Identity matrix of size $N \times N$
$k(\cdot, \cdot)$	Positive definite kernel function with $k(\cdot, \cdot) = \sigma^2 c(\cdot, \cdot)$
K	Number of clusters in the K-means algorithm
$\mathbf{K}_N$	Covariance matrix of size $N \times N$
l	Average vehicle length
l_i	Length-scale (hyper-parameter), $i \in \{1, 2\}$
l_i^C	Congestion length-scale (hyper-parameter), $i \in \{1, 2\}$
l_i^F	Free flow length-scale (hyper-parameter), $i \in \{1, 2\}$
$l_j(\rho, w)$	Left eigenvector of the 2×2 hyperbolic system, $j \in \{1, 2\}$
$\lambda_j(\rho, w)$	Eigenvalue of the 2×2 hyperbolic system, $j \in \{1, 2\}$
$\mathbf{L^1}(\Delta x)$	$\mathbf{L^1}$-error for the mesh size Δx
$\mathcal{L}(\sigma^2, l_1, l_2, g, \mathbf{b})$	Likelihood function
$\tilde{\mathcal{L}}(l_1, l_2, g, \mathbf{b})$	Concentrated likelihood function
$m_N(\cdot)$	Predictive mean, used in the GP modeling
μ_θ	Prior mean, used in the MCMC approach
M	Number of (space) cells in the numerical scheme
n_t	Number of time observations
$\hat{n}_{\hat{t}}$	Number of future time observations
n_x	Number of loop detectors
N	Number of observation points, i.e. $N = n_x \cdot n_t$
$\hat{N}$	Number of prediction points
$\hat{N}_B$	Number of prediction points at boundary loop detector positions
$\tilde{N}$	Number of virtual points
N_τ	Number of departure instants
N^{iter}	Number of iterations in an algorithm

O	Occupancy rate
Ω	Domain of the 2×2 hyperbolic system consisting in (ρ, w)-tuples
$\tilde{\Omega}$	Domain of the conservative variables of the 2×2 hyperbolic system consisting in $(\rho, \rho w)$-tuples
$p = p(\rho)$	Pressure function
$\rho = \rho(t, x)$	Traffic density
ρ_0	Initial density
ρ_B	Density at boundary
ρ_{in}	Density at left boundary x_{in}
ρ_{out}	Density at right boundary x_{out}
ρ_{cr}, $\rho_{cr}(w)$	Critical density
$\pi(\cdot)$	Prior distribution, used in the MCMC approach
$\pi(\cdot \mid y^F)$	Posterior distribution given the field observations, used in the MCMC approach
$q = q(t, x)$	Traffic flow
q_{in}	Flow at left boundary x_{in}
q_{out}	Flow at right boundary x_{out}
$Q(\rho, w)$	Flux function, used in the macroscopic traffic flow model
$Q^n_{HLL,j}$	HLL numerical flux at space position x_j and in the time interval $[t^n, t^{n+1}[$
$\mathcal{Q}$	Entropy flux
$\mathbf{r}^n_j$	On-ramp numerical flux at space position x_j and in the time interval $[t^n, t^{n+1}[$
$r_j(\rho, w)$	Right eigenvector of the 2×2 hyperbolic system, $j \in \{1, 2\}$
R, $R(w)$	Maximum density (calibration parameter), possibly dependent on w
$\mathcal{R}(v, w)$	Density function, used in the macroscopic traffic flow model
$\mathbf{s}^n_j$	On-ramp numerical flux at space position x_j and in the time interval $[t^n, t^{n+1}[$
$s^2_N(\cdot, \cdot)$	Predictive covariance, used in the GP modeling
$\mathrm{sgn}(\cdot)$	Sign function
σ_s	Propagation speed of a shock wave
σ^2	Process variance (hyper-parameter)
σ^2_C	Congestion process variance (hyper-parameter)
σ^2_F	Free flow process variance (hyper-parameter)
σ^2_ε	Variance of observation error
$\mathbf{S}$	Supply function, used in the Godunov scheme
$\mathbf{\Sigma}_\theta$	Prior covariance matrix, used in the MCMC approach
$\mathbf{\Sigma}^p$	Proposal covariance matrix, used in the MCMC approach
t	Time variable
t_c	Computation time (in seconds) for running a numerical scheme
Δt	Time step in the numerical scheme
τ	Reference travel time
$\hat{\tau}$	Approximated travel time

T	Time horizon
u	Vector of conservative variables, i.e. $(\rho, \rho w)$-tuple
$u_j^n = (\rho_j^n, \rho_j^n w_j^n)^\top$	Vector of approximate conservative variables at space position x_j and in the time interval $[t^n, t^{n+1}[$
U	Vector of (ρ, w)-tuple
$v = v(t, x)$	Mean traffic speed
v_0	Initial speed
v_B	Speed at boundary
v_{in}	Speed at left boundary x_{in}
v_{out}	Speed at right boundary x_{out}
$v_{cr}(w)$	Speed at critical density, i.e. $\mathcal{V}(\rho_{cr}(w), w)$
V	Maximum speed (calibration parameter)
$\mathcal{V}(\rho, w)$	Speed function, used in the macroscopic traffic flow model
$\mathcal{V}^+(\rho, w)$	Non-negative part of the speed function $\mathcal{V}$
$w = w(t, x)$	Lagrangian vehicle property (or empty road velocity)
w_0	Initial empty road velocity
w_B	Empty road velocity at boundary
w_{in}	Empty road velocity at left boundary x_{in}
w_{out}	Empty road velocity at right boundary x_{out}
w_{min}	Minimum empty road velocity
w_{max}	Maximum empty road velocity
W	Vector of Riemann invariants, i.e. (v, w)-tuple
W_{in}	Vector of Riemann invariants at left boundary, i.e. (v_{in}, w_{in})-tuple
W_{out}	Vector of Riemann invariants at right boundary, i.e. (v_{out}, w_{out})-tuple
$\mathcal{W}$	Domain of Riemann invariants consisting in (v, w)-tuples
$\mathcal{W}_0$	Vacuum set consisting in (v, w)-tuples
$\mathcal{W}_0^c = \mathcal{W} \setminus \mathcal{W}_0$	Non-vacuum set consisting in (v, w)-tuples
x	Space variable
$x\pm$	Limit notation, i.e. $\lim_{x_0 \to x, x_0 \gtrless x} x_0$
x_{in}	Left boundary space position
x_{out}	Right boundary space position
Δx_j	Mesh size in a numerical scheme, $j \in \{1, \dots, M\}$
$\mathcal{X}_N$	Set of time-space points where observations have been recorded
$\hat{\mathcal{X}}_{\hat{N}}$	Set of time-space points at predicted positions
$\hat{\mathcal{X}}_{\hat{N}_B}$	Set of time-space points at predicted positions and boundary loop detector positions
$\tilde{\mathcal{X}}_{\tilde{N}}$	Set of virtual time-space points, used in the MOO approach
y	Conservative variable with $y = \rho w$
$y^F(t, x)$	Field observation at time t and position x
$y_k^F(t, x)$	Flow, speed, or density field observation at time t and position x, $k \in \{q, v, \rho\}$

$y^M(t,x,\theta)$	Numerical solution of the macroscopic traffic flow model at time t and position x and calibration parameter θ
$y_c^M(t,x,\theta)$	Corrected simulated data at time t and position x and calibration parameter θ
δy^M	Derivative matrix of the simulation output
$y^P(t,x)$	Real observation at time t and position x
$\hat{\mathbf{y}}_B$	Predicted boundary loop detector data
$\bar{\mathbf{y}}_N$	Average over N-observed data
$z_j(\rho,w)$	Riemann invariant of the 2×2 hyperbolic system, $j\in\{1,2\}$
$\|\cdot\|_F$	Frobenius norm

Introduction

Macroscopic traffic flow models, consisting of hyperbolic partial differential equations (PDEs) and based on the mass conservation principle, are employed since several decades [PG06, TK14] to describe vehicular traffic dynamics. Reliable and realistic traffic models are gaining more and more importance, not only in mathematical research but also in transportation departments, particularly in response to rising traffic flow [FSS18] and thereby induced congestion. In general, a reduced congestion occurrence leads to shorter travel times and less pollution, which in turn improves human health, the environment and economic efficiency [WYG+22]. Compared to microscopic models, which track each vehicle individually by ordinary differential equations [FHS14, Wag10], macroscopic models describe the spatio-temporal evolution of aggregate quantities such as vehicle density, flow and mean velocity. Since they offer the advantage of involving few parameters and being computationally less expensive, they can be easily adapted to large road networks. In addition, their analytical properties make them suitable for solving optimal control problems in order to provide a good route guidance and to manage reasonably the traffic volume and congestion.

The best known macroscopic traffic flow model was proposed in the mid fifties by Lighthill-Whitham-Richards (LWR) [LW55, Ric56]. It describes via a PDE the conservation of the number of cars on the road as well as the spatio-temporal evolution of measured traffic quantities. The key assumption behind the model is that the mean traffic speed v is described by the density ρ via a function $\mathcal{V}$, i.e. $v = \mathcal{V}(\rho)$, which is referred to as the fundamental diagram. Moreover, the traffic flow q is linked with the other quantities by the so called hydrodynamic flow relation $q(\rho) = \rho\mathcal{V}(\rho)$ [DGDMF22]. Since the model consists in one scalar equation for the traffic density, which reads as

$$\partial_t \rho + \partial_x \left(\rho \mathcal{V}(\rho)\right) = 0,$$

it belongs to the first order models. In general, the LWR model allows to distinguish between free flow and congested traffic regimes, but it is less suitable for describing more complex situations, such as capacity drops and stop-and-go waves. Additionally, a single fundamental curve is not able to capture complex dynamics observed in congested regimes, where the same density value can correspond to several speeds. This can be explained by different driving characteristics of road users. The problem can be addressed by considering the so called "second order" models, whose prototype is the Payne-Whitham (PW) model [Pay71, Whi74]. However, this model can show non physical effects in the traffic context, such as negative speeds and wave speeds faster than car velocity [Dag95]. Therefore, the Aw-Rascle-Zhang (ARZ) model [AR00, Zha02] was developed, which corrects the drawbacks of PW model by integrating an anticipation term describing an average driver reaction.

In this thesis, we will focus on the Generic Second Order traffic flow Model (GSOM), which was introduced in [LMHS07b] and provides a general framework for macroscopic traffic flow modeling. In particular, it generalizes the classical LWR model and includes the widely used ARZ system. In contrast to the first order model, the speed function depends not only on the density but also on a Lagrangian vehicle property which is often interpreted as an empty road velocity, i.e. the speed that would be chosen by the driver if the road was empty. Thus, a driver dependent behavior is integrated in the model. This results in a family of fundamental curves, which can capture better the spread of the data in the congested region.
From a mathematical point of view, the GSOM consists in the 2×2 hyperbolic system whose conservative form reads

$$\begin{cases} \partial_t \rho + \partial_x(\rho v) = 0, \\ \partial_t(\rho w) + \partial_x(\rho w v) = 0, \end{cases} \qquad x \in \mathbb{R},\ t > 0, \tag{I}$$

defined on a domain $\Omega \subset \big\{(\rho, w) \in \mathbb{R}^2, \rho \geq 0, w \geq 0\big\}$, where $\rho = \rho(t,x)$ denotes the traffic density and $w = w(t,x)$ the Lagrangian vehicle property. As pointed out in [WYG$^+$22], the first equation represents the physical law, namely the conservation of vehicles. However, the second equation, which accounts for the dynamics in the traffic mean velocity, is less interpretable and only an approximation for the traffic evolution. In analogy with gas dynamics, it is typically referred to as the momentum equation [Fan13].
The average speed of vehicles $v = \mathcal{V}(\rho, w)$ is given by a function $\mathcal{V} : \Omega \to \mathbb{R}_{\geq 0}$, which is required to satisfy the following hypotheses [FHS14]:

$$\mathcal{V}(\rho, w) \geq 0, \quad \mathcal{V}(0, w) = w, \tag{II.a}$$
$$2\mathcal{V}_\rho(\rho, w) + \rho \mathcal{V}_{\rho\rho}(\rho, w) < 0 \text{ for } \rho \in]0, R(w)[\text{ and } w > 0, \tag{II.b}$$
$$\mathcal{V}_w(\rho, w) > 0 \text{ for } \rho \in]0, R(w)[\text{ and } w > 0, \tag{II.c}$$
$$\forall w > 0 \quad \exists\, R(w) > 0 : \quad \mathcal{V}(R(w), w) = 0, \tag{II.d}$$

where $R(w)$ represents the density for which the street is fully congested and vehicles cannot move. We may have $R(w) = R$ for all $w > 0$, meaning that there is only one maximum density R on the road independently of the users, which is indeed realistic. Moreover, as in [CFGG20, FHS14], we observe that (II.b) implies that $Q(\rho, w) := \rho \mathcal{V}(\rho, w)$ is strictly concave and $\mathcal{V}_\rho(\rho, w) < 0$ for $w > 0$, if $\mathcal{V}$ is a $\mathbf{C}^2$ function in ρ. If we now choose $\mathcal{V}(\rho, w) = w - p(\rho)$ for a suitable "pressure" function p, the system (I) corresponds to the ARZ model [AR00, Zha02]. Moreover, by taking $w = constant$, we recover the LWR model since only the first equation remains.
Under the assumptions (II), it holds that the two eigenvalues of the above system (I) differ if we assume $\rho > 0$. However, we want to integrate the interesting case of $\rho = 0$, because this so called *vacuum scenario* typically induces instabilities [AR00, Section 4]. By taking vacuum states into account, we are still in the setting of a hyperbolic system, but we loose strict hyperbolicity. It is therefore not possible to define uniquely the solutions of Riemann problems involving vacuum states, even enforcing entropy conditions, as pointed out in [ADR16]. It is also worth mentioning that one characteristic field is genuinely non-linear with coinciding shock and rarefaction curves and the other one is linearly degenerate (but not straight). Thus, the GSOM system belongs to the Temple class systems [Tem83].

In traffic flow applications, it is natural to consider the initial boundary value problem (IBVP) for (I) on a bounded interval $]x_{in}, x_{out}[\subset \mathbb{R}$, where the variables ρ and w are equipped with

prescribed initial and boundary data at $t = 0$ and $x = x_{in}$, $x = x_{out}$. In the literature, two definitions of boundary conditions for systems of conservation laws are commonly considered: a *boundary entropy inequality* derived by viscosity approximation [BlRN79, Ben86] and a *Riemann boundary condition* based on the Riemann solver associated to (I). Dubois and Le Floch [DLF88] showed that the two formulations are equivalent for scalar conservation laws, linear systems and a 2×2 system whose fields are both linearly degenerate. For non-linear hyperbolic systems, Benabdallh and Serre [BS87] proved that the Riemann boundary condition implies the entropy one, and equivalence holds in the case of 2×2 systems with straight-line characteristic fields and never vanishing eigenvalues. This result was further extended to $n \times n$ strictly hyperbolic Temple class systems with non-characteristic boundary in [AG02, Section 8]. We just note that [PH13, Section 4] gives a characterization of the boundary entropy set for the ARZ model with Chaplygin pressure (fully linearly degenerate). Well-posedness results for the IBVP with both characteristic and non-characteristic boundary for general, strictly hyperbolic systems of conservation laws were provided in [Ama97, AC97] for data with small total variation. For strictly hyperbolic Temple class systems with data of bounded variation (BV), no monotonicity assumption on the eigenvalues along the Lax curves and possibly characteristic boundary, we refer to [CG04] and with $\mathbf{L}^\infty$ data, genuinely non-linear characteristic fields and non-characteristic boundary see [AG02].
Concerning second order traffic flow models, and in particular the ARZ model with vacuum (i.e. non-strictly hyperbolic), existence results for the Cauchy problem were provided in [ADR16, GHO08], while $\mathbf{L^1}$ stability is provided in [BR03, GHO10] for the system in Lagrangian coordinates. We notice that, to avoid problems at vacuum, several "phase-transition" or "collapsed" models were introduced in the literature, see e.g. [BWG$^+$11, Col02, FSP$^+$17, Goa06]. Vacuum issues can also be avoided by suitably modifying the speed function near the vacuum, as proposed in [LMHS07a].
We remark that all these results do not apply in the present setting, since the system (I) is non-strictly hyperbolic and the boundary conditions can be characteristic [Ama97].

Before employing traffic flow models for real world applications, they must be calibrated and validated against real traffic data in order to reproduce the reality as good as possible [SPP$^+$17]. Parameter identification can be seen as an example of an inverse problem [Gra20]. In the case of GSOM, calibration is needed to determine unknown parameters appearing in the speed function $\mathcal{V}$. After the parameters are identified, the model needs to be validated, i.e. to be tested on data sets which were not considered in the calibration procedure. A good mathematical model should be able to both appropriately match real data and predict the system evolution in the future [WYG$^+$22].
Classically, the model parameters are identified by fitting the fundamental diagram, i.e. the density-flow or density-speed mapping described by the model flux function (see e.g. [DGK$^+$09, Fan13, FHS14, FSP$^+$17]). Another possibility to specify the unknown values is to minimize some error measure of the simulation output, against either data provided by loop detectors at fixed locations [NH03, SPN$^+$18, Wag10] or trajectory data, where we refer to [CB11, PHF$^+$15, WBT$^+$10]. Since we focus on macroscopic models, average and aggregated data are necessary to produce the simulation output, obtained by the numerical solution of the discretized version of the system (I). For a good approximation, [KGG17, LHSM05] consider the Godunov scheme [God59], which is based on an implementation of density or flow boundary conditions, as discussed in [BCO23]. The coarser grained data are typically measured by fixed sensors which usually count the vehicles passing by and possibly also measure

there speed or occupancy rate.
Moreover, it turns out that the inherent simplification of the dynamics induced by the models, their non-linearity and the data noise are all sources of challenging difficulties when dealing with parameter identification. In particular, [TW15] emphasizes that the simulation output can rarely fit the physical response perfectly, even if the true values of the calibration parameters are known. Therefore, it is a natural idea to improve the simulator by extending the model in order to better match the reality. In [PS15], the authors propose to correct the misestimate of the system state by a Bayesian learning algorithm. Specifically, they focus on quantifying the uncertainty of the road capacity, considering solely the LWR model with a triangular fundamental diagram, where the bias correction is applied after fixing calibration parameters. Also, data information can be leveraged to improve existing models or design new ones, as proposed by [DMCC$^+$21, Fan13, FHS14, FSP$^+$17, HFV18, MDdWS19]. Nevertheless, up to our knowledge, few works have been devoted to evaluate the inherent uncertainty of both models and data and its impact on model-based predictions. Thus, we adopt the statistical framework proposed in [HKC$^+$04, KO01] by introducing a bias term to better account for possible discrepancies between the mathematical models and reality. This generic framework has been applied in a variety of fields, ranging e.g. from physics [HKC$^+$04] to engineering [BBK$^+$09, HGBL20] or biology [Plu17]. See also [CBC$^+$19] for a recent review of the methods and [BO14] for a discussion on the model discrepancy. Following [KO01], we model the bias by a Gaussian process (GP), which is a classical choice when dealing with computer simulations [Gra20, RW06], since it provides a flexible nonparametric framework. In general, GPs are completely specified by their mean and covariance, which involves some hyper-parameter tuning. In [LLW$^+$23], they consider a Newton method for the parameter estimation, however in this work we will rely on a simple maximum likelihood estimation in a 2-level nested optimization procedure. Finally, it is also worth mentioning the paper [Plu17], whose approach forces the bias to be orthogonal to the derivative of the simulator. This modeling trick should overcome some drawbacks which are observed in [Gra20, TW15] probably due to a too high flexibility in the original bias modeling.

Calibrated models can be used for traffic state estimation and prediction. The former consists in reconstructing traffic states for already realized traffic scenarios, whereas the second one turns out to be more challenging because it deals with the prediction of the unknown future. However, it is also the more interesting case since a good traffic prediction can lead to better traffic control and management, which reduces congestion [AEG$^+$16]. In general, we can distinguish between model-driven and data-driven approaches.
In the first case, physical knowledge and therefore also the calibration parameters are used to estimate and predict the traffic state [MHG21]. In order to run the simulation code in the setting of prediction, it is also necessary to forecast boundary data, which is often a challenging task. Moreover, the purely model-driven approach is often criticized to reflect only those dynamics in traffic situations that are explainable by the functional assumptions of the model [SMD21]. Therefore, it is often seen as an over-simplification of the reality [BCO23].
In contrast, when considering data-driven approaches, the estimation of the traffic state is only based on real (historical) data. This alternative is said to be capable to deal with irregularities such as noisy data or individual driving behaviors [BCO23]. In [MK18], they compare four different approaches based on machine learning for short time traffic flow prediction. Also, less expensive regression models can be used as in [KCB00], where they estimate travel times from detector measurements, or in [RVZ04], where they assume a linear relationship

between future, current and historical travel times. In [IK09], they use a GP regression in order to predict travel times along an unknown path. However, these approaches typically need a large amount of good quality data [MHG21], which are often not available. Moreover, they fail to predict non-recurring traffic situations such as accidents, because they cannot be learned from empirical data [AEG$^+$16].
Thus, a natural idea is to consider hybrid approaches for vehicular traffic determination to overcome the drawbacks of the two previous ones [AEG$^+$16, BCO23]. Currently, the so called physics-informed neural networks (PINNs) are gaining more and more attention in the literature (see e.g. [RPK17, SMD21]). They consist of the combination of model- and data-driven components. In PINNs, neural networks are trained to solve any kind of PDEs whose residual is integrated in the training loss function. The applied machine learning components help to learn the solution of the equations and they can be also used for identifying calibration parameters. Analogously to our work, [SMD21] focuses on the reconstruction of vehicular traffic dynamics as well as the fundamental diagram, which is replaced by a neural network. However, they deal only with traffic estimation and do not consider the prediction part. Another way to combine data- and model-driven approaches in the macroscopic traffic context is proposed by [BCO23], where they first run a recursive neural network, whose results are then used to predict boundary loop detector data. However, approaches based on neural networks usually require a large amount of data and are often difficult to tune. This motivates a new form of hybrid approaches, focusing on combining the physics with GPs, as in [CCZW22, CHOS21, LWK$^+$22]. These methods can be also easily employed for prediction (and not only estimation). They have in common that they use a GP in order to model the observed data. Moreover, the physics are injected by forcing the PDE to be satisfied at virtual, i.e. unobserved points.
We emphasize that all the above mentioned hybrid approaches are only tested for reproducing and predicting average and aggregated data. In order to obtain travel times which are often the main focus in real world applications, further steps have to be conducted which will be detailed in this work.

At last, we wish to point out the difficulties of dealing with real traffic data. From an application point of view, traffic departments and drivers are typically interested in reasonable travel time predictions for a better traffic management. Thus, a good speed reconstruction performance of the model is desirable. However, the traffic speed is sometimes not directly measured by loop and other fixed detectors and it is therefore a derived quantity. For this reason, a performance evaluation based on the speed can be challenging [WYG$^+$22]. Additionally, the access to real travel times is mostly restricted or even not available [KCB00], limiting the validation of the model against real data. As a replacement, the travel times can be reconstructed by average loop detector data (see e.g. [RVZ04]), which is not always easy to justify, especially in complex traffic scenarios involving congestion, lane changes and ramps [TK14]. As a result, several papers test their approach by considering artificially constructed data as in [PS15, SMD21]. There, the data are either simulated by a macroscopic model, where some noise is typically added to create more realistic scenarios. Otherwise, data can also be generated by a microscopic simulator as in this thesis and for example in [IK09], where they exploit an agent-based traffic simulator developed at IBM in Tokyo.

Contribution and structure of the thesis

In Chapter 1, we prove the existence of entropy weak solutions of the IBVP for (I) with possibly characteristic boundaries for BV initial and boundary data on domains including vacuum states. After introducing the Riemann solver based on [ADR16] in Section 1.1, in Section 1.2 we describe the sets of admissible traces at the boundaries given both by the Riemann solver and the boundary entropy inequality. Based on the available entropy families, we can prove the equivalence of these conditions at the right boundary, while at the left boundary the two sets differ for a subset of the vacuum states. This analysis ensures that the wave-front tracking approximations constructed in Section 1.3.1 are approximate entropy weak solutions in the sense of [CF99a, CF99b]. Finally, uniform BV bounds allow to pass to the limit in the sequence of approximate solutions in Section 1.3.2, thus guaranteeing the desired existence result. The content of this chapter is published as

> [GW23] P. Goatin and A. Würth. *The initial boundary value problem for second order traffic flow models with vacuum: existence of entropy weak solutions.* Nonlinear Analysis, 2023.

In Chapter 2, we introduce the numerical schemes used to compute approximate solutions of the IBVP. In addition to the classically applied Godunov scheme (see Section 2.1) including ramp contributions, we recall in Section 2.2 the approximate Godunov method based on Harten, Lax and van Leer [HLvL83]. Then, in Section 2.3, we extend the finite volume numerical scheme proposed by Hilliges and Weidlich [HW95] to second order traffic flow models consisting in 2×2 systems of non strictly hyperbolic conservation laws of Temple class. It can be seen as a cheap and easy to implement scheme, which performs faster than the previous ones while showing a similar performance. This is demonstrated in the numerical tests in Section 2.6. Moreover, in Section 2.4 we state two possible implementations of boundary conditions, followed by a projection algorithm in case of data outliers in Section 2.5. Parts of this chapter are published as

> [WBG23] M. Binois, P. Goatin and A. Würth. *Validation of calibration strategies for macroscopic traffic flow models on synthetic data.* MT-ITS 2023 Proceedings, 2023.
>
> [WGV23] P. Goatin, L. M. Villada and A. Würth. *A cheap and easy-to-implement upwind scheme for second order traffic flow models.* HYP2023 Proceedings, 2023.
>
> [WBGG22] M. Binois, P. Goatin, S. Göttlich and A. Würth. *Data-driven uncertainty quantification in macroscopic traffic flow models.* Advances in Computational Mathematics, 2022.

After introducing some notation, Chapter 3 provides an introduction to GP modeling. We explain in Section 3.2.1 how the typically considered formulas can be exploited for a performance gain and prediction improvement. Then, we give an overview of the calibration approaches that will be applied in the last chapters. In general, we distinguish the classical fundamental fit approach from methods involving the PDE system. We emphasize that the presented approaches refers to off-line (and not real-time) parameter identification for traffic state reconstruction, which is usually addressed with other data assimilation techniques such as extensions of Kalman filter (see e.g. [WP05]) or more general particle filtering [PS15]. Parts of this chapter are published as

[WBGG22] M. Binois, P. Goatin, S. Göttlich and A. Würth. *Data-driven uncertainty quantification in macroscopic traffic flow models.* Advances in Computational Mathematics, 2022.

Chapter 4 introduces the concepts of traffic estimation and prediction, focusing on prediction. As already pointed out, real travel time data are rarely available; this problem is addressed in Section 4.1: if trajectory data are available, an averaging procedure is performed to generate the travel times used in the validation; otherwise, methods based on aggregated data are considered, as discussed in 4.1.2. We then present the statistical approaches used to approximate the reference travel times. For this, we distinguish between data- and model-driven approaches. Finally, we propose a hybrid method, which overcomes some difficulties appearing in already existing approaches (see e.g. [CCZW22, CHOS21, LWK$^+$22]): it is applicable to all kind of (non-)linear PDEs and the set of unknown parameters do not increase compared to the pure GP modeling. The method is based on multi-objective optimization (MOO), where the second objective reminds of the residual function in the PINNs approach. However, in our case, we integrate a GP, which is computationally very efficient, especially when dealing with large amount of data.

In Chapter 5, we describe two traffic data sets that will be considered for the validation of the proposed calibration and prediction approaches in Chapter 6. The analysis will be performed with purely synthetic data generated by a microscopic simulator. This enables us to have access to reference travel times to validate our prediction approaches. Additionally, we also consider a real world traffic data set from a highway section in Minnesota (USA). However, in this case, trajectory data are not available, thus we can solely test our approaches for the reconstruction of coarser grained data. We remark that this work is only applicable to short stretches of roadways, otherwise more complex models would be necessary to capture sufficiently the road dynamics.

Finally, we close this thesis by stating a conclusion and presenting topics for future work.

Chapter 1

The initial boundary value problem for second order traffic flow models with vacuum: existence of entropy weak solutions

In this chapter we prove the existence of entropy weak solutions of the initial boundary value problem (IBVP) for (I) on a bounded interval $]x_{in}, x_{out}[\subset \mathbb{R}$, namely

$$\begin{cases} \partial_t \rho + \partial_x(\rho v) = 0, \\ \partial_t(\rho w) + \partial_x(\rho w v) = 0, \end{cases} \qquad x \in]x_{in}, x_{out}[,\ t > 0, \tag{1.0.1a}$$

$$(\rho, w)(0, x) = (\rho_0, w_0)(x), \qquad x \in]x_{in}, x_{out}[, \tag{1.0.1b}$$

$$(\rho, w)(t, x_{in}) = (\rho_{in}, w_{in})(t), \qquad t > 0, \tag{1.0.1c}$$

$$(\rho, w)(t, x_{out}) = (\rho_{out}, w_{out})(t), \qquad t > 0, \tag{1.0.1d}$$

for initial and boundary data of bounded variation on domains including vacuum states. This study has been detailed in [GW23]. To the best of our knowledge previous results in the literature concerning IBVPs do not apply in the present setting, since (1.0.1a) is non-strictly hyperbolic and the boundaries (1.0.1c) and (1.0.1d) can be characteristic [Ama97].

1.1 The Riemann solver for the GSOM model

The invariant domain of our IBVP setting (1.0.1) has the form

$$\Omega := \left\{ U = (\rho, w) \in \mathbb{R}^2 \colon \rho \in [0, R(w_{max})], w \in [w_{min}, w_{max}] \right\}, \tag{1.1.1}$$

for some $0 < w_{min} \leq w_{max} < +\infty$.
Under the above hypotheses (II), system (I) is non-strictly hyperbolic with eigenvalues

$$\lambda_1(\rho, w) = \mathcal{V}(\rho, w) + \rho \mathcal{V}_\rho(\rho, w), \qquad \lambda_2(\rho, w) = \mathcal{V}(\rho, w), \tag{1.1.2}$$

which coalesce at vacuum states, i.e. $\rho = 0$, leading to instabilities [AR00, Section 4]. The corresponding eigenvectors

$$r_1(\rho, w) = \begin{pmatrix} -1 \\ 0 \end{pmatrix}, \qquad r_2(\rho, w) = \begin{pmatrix} \mathcal{V}_w(\rho, w) \\ -\mathcal{V}_\rho(\rho, w) \end{pmatrix}. \tag{1.1.3}$$

Moreover, the GSOM system can be related to the Temple class [Tem83] since the first characteristic field is genuinely non-linear (i.e. $\nabla^\top \lambda_1(\rho, w) \cdot r_1(\rho, w) \neq 0$ for all $(\rho, w) \in \Omega$ [Bre00]) with coinciding shock and rarefaction curves and the second one is linearly degenerate (i.e. $\nabla^\top \lambda_2(\rho, w) \cdot r_2(\rho, w) = 0$ for all $(\rho, w) \in \Omega$) but not straight. The associated Riemann invariants [Daf05, Chapter 7.3] are

$$z_1(\rho, w) = \mathcal{V}(\rho, w), \qquad z_2(\rho, w) = w\,.$$

Due to $\mathcal{V}_\rho(\rho, w) < 0$ and $\mathcal{V}(0, w) = w$, the range of $v = \mathcal{V}(\rho, w)$ is given by $v \in [0, w]$ for any $w \in [w_{min}, w_{max}]$. Therefore, the inverse function $\rho = \mathcal{R}(v, w)$ is uniquely defined in the invariant domain

$$\mathcal{W} := \Big\{ W = (v, w) \in \mathbb{R}^2 \colon 0 \leq v \leq w, w \in [w_{min}, w_{max}] \Big\}. \tag{1.1.4}$$

Following [ADR16], the vacuum set, i.e. $\rho = 0$, corresponds to $\mathcal{W}_0 := \{(v, w) \in \mathcal{W} : v = w\}$ and the non-vacuum set is denoted $\mathcal{W}_0^c = \mathcal{W} \setminus \mathcal{W}_0$.
For later use in the definition of boundary conditions and in the construction of approximate solutions, we recall in this section the definition of the Riemann solver for the GSOM model (I) with initial conditions of the form

$$(\rho, w)(0, x) = \begin{cases} U_L = (\rho_L, w_L) & \text{if } \ x < 0, \\ U_R = (\rho_R, w_R) & \text{if } \ x > 0, \end{cases} \tag{1.1.5}$$

and their corresponding velocities denoted by $v_L = \mathcal{V}(\rho_L, w_L)$, $v_R = \mathcal{V}(\rho_R, w_R)$.
It is well known that the solution of a Riemann problem is based on the theory of elementary waves [Lax57], such as rarefaction waves, shock waves and contact discontinuities. To define the solution, we introduce the notion of intermediate state $U_M = (\rho_M, w_M)$: in general, the left state U_L is connected to U_M by a first family wave (rarefaction or shock), i.e. $z_2(\rho_L, w_L) = z_2(\rho_M, w_M)$, while U_M is connected to the right state U_R by a contact-discontinuity with $z_1(\rho_M, w_M) = v_M = \mathcal{V}(\rho_M, w_M) = v_R = z_1(\rho_R, w_R)$. Thus, the intermediate state U_M is identified by the system of equations

$$\begin{cases} w_M = w_L, \\ v_M = v_R, \\ \rho_M = \mathcal{R}(v_R, w_L). \end{cases}$$

If $w_L \leq v_R$, we set $\rho_M = 0$, meaning that U_M corresponds to the vacuum. This case is treated separately in Definition 1 (see case 6).

Remark 1. The propagation speed σ_s of a shock wave between two states U_- and U_+ is given by the Rankine-Hugoniot condition

$$\sigma_s(U_-, U_+) = \frac{\rho_+ v_+ - \rho_- v_-}{\rho_+ - \rho_-}. \tag{1.1.6}$$

In this work, we will rely on the following solutions of (I), (1.1.5).

Definition 1 ([ADR16])**.** *For any $U_L, U_R \in \Omega$, the Riemann solver*

$$\mathcal{RS} : \Omega \times \Omega \to \mathbf{C^0}\left(]0, +\infty[; \mathbf{L}^1_{loc}(\mathbb{R}; \Omega)\right), \qquad (U_L, U_R) \mapsto \mathcal{RS}(U_L, U_R)$$

is defined as follows:

1. *If $(v_L, w_L), (v_R, w_R) \in \mathcal{W}_0^c$, $w_L = w_R$ and $v_L > v_R$, then*

$$\mathcal{RS}(U_L, U_R)(t, x) = \begin{cases} U_L & \text{if } x < \sigma_s(U_L, U_R)t, \\ U_R & \text{if } x > \sigma_s(U_L, U_R)t, \end{cases}$$

   with σ_s defined in (1.1.6)*.*

2. *If $(v_L, w_L), (v_R, w_R) \in \mathcal{W}_0^c$, $w_L \neq w_R$ and $v_L > v_R$, then*

$$\mathcal{RS}(U_L, U_R)(t, x) = \begin{cases} U_L & \text{if } x < \sigma_s(U_L, U_M)t, \\ U_M & \text{if } \sigma_s(U_L, U_M)t < x < v_R t, \\ U_R & \text{if } x > v_R t, \end{cases}$$

   with σ_s defined in (1.1.6)*.*

3. *If $(v_L, w_L), (v_R, w_R) \in \mathcal{W}_0^c$, $w_L = w_R$ and $v_L < v_R$, then*

$$\mathcal{RS}(U_L, U_R)(t, x) = \begin{cases} U_L & \text{if } x < \lambda_1(\rho_L, w_L)t, \\ \hat{U} & \text{if } \lambda_1(\rho_L, w_L)t < x < \lambda_1(\rho_R, w_R)t, \\ U_R & \text{if } \lambda_1(\rho_R, w_R)t < x, \end{cases}$$

   with $\hat{U} = (\rho, w_L)$ solving $\lambda_1(\rho, w_L) = \frac{x}{t}$.

4. *If $(v_L, w_L), (v_R, w_R) \in \mathcal{W}_0^c$, $w_L \neq w_R$ and $v_L < v_R < w_L$, then*

$$\mathcal{RS}(U_L, U_R)(t, x) = \begin{cases} U_L & \text{if } x < \lambda_1(\rho_L, w_L)t, \\ \hat{U} & \text{if } \lambda_1(\rho_L, w_L)t < x < \lambda_1(\rho_M, w_M)t, \\ U_M & \text{if } \lambda_1(\rho_M, w_M)t < x < v_R t, \\ U_R & \text{if } x > v_R t, \end{cases}$$

   with $\hat{U} = (\rho, w_L)$ solving $\lambda_1(\rho, w_L) = \frac{x}{t}$.

5. *If $(v_L, w_L), (v_R, w_R) \in \mathcal{W}_0^c$ and $v := v_L = v_R$, then*

$$\mathcal{RS}(U_L, U_R)(t, x) = \begin{cases} U_L & \text{if } x < vt, \\ U_R & \text{if } x > vt. \end{cases}$$

6. *If* $(v_L, w_L), (v_R, w_R) \in \mathcal{W}_0^c$ *and* $w_L \leq v_R$, *then*

$$\mathcal{RS}(U_L, U_R)(t,x) = \begin{cases} U_L & \text{if } x < \lambda_1(\rho_L, w_L)t, \\ \hat{U} & \text{if } \lambda_1(\rho_L, w_L)t < x < \lambda_1(\rho_M, w_M)t, \\ U_M & \text{if } \lambda_1(\rho_M, w_M)t < x < v_R t, \\ U_R & \text{if } x > v_R t, \end{cases}$$

with $\hat{U} = (\rho, w_L)$ *solving* $\lambda_1(\rho, w_L) = \frac{x}{t}$ *and* $U_M = (0, w_L)$.

7. *If* $(v_L, w_L) \in \mathcal{W}_0$ *and* $(v_R, w_R) \in \mathcal{W}_0^c$, *then*

$$\mathcal{RS}(U_L, U_R)(t,x) = \begin{cases} U_L & \text{if } x < v_R t, \\ U_R & \text{if } x > v_R t. \end{cases} \tag{1.1.7}$$

8. *If* $(v_L, w_L) \in \mathcal{W}_0^c$ *and* $(v_R, w_R) \in \mathcal{W}_0$, *then*

$$\mathcal{RS}(U_L, U_R)(t,x) = \begin{cases} U_L & \text{if } x < \lambda_1(\rho_L, w_L)t, \\ \hat{U} & \text{if } \lambda_1(\rho_L, w_L)t < x < \lambda_1(0, w_L)t, \\ \tilde{U}_R & \text{if } \lambda_1(0, w_L)t < x, \end{cases} \tag{1.1.8}$$

with $\hat{U} = (\rho, w_L)$ *solving* $\lambda_1(\rho, w_L) = \frac{x}{t}$ *and* $\tilde{U}_R = (0, w_L)$.

9. *If* $(v_L, w_L) \in \mathcal{W}_0$ *and* $(v_R, w_R) \in \mathcal{W}_0$, *then*

$$\mathcal{RS}(U_L, U_R)(t,x) \equiv U_L. \tag{1.1.9}$$

Remark 2. We emphasize that in case 7 of Definition 1, if $\rho_M \neq 0$ (i.e. $w_L > v_R$) the solution is either a juxtaposition of a shock wave and a contact discontinuity (if $w_L \neq w_R$) or a shock wave with $U_R = U_M$ (if $w_L = w_R$). The speed of the wave connecting U_L to U_M is given by $\sigma_s(U_L, U_M) = \frac{\rho_M v_M - \rho_L v_L}{\rho_M - \rho_L} \overset{\rho_L = 0}{=} v_M = v_R$. Thus, the solution can be also seen as a contact discontinuity. This justifies the definition of the Riemann solver in (1.1.7).

Remark 3. Case 8 of Definition 1 is based on [ADR16], see also [AR00, Section 3, Case 4]. The solution in the right vacuum case is obtained by a rarefaction wave independent of $v_R = w_R$. The right state $\tilde{U}_R$ of the solution is not the original state U_R anymore since the speed v and the Lagrangian vehicle property w are set equal to w_L (see Figure 1.1). This choice is the one best matching real observations: if the road is empty downstream, for example when a traffic light turns green, the solution is expected to be a rarefaction wave, and not a juxtaposition of a rarefaction wave and contact discontinuity or vacuum wave as it is proposed in [Fan13] (see Figure 1.2a and 1.2b). Nevertheless, this choice is not compatible with Case 7: the solution to piece-wise constant initial data consisting of threes states U_L, U_M and U_R, with $U_M = (0, w_M)$, can be constructed by gluing together the Riemann solutions defined in Cases 7 and 8 if and only if $w_M = w_L$. This is why, for the construction of approximate solutions in Section 1.3.1, we will need well-prepared initial data (see Remark 13), as in [ADR16, Section 2.1]. Moreover, the choice made in Case 8 do not provide a $\mathbf{L^1}$-stable Riemann solver close to the vacuum.

The solution for the case $v_L = v_R = w_R$ (resp. $v_R = w_R < v_L$) could also consist of a contact discontinuity (resp. shock wave and contact discontinuity) to U_R (see resp. Figure 1.2c and Figure 1.2d) instead of a rarefaction wave to the state $\tilde{U}_R$. This would be consistent with the structure of the solutions corresponding to U_R close to the vacuum (with $\rho_R > 0$), guaranteeing the $\mathbf{L^1}$ continuity of the Riemann solver. We emphasize that, as remarked in [ADR16], the set of entropies considered later does not allow to select a unique solution when vacuum is involved. However, the above mentioned alternative choices look unrealistic for traffic applications.

Remark 4. Case 9 of Definition 1 is motivated by coherence with case 8. In general, from a practical point of view, the interpretation of the speed v and the Lagrangian vehicle property w is lost in the vacuum.

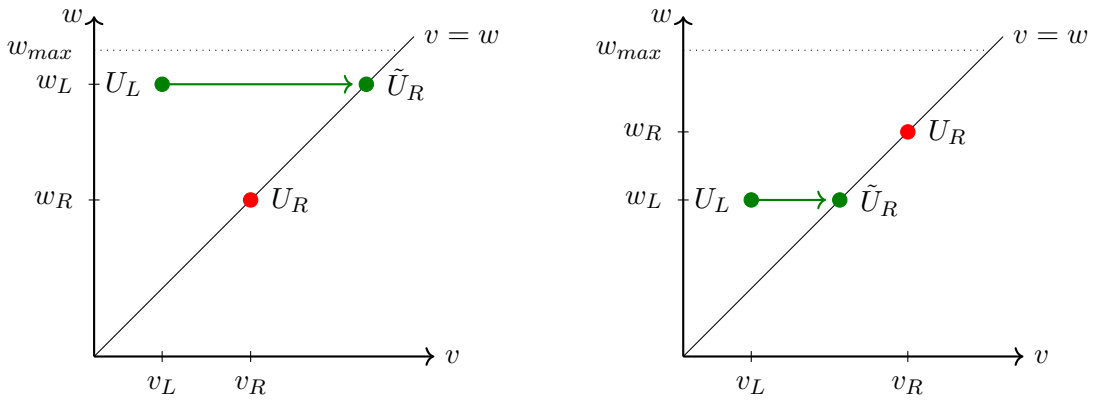

(a) $v_R = w_R < w_L$ (b) $w_L \leq v_R = w_R$

Figure 1.1: Definition 1, case 8: the solution consists of a rarefaction wave from U_L to $\tilde{U}_R$.

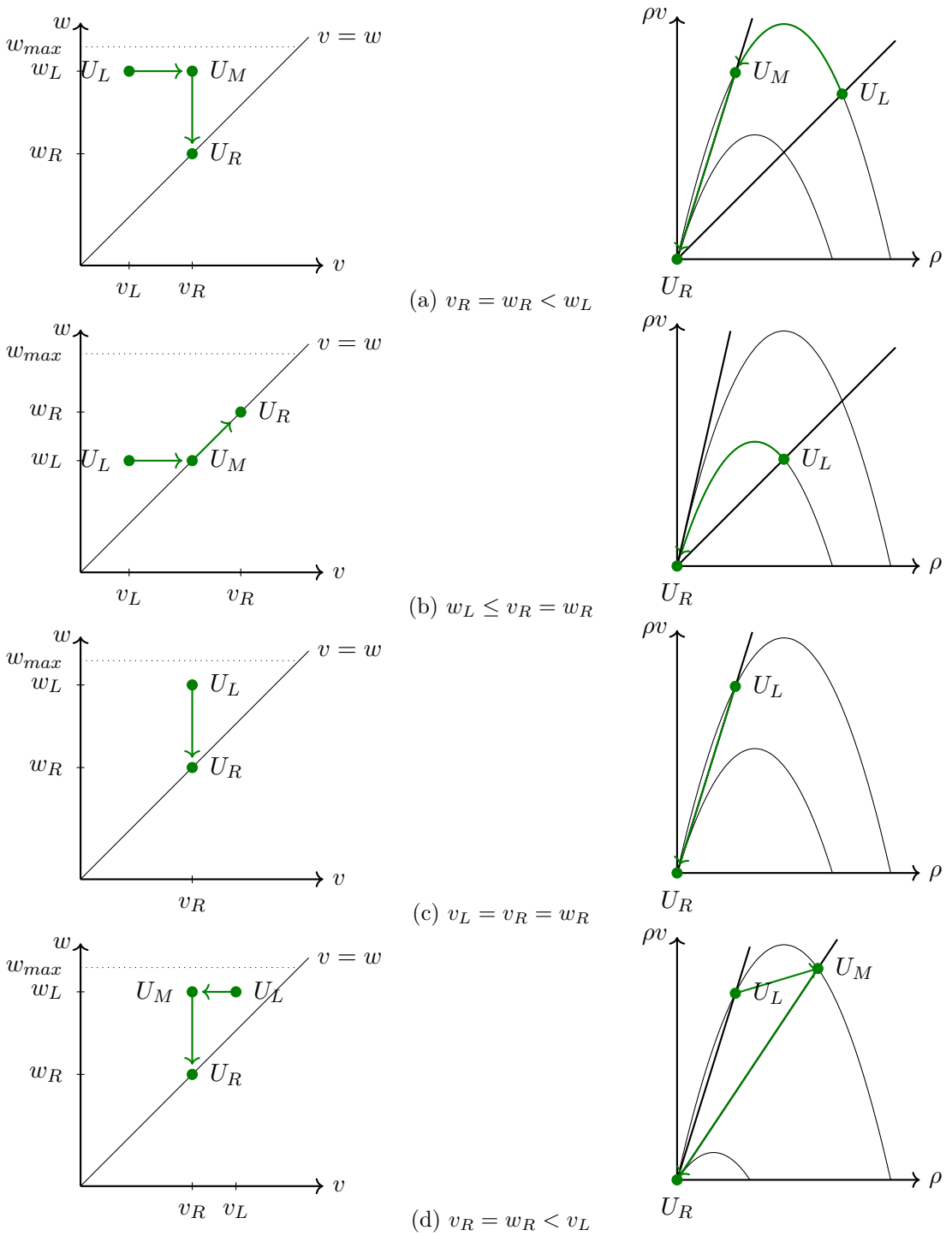

Figure 1.2: Alternative solutions for the right vacuum case illustrated in (v, w)-plane (left column) and $(\rho, \rho v)$-plane (right column). (a) A rarefaction wave from U_L to U_M and a contact discontinuity from U_M to U_R. (b) A rarefaction wave from U_L to U_M and a vacuum wave from U_M to U_R. (c) A contact discontinuity from state U_L to U_R. (d) A shock wave from U_L to U_M and a contact discontinuity from U_M to U_R.

1.2 Admissible boundary sets

Since we are dealing with an initial boundary value problem, we describe in this section the sets of admissible values for both the left and right boundaries of (1.0.1).
In the literature, two definitions of boundary conditions for systems of conservation laws are commonly considered: a *boundary entropy inequality* derived by viscosity approximation [BlRN79, Ben86] and a *Riemann boundary condition* based on the Riemann solver associated to (I). In [AG02, BS87, DLF88] several results are provided in order to prove the equivalence between those two. However, we emphasize that these results do not apply in the present setting, since (1.0.1a) is non-strictly hyperbolic and the boundaries (1.0.1c) and (1.0.1d) can be characteristic [Ama97] meaning that waves can be parallel to the boundary, so $\lambda_1(\rho, w) = 0$.

1.2.1 Riemann boundary sets

On the left boundary, only the states (ρ_0, w_0) reachable from a constant boundary datum (ρ_B, w_B) with non-positive waves in the Riemann problem (I), (1.1.5) with data

$$(\rho, w)(0, x) = \begin{cases} (\rho_B, w_B) & \text{if } x < x_{in}, \\ (\rho_0, w_0) & \text{if } x > x_{in}, \end{cases}$$

are admissible. Since second family wave speeds are positive, except those with zero speed, the remaining admissible waves are shock or rarefactions of the first family with non-positive speed. In this case, the admissible states at the left boundary belong to the curve

$$w = w_B. \tag{1.2.1}$$

From (II.b) we know that the curve (1.2.1) is strictly concave in the $(\rho, \rho v)$-plane. In particular, there exists a *critical density* $\rho_{cr}(w)$ which maximizes the flow ρv on the curve (1.2.1), i.e.

$$\rho_{cr}(w) = \operatorname*{argmax}_{\rho} Q(\rho, w) = \operatorname*{argmax}_{\rho} \big(\rho \mathcal{V}(\rho, w)\big) \quad \text{for any } w \in [w_{min}, w_{max}]. \tag{1.2.2}$$

Additionally, there exists a unique density $\tau(\rho) \neq \rho$ such that $Q(\tau(\rho), w) = Q(\rho, w)$ for each $\rho \neq \rho_{cr}(w)$ and any $w \in [w_{min}, w_{max}]$.

Remark 5. From a geometrical point of view, it is worth noticing that the slope of the tangent to the curve (1.2.1) in the $(\rho, \rho v)$-plane coincides with the first eigenvalue, indeed

$$Q_\rho(\rho, w) = \mathcal{V}(\rho, w) + \rho \mathcal{V}_\rho(\rho, w) = \lambda_1(\rho, w) \quad \text{for any } w \in [w_{min}, w_{max}].$$

Moreover, the slope of the secant between any two points, U_- and U_+, in the $(\rho, \rho v)$-plane is given by the shock wave speed (1.1.6).

Proposition 1 describes the admissible states on the left boundary (see also [HB07, HMR06]):

Proposition 1. *Let $U_B := (\rho_B, w_B) \in \Omega$ with $\rho_B > 0$ be the left boundary datum at $x = x_{in}$. The Riemann admissible boundary set $\mathcal{B}_L^{Rie}(\rho_B, w_B)$ is composed of the following states $U_0 = (\rho_0, w_0)$:*

- $w_0 = w_B$ *and*

  1. *if* $\rho_B < \rho_{cr}(w_B)$*:* $U_0 = U_B$ *or* $\rho_0 \geq \tau(\rho_B)$ *(see Figure 1.3a);*
  2. *if* $\rho_B \geq \rho_{cr}(w_B)$*:* $\rho_0 \geq \rho_{cr}(w_B)$ *(see Figure 1.3b);*

- *the set of points* $\{U_0 = (R(w_0), w_0) \colon w_0 \in [w_{min}, w_{max}]\}$*, which can be reached from* U_B *with a negative 1-shock to* $(R(w_B), w_B)$*, followed by a contact discontinuity with zero speed.*

In the vacuum case $\rho_B = 0$ *and* $v_B = \mathcal{V}(0, w_B) = w_B$*, then the admissible states are* $U_0 = U_B$ *and* $\{U_0 = (R(w_0), w_0) \colon w_0 \in [w_{min}, w_{max}]\}$ *(contact discontinuity with zero speed) (see Figure 1.3c).*

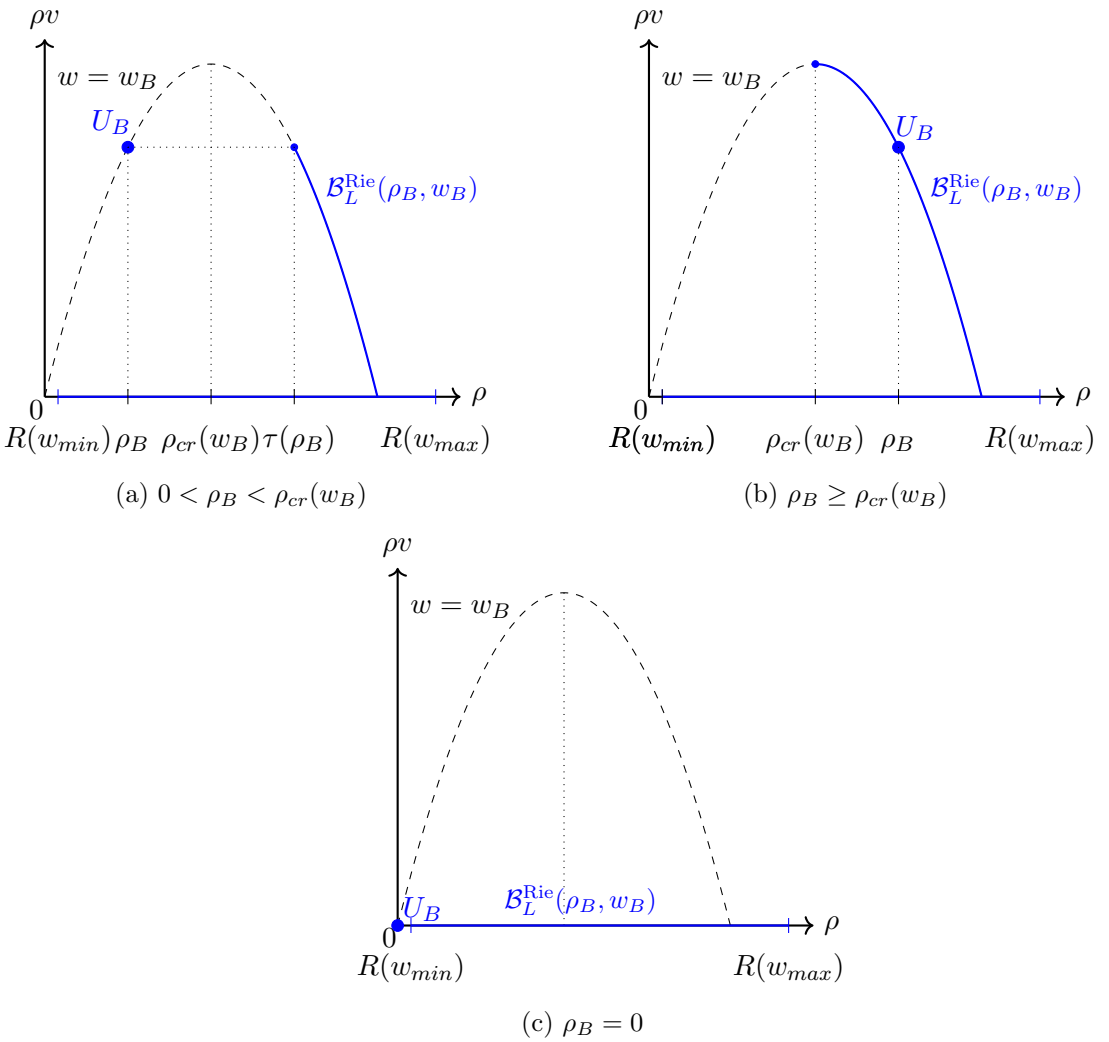

(a) $0 < \rho_B < \rho_{cr}(w_B)$

(b) $\rho_B \geq \rho_{cr}(w_B)$

(c) $\rho_B = 0$

Figure 1.3: Riemann admissible boundary sets $\mathcal{B}_L^{\mathrm{Rie}}(\rho_B, w_B)$ at the left boundary.

Concerning the right boundary, first and second family curves with non-negative wave speeds

are admissible when solving the Riemann problem (I), (1.1.5) with data

$$(\rho, w)(0, x) = \begin{cases} (\rho_0, w_0) & \text{if } x < x_{out}, \\ (\rho_B, w_B) & \text{if } x > x_{out}\,. \end{cases}$$

The admissible set will thus be 2-dimensional.

Proposition 2. *Let $U_B := (\rho_B, w_B) \in \Omega$ with $\rho_B > 0$ be the right boundary datum at $x = x_{out}$. Then, the Riemann admissible boundary set $\mathcal{B}_R^{Rie}(\rho_B, w_B)$ is composed of the states $U_0 = (\rho_0, w_0)$ such that (see Figure 1.4a):*

- $z_1(\rho_0, w_0) = v_B$;
- $\mathcal{V}(\rho_{cr}(w_0), w_0) \leq v_B$ *and* $\rho_0 \leq \rho_{cr}(w_0)$;
- $\mathcal{V}(\rho_{cr}(w_0), w_0) > v_B$ *and* $\rho_0 \leq \tau(\mathcal{R}(v_B, w_0))$.

In the vacuum case $\rho_B = 0$ and $v_B = \mathcal{V}(0, w_B) = w_B$, then U_0 is admissible if and only if $\rho_0 \leq \rho_{cr}(w_0)$ (rarefaction wave with non-negative speed, see Figure 1.4b).

Remark 6. We emphasize that in Proposition 2 we do not need to distinguish between two different cases for the vacuum case $\rho_B = 0$ (in contrast to $\rho_B > 0$), due to the definition of the Riemann solver (case 8 in Definition 1): the solution is always a rarefaction wave.

Remark 7. In the case $\rho_B > 0$, any state on the curve $\{z_1(\rho, w) = v_B\}$ is admissible since we can connect it to ρ_B by a contact discontinuity (see case 5 in Definition 1).

Remark 8. We note that the right Riemann boundary set $\mathcal{B}_R^{Rie}(\rho_B, w_B)$ is independent of the variable w_B, i.e. $\mathcal{B}_R^{Rie}(\rho_B, w_B) = \mathcal{B}_R^{Rie}\big(\mathcal{R}(v_B, w), w\big)$ for all $w \in [w_{min}, w_{max}]$, with $v_B = \mathcal{V}(\rho_B, w_B)$. This holds for all $(\rho_B, w_B) \in \Omega$.

1.2.2 Entropy boundary sets

Defining $u = (\rho, \rho w)^\top \in \tilde{\Omega}$ with $\tilde{\Omega} = \big\{(\rho, \rho w) \in \mathbb{R}^2 \colon \rho \in [0, R(w_{max})], w \in [w_{min}, w_{max}]\big\}$ and $f(u) = (\rho v, \rho w v)^\top$, system (I) can be written more compactly as

$$\partial_t u + \partial_x f(u) = 0, \qquad x \in \mathbb{R},\ t > 0\,. \tag{1.2.3}$$

The definition of admissible values at the boundary is based on the notion of boundary entropy inequality [BlRN79, DLF88]:

Definition 2. *For each boundary state $u_B = (\rho_B, \rho_B w_B) \in \tilde{\Omega}$, the set of entropy admissible values at the left (resp. right) boundary, denoted by $\mathcal{B}_L^{Ent}(\rho_B, w_B)$ (resp. $\mathcal{B}_R^{Ent}(\rho_B, w_B)$), is defined as all the states $u = (\rho, \rho w) \in \tilde{\Omega}$ satisfying*

$$\beta(u, u_B) = \mathcal{Q}(u) - \mathcal{Q}(u_B) - \nabla\mathcal{E}(u_B) \cdot \{f(u) - f(u_B)\} \leq (\geq)\ 0, \tag{1.2.4}$$

for each entropy-flux pair $(\mathcal{E}, \mathcal{Q})$.

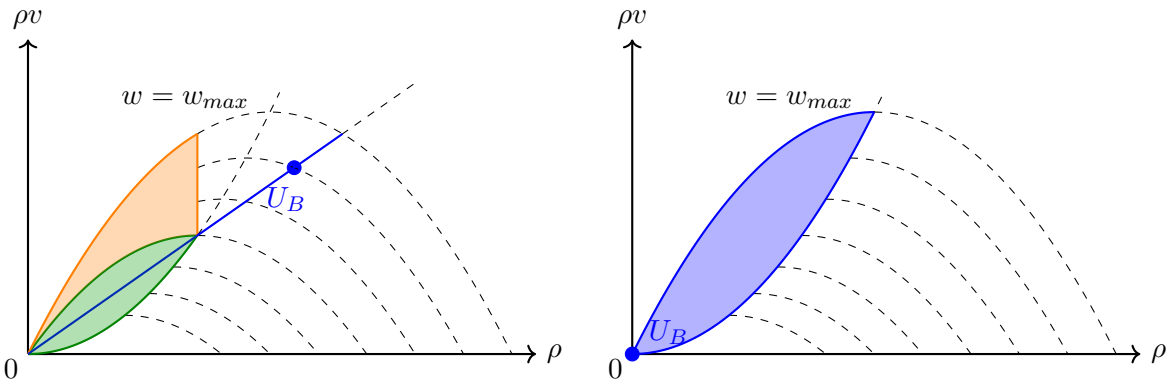

(a) $\rho_B > 0$ (b) $\rho_B = 0$

Figure 1.4: Riemann admissible boundary sets $\mathcal{B}_R^{\mathrm{Rie}}(\rho_B, w_B)$ at the right boundary for $Q(\rho, w) = \rho(w - \rho)$.
(a) The green (resp. orange) region refers to case $\mathcal{V}(\rho_{cr}(w_0), w_0) \leq v_B$ (resp. $\mathcal{V}(\rho_{cr}(w_0), w_0) > v_B$) in Proposition 2. The blue line represents the admissible points on the curve $\{z_1(\rho, w) = v_B\}$.
(b) The admissible region for the vacuum boundary datum is indicated in blue.

Following [Daf05, Section 7.4], we seek for entropy-flux pairs $(\mathcal{E}^j, \mathcal{Q}^j)$, $j \in \{1, 2\}$, which are functions of the Riemann invariants $W = (v, w)$, then setting $u = u(W)$. In particular, we consider the family of entropy-flux pairs derived in [ADR16, Equation 2.13]:

$$\mathcal{E}^1(u(W)) = \begin{cases} 0 & \text{if } v \leq \bar{v}, \\ 1 - \frac{\mathcal{R}(v,w)}{\mathcal{R}(\bar{v},w)} & \text{if } v > \bar{v}, \end{cases} \tag{1.2.5a}$$

$$\mathcal{Q}^1(u(W)) = \begin{cases} 0 & \text{if } v \leq \bar{v}, \\ \bar{v} - \frac{v\mathcal{R}(v,w)}{\mathcal{R}(\bar{v},w)} & \text{if } v > \bar{v}, \end{cases} \tag{1.2.5b}$$

for any $\bar{v} \in [0, w_{max}]$.
Additionally, we consider the pairs identified by the left eigenvector $l_2(u(W)) = \begin{pmatrix} w & -1 \end{pmatrix}$ (see [Ser96, Chapter 13]):

$$\mathcal{E}^2(u(W)) = |l_2(u(\bar{W})) \cdot \big(u(W) - u(\bar{W})\big)| = \mathcal{R}(v, w)|\bar{w} - w|, \tag{1.2.6a}$$

$$\begin{aligned} \mathcal{Q}^2(u(W)) &= l_2(u(\bar{W})) \cdot \big(f(u(W)) - f(u(\bar{W}))\big) \operatorname{sgn}\Big(l_2(u(\bar{W})) \cdot \big(u(W) - u(\bar{W})\big)\Big) \\ &= v\mathcal{R}(v, w)|\bar{w} - w|, \end{aligned} \tag{1.2.6b}$$

for any $\bar{w} \in [w_{min}, w_{max}]$.
For notational simplicity, throughout this section we will drop the u-variable dependency and we write $\mathcal{E}^j(W) = \mathcal{E}^j(v, w)$ (resp. $\mathcal{Q}^j(W) = \mathcal{Q}^j(v, w)$) instead of $\mathcal{E}^j(u(W))$ (resp. $\mathcal{Q}^j(u(W))$) and $f(W) = f(v, w) = \begin{pmatrix} \mathcal{R}(v, w)v \\ \mathcal{R}(v, w)wv \end{pmatrix}$ instead of $f(u(W))$ when possible. Thus, the entropy boundary condition (1.2.4) expressed in Riemann invariants reads

$$\beta^j(W, W_B) := \mathcal{Q}^j(W) - \mathcal{Q}^j(W_B) - \nabla_u \mathcal{E}^j(W_B) \cdot (f(W) - f(W_B)) \leq (\geq) 0\,, \tag{1.2.7}$$

for $j \in \{1, 2\}$, where

$$\nabla_u \mathcal{E}^j(W) = \nabla_u \mathcal{E}^j(v, w) = \begin{pmatrix} \frac{\partial v}{\partial \rho}\mathcal{E}^j_v(v, w) + \frac{\partial w}{\partial \rho}\mathcal{E}^j_w(v, w) \\ \frac{\partial v}{\partial y}\mathcal{E}^j_v(v, w) + \frac{\partial w}{\partial y}\mathcal{E}^j_w(v, w) \end{pmatrix},$$

with $y = \rho w$ and

$$\begin{aligned}
\frac{\partial v}{\partial \rho}(v, w) &= \frac{\partial \mathcal{V}(\rho, \frac{y}{\rho})}{\partial \rho} = \mathcal{V}_\rho(\rho, \frac{y}{\rho}) - \frac{y}{\rho^2}\mathcal{V}_w(\rho, \frac{y}{\rho}) = \mathcal{V}_\rho(\mathcal{R}(v, w), w) - \frac{w}{\mathcal{R}(v, w)}\mathcal{V}_w(\mathcal{R}(v, w), w)\,, \\
\frac{\partial v}{\partial y}(v, w) &= \frac{\partial \mathcal{V}(\rho, \frac{y}{\rho})}{\partial y} = \frac{1}{\rho}\mathcal{V}_w(\rho, \frac{y}{\rho}) = \frac{1}{\mathcal{R}(v, w)}\mathcal{V}_w(\mathcal{R}(v, w), w)\,, \\
\frac{\partial w}{\partial \rho}(v, w) &= -\frac{y}{\rho^2} = -\frac{w}{\mathcal{R}(v, w)}\,, \\
\frac{\partial w}{\partial y}(v, w) &= \frac{1}{\rho} = \frac{1}{\mathcal{R}(v, w)}\,.
\end{aligned}$$

In the case $v \neq \bar{v}$, the partial derivatives of $\mathcal{E}^1$ are given by

$$\mathcal{E}^1_v(v, w) = \begin{cases} 0 & \text{if } v < \bar{v}, \\ -\frac{\mathcal{R}_v(v,w)}{\mathcal{R}(\bar{v},w)} & \text{if } v > \bar{v}, \end{cases}$$

$$\mathcal{E}^1_w(v, w) = \begin{cases} 0 & \text{if } v < \bar{v}, \\ -\frac{\mathcal{R}_w(v,w)\mathcal{R}(\bar{v},w) - \mathcal{R}(v,w)\mathcal{R}_w(\bar{v},w)}{\mathcal{R}(\bar{v},w)^2} & \text{if } v > \bar{v}. \end{cases}$$

If $v = \bar{v}$, the sub-differential of $\mathcal{E}^1$ reads as

$$\begin{aligned}
\mathcal{E}^1_v(v, w) &= \left\{ \alpha \colon \alpha \in \left[0, -\frac{\mathcal{R}_v(v, w)}{\mathcal{R}(v, w)}\right] \right\}, \\
\mathcal{E}^1_w(v, w) &= 0.
\end{aligned}$$

By (1.2.6a), the gradient of $\mathcal{E}^2$ can be computed directly by

$$\nabla \mathcal{E}^2_u(W) = \begin{cases} l_2(u(\bar{W}))\,\operatorname{sgn}\left(l_2(u(\bar{W})) \cdot (u(W_B) - u(\bar{W}))\right) & \text{if } u(W_B) \neq u(\bar{W}), \\ \{\gamma l_2(u(\bar{W})); \gamma \in [-1, 1]\} & \text{if } u(W_B) = u(\bar{W}). \end{cases}$$

Remark 9. Deriving $\mathcal{V}(\mathcal{R}(v, w), w) = v$ with respect to v, we get

$$\mathcal{V}_\rho(\mathcal{R}(v, w), w)\mathcal{R}_v(v, w) = 1 \text{ and thus } \mathcal{R}_v(v, w) = \frac{1}{\mathcal{V}_\rho(\mathcal{R}(v, w), w)}\,.$$

Moreover, deriving $\mathcal{V}(\mathcal{R}(v, w), w) = v$ with respect to w, we obtain

$$\mathcal{V}_\rho(\mathcal{R}(v, w), w)\mathcal{R}_w(v, w) + \mathcal{V}_w(\mathcal{R}(v, w), w) = 0 \text{ and thus } \mathcal{R}_w(v, w) = -\frac{\mathcal{V}_w(\mathcal{R}(v, w), w)}{\mathcal{V}_\rho(\mathcal{R}(v, w), w)}\,.$$

Using the above identities, we can prove that (1.2.5) and (1.2.6) satisfy

$$\mathcal{Q}_v^j = \lambda_1(v,w)\mathcal{E}_v^j(v,w), \qquad \mathcal{Q}_w^j = \lambda_2(v,w)\mathcal{E}_w^j(v,w),$$

with $\lambda_1(v,w) = v + \mathcal{R}(v,w)\mathcal{V}_\rho(\mathcal{R}(v,w),w)$ and $\lambda_2(v,w) = v$, and are therefore entropy-flux pairs, see [Daf05, Equation (7.4.12)].

Finally, for $j = 1$ we obtain

$$\beta^1(W,W_B) = \begin{cases} \begin{cases} \rho v \left(\frac{1}{\mathcal{R}(\bar v, w_B)} - \frac{1}{\mathcal{R}(\bar v, w)} + \frac{1}{\mathcal{R}(\bar v, w_B)^2} \frac{\mathcal{V}_w(\mathcal{R}(\bar v, w_B), w_B)}{\mathcal{V}_\rho(\mathcal{R}(\bar v, w_B), w_B)} (w - w_B) \right) & \text{if } v > \bar v, \\ -\bar v + \rho v \left(\frac{1}{\mathcal{R}(\bar v, w_B)} + \frac{1}{\mathcal{R}(\bar v, w_B)^2} \frac{\mathcal{V}_w(\mathcal{R}(\bar v, w_B), w_B)}{\mathcal{V}_\rho(\mathcal{R}(\bar v, w_B), w_B)} (w - w_B) \right) & \text{if } v \le \bar v, \end{cases} & \text{if } v_B > \bar v, \\ \begin{cases} \bar v - \rho v \frac{1}{\mathcal{R}(\bar v, w)} & \text{if } v > \bar v, \\ 0 & \text{if } v \le \bar v, \end{cases} & \text{if } v_B < \bar v, \end{cases} \tag{1.2.8a}$$

if $\bar v \neq v_B$ and

$$\beta^1(W,W_B) = \begin{cases} \begin{cases} \rho v \left(\frac{1}{\rho_B} - \frac{1}{\mathcal{R}(v_B, w)} + \frac{1}{\rho_B^2} \frac{\mathcal{V}_w(\rho_B, w_B)}{\mathcal{V}_\rho(\rho_B, w_B)} (w - w_B) \right) & \text{if } v > v_B, \\ -v_B + \rho v \left(\frac{1}{\rho_B} + \frac{1}{\rho_B^2} \frac{\mathcal{V}_w(\rho_B, w_B)}{\mathcal{V}_\rho(\rho_B, w_B)} (w - w_B) \right) & \text{if } v \le v_B, \end{cases} & \text{if } \alpha = -\dfrac{\mathcal{R}_v(v_B, w_B)}{\mathcal{R}(v_B, w_B)}, \\ \begin{cases} v_B - \rho v \frac{1}{\mathcal{R}(v_B, w)} & \text{if } v > v_B, \\ 0 & \text{if } v \le v_B, \end{cases} & \text{if } \alpha = 0, \end{cases} \tag{1.2.8b}$$

if $\bar v = v_B$.
For $j = 2$, it holds

$$\beta^2(W,W_B) = \rho v (w - \bar w) \left(\operatorname{sgn}\left(\mathcal{R}(v_B, w_B)(\bar w - w_B) \right) - \operatorname{sgn}\left(\rho(\bar w - w) \right) \right), \tag{1.2.9a}$$

if $u(\bar W) \neq u(W_B)$ and

$$\beta^2(W,W_B) = \begin{cases} \begin{cases} 0 & \text{if } w > w_B, \\ 2\rho v (w_B - w) & \text{if } w \le w_B, \end{cases} & \text{if } \gamma = -1, \\ \begin{cases} 2\rho v (w - w_B) & \text{if } w > w_B, \\ 0 & \text{if } w \le w_B, \end{cases} & \text{if } \gamma = 1, \end{cases} \tag{1.2.9b}$$

if $u(\bar W) = u(W_B)$.
We now verify that the Riemann boundary condition implies the entropy one, as already proven in [BS87, Theorem 1].

Proposition 3. *The admissible states defined by the Riemann solver satisfy the entropy boundary condition, i.e. $\mathcal{B}_i^{Rie}(\rho_B, w_B) \subseteq \mathcal{B}_i^{Ent}(\rho_B, w_B)$ for $i \in \{L, R\}$.*

Proof. We start considering $\mathcal{B}_L^{Rie}(\rho_B, w_B)$, which is described by Proposition 1.
Let us assume first that $\rho_B > 0$ and $w_B = w$, which implies $\beta^2(W, W_B) = 0$. For $j = 1$, it suffices to consider the case $\bar v \in [\min\{v, v_B\}, \max\{v, v_B\}]$, since otherwise $\beta^1(W, W_B) = 0$.

- If $\rho_B < \rho_{cr}(w_B)$, it holds $(\rho, w) = (\rho_B, w_B)$ or $\rho \geq \tau(\rho_B)$. Therefore, we have $v \leq \bar{v} \leq v_B$, $\rho_B \leq \mathcal{R}(\bar{v}, w_B) \leq \rho$ and $\mathcal{R}(\bar{v}, w_B)\bar{v} \geq \rho v$ (see Figure 1.3a). Thus,

$$\beta^1(W, W_B) = -\bar{v} + \frac{\rho v}{\mathcal{R}(\bar{v}, w_B)} \leq 0.$$

- If $\rho_B \geq \rho_{cr}(w_B)$, it holds $\rho \geq \rho_{cr}(w_B)$. Thus, we either have $v \leq \bar{v} \leq v_B$ with $\mathcal{R}(\bar{v}, w_B)\bar{v} \geq \rho v$ and again $\beta^1(W, W_B) \leq 0$ or $v_B \leq \bar{v} < v$, $\rho < \mathcal{R}(\bar{v}, w_B) \leq \rho_B$ and $\mathcal{R}(\bar{v}, w_B)\bar{v} < \rho v$ (see Figure 1.3b), leading to

$$\beta^1(W, W_B) = \bar{v} - \frac{\rho v}{\mathcal{R}(\bar{v}, w_B)} < 0.$$

Finally, we consider the set of points

$$\left\{(R(w), w) \colon w \in [w_{min}, w_{max}]\right\}.$$

Since $v = 0$, it holds $\beta^2(W, W_B) = 0$. Concerning $\beta^1(W, W_B)$, the only possible cases are $0 = v \leq \bar{v} \leq v_B$ and $0 = v \leq v_B < \bar{v}$. In any case, we obtain $\beta^1(W, W_B) \leq 0$.
Let us now consider the vacuum case, i.e. $\rho_B = 0$ (see Figure 1.3c). Since $v = \mathcal{V}(R(w), w) = 0$, we get $\beta^2(W, W_B) = 0$.
If $\bar{v} \neq v_B$, it holds that $\mathcal{Q}^1(W) = 0$,

$$\mathcal{Q}^1(W_B) = \begin{cases} 0 & \text{if } v_B \leq \bar{v}, \\ \bar{v} & \text{if } v_B > \bar{v}, \end{cases}$$

and $f(W) = f(W_B) = 0$, implying $\beta^1(W, W_B) = -\mathcal{Q}^1(W_B) \leq 0$.
If $\bar{v} = v_B$, it holds $\mathcal{Q}^1(W) = \mathcal{Q}^1(W_B) = 0$ and

$$\begin{aligned} \beta^1(W, W_B) &= -\alpha \begin{pmatrix} \frac{\partial v}{\partial \rho}(W_B) \\ \frac{\partial v}{\partial y}(W_B) \end{pmatrix} \cdot \{\underbrace{f(W)}_{(0,0)^\top} - f(W_B)\} \\ &= \alpha \begin{pmatrix} \frac{\partial v}{\partial \rho}(W_B) \\ \frac{\partial v}{\partial y}(W_B) \end{pmatrix} \cdot f(W_B) \\ &= -\frac{1}{\mathcal{V}_\rho(\rho_B, w_B)\rho_B} \mathcal{V}_\rho(\rho_B, w_B)\rho_B v_B = -v_B \leq 0\,. \end{aligned}$$

If instead $\rho = 0$, implying again $\beta^2(W, W_B) = 0$, we know from the Riemann solver (Definition 1, case 9) that $(\rho, w) = (0, w) = (0, w_B) = (\rho_B, w_B)$ which directly leads to $\beta^1(W, W_B) = 0$.
This shows that $\mathcal{B}_L^{Rie}(\rho_B, w_B) \subseteq \mathcal{B}_L^{Ent}(\rho_B, w_B)$.

We now consider the right boundary case, i.e. $i = R$ (see Proposition 2). We recall that $\mathcal{B}_R^{Rie}(\rho_B, w_B) = B_R^{Rie}(\mathcal{R}(v_B, w), w)$ for all $w \in [w_{min}, w_{max}]$, with $v_B = \mathcal{V}(\rho_B, w_B)$ (see Remark 8). Therefore we can assume $w = w_B$, leading to $\beta^2(W, W_B) = 0$ due to $w = w_B$ or $\rho = 0$.
We first look at the case $\rho_B > 0$. As for the left boundary, it suffices to treat the cases $\bar{v} \in [\min\{v, v_B\}, \max\{v, v_B\}]$, otherwise we directly obtain $\beta^1(W, W_B) = 0$.

- If $\mathcal{V}(\rho_{cr}(w), w) \leq v_B$ and $\rho \leq \rho_{cr}(w)$, we either have $v_B \leq \bar{v} < v$ with $\mathcal{R}(\bar{v}, w_B)\bar{v} > \rho v$ and
$$\beta^1(W, W_B) = \bar{v} - \frac{\rho v}{\mathcal{R}(\bar{v}, w_B)} \geq 0,$$
or it holds $v \leq \bar{v} \leq v_B$, $\rho_B \leq \mathcal{R}(\bar{v}, w_B) \leq \rho$ together with $\mathcal{R}(\bar{v}, w_B)\bar{v} \leq \rho v$, which implies
$$\beta^1(W, W_B) = -\bar{v} + \frac{\rho v}{\mathcal{R}(\bar{v}, w_B)} \geq 0.$$

- If $\mathcal{V}(\rho_{cr}(w), w) > v_B$ and $\rho \leq \tau(\mathcal{R}(v_B, w))$, we have $v_B \leq \bar{v} \leq v$, $\rho \leq \mathcal{R}(\bar{v}, w_B) \leq \rho_B$ and $\mathcal{R}(\bar{v}, w_B)\bar{v} \geq \rho v$. Thus, we have again
$$\beta^1(W, W_B) = \bar{v} - \frac{\rho v}{\mathcal{R}(\bar{v}, w_B)} \geq 0.$$

Concerning the vacuum case, i.e. $\rho_B = 0$, which implies $\operatorname{sgn}\big(\rho_B(\bar{w} - w_B)\big) \in [-1, 1]$, we know that the admissible points satisfy $\rho \leq \rho_{cr}(w)$.
Moreover, since $\mathcal{B}_R^{Rie}(\rho_B, w_B) = B_R^{Rie}(\mathcal{R}(v_B, w), w)$, we can again consider $w = w_B$. For $j = 2$, we have to distinguish between $\bar{w} > w, \bar{w} < w$ and $\bar{w} = w = w_B$. In any case, we obtain $\beta^2(W, W_B) \geq 0$ in (1.2.9).
Next, assuming $\rho = \mathcal{R}(v, w) > 0$, we know that $v < v_B = w_B$.
It suffices now to consider the case $v \leq \bar{v} \leq v_B$ (and $v < v_B$) and thus $\rho v \geq \mathcal{R}(\bar{v}, w_B)\bar{v}$. It holds
$$\beta^1(W, W_B) = -\bar{v} + \frac{\rho v}{\mathcal{R}(\bar{v}, w)} \geq 0.$$
On the other hand, if $\rho = 0$, we can set $(\rho_B, w_B) = (0, w_B) = (0, w) = (\rho, w)$, which directly leads to $\beta^1(W, W_B) = 0$.
This shows that $\mathcal{B}_R^{Rie}(\rho_B, w_B) \subseteq \mathcal{B}_R^{Ent}(\rho_B, w_B)$. □

Finally, we end this section by verifying the following Proposition.

Proposition 4. *The following equalities hold for the boundary sets:*

$$\begin{aligned} \mathcal{B}_L^{Ent}(\rho_B, w_B) &= \mathcal{B}_L^{Rie}(\rho_B, w_B) \cup \mathcal{B}_L^{*}(\rho_B, w_B), \\ \mathcal{B}_R^{Ent}(\rho_B, w_B) &= \mathcal{B}_R^{Rie}(\rho_B, w_B), \end{aligned} \tag{1.2.10}$$

with $\mathcal{B}_L^{*}(\rho_B, w_B) = \{(\rho, w) \mid \rho = 0, w < w_B, \mathcal{V}(\rho, w) \leq \mathcal{V}(\rho_B, w_B)\}$.

Proof. Due to Proposition 3, it suffices to prove

1. $\mathcal{B}_L^{*}(\rho_B, w_B) \subset \mathcal{B}_L^{Ent}(\rho_B, w_B)$;
2. $\mathcal{B}_L^{Ent}(\rho_B, w_B) \subseteq \mathcal{B}_L^{Rie}(\rho_B, w_B) \cup \mathcal{B}_L^{*}(\rho_B, w_B)$;
3. $\mathcal{B}_R^{Ent}(\rho_B, w_B) \subseteq \mathcal{B}_R^{Rie}(\rho_B, w_B)$.

We treat separately the above points.

1. We observe that $\beta^2(W, W_B) = 0$ in (1.2.9a) for any $\bar{w} \in [w_{min}, w_{max}]$ since $\rho = 0$. Moreover, for any $\bar{v} \in [0, w_{max}]$, it holds in (1.2.8a) and (1.2.8b) that $\beta^1(W, W_B) \leq 0$ due to $v \leq v_B$ and $\rho = 0$.

To prove inclusion 2 and 3, we will show that for any $(\rho, w) \notin B_i^{Rie}(\rho_B, w_B)$ (and $(\rho, w) \notin \mathcal{B}_L^*(\rho_B, w_B)$ if $i = L$), there exists a $\bar{v} \in [0, w_{max}]$ or $\bar{w} \in [w_{min}, w_{max}]$ for which $(\rho, w) \notin \mathcal{B}_i^{Ent}(\rho_B, w_B)$, $i \in \{L, R\}$.

2. From Proposition 1, we observe that $\Omega \backslash \Big(\mathcal{B}_L^{Rie}(\rho_B, w_B) \cup \mathcal{B}_L^*(\rho_B, w_B) \Big) = \bigcup_{i=1}^{5} \mathcal{K}_L^i(\rho_B, w_B)$, where

$$
\begin{aligned}
\mathcal{K}_L^1(\rho_B, w_B) &= \{(\rho, w) \mid \rho \in [0, \rho_B[,\ w = w_B,\ 0 < \rho_B < \rho_{cr}(w_B)\},\\
\mathcal{K}_L^2(\rho_B, w_B) &= \{(\rho, w) \mid \rho \in\ ]\rho_B, \tau(\rho_B)[,\ w = w_B,\ 0 < \rho_B < \rho_{cr}(w_B)\},\\
\mathcal{K}_L^3(\rho_B, w_B) &= \{(\rho, w) \mid \rho < \rho_{cr}(w_B),\ w = w_B,\ \rho_B \geq \rho_{cr}(w_B)\},\\
\mathcal{K}_L^4(\rho_B, w_B) &= \{(\rho, w) \mid \mathcal{V}(\rho, w) > 0,\ w \neq w_B,\ \rho_B \geq 0\} \setminus \mathcal{B}_L^*(\rho_B, w_B),\\
\mathcal{K}_L^5(\rho_B, w_B) &= \{(\rho, w) \mid \mathcal{V}(\rho_B, w_B) \neq \mathcal{V}(\rho, w) > 0,\ w = w_B,\ \rho_B = 0\}.
\end{aligned}
$$

Thus, $(\rho, w) \notin \Big(\mathcal{B}_L^{Rie}(\rho_B, w_B) \cup \mathcal{B}_L^*(\rho_B, w_B) \Big)$ if and only if $(\rho, w) \in \bigcup_{i=1}^{5} \mathcal{K}_L^i(\rho_B, w_B)$.
Let $(\rho, w) \in \mathcal{K}_L^1(\rho_B, w_B)$. Since $v > v_B$, it holds $\rho v < \rho_B v_B$. Choosing $v_B < \bar{v} < v$, we have $\mathcal{R}(\bar{v}, w) > \rho v$ and thus, by (1.2.8a), $\beta^1(W, W_B) > 0$.
If $(\rho, w) \in \mathcal{K}_L^2(\rho_B, w_B)$, it holds $v < v_B$. Setting $\bar{v} = v_B$, we obtain $\rho v > \rho_B v_B = \mathcal{R}(\bar{v}, w_B)\bar{v}$ and, by (1.2.8b), again that $\beta^1(W, W_B) > 0$.
If $(\rho, w) \in \mathcal{K}_L^3(\rho_B, w_B)$, we have $v > v_B$. Choosing $\bar{v} = V(\rho_{cr}(w_B), w_B)$, it holds $v_B \leq \bar{v} < v$ leading to $\rho v < \mathcal{R}(\bar{v}, w)\bar{v}$ and therefore $\beta^1(W, W_B) > 0$.
If $(\rho, w) \in \mathcal{K}_L^4(\rho_B, w_B)$, we distinguish between the following two cases:

- $w > w_B$:
  - If $v > v_B$, we either have $\mathcal{R}(v_B, w) \leq \rho_{cr}(w)$, resulting in $\mathcal{R}(v_B, w)v_B > \rho v$. Choosing $\bar{v} = v_B < v$, we obtain $\beta^1(W, W_B) > 0$. Or it holds $\mathcal{R}(v_B, w) > \rho_{cr}(w)$, leading to $\mathcal{R}(\bar{v}, w)\bar{v} > \rho v$ by considering $\bar{v} = \mathcal{V}(\rho_{cr}(w), w)$. Thus, it holds again $\beta^1(W, W_B) > 0$.
  - If $0 < v \leq v_B$, we know that $\rho \neq 0$. Choosing $\bar{w} \in]w_B, w[$ implies, by (1.2.9a), $\beta^2(W, W_B) > 0$.
- $w < w_B$:
  - If $v > v_B$, we obtain with the same argumentation as in the case $w > w_B$ that $\beta^1(W, W_B) > 0$.
  - If $0 < v \leq v_B$, $\rho \neq 0$ implies $\beta^2(W, W_B) > 0$ by choosing $\bar{w} \in]w, w_B[$.

Finally, let $(\rho, w) \in \mathcal{K}_L^5(\rho_B, w_B)$. It holds $w = w_B = v_B > v$ (otherwise $(\rho, w) = (\rho_B, w_B) \in B^{Rie}(\rho_B, w_B)$). Since $0 = \rho_B v_B < \rho v$ and considering $\bar{v} = v_B$, we conclude $\beta^1(W, W_B) > 0$.
This shows that $\mathcal{B}_L^{Ent}(\rho_B, w_B) \subseteq \mathcal{B}_L^{Rie}(\rho_B, w_B) \cup \mathcal{B}_L^*(\rho_B, w_B)$.

3. By Proposition 2, we observe that $\Omega \setminus \mathcal{B}_R^{Rie}(\rho_B, w_B) = \bigcup_{i=1}^{3} \mathcal{K}_R^i(\rho_B, w_B)$, where

$$
\begin{aligned}
\mathcal{K}_R^1(\rho_B, w_B) &= \{(\rho, w) \mid \rho > \rho_{cr}(w),\ V(\rho_{cr}(w), w) \leq v_B\},\\
\mathcal{K}_R^2(\rho_B, w_B) &= \{(\rho, w) \mid \rho > \mathcal{R}(v_B, w),\ V(\rho_{cr}(w), w) > v_B\},
\end{aligned}
$$

$$\mathcal{K}_R^3(\rho_B, w_B) = \{(\rho, w) \mid \rho \in \ ]\tau(\mathcal{R}(v_B, w), \mathcal{R}(v_B, w)[,\ V(\rho_{cr}(w), w) > v_B\}.$$

Thus, $(\rho, w) \notin \mathcal{B}_R^{Rie}(\rho_B, w_B)$ if and only if $(\rho, w) \in \bigcup_{i=1}^{3} \mathcal{K}_R^i(\rho_B, w_B)$. Moreover, as in Remark 8, it holds $\mathcal{K}_R^i(\rho_B, w_B) = \mathcal{K}_R^i(\mathcal{R}(v_B, w), w)$ for $i \in \{1, 2, 3\}$, since the sets are defined by v_B. Thus it suffices to consider $w = w_B$.

Let $(\rho, w) \in \mathcal{K}_R^1(\rho_B, w_B)$. Since $v < v_B$, we choose $v < \bar{v} = \mathcal{V}(\rho_{cr}(w), w) \leq v_B$ implying $\bar{v}\mathcal{R}(\bar{v}, w_B) > \rho v$ and leading to $\beta^1(W, W_B) < 0$.
If $(\rho, w) \in \mathcal{K}_R^2(\rho_B, w_B)$ we consider $\bar{v} = v_B > v$ which results in $\rho_B v_B > \rho v$ and thus $\beta^1(W, W_B) < 0$.
Finally, let $(\rho, w) \in \mathcal{K}_R^3(\rho_B, w_B)$. Thus, taking $\bar{v} = v_B < v$, it follows $v_B\mathcal{R}(v_B, w) < \rho v$ and again $\beta^1(W, W_B) < 0$.
This shows that $\mathcal{B}_R^{Ent}(\rho_B, w_B) \subseteq \mathcal{B}_R^{Rie}(\rho_B, w_B)$.

□

Remark 10. The family of entropy-flux pairs $(\mathcal{E}^2, \mathcal{Q}^2)$ defined by (1.2.6) are essential to obtain the first equality in (1.2.10). If we considered only the family $(\mathcal{E}^1, \mathcal{Q}^1)$ constructed by (1.2.6), there would be points (away from the vacuum) which are admissible for the left entropy but not for the left Riemann boundary set: as a demonstration, we choose $Q(\rho, w) = \rho(w - \rho)$ (see Figure 1.4), $W_B = (v_B, w_B) = (1, 1.6)$, $W = (v, w) = (0.4417, 1.8)$. In this specific case, we observe for any $\bar{v} \in [0, w_{max}]$ that $\beta^1(W, W_B) \leq 0$ (see Figure 1.5). However, $(\rho, w) \notin \mathcal{B}_L^{Rie}(\rho_B, w_B)$ since $w \neq w_B$.

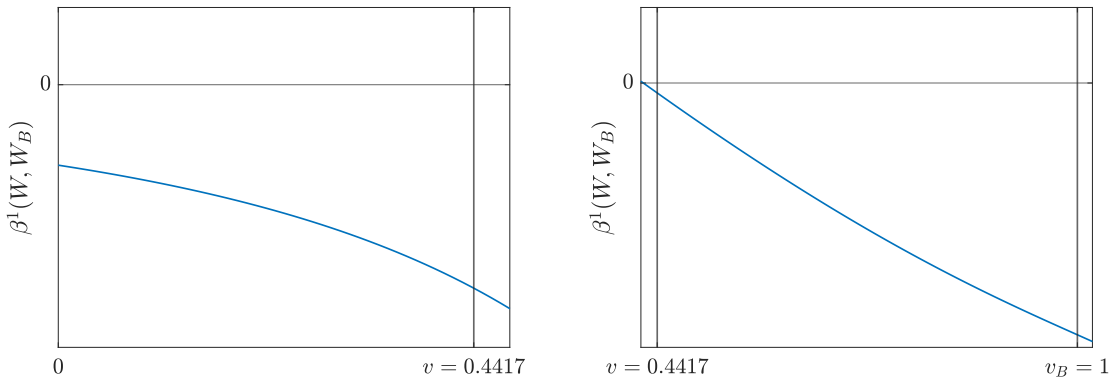

(a) $0 \leq \bar{v} < v$ (b) $v \leq \bar{v} \leq v_B$

Figure 1.5: Illustration of the entropy boundary condition $\beta^1(W, W_B)$ for a point (ρ, w) which is not admissible for the left Riemann boundary set. The case $\bar{v} > v_B$ is not depicted in the Figure since it holds $\beta^1(W, W_B) = 0$ due to (1.2.8a).

Remark 11. The chosen entropy families (1.2.5) and (1.2.6) do not provide the equality between the left Riemann and entropy boundary sets. In fact, the two sets differ for points in the vacuum positioned as in Figures 1.2c and 1.2d with respect to the boundary datum ($v_L = v_B \geq v = v_R$ and $w_L = w_B > w = w_R$), which are described by the set $\mathcal{B}_L^*(\rho_B, w_B)$. We emphasize that this is the only case, where the two sets do not coincide. Possibly, the selection of further entropies could allow to remove these unphysical states.

One could avoid this problem by setting $w = w_{max}$ whenever $\rho = 0$. However, even if this choice would allow to prove the equivalence between the two boundary sets, it cannot be guaranteed when passing to the limit in approximate solutions (as done in the proof of Proposition 7), since we can end up with vacuum states $U = (0, w)$, $w \notin w_{max}$, which do not belong to the Riemann solver.
Nevertheless, if we consider an invariant domain not including the vacuum, i.e.

$$\mathcal{W} := \left\{ W = (v, w) \in \mathbb{R}^2 \colon 0 \leq v < w, w \in [w_{min}, w_{max}], v \in [v_{min}, v_{max}], v_{max} < w_{min} \right\},$$

for some $0 \leq v_{min} < v_{max}$, it holds $\mathcal{B}_i^{Rie}(\rho_B, w_B) = \mathcal{B}_i^{Ent}(\rho_B, w_B)$ for $i \in \{L, R\}$ (and not only $i = R$). This is a new result compared to [AG02, BS87, DLF88], since it applies to a Temple class system whose characteristic lines of the second family are not straight (see Remark 12) and the boundary is possibly characteristic (the first eigenvalue can change sign).

Remark 12. Unlike in [AG02], the family of functions

$$\eta(u(W)) = |l_1(u(\bar{W})) \cdot \big(u(W) - u(\bar{W})\big)|, \quad \bar{W} \in \mathcal{W},$$

corresponding to the first left eigenvector $l_1(u) = \begin{pmatrix} \rho \mathcal{V}_\rho(\rho, w) - w \mathcal{V}_w(\rho, w) & \mathcal{V}_w(\rho, w) \end{pmatrix}$, are not of use in this setting, since the level sets of the first Riemann invariant $z_1(\rho, w)$ are not straight lines in the conservative variables $u = (\rho, y)$, see for example [AR00] in the case of the ARZ model.

1.3 Existence of entropy weak solutions

In the literature, several well-posedness results for IBVP of systems of conservation laws do already exists. We emphasize again that these results do not apply in our present setting, due to the non-strict hyperbolicity and possibly characteristic boundaries.

In the following sections, we prepare the existence proof for problem (1.0.1). Since we are dealing with entropy-flux pairs $(\mathcal{E}, \mathcal{Q})$ expressed in Riemann invariants, it is convenient to rewrite (1.0.1) into the same variables, and on a limited time interval, i.e.

$$\partial_t u(W) + \partial_x f(u(W)) = 0, \qquad x \in]x_{in}, x_{out}[,\ t \in]0, T[, \tag{1.3.1a}$$
$$W(0, x) = W_0(x), \qquad x \in]x_{in}, x_{out}[, \tag{1.3.1b}$$
$$W(t, x_{in}) = W_{in}(t) = (v_{in}, w_{in})(t), \qquad t \in]0, T[, \tag{1.3.1c}$$
$$W(t, x_{out}) = W_{out}(t) = (v_{out}, w_{out})(t), \qquad t \in]0, T[, \tag{1.3.1d}$$

where $u(W) = (\mathcal{R}(v, w), \mathcal{R}(v, w)w)^\top$, $f(u(W)) = v \cdot u(W)$. Observe that problem (1.3.1), set on a bounded time interval, is equivalent to (1.0.1) since we deal with solutions in weak (distributional) sense. We remark that, as usual with hyperbolic equations, solutions have to be intended in the weak sense. In particular, the boundary conditions may not be satisfied in the classical sense, i.e. the traces of the solutions at the boundaries may not be equal the corresponding boundary values.
We also introduce the notation for the total variation with respect to a 1-dimensional variable (here the space x or time t) of a function $W :]a, b[\to \mathbb{R}^2$ [Bre00], which is given by $\mathrm{TV}(W)$.

Moreover, if the total variation is bounded, we say that W has bounded total variation, denoted by $W \in \mathrm{BV}(]a,b[;\mathbb{R}^2)$. It is also convenient, for the existence proof, to set $W_0(x+) = (w_0(x-), w_0(x-))$ whenever $W_0(x+) \in \mathcal{W}_0$, assuming $W_0 \in \mathrm{BV}\left(]x_{in}, x_{out}[;\mathcal{W}\right)$ (see Remark 13) and therefore traces are defined at each point $x \in]x_{in}, x_{out}[$. Indeed, this does not change the initial condition in conservative variables, since $u(W_1) = u(W_2) = (0,0)^\top$ if $W_1, W_2 \in \mathcal{W}_0$. Moreover, we set $W_{out}(t) = (w_{max}, w_{max})$ whenever $W_{out}(t) \in \mathcal{W}_0$. This does not impact the solution, which is independent of w_{out} (as $\mathcal{B}_R^{Ent}(\rho_B, w_B) = \mathcal{B}_R^{Rie}(\rho_B, w_B)$ is independent of w_B).

Remark 13. We remark that if $W_0 = W_0^- \in \mathrm{BV}\left(]x_{in}, x_{out}[\,;\mathcal{W}\right)$ before the above mentioned replacement of vacuum states, then also the new initial datum $W_0 = W_0^+ \in \mathrm{BV}\left(]x_{in}, x_{out}[;\mathcal{W}\right)$. Indeed, for each state $W_M^- \in \mathcal{W}_0$ of $W_0^-(\cdot)$, let W_L, W_R the left and right values involved in the computation of the total variation (so that W_M^- is replaced by $W_M^+ = (w_L, w_L)$). Then we have, applying twice the triangle inequality,

$$
\begin{aligned}
&\Big\{|W_L - W_M^+| + |W_M^+ - W_R|\Big\} - \Big\{|W_L - W_M^-| + |W_M^- - W_R|\Big\} \\
&\quad = \Big\{|v_L - w_L| + |w_L - v_R| + |w_L - w_R|\Big\} - \Big\{|v_L - w_M^-| + |w_L - w_M^-| + |w_M^- - v_R| + |w_M^- - w_R|\Big\} \\
&\quad \le \Big\{|w_L - v_R| + |w_L - w_R|\Big\} - \Big\{|w_M^- - v_R| + |w_M^- - w_R|\Big\} \\
&\quad \le |w_L - v_R| + |w_L - w_R| \\
&\quad \le 2|w_L - w_M^-| + |w_M^- - v_R| + |w_M^- - w_R| \\
&\quad \le 2\Big\{|W_L - W_M^-| + |W_M^- - W_R|\Big\},
\end{aligned}
$$

leading to the bound $\mathrm{TV}(W_0^+) \le 3\mathrm{TV}(W_0^-)$.

In the following sections, we construct a sequence of approximate solutions and we show that it converges to an entropy weak solution of (1.3.1), which is defined below. First, we need to recall the notion of boundary entropy pairs, see [CF99a, Definition 4.1], where we drop the convexity assumption.

Definition 3 (**Boundary entropy pair**). *An entropy pair*

$$\big(\alpha(u(W_1), u(W_2)), \beta(u(W_1), u(W_2))\big), \qquad W_1, W_2 \in \mathcal{W},$$

is called a boundary entropy pair if for every fixed $W_2 \in \mathcal{W}$ it satisfies

$$\alpha\left(u(W_2), u(W_2)\right) = \beta\left(u(W_2), u(W_2)\right) = \nabla_1\alpha\left(u(W_2), u(W_2)\right) = (0,0)^\top.$$

Definition 4 (**Entropy weak solution**). *A function $W \in \mathbf{L}^\infty\left(\left(]0,T[\times]x_{in}, x_{out}[\right);\mathcal{W}\right)$ is an entropy weak solution of IBVP* (1.3.1) *if*

- *for any entropy-flux pair $(\mathcal{E}, \mathcal{Q})$ and any test function $\phi \in \mathbf{C}_{\mathbf{c}}^\infty\left(\left(]-\infty, T[\times]x_{in}, x_{out}[\right);\mathbb{R}_{\ge 0}\right)$, it holds*

$$\int_0^T \int_{x_{in}}^{x_{out}} \left\{\mathcal{E}(u(W))\partial_t\phi + \mathcal{Q}(u(W))\partial_x\phi\right\} \mathrm{dxdt} + \int_{x_{in}}^{x_{out}} \mathcal{E}(u(W_0(x)))\phi(0,x)\,\mathrm{dx} \ge 0; \tag{1.3.2}$$

- *for any boundary entropy pair* (α, β) *and any* $\gamma(t) \in \mathbf{L^1}\left(]0,T[;\mathbb{R}_{\geq 0}\right)$*, it holds*

$$\begin{aligned} \operatorname*{ess\,lim}_{x\to x_{in}+} \int_0^T \beta(u(W(t,x)), u(W_{in}(t)))\gamma(t)\mathrm{dt} \leq 0, \\ \operatorname*{ess\,lim}_{x\to x_{out}-} \int_0^T \beta(u(W(t,x)), u(W_{out}(t)))\gamma(t)\mathrm{dt} \geq 0. \end{aligned} \tag{1.3.3}$$

For future reference, we also recall the corresponding definition of a weak solution [Bre00].

Definition 5 (Weak solution). *We call* $W \in \mathbf{L}^\infty\left(\left(]0,T[\times]x_{in},x_{out}[\right);\mathcal{W}\right)$ *a weak solution to the IBVP* (1.3.1)*, if for any test function* $\phi \in \mathbf{C_c^\infty}\left(\left(]-\infty,T[\times]x_{in},x_{out}[\right);\mathbb{R}\right)$ *it satisfies*

$$\int_0^T \int_{x_{in}}^{x_{out}} \left\{u(W)\phi_t + f(u(W))\phi_x\right\}\mathrm{dxdt} + \int_{x_{in}}^{x_{out}} u(W_0(x))\phi(0,x)\mathrm{dx} = 0. \tag{1.3.4}$$

We can now state the main result of this chapter:

Theorem 1. *Let us assume* $W_0 \in \mathrm{BV}\left(]x_{in},x_{out}[;\mathcal{W}\right)$*,* $W_{in}, W_{out} \in \mathrm{BV}\left(]0,T[;\mathcal{W}\right)$*. Then, for any* $T > 0$*, the IBVP* (1.3.1) *admits an entropy weak solution* $W \in \mathbf{L}^\infty\left(]0,T[\times]x_{in},x_{out}[;\mathcal{W}\right)$ *in the sense of Definition 4. Additionally,* W *satisfies the following bounds:*

$$\mathrm{TV}(W(t,\cdot)) \leq \gamma_0 \text{ and } \|W(t)\|_\infty \leq \|W_0\|_\infty \quad \forall\ t \in [0,T[\text{ and } x \in]x_{in},x_{out}[\,,$$

where $\gamma_0 = \mathrm{TV}(W_0) + \left|W_{in}(0) - W_0(x_{in}+)\right| + \left|v_{out}(0) - v(0,x_{out}-)\right| + 3\mathrm{TV}\left(W_{in}(s); s \in]0,T[\right) + \mathrm{TV}\left(v_{out}(s); s \in]0,T[\right)$.

The proof is postponed to Section 1.3.2 (see Propositions 6 and 7).

1.3.1 Wave-front tracking (WFT) algorithm

The WFT algorithm [Daf72, Ris93] allows to construct piece-wise constant approximate entropy weak solutions W^h of the IBVP problem (1.3.1) by means of an approximate Riemann solver obtained by approximating the rarefaction waves by piece-wise constant functions with values in a fixed grid of mesh size ε^h, see [AG02, ADR16] for an implementation in the case of Temple and ARZ systems. This strategy allows to avoid the cumbersome technicalities related to a limiting procedure involving the solution boundary traces, see e.g. [Ama97]. The procedure is briefly summarized below.

1. Fix $h \in \mathbb{N}$ sufficiently large, $\varepsilon^h = 2^{-h}\|W_0\|_\infty$, $\mathcal{W}^h = \mathcal{W} \cap [\varepsilon^h\mathbb{N}^2]$ (see Figure 1.6).
2. Approximate the initial and boundary data with piece-wise constant functions, i.e. $W_0^h \in PC\left(]x_{in},x_{out}[;\mathcal{W}^h\right)$, $W_{in}^h, W_{out}^h \in PC\left(]0,T[;\mathcal{W}^h\right)$ such that [Ama97]:
   - $\mathrm{TV}(W_0^h) \leq \mathrm{TV}(W_0)$, $\mathrm{TV}(W_{in}^h) \leq \mathrm{TV}(W_{in})$, $\mathrm{TV}(W_{out}^h) \leq \mathrm{TV}(W_{out})$,
   - $\lim_{h\to\infty} \|W_0 - W_0^h\|_1 = 0$, $\lim_{h\to\infty} \|W_{in} - W_{in}^h\|_1 = 0$, $\lim_{h\to\infty} \|W_{out} - W_{out}^h\|_1 = 0$,
   - $W_0^h(x+) = (w_0^h(x-), w_0^h(x-))$ whenever $W_0^h(x+) \in \mathcal{W}_0$,
     $|W_{in}^h(0+) - W_0^h(x_{in}+)| \leq |W_{in}(0+) - W_0(x_{in}+)|$,
     $|W_{out}^h(0+)^- W_0^h(x_{out}-)| \leq |W_{out}(0+) - W_0(x_{out}-)|$,

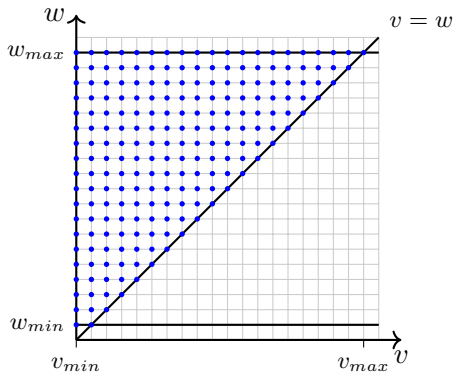

Figure 1.6: Illustration of the discretized domain $\mathcal{W}^h$. The grid points are illustrated in blue.

- $\|W_0^h\|_\infty \leq \|W_0\|_\infty$, $\|W_{in}^h\|_\infty \leq \|W_{in}\|_\infty$, $\|W_{out}^h\|_\infty \leq \|W_{out}\|_\infty$.

3. Approximately solve the Riemann problem at $x = x_{in}, x_{out}$ and at every jump discontinuity in the approximate initial data. Notice that the total variation of these approximations is bounded by $\mathrm{TV}(W_0^h) + \left|W_{in}^h(0) - W_0^h(x_{in}+)\right| + \left|v_{out}^h(0) - v^h(0, x_{out}-)\right|$ even in the presence of vacuum states.

4. Glue together these solutions to obtain a piece-wise constant approximate solution $W^h = (v^h, w^h)$ defined up to the first time $\hat{t}$ at which an interaction between two or more wave-fronts takes place, or a wave hits the boundary, or a jump discontinuity occurs in the boundary data (see [AC97, page 240] or [CR05, page 690]).

5. Solve the new Riemann problem arisen at $t = \hat{t}$ and prolong the solution until the next interaction.

This process can be extended to any time $t > 0$, as proven by the following result.

Proposition 5. *For any h fixed, the number of waves in the approximate solution W^h is finite for all $t \in]0, T[$ and the functional $\gamma^h : [0, T] \to \mathbb{R}_{\geq 0}$ defined by*

$$\begin{aligned}\gamma^h(t) = \mathrm{TV}(W^h(t,\cdot)) + \left|W_{in}^h(t) - W^h(t, x_{in}+)\right| + \left|v_{out}^h(t) - v^h(t, x_{out}-)\right| \\ + 3\,\mathrm{TV}\left(W_{in}^h(s); s \in]t, T[\right) + \mathrm{TV}\left(v_{out}^h(s); s \in]t, T[\right)\end{aligned} \tag{1.3.5}$$

is non-increasing.

Remark 14. Note that (1.3.5) does not depend on the total variation of w_{out}^h, which is in line with the fact that the set $\mathcal{B}_R^{Rie}(U_B)$ is independent of the w-variable (see Remark 8).

Proof. By construction, W^h is a piece-wise constant function, i.e.
$W^h(t,\cdot) \in PC\left(]x_{in}, x_{out}[; \mathcal{W}^h\right)$ for all $t \geq 0$ for which it is defined. By slightly changing the wave positions, it is not restrictive to assume that at any interaction time $\hat{t}$, either two waves interact in the interior of the domain, or a single wave hits the boundary, or a change in the boundary state occurs.
Regarding interactions not involving vacuum states occurring in $]x_{in}, x_{out}[$, the number of waves can increase only if one of the outgoing waves is a rarefaction. However, for Temple

class systems, a rarefaction wave can only occur if one of the incoming waves already was a rarefaction. Thus, the number of waves does not increase. Additionally, we know from the standard theory of Temple class systems that the space total variation in the Riemann invariants is non-increasing [BB97, GHO08] as long as the waves have finite speeds.
Therefore it suffices to focus on the following three cases that may occur at $t = \hat{t}$:

(A) an interaction between waves in $]x_{in}, x_{out}[$ involving at least a vacuum state;

(B) a wave hitting the boundary at $x = x_{in}$ or $x = x_{out}$;

(C) a jump in the approximate boundary data W^h_{in} or W^h_{out}.

For notational simplicity, we will drop the h, t and x dependencies in the rest of the proof, thus writing W instead of $W^h(t,x)$, ε instead of ε^h and γ instead of γ^h. Additionally, we still denote the critical density, defined in (1.2.2), as $\rho_{cr}(w)$ (instead of expressing it in Riemann invariant coordinates). We also set

$$\Delta\gamma = \gamma(\hat{t}+) - \gamma(\hat{t}-)$$

for the variation of the functional (1.3.5) at $t = \hat{t}$. Finally, we recall that the absolute difference between a left (non-vacuum) state $W_L = (v_L, w_L) \in \mathcal{W}_0^c$ and a right (vacuum) state $W_R \in \mathcal{W}_0$ is computed by

$$|W_L - W_R| = |v_L - w_L| + |w_L - w_L| = |v_L - w_L|.$$

Remark that, since the vacuum states in the interior of the domain are the results of Riemann problem solutions, we must have $w_R = w_L$ by case 8 in Definition 1.

Let us first consider case (A). Following [ADR16], we will look at the solution of the Riemann problem after the interaction of a wave connecting the state W_L to W_M and a wave connecting W_M to W_R (see Figure 1.7).

(A.1) If $W_L = (w_L, w_L) \in \mathcal{W}_0$, we know that $W_M \in \mathcal{W}_0^c$ (otherwise case 9 in Definition 1 implies $W_M = W_L$). By case 7 in Definition 1, it holds that the first wave travels with propagation speed v_M. If the second wave was a contact discontinuity, it would travel with the same speed of propagation leading to no interaction between the waves. Thus, the second wave must be either a shock or a rarefaction, i.e. $w_M = w_R$. Moreover it holds that $W_R \in \mathcal{W}_0^c$ otherwise the solution of the Riemann problem between the states W_M and $W_R \in \mathcal{W}_0$ would be an ε-step size rarefaction with the same speed as the first wave ($\rightarrow$ no interaction). Finally, the solution of the Riemann problem associated to the interaction is a discontinuity travelling with speed v_R. Thus, the number of waves does not increase and it holds by means of the triangle inequality

$$\Delta\gamma = \Big\{|w_L - v_R| + |w_L - w_R|\Big\} - \Big\{|w_L - v_M| + |w_L - \underbrace{w_M}_{=w_R}| + |v_M - v_R|\Big\} \leq 0.$$

(A.2) If $W_M \in \mathcal{W}_0$, we know with the same argument as in (A.1) that $W_L \in \mathcal{W}_0^c$ and $W_R \in \mathcal{W}_0^c$. The first wave, connecting W_L to $W_M = (w_L, w_L)$, is an ε-step size rarefaction with propagation speed $v_L = w_L - \varepsilon$. The propagation speed of the second wave (discontinuity) is v_R. Moreover it must hold that $v_R < w_L - \varepsilon$ (otherwise the waves do

not interact). Finally, the solution of the Riemann problem associated to the interaction is a shock-wave travelling from W_L to an intermediate state $W_{M'}$, followed by a contact discontinuity from $W_{M'}$ to W_R with propagation speed $v_{M'} = v_R$. Thus, the number of waves does not increase and it holds by means of the triangle inequality

$$\Delta\gamma = \Big\{|v_L - \underbrace{v_{M'}}_{=v_R}| + |\underbrace{w_{M'}}_{=w_L} - w_R|\Big\} - \Big\{|v_L - w_L| + |w_L - v_R| + |w_L - w_R|\Big\} \leq 0.$$

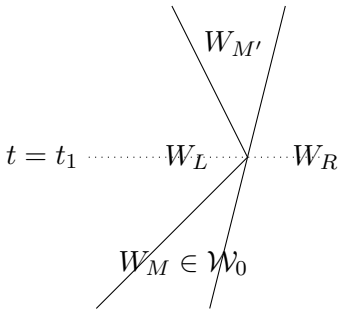

Figure 1.7: Sample illustration of the interacting waves in the vacuum case (A.2).

(A.3) If $W_R \in \mathcal{W}_0$, the second wave connecting W_M to $W_R = (w_M, w_M)$ is an ε-rarefaction with speed $v_M = w_M - \varepsilon$. Thus, the first wave cannot be a contact discontinuity since it would have the same speed as the second wave ($\rightarrow$ no interaction), this implies $w_L = w_M$. However, an interaction between the two waves can only occur if the first wave travels faster than $w_M - \varepsilon$ which is not possible.

(A.4) If $W_{M'} \in \mathcal{W}_0$ (and $W_L \in \mathcal{W}_0^c$, $W_M \in \mathcal{W}_0^c$, $W_R \in \mathcal{W}_0^c$), we know by the Riemann solver that $W_{M'} = (w_L, w_L)$ with $v_{M'} = w_L > v_L$. Moreover, we have that $v_L < v_{M'} \leq v_R$, otherwise $W_{M'} \in W_0^c$. Since the speed of the first wave before the interaction is higher than the second wave speed, it must be a contact discontinuity (from W_L to W_M) followed by a ε-rarefaction from $W_M = (v_L, w_R)$ to W_R with $v_R = v_L + \varepsilon$. Assuming that $v_{M'} < v_R$, we obtain a contradiction due to our ε-discretization: $v_L < v_{M'} < v_R = v_L + \varepsilon$. Thus, it must hold $w_L = v_{M'} = v_R = v_L + \varepsilon$ and $W_{M'} = (v_R, w_L)$. Finally, the number of waves does not increases (since we only have an ε-rarefaction wave) and it holds

$$\Delta\gamma = \Big\{|v_L - v_R| + |w_L - w_R|\Big\} - \Big\{|w_L - \underbrace{w_M}_{=v_R}| + |\underbrace{v_M}_{=v_L} - v_R|\Big\} = 0.$$

Next, we consider case (B). For the left (resp. right) boundary case, the states before the interaction will be denoted by W_B, W_M and W_R (resp. W_L) (see Figure 1.8a (resp. 1.8b)). To prove that the functional γ is non-increasing, it suffices to show that

$$\Delta\gamma = \Big\{|W_B - W_{M'}| + |W_{M'} - W_R|\Big\} - \Big\{|W_B - W_M| + |W_M - W_R|\Big\} \leq 0$$

(resp.

$$\Delta\gamma = \Big\{|W_L - W_{M'}| + |v_{M'} - v_B|\Big\} - \Big\{|W_L - W_M| + |v_M - v_B|\Big\} \leq 0).$$

Moreover, we assume that $U_M = (\mathcal{R}(v_M, w_M), w_M) \in \mathcal{B}_i^{Rie}(U_B)$ with $i \in \{L, R\}$ and $U_B = (\mathcal{R}(v_B, w_B), w_B)$.

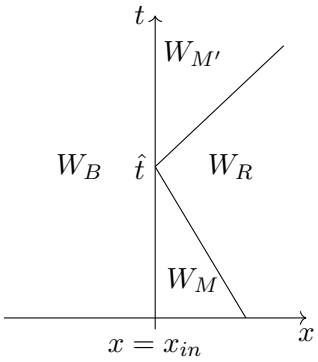

(a) Illustration of the states and the corresponding interacting waves at the left boundary (B.L).

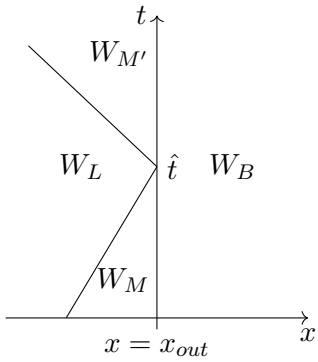

(b) Illustration of the states and the corresponding interacting waves at the right boundary (B.R).

Figure 1.8: Case (B).

In the left boundary case (B.L), i.e. $i = L$, we define the subset of the admissible states with zero speed (see Proposition 1) as

$$\mathcal{W}_L = \{(v, w) \in \mathcal{W}_0^c \mid v = 0\}. \tag{1.3.6}$$

(B.L.1) If $W_B \in \mathcal{W}_0^c$, $W_M \notin \mathcal{W}_L$ and $\mathcal{R}(v_B, w_B) < \rho_{cr}(w_B)$, we know that $w_B = w_M = w_R = w_{M'}$. By case 1 in Proposition 1, it follows that W_B is connected to W_M by a negative shock. Thus, the only possible wave with negative speed (joining W_M to W_R) leading to a visible wave (with positive speed) after the interaction has to be a negative rarefaction, i.e. $v_R = v_M + \varepsilon$ and $\mathcal{R}(v_R, w_R)v_R > \mathcal{R}(v_B, w_B)v_B$. Finally, the solution of the Riemann problem associated to the interaction is a positive shock-wave travelling from $W_B = W_{M'}$ to W_R. Thus, the number of waves does not increase and it holds by means of the triangle inequality

$$\Delta\gamma = \Big\{|v_B - v_R|\Big\} - \Big\{|v_B - v_M| + |v_M - v_R|\Big\} \leq 0.$$

(B.L.2) If $W_B \in \mathcal{W}_0^c$, $W_M \notin \mathcal{W}_L$ and $\mathcal{R}(v_B, w_B) \geq \rho_{cr}(w_B)$, we know that $w_B = w_M = w_R$. It holds that both the wave connecting W_M to W_R and the wave travelling from W_B via $W_{M'}$ to W_R are negative. Therefore, no wave emerges from the interaction and $\Delta\gamma \leq 0$.

Additionally, as shown later in the cases (C.L.1) and (C.L.3), it can appear the situation, where $U_M \notin \mathcal{B}_L^{Rie}(U_B)$. However, applying the same argumentation as before, the result does not change.

(B.L.3) If $W_B \in \mathcal{W}_0^c$, $W_M \in \mathcal{W}_L$ (see Figure 1.9), it holds that $v_M = 0$ and $w_M = w_R$. Thus, the boundary wave travelling from W_M to W_R is a negative ε-rarefaction, implying $v_R = v_M + \varepsilon = \varepsilon$. The solution of the Riemann problem associated to the interaction is a first family wave travelling from W_B to $W_{M'} = (v_{M'}, w_B)$ followed by a contact discontinuity from $W_{M'}$ to W_R, i.e. $v_{M'} = v_R$. If $W_{M'} \neq W_B$ is admissible (see Figure 1.9b), we have only one outgoing wave, the number of waves does not increase and it holds by means of the triangle inequality

$$\Delta\gamma = \Big\{|v_B - \underbrace{v_{M'}}_{=v_R}| + |\underbrace{w_{M'}}_{=w_B} - w_R|\Big\} - \Big\{|v_B - v_M| + |w_B - \underbrace{w_M}_{=w_R}| + |v_M - v_R|\Big\} \leq 0.$$

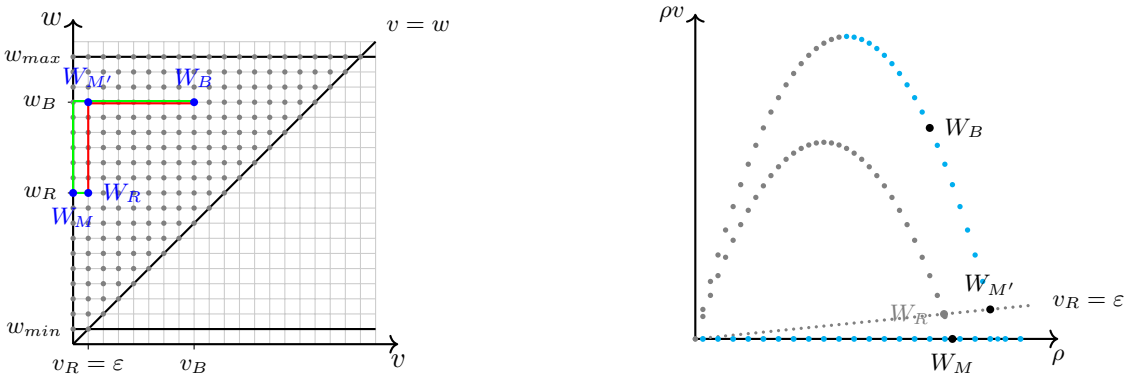

(a) (v, w)-plane. (b) $(\mathcal{R}(v, w), \mathcal{R}(v, w)v)$-plane.

Figure 1.9: Sample illustration of the states in the case (B.L.3) in two different planes.
(a) waves before (resp. after) the interaction are drawn in green (resp. red).
(b) the admissible states for U_B are indicated in light blue.

Otherwise, we have two outgoing waves (see Figure 1.10). We thus consider an additional intermediate state $W_{M''}$ between $W_{M'}(= W_B)$ and W_R. The first wave is a positive shock (from W_B to $W_{M''}$), followed by a contact discontinuity (from $W_{M''}$ to W_R). It holds $v_B > v_R \neq 0$. Thus, the number of waves increases by one, but it holds that

$$\Delta\gamma = \Big\{v_B - v_R + |\underbrace{w_{M'}}_{=w_B} - w_R|\Big\} - \Big\{v_B + v_R + |w_B - \underbrace{w_M}_{=w_R}|\Big\} = -2v_R = -2\epsilon.$$

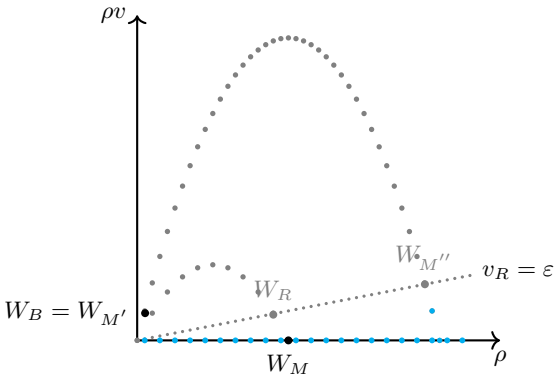

Figure 1.10: Illustration of case (B.L.3) with $U_{M''} = (\mathcal{R}(v_R, w_B), w_B) \notin \mathcal{B}_L^{Rie}(U_B)$, i.e. $\mathcal{R}(v_B, w_B)v_B < \mathcal{R}(v_R, w_B)v_R$. The admissible states for U_B are indicated in light blue.

(B.L.4) If $W_B = (w_B, w_B) \in \mathcal{W}_0$, it holds that $v_M = 0$ and $w_M = w_R$. Thus again, the boundary wave travelling from W_M to W_R is a negative ε-rarefaction, i.e. $v_R = v_M + \varepsilon = \varepsilon$. The solution of the Riemann problem associated to the interaction is a discontinuity from $W_B = W_{M'}$ to W_R travelling with speed v_R. Hence, the number of waves does not

increase and it holds by means of the triangle inequality

$$\Delta\gamma = \Big\{|w_B - v_R| + |w_B - w_R|\Big\} - \Big\{|w_B - v_M| + |w_B - \underbrace{w_M}_{=w_R}| + |v_M - v_R|\Big\} \leq 0.$$

We now focus on the right boundary case (B.R), i.e. $i = R$.

(B.R.1) If $W_B \in \mathcal{W}_0^c$ and the boundary wave from W_L to W_M is a contact discontinuity travelling with speed $v_M = v_L$ (see Figure 1.11), the solution to the boundary Riemann problem associated to the interaction displays at most a first family-curve travelling with negative speed from W_L to $W_{M'} = (v_{M'}, w_L)$. It holds either that $v_L < v_{M'} \leq v_B$ (rarefaction wave from W_L to $W_{M'}$) or $v_{M'} = v_B < v_L$ (shock wave from W_L to $W_{M'} = \tilde{W}$). In the first case, the number of waves can increase; in the second case, the number of waves does not change. By means of the triangle inequality it follows that

$$\Delta\gamma = \Big\{\underbrace{|v_L - v_{M'}| + |v_{M'} - v_B|}_{=|v_L - v_B|}\Big\} - \Big\{|w_L - w_M| + |\underbrace{v_M}_{=v_L} - v_B|\Big\} \leq -\varepsilon < 0,$$

since $W_L \neq W_M$.
Remark: In the case of a negative rarefaction wave from W_L to $W_{M'}$ (only possible if $\mathcal{R}(v_L, w_L) > \rho_{cr}(w_L)$) and $v_{M'} \neq v_B$, then $W_{M'}$ will be the point the propagation speed of the rarefaction wave changes from negative into positive speed. If the state $U_{cr} = (\rho_{cr}(w_L), w_L) \in \mathcal{B}_R^{Rie}(U_B)$ is lying on the grid, we know that $U_{cr} = U_{M'} = (\mathcal{R}(v_{M'}, w_L), w_L)$. On the contrary, if the state U_{cr} is not lying on the grid (see Figure 1.11b), then it can appear the situation that $U_{M'} \notin \mathcal{B}_R^{Rie}(U_B)$. However, since we move with an ε-step size along the $v-$variable on the grid, it holds that $|v_{M'} - v_{cr}| < \varepsilon$ and $v_{cr} = \mathcal{V}(\rho_{cr}(w_L), w_L)$.

Due to the previous remark (and also case (C.R.2)), we can also have $U_M \notin \mathcal{B}_R^{Rie}(U_B)$. However, applying the same argumentation as before, the result does not change.

(B.R.2) If $W_B \in \mathcal{W}_0^c$ and the boundary wave from W_L to W_M is a first family curve, i.e. $w_M = w_L$, travelling with positive speed, the boundary solution after the interaction displays at most a negative shock-wave travelling from W_L to $W_{M'}$. Thus, the number of waves does not increase and it holds by means of the triangle inequality

$$\Delta\gamma = \Big\{|v_L - \underbrace{v_{M'}}_{=v_B}|\Big\} - \Big\{|v_L - v_M| + |v_M - v_B|\Big\} \leq 0.$$

As we have seen in the case (B.R.1) (see also (C.R.2)), it can happen that $U_M \notin \mathcal{B}_R^{Rie}(U_B)$. However, due to $\mathcal{R}(v_B, w_M) < \rho_{cr}(w_M)$, there will be no visible solution.

(B.R.3) If $W_B = (w_{max}, w_{max}) \in \mathcal{W}_0$, we know that the wave travelling from W_L to W_M is either a positive first family curve or a contact discontinuity. In the first case, the solution to the Riemann problem after the interaction will be a positive rarefaction wave which is not visible in the domain. However, in the case of a contact discontinuity, the solution to the boundary Riemann problem between W_L and W_B may consist of a negative

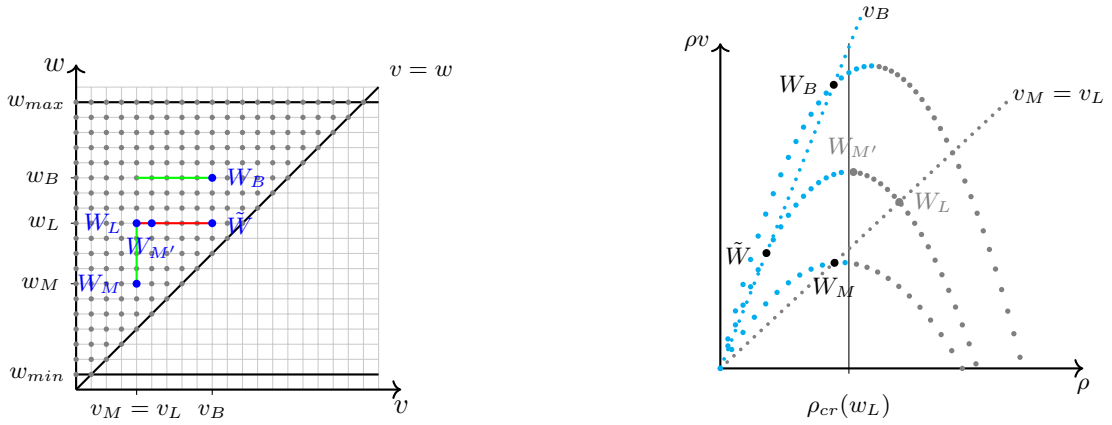

(a) (v, w)-plane. (b) $(\mathcal{R}(v, w), \mathcal{R}(v, w)v)$-plane.

Figure 1.11: Sample illustration of the states in the case (B.R.1) in two different planes.
(a) waves before (resp. after) the interaction are drawn in green (resp. red).
(b) the admissible states for U_B are indicated in light blue. In this case, $W_{M'} \notin \mathcal{B}_R^{Rie}(U_B)$.

rarefaction fan, travelling from W_L to $W_{M'}$ and it holds $v_L = v_M < v_{M'} < w_B = w_{max}$. Thus, the number of waves can increase, but

$$\begin{aligned}\Delta\gamma &= \Big\{ \underbrace{|v_L - v_{M'}| + |v_{M'} - w_{max}|}_{=|v_L - w_{max}|} \Big\} - \Big\{ |w_L - w_M| + |\underbrace{v_M}_{=v_L} - w_{max}| \Big\} \\ &= -|w_L - w_M| \leq -\varepsilon.\end{aligned}$$

We remark that in this case, we use the assumption of $w_B = w_{max}$ (if $W_B \in \mathcal{W}_0$) in order to obtain a negative value for $\Delta\gamma$.

As shown later in the case (C.R.4), we may have $U_M \notin \mathcal{B}_R^{Rie}(U_B)$. However, this does not change the above argumentation.

Finally, we consider case (C): we analyse the solution of the boundary Riemann problem after a jump discontinuity in the boundary state from W_B^- to W_B^+. From Figure 1.12, we see that in this scenario the number of waves can increase. However, since there is a finite number of jumps in the approximate boundary states, the total number of new waves remains finite. Therefore, it is sufficient to prove that the functional γ is non-increasing, i.e.

$$\Delta\gamma = \Big\{ \Big| W_B^+ - W_{M'} \Big| + |W_{M'} - W_R| \Big\} - \Big\{ \Big| W_B^- - W_R \Big| + 3 \Big| W_B^- - W_B^+ \Big| \Big\} \leq 0$$

(resp.

$$\Delta\gamma = \Big\{ |W_L - W_{M'}| + \Big| v_{M'} - v_B^+ \Big| \Big\} - \Big\{ \Big| v_L - v_B^- \Big| + \Big| v_B^- - v_B^+ \Big| \Big\} \leq 0).$$

Moreover, we assume that $U_R = (\mathcal{R}(v_R, w_R), w_R) \in \mathcal{B}_L^{Rie}(U_B^-)$ and $U_L = (\mathcal{R}(v_L, w_L), w_L) \in \mathcal{B}_R^{Rie}(U_B^-)$ with $U_B^- = (\mathcal{R}(v_B^-, w_B^-), w_B^-)$.
First, we consider the left boundary case (C.L), i.e. $i = L$.

(C.L.1) If $W_B^- \in \mathcal{W}_0^c$, $W_B^+ \in \mathcal{W}_0^c$ and $W_R \notin \mathcal{W}_L$ (defined in (1.3.6)), it holds that W_B^- and W_R are connected by a first family wave (possibly null if $W_B^- = W_R$), i.e. $w_B^- = w_R$.

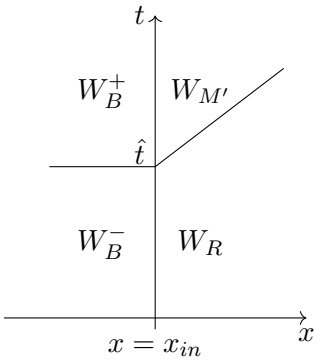

(a) Illustration of the states and the corresponding waves at the left boundary (C.L).

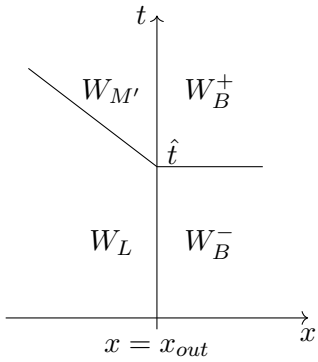

(b) Illustration of the states and the corresponding waves at the right boundary (C.R).

Figure 1.12: Case (C).

The solution of the Riemann problem, associated to the change of the boundary state, is a first family curve from W_B^+ to $W_{M'}$, i.e. $w_B^+ = w_{M'}$, followed by either a contact discontinuity, travelling with propagation speed $v_{M'} = v_R$, or a first family wave, i.e. $w_B^- = w_R = w_{M'} = w_B^+$, from the state $W_{M'}$ to W_R.
The boundary Riemann problem consists than in (a first family wave followed by) a contact discontinuity, it holds by means of the triangle inequality

$$\begin{aligned}\Delta\gamma &= \Big\{|v_B^+ - \underbrace{v_{M'}}_{=v_R}| + |\underbrace{w_{M'}}_{=w_B^+} - w_R|\Big\} - \Big\{\Big|v_B^- - v_R\Big| + 3|v_B^- - v_B^+| + 3|\underbrace{w_B^-}_{=w_R} - w_B^+|\Big\} \\ &\leq -2\Big\{|v_B^- - v_B^+| + |w_B^- - w_B^+|\Big\} \leq -2\varepsilon < 0.\end{aligned}$$

Remark: We can have two outgoing waves, this means having an additional state $W_{M''} = (v_R, w_B^+)$ between $W_{M'}$ and W_R. This can happen in two situations: either if $\mathcal{R}(v_B^+, w_B^+) < \rho_{cr}(w_B^+)$ and $W_{M'} = W_B^+$ or if $\mathcal{R}(v_B^+, w_B^+) \geq \rho_{cr}(w_B^+)$ and $\mathcal{R}(v_R, w_B^+) < \rho_{cr}(w_B^+)$. In the first case, we observe a positive shock wave (from W_B^+ to $W_{M''}$) and a contact discontinuity (from $W_{M''}$ to W_R). In the second case, the wave connecting $W_{M'}$ to $W_{M''}$ is a positive rarefaction followed again by a contact discontinuity (from $W_{M''}$ to W_R). However, both scenarios do not change the computation of the total variation, hence it still holds $\Delta\gamma \leq 0$.

Assuming the solution is a first family shock wave which implies $W_B^+ = W_{M'}$, it holds

$$\Delta\gamma = \Big\{|v_B^+ - v_R|\Big\} - \Big\{\Big|v_B^- - v_R\Big| + 3|v_B^- - v_B^+| + 3|\underbrace{w_B^- - w_B^+}_{=0}|\Big\} \leq 0.$$

Finally, assuming the outgoing wave is a first family rarefaction, the only possible solution, which is visible in the domain, leads to $W_R = W_B^-$. Thus,

$$\Delta\gamma = \Big\{\underbrace{|v_B^+ - v_{M'}| + |v_{M'} - v_R|}_{|v_B^+ - v_R|}\Big\} - \Big\{|\underbrace{v_B^- - v_R}_{=0}| + 3|\underbrace{v_B^-}_{=v_R} - v_B^+| + 3|\underbrace{w_B^- - w_B^+}_{=0}|\Big\} \leq 0.$$

Remark: For the first (resp. third) case above, if we are in the case of a positive rarefaction wave from $W_{M'}$ to $W_{M''}$ (resp. W_R) (only possible if $\mathcal{R}(v_B^+, w_B^+) > \rho_{cr}(w_B^+)$), then $W_{M'}$ will be the point the propagation speed of the rarefaction wave changes from negative into positive speed. If the state $U_{cr} = (\rho_{cr}(w_B^+), w_B^+) \in \mathcal{B}_L^{Rie}(U_B^+)$ with $U_B^+ = (\mathcal{R}(v_B^+, w_B^+), w_B^+)$ is lying on the grid, we know that $U_{cr} = U_{M'} = (\mathcal{R}(v_{M'}, w_B^+)$. On the contrary, if the state U_{cr} is not lying on the grid, then it can appear the situation that $U_{M'} \notin \mathcal{B}_L^{Rie}(U_B^+)$. However, since we move with an ε-step size along the $v-$variable on the grid, it holds that $|v_{M'} - v_{cr}| < \varepsilon$ and $v_{cr} = \mathcal{V}(\rho_{cr}(w_B^+), w_B^+)$.

By the remark above (and also case (C.L.3)), it may happen that $U_R \notin \mathcal{B}_L^{Rie}(U_B^-)$. However, the computations for the contact discontinuity and first family shock do not change. The rarefaction case cannot appear anymore since $W_R \neq W_B^-$.

(C.L.2) If $W_R \in \mathcal{W}_L$, we have that $W_R \in \mathcal{B}_L^{Rie}(U_B^+)$ and no new wave is created, thus $\Delta\gamma \leq 0$.

(C.L.3) If $W_B^- = (w_B^-, w_B^-) \in \mathcal{W}_0$ and $W_B^+ \in \mathcal{W}_0^c$ (see Figure 1.13), it follows that $W_R \in \mathcal{W}_L \cup \{W_B^-\}$. If $W_R \in \mathcal{W}_L$, then case (C.L.2) applies. If $W_R = W_B^-$, the visible solution of the Riemann problem after the change of the boundary state will be the positive part of the rarefaction fan wave travelling from W_B^+ to $W_R^+ = (w_B^+, w_B^+)$. **In particular, we have an infinite speed wave jump from** $W_R = W_B^- = (w_B^-, w_B^-)$ **to** $W_R^+ = (w_B^+, w_B^+)$ (see case 8 in Definition 1 and Figure 1.14).
If $\mathcal{R}(v_B^+, w_B^+) > \rho_{cr}(w_B^+)$, it can exist an intermediate state $W_{M'} = (v_{M'}, w_M^+)$ with $v_{M'} > v_B^+$. Otherwise, it holds $v_{M'} = v_B^+$, implying $W_{M'} = W_B^+$. Thus, it holds by means of the triangle inequality

$$\begin{aligned}\Delta\gamma &= \Big\{ \underbrace{|v_B^+ - v_{M'}| + |v_{M'} - w_B^+|}_{=|v_B^+ - w_B^+|} \Big\} - 3\Big\{ |w_B^- - v_B^+| + |w_B^- - w_B^+| \Big\} \\ &\leq -2\Big\{ |w_B^- - v_B^+| + |w_B^- - w_B^+| \Big\} \leq -2\varepsilon < 0.\end{aligned}$$

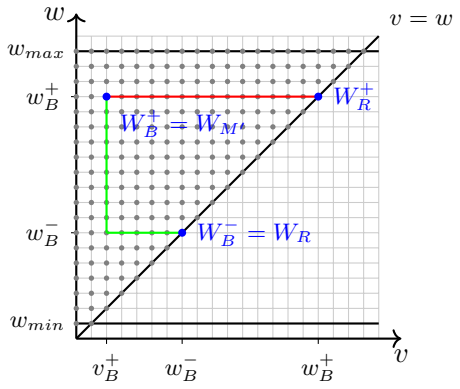

Figure 1.13: Sample illustration of the states in the case (C.L.3) with $\mathcal{R}(v_B^+, w_B^+) \leq \rho_{cr}(w_B^+)$, i.e. $W_{M'} = W_B^+$. The waves before (resp. after) the interaction are drawn in green (resp. red).

Due to the presence of the infinite speed wave between W_R and W_R^+, we additionally have to check the change of the total variation when this wave interacts with others in the interior of the domain. Thus, we are interested in the solution of the Riemann

problem from the state W_R^+ to a state $\hat{W} = (\hat{v}, \hat{w})$ after the interaction of the wave between W_R and $\hat{W}$, which travels with propagation speed $\hat{v}$ (by case 7 in Definition 1). The solution of the new Riemann problem is again a discontinuity with speed $\hat{v}$. This scenario is illustrated in Figure 1.14.

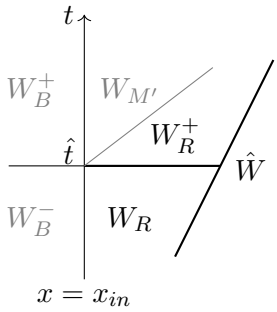

Figure 1.14: Interaction of an infinite speed wave with a wave in the interior of the domain.

Finally, thanks to the triangle inequality, we have:

$$\begin{aligned}\Delta\gamma =& |W_B^+ - W_{M'}| + |W_{M'} - W_R^+| + |W_R^+ - \hat{W}| - \\ & \Big\{ \underbrace{|W_B^- - W_R|}_{=0} + |W_R - \hat{W}| + 3|W_B^- - W_B^+| \Big\} \\ =& \underbrace{|v_B^+ - v_{M'}| + |v_{M'} - w_B^+|}_{=|v_B^+ - w_B^+|} + |w_B^+ - \hat{v}| + |w_B^+ - \hat{w}| - \\ & \Big\{ |w_B^- - \hat{v}| + |w_B^- - \hat{w}| + 3|w_B^- - v_B^+| + 3|w_B^- - w_B^+| \Big\} \leq -2|w_B^- - v_B^+| \leq 0.\end{aligned}$$

Remark: $W_{M'}$ is the point the propagation speed of the rarefaction wave changes from negative to positive (only possible if $\mathcal{R}(v_B^+, w_B^+) > \rho_{cr}(w_B^+)$). If the state $U_{cr} = (\rho_{cr}(w_B^+), w_B^+) \in \mathcal{B}_L^{Rie}(U_B^+)$ is lying on the grid, it holds $U_{cr} = U_{M'} = (\mathcal{R}(v_{M'}, w_B^+), w_B^+)$. Otherwise, we may have $U_{M'} \notin \mathcal{B}_L^{Rie}(U_B^+)$. However, since we move with an ε-step size along the $v-$variable on the grid, it holds that $|v_{M'} - v_{cr}| < \varepsilon$ and $v_{cr} = \mathcal{V}(\rho_{cr}(w_B^+), w_B^+)$.

(C.L.4) If $W_B^- \in \mathcal{W}_0^c$, $W_B^+ = (w_B^+, w_B^+) \in \mathcal{W}_0$ and $W_R \notin \mathcal{W}_L$, we know that $w_B^- = w_R$. Thus, the solution of the Riemann problem associated to the change of the boundary state is a discontinuity from $W_B^+ = W_{M'}$ to W_R travelling with speed v_R. Thus, a new wave is produced and it holds

$$\begin{aligned}\Delta\gamma &= \Big\{ |w_B^+ - v_R| + |w_B^+ - \underbrace{w_R}_{=w_B^-}| \Big\} - \Big\{ |v_B^- - v_R| + 3|v_B^- - w_B^+| + 3|w_B^- - w_B^+| \Big\} \\ &\leq -2\Big\{ |v_B^- - w_B^+| + |w_B^- - w_B^+| \Big\} \leq -2\varepsilon < 0.\end{aligned}$$

As seen in cases (C.L.1) and (C.L.3), it can happen that $U_R \notin \mathcal{B}_L^{Rie}(U_B^-)$. However, the computation above remains unchanged.

(C.L.5) If $W_B^- \in \mathcal{W}_0$ and $W_B^+ \in \mathcal{W}_0$, it follows that $W_R \in \mathcal{W}_L \cup \{W_B^-\}$ and no new wave is produced and $\Delta\gamma \leq 0$.

We now turn to the study of the right boundary case (C.R), i.e. $i = R$.

(C.R.1) If $W_B^- \in \mathcal{W}_0^c$, $W_B^+ \in \mathcal{W}_0^c$ and $R(v_L, w_L) \leq \rho_{cr}(w_L)$, then the solution of the boundary Riemann problem associated to the change of the boundary state displays at most a negative shock-wave travelling from W_L to an intermediate state $W_{M'}$ with $v_{M'} = v_B^+$. Thus, the number of waves may increase and it holds by means of the triangle inequality

$$\Delta\gamma = |v_L - \underbrace{v_{M'}}_{=v_B^+}| - \Big\{|v_L - v_B^-| + |v_B^- - v_B^+|\Big\} \leq 0.$$

(C.R.2) If $W_B^- \in \mathcal{W}_0^c$, $W_B^+ \in \mathcal{W}_0^c$ and $R(v_L, w_L) > \rho_{cr}(w_L)$, we know that $v_L = v_B^-$. Thus, the solution to the Riemann problem is a first family-curve travelling with negative propagation speed from W_L to $W_{M'}$, possibly continued by another (first family) curve travelling with positive speed from $W_{M'}$ to the point $\tilde{W} = (v_B^+, w_{M'})$ and finally followed by a contact discontinuity from $\tilde{W}$ to W_B^+. It holds either that $v_L < v_{M'} \leq v_B^+$ (rarefaction wave from W_L to $W_{M'}$) or $v_{M'} = v_B^+ < v_L$ (shock wave from W_L to $W_{M'} = \tilde{W}$). By means of the triangle inequality it follows that

$$\Delta\gamma = \Big\{ \underbrace{|v_L - v_{M'}| + |v_{M'} - v_B^+|}_{=|v_L - v_B^+|} \Big\} - |\underbrace{v_B^-}_{=v_L} - v_B^+| = 0.$$

Remark: If the solution is a negative rarefaction wave from W_L to $W_{M'}$ and $v_{M'} \neq v_B^+$, then $W_{M'}$ will be the point the propagation speed of the rarefaction wave changes from negative into positive speed. If the state $U_{cr} = (\rho_{cr}(w_L), w_L) \in \mathcal{B}_R^{Rie}(U_B^+)$ is lying on the grid, we know that $U_{cr} = U_{M'} = (\mathcal{R}(v_{M'}, w_L)$. On the contrary, if the state U_{cr} is not lying on the grid, then we may have $U_{M'} \notin \mathcal{B}_R^{Rie}(U_B^+)$. However, since we move with an ε-step size along the $v-$variable on the grid, it holds that $|v_{M'} - v_{cr}| < \varepsilon$ and $v_{cr} = \mathcal{V}(\rho_{cr}(w_L), w_L)$.

Due to the previous remark (and also case (B.R.1)), we can have $U_L \notin \mathcal{B}_R^{Rie}(U_B^-)$. In contrast to above, it holds $v_B^- > v_L$ which still leads to the desired inequality, i.e.

$$\Delta\gamma = |v_L - v_B^+| - \{|v_L - v_B^-| + |v_B^- - v_B^+|\} = -2(v_B^- - v_L) \leq -2\varepsilon < 0.$$

(C.R.3) If $W_B^- = (w_{max}, w_{max}) \in \mathcal{W}_0$ and $W_B^+ \in \mathcal{W}_0^c$, then the solution of the boundary Riemann problem from W_L to W_B^+ is at most a negative shock wave from W_L to $W_{M'} = (v_{M'}, w_L)$ with $v_{M'} = v_B^+$. Thus, again, the number of waves can increase and

$$\Delta\gamma = |v_L - \underbrace{v_{M'}}_{=v_B^+}| - \Big\{|v_L - w_{max}| + |w_{max} - v_B^+|\Big\} = -2(w_{max} - v_L) \leq -2\varepsilon.$$

As we will see in case (C.R.4), we can have $U_L \notin \mathcal{B}_R^{Rie}(U_B^-)$. However, this does not change anything in the above argumentation.

(C.R.4) If $W_B^- \in \mathcal{W}_0^c$ and $W_B^+ = (w_{max}, w_{max}) \in \mathcal{W}_0$, new waves are produced only if $v_L = v_B^-$. In this case, we may have a negative rarefaction wave travelling from W_L to $W_{M'}$ Finally, it holds

$$\Delta\gamma = \Big\{ \underbrace{|v_L - v_{M'}| + |v_{M'} - w_{max}|}_{=|v_L - w_{max}|} \Big\} - |\underbrace{v_B^-}_{=v_L} - w_{max}| = 0.$$

Remark: Again, if $W_{M'}$ is the point the propagation speed of the rarefaction wave changes from negative into positive speed and if the state $U_{cr} = (\rho_{cr}(w_L), w_L)$ is not lying on the grid, it may happen that $U_{M'} \notin \mathcal{B}_R^{Rie}(U_B^+)$ with $U_{M'} = (\mathcal{R}(v_{M'}, w_L), w_L)$ and $U_B^+ = (0, w_{max})$. However, since we move with an ε-step size along the $v-$variable on the grid, it holds that $|v_{M'} - v_{cr}| < \varepsilon$ and $v_{cr} = \mathcal{V}(\rho_{cr}(w_L), w_L)$.

As we have seen in the cases (B.R.1) and (C.R.2), we may have $U_L \notin \mathcal{B}_R^{Rie}(U_B^-)$. Since it also holds that $v_B^- > v_L$, no new wave emerges from the interaction and $\Delta\gamma \leq 0$.

The proof of Proposition 5 is now complete. In particular, the number of waves can increase only a finite number of times and we have the following uniform bound for γ:

$$\begin{aligned}\gamma(t) \leq \gamma(0) = \mathrm{TV}(W_0^h) + \left|W_{in}^h(0) - W_0^h(x_{in}+)\right| + \left|v_{out}^h(0) - v^h(0, x_{out}-)\right| \\ + 3\mathrm{TV}\left(W_{in}^h(s); s \in]0,T[\right) + \mathrm{TV}\left(v_{out}^h(s); s \in]0,T[\right).\end{aligned} \tag{1.3.7}$$

□

1.3.2 Convergence to an entropy weak solution

We first prove the convergence of the sequence of approximate solutions constructed in Section 1.3.1.

Proposition 6. *The sequence $\{W^h\}_h$ converges up to a subsequence to a function W in $\mathbf{L^1}_{loc}$.*

Proof. In our case, we cannot apply Helly's Theorem in the form of [Bre00, Theorem 2.4] to prove the convergence to W. This is due to the possible occurrence of infinite speed waves in the case (C.L.3) of Proposition 5, which prevents us from obtaining the $\mathbf{L^1}$ Lipschitz continuity in time of approximate solutions. Therefore, we have to prove explicitly the space-time BV bounds, which will lead to convergence (see e.g. [EGH00, Lemma 5.6]). To this end, we need to show that for every $x \in]x_{in}, x_{out}[$, $t \in]0,T[$, it holds

$$\|W^h\|_{\mathbf{L}^\infty(]0,T[\times]x_{in},x_{out}[)} \leq M, \tag{1.3.8a}$$

$$\mathrm{TV}_{(t,x)}(W^h) \leq C, \tag{1.3.8b}$$

where the constants C, $M > 0$ are independent of h and $TV_{(t,x)}$ denotes the total variation in time and space, defined as

$$\mathrm{TV}_{(t,x)}(W^h) := \sup\left\{\int_0^T \int_{x_{in}}^{x_{out}} W^h \cdot (\partial_t\phi + \partial_x\phi)\,\mathrm{dx}\,\mathrm{dt} \colon \phi \in \mathbf{C_c^1}\left(]0,T[\times]x_{in},x_{out}[;\mathbb{R}^2\right),\ \|\phi\|_\infty \leq 1\right\}.$$

To prove that W^h has uniformly bounded total variation, it is therefore sufficient to show that there exists C such that

$$\left|\int_0^T \int_{x_{in}}^{x_{out}} W^h \cdot (\partial_t\phi + \partial_x\phi)\,\mathrm{dx}\,\mathrm{dt}\right| \leq C\|\phi\|_\infty, \tag{1.3.9}$$

for all $\phi \in \mathbf{C_c^1}\left(]0,T[\times]x_{in},x_{out}[;\mathbb{R}^2\right)$ (see [Bre00, Equation 2.29]).

The $\mathbf{L}^\infty$-bound (1.3.8a) follows easily from the invariance of the domain $\mathcal{W}^h \subset \mathcal{W}$, which is bounded by w_{min}, $w_{max} > 0$, $v_{min} \geq 0$ and $v_{max} = w_{max}$ (see Figure 1.6).
To prove (1.3.8b), it suffices to prove the boundedness of the total variation in time and space separately.
Proposition 5 guarantees that the approximate solutions are uniformly BV in space for all $t \in [0, T[$:

$$\begin{aligned}\mathrm{TV}(W^h(t,\cdot)) \leq \mathrm{TV}(W_0) + \big|W_{in}(0) - W_0(x_{in}+)\big| + \big|v_{out}(0) - v(0, x_{out}-)\big| \\ + 3\mathrm{TV}\left(W_{in}(s); s \in]0,T[\right) + \mathrm{TV}\left(v_{out}(s); s \in]0,T[\right) := \gamma_0.\end{aligned}$$

Therefore, we have in (1.3.9)

$$\begin{aligned}\left|\int_0^T \int_{x_{in}}^{x_{out}} W^h \cdot \partial_x \phi \,\mathrm{dx}\,\mathrm{dt}\right| &= \left|\lim_{h\to 0} \int_0^T \int_{x_{in}}^{x_{out}} W^h \cdot \frac{\phi(t,x+h) - \phi(t,x)}{h} \,\mathrm{dx}\,\mathrm{dt}\right| \\ &= \left|\lim_{h\to 0} \int_0^T \int_{x_{in}}^{x_{out}} \frac{W^h(t,x) - W^h(t,x-h)}{h} \cdot \phi(t,x) \,\mathrm{dx}\,\mathrm{dt}\right| \\ &\leq \int_0^T \left\{ \limsup_{h\to 0} \frac{1}{h} \int_{x_{in}}^{x_{out}} \Big|W^h(t,x) - W^h(t,x-h)\Big| \,\mathrm{dx} \right\} \|\phi\|_\infty \,\mathrm{dt} \\ &\leq \gamma_0 \, T \, \|\phi\|_\infty. \end{aligned} \tag{1.3.10}$$

Concerning the time component, let us assume first that in the interval $[s,t] \subset]0,T[$ there are no infinite speed waves (see case (C.L.3) of Proposition 5). In this case the $\mathbf{L^1}$- continuity in time holds, i.e.

$$\begin{aligned}\Big\|W^h(t) - W^h(s)\Big\|_1 &= \int_{x_{in}}^{x_{out}} \Big|W^h(t,x) - W^h(s,x)\Big| \mathrm{dx} \\ &\leq \gamma^h(0) \underbrace{\max_{W^h \in \mathcal{W}^h} \left\{ \Big|\lambda_1(W^h)\Big|, \Big|\lambda_2(W^h)\Big| \right\}}_{=:\,\Lambda} |t-s| \\ &\leq L|t-s|, \end{aligned} \tag{1.3.11}$$

with $L = \gamma_0 \, \Lambda$.
Let us assume now that a wave with infinite speed occurs at time t_i, $i = 1, \ldots, Z^h$, which can only happen through a change in the left boundary state. Since the number of changes is bounded by construction, Z^h is finite. Referring to case (C.L.3), Figure 1.14, and fixing $x \in]x_{in}, x_{out}[$, we compute

$$\begin{aligned}\mathrm{TV}(W^h(\cdot,x)) &= \mathrm{TV}(W^h(s,x); s \in]0,t_1[) + \mathrm{TV}(W^h(s,x); s \in]t_Z, T[) + \\ &\quad \sum_{i=1}^{Z^h} \mathrm{TV}(W^h(s,x); s \in]t_i, t_{i+1}[) + \sum_{i=1}^{Z^h} \underbrace{\Big|W^h(t_i^-, x) - W^h(t_i^+, x)\Big|}_{=2\left|w_{in}^h(t_i+) - w_{in}^h(t_i-)\right|} \\ &\leq LT + 2\,\mathrm{TV}(W_{in}).\end{aligned}$$

Acting as in (1.3.10), we recover the estimate for the time-component of (1.3.9), thus showing that the sequence $\{W^h\}_h$ has uniformly bounded total variation.

Hence, by Helly's Theorem [EGH00, Lemma 5.6], there exists $W \in \mathbf{L}^\infty\left(]0,T[\times]x_{in},x_{out}[;\mathcal{W}\right)$ and a subsequence, still denoted by $\{W^h\}_h$, which converges to W in $\mathbf{L^1_{loc}}\left(]0,T[\times]x_{in},x_{out}[;\mathcal{W}\right)$ as $h\to\infty$. Additionally, W satisfies the following inequalities:

$$\mathrm{TV}(W(t,\cdot))\leq\gamma_0 \text{ and } \|W(t,\cdot)\|_\infty\leq M \quad \forall\, t\in[0,T[\text{ and } x\in]x_{in},x_{out}[\,.$$

At this point, we emphasize that, in contrast to [Bre00, Theorem 2.4], we loose the $\mathbf{L^1}$-continuity in time for the limit function W. □

We are now left to show that the limit function W is indeed an entropy weak solution of the IBVP (1.3.1).
As in Section 1.2.2, we drop the u-variable dependency for notational simplicity, i.e. we write W instead of $u(W)$. Following [CF99a, Theorem 4.1], we consider the following boundary entropy pairs:

$$\alpha^j(W_1,W_2)=\mathcal{E}^j(W_1)-\mathcal{E}^j(W_2)-\nabla_u\mathcal{E}^j(W_2)\,(W_1-W_2)\,, \tag{1.3.12}$$

$$\beta^j(W_1,W_2)=\mathcal{Q}^j(W_1)-\mathcal{Q}^j(W_2)-\nabla_u\mathcal{E}^j(W_2)\left(f(W_1)-f(W_2)\right), \tag{1.3.13}$$

where $\mathcal{E}^j,\mathcal{Q}^j$ are defined as in (1.2.5) for $j=1$ and (1.2.6) for $j=2$. We remark that, by setting $W_2=W_B=(v_B,w_B)$ in (1.3.13), we obtain the entropy boundary condition defined in (1.2.7).

Proposition 7. *The limit function W defined in Proposition 6 is an entropy weak solution of the IBVP* (1.3.1) *in the sense of Definition 4.*

Proof. We follow [CF99a, Theorem 4.1]. We start by verifying that W^h satisfies Definition 4 up to an error which decreases to 0 for h going to infinity.
We know that $W^h\in\mathbf{L}^\infty$. Let us now consider $\phi\in\mathbf{C^\infty_c}\left(\left(]-\infty,T[\times]x_{in},x_{out}[\right);\mathbb{R}_{\geq0}\right)$. Since $\phi(0,x)\geq0$ and, for our choice of the entropies, $\mathcal{E}^j(W)\geq0$ for all $W\in\mathcal{W}$ and $j\in\{1,2\}$ (see Equation (1.2.5a) and (1.2.6a)), we directly obtain $\int_{x_{in}}^{x_{out}}\mathcal{E}^j(W_0^h(x))\phi(0,x)\mathrm{d}x\geq0$. Regarding the term

$$\int_0^T\int_{x_{in}}^{x_{out}}\left\{\mathcal{E}^j(W^h)\partial_t\phi+\mathcal{Q}^j(W^h)\partial_x\phi\right\}\mathrm{d}x\,\mathrm{d}t, \tag{1.3.14}$$

following the proof of [ADR16, Proposition 5.2], we need to consider the three different types of discontinuities (i.e. shocks, contact discontinuities and rarefaction shocks) that may arise at some point $x_i\in]x_{in},x_{out}[$ with left and right values W_i and W_{i+1} respectively. By the Green Gauss-Formula, (1.3.14) is equivalent to

$$\int_0^T\Big\{\sum_i\dot{x}_i(t)\Delta\mathcal{E}_i^j(t)-\Delta Q_i^j(t)\Big\}\,\phi(t,x_i(t))\,\mathrm{d}t,$$

where $\Delta\mathcal{E}_i^j=\mathcal{E}^j(W_{i+1})-\mathcal{E}^j(W_i)$, $\Delta\mathcal{Q}_i^j=\mathcal{Q}^j(W_{i+1})-\mathcal{Q}^j(W_i)$ and $\dot{x}_i=\sigma_s(W_i,W_{i+1})$ is the speed of the discontinuity given by the Rankine-Hugoniot condition (1.1.6). Neglecting the time dependence, we set

$$\hat{s}_i^j:=\dot{x}_i\Delta\mathcal{E}_i^j-\Delta Q_i^j,$$

and we consider separately the different types of waves in the following.

1. If the discontinuity is a shock, it holds $w_i = w_{i+1}$ and $v_i > v_{i+1}$.
   For $j = 1$:

   - If $\bar{v} < v_{i+1}$, it follows that also $\bar{v} < v_i$. Thus,

$$\hat{s}_i^1 = \frac{\mathcal{R}(v_{i+1}, w_i)v_{i+1} - \mathcal{R}(v_i, w_i)v_i}{\mathcal{R}(v_{i+1}, w_i) - \mathcal{R}(v_i, w_i)} \left\{ 1 - \frac{\mathcal{R}(v_{i+1}, w_i)}{\mathcal{R}(\bar{v}, w_i)} - \left(1 - \frac{\mathcal{R}(v_i, w_i)}{\mathcal{R}(\bar{v}, w_i)} \right) \right\}$$
$$- \left\{ \bar{v} - \frac{\mathcal{R}(v_{i+1}, w_i)v_{i+1}}{\mathcal{R}(\bar{v}, w_i)} - \left(\bar{v} - \frac{\mathcal{R}(v_i, w_i)v_i}{\mathcal{R}(\bar{v}, w_i)} \right) \right\} = 0.$$

   - If $\bar{v} \geq v_i$, it follows that $\bar{v} > v_{i+1}$ and we directly obtain $\hat{s}_i^1 = 0$ since $\mathcal{E}^1(W_i) = \mathcal{E}^1(W_{i+1}) = \mathcal{Q}^1(W_i) = \mathcal{Q}^1(W_{i+1}) = 0$.
   - If $\bar{v} \in [v_{i+1}, v_i[$ and thus $\mathcal{E}^1(W_{i+1}) = \mathcal{Q}^1(W_{i+1}) = 0$, it holds

$$\hat{s}_i^1 = \mathcal{Q}^1(W_i) - \dot{x}_i \mathcal{E}^1(W_i) = \bar{v} - \frac{\mathcal{R}(v_i, w_i)v_i}{\mathcal{R}(\bar{v}, w_i)} - \dot{x}_i \left(1 - \frac{\mathcal{R}(v_i, w_i)}{\mathcal{R}(\bar{v}, w_i)} \right) \geq 0, \quad (1.3.15)$$

     since $\mathcal{R}(\bar{v}, w_i)\bar{v} \geq \mathcal{R}(v_i, w_i)v_i + \dot{x}_i \left(\mathcal{R}(\bar{v}, w_i) - \mathcal{R}(v_i, w_i) \right) \geq 0$ by concavity of $\rho \mapsto Q(\rho, w_i) = \rho \mathcal{V}(\rho, w_i)$, which is illustrated by Figure 1.15.

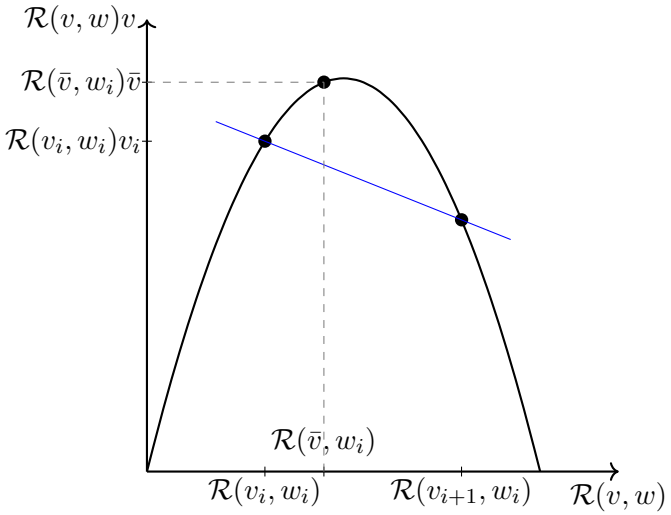

Figure 1.15: Graphical proof of inequality (1.3.15). The slope of the blue line is given by $\dot{x}_i$.

   For $j = 2$:

$$\hat{s}_i^2 = \frac{\mathcal{R}(v_{i+1}, w_i)v_{i+1} - \mathcal{R}(v_i, w_i)v_i}{\mathcal{R}(v_{i+1}, w_i) - \mathcal{R}(v_i, w_i)} \left\{ \mathcal{R}(v_{i+1}, w_i)|\bar{w} - w_i| - \mathcal{R}(v_i, w_i)|\bar{w} - w_i| \right\}$$
$$- \left\{ \mathcal{R}(v_{i+1}, w_i)v_{i+1}|\bar{w} - w_i| - \mathcal{R}(v_i, w_i)v_i|\bar{w} - w_i| \right\} = 0.$$

2. If the jump is a contact discontinuity, it holds $\dot{x}_i = v_i = v_{i+1}$.
   For $j = 1$:

- If $v_i = v_{i+1} \leq \bar{v}$, we directly obtain $\hat{s}_i^1 = 0$,
  since $\mathcal{E}^1(W_i) = \mathcal{E}^1(W_{i+1}) = \mathcal{Q}^1(W_i) = \mathcal{Q}^1(W_{i+1}) = 0$.
- If $v_i = v_{i+1} > \bar{v}$, then

$$\begin{aligned}\hat{s}_i^1 = \ & \dot{x}_i \left\{ 1 - \frac{\mathcal{R}(v_{i+1}, w_{i+1})}{\mathcal{R}(\bar{v}, w_{i+1})} - \left(1 - \frac{\mathcal{R}(v_i, w_i)}{\mathcal{R}(\bar{v}, w_i)} \right) \right\} \\ & - \left\{ \bar{v} - \frac{\mathcal{R}(v_{i+1}, w_{i+1})\dot{x}_i}{\mathcal{R}(\bar{v}, w_{i+1})} - \left(\bar{v} - \frac{\mathcal{R}(v_i, w_i)\dot{x}_i}{\mathcal{R}(\bar{v}, w_i)} \right) \right\} = 0.\end{aligned}$$

For $j = 2$:

$$\begin{aligned}\hat{s}_i^2 = \ & \dot{x}_i \left\{ \mathcal{R}(v_{i+1}, w_{i+1}) |\bar{w} - w_{i+1}| - \mathcal{R}(v_i, w_i) |\bar{w} - w_i| \right\} \\ & - \left\{ \mathcal{R}(v_{i+1}, w_{i+1})\dot{x}_i |\bar{w} - w_{i+1}| - \mathcal{R}(v_i, w_i)\dot{x}_i |\bar{w} - w_i| \right\} = 0.\end{aligned}$$

3. Finally, if the discontinuity is a ε-rarefaction, it holds $w_i = w_{i+1}$ and $v_i < v_{i+1}$ with $v_{i+1} = v_i + \varepsilon$. By similar calculations as for the shock case, we obtain that $\hat{s}_i^2 = 0$, and $\hat{s}_i^1 = 0$ if $\bar{v} < v_i$ or $\bar{v} \geq v_{i+1}$. However, if $\bar{v} \in [v_i, v_{i+1}[$, it follows that $\mathcal{E}^1(W_i) = \mathcal{Q}^1(W_i) = 0$ and, by the same concavity argument as above, we compute that $\hat{s}_i^1 \leq 0$. Moreover,

$$\begin{aligned}\hat{s}_i^1 &= \dot{x}_i \, \mathcal{E}^1(W_{i+1}) - \mathcal{Q}^1(W_{i+1}) \\ &= \frac{\mathcal{R}(v_{i+1}, w_{i+1})v_{i+1} - \mathcal{R}(v_i, w_i)v_i}{\mathcal{R}(v_{i+1}, w_{i+1}) - \mathcal{R}(v_i, w_i)} \left(1 - \frac{\mathcal{R}(v_{i+1}, w_{i+1})}{\mathcal{R}(\bar{v}, w_{i+1})} \right) - \bar{v} + \frac{\mathcal{R}(v_{i+1}, w_{i+1})v_{i+1}}{\mathcal{R}(\bar{v}, w_{i+1})} \, .\end{aligned}$$

Let us set $\varphi(\rho) := \mathcal{R}(\mathcal{V}(\rho, w_i), w_i)\mathcal{V}(\rho, w_i) = \rho \mathcal{V}(\rho, w_i)$, which is a strictly concave function by assumption (II.b), and rewrite the above quantity as

$$\begin{aligned}\hat{s}_i^1 &= \frac{\varphi(\rho_{i+1}) - \varphi(\rho_i)}{\rho_{i+1} - \rho_i} \left(1 - \frac{\rho_{i+1}}{\bar{\rho}} \right) - \mathcal{V}(\bar{\rho}, w_i) + \frac{\varphi(\rho_{i+1})}{\bar{\rho}} \\ &= \dot{\varphi}(\rho_{i+1/2}) \frac{\bar{\rho} - \rho_{i+1}}{\bar{\rho}} - \frac{\varphi(\bar{\rho}) - \varphi(\rho_{i+1})}{\bar{\rho}} \\ &= \dot{\varphi}(\rho_{i+1/2}) \frac{\bar{\rho} - \rho_{i+1}}{\bar{\rho}} - \dot{\varphi}(\tilde{\rho}) \frac{\bar{\rho} - \rho_{i+1}}{\bar{\rho}} \\ &= \ddot{\varphi}(\hat{\rho})(\rho_{i+1/2} - \tilde{\rho}) \frac{\bar{\rho} - \rho_{i+1}}{\bar{\rho}} \\ &\geq \min_{\rho \in [0, R(w_i)]} \ddot{\varphi}(\rho) \, (\rho_i - \rho_{i+1}) \\ &\geq -C(v_{i+1} - v_i),\end{aligned}$$

for some constant $C > 0$, with $0 \leq \rho_{i+1} < \tilde{\rho} < \hat{\rho} < \rho_{i+1/2} < \rho_i$ and $\rho_{i+1} < \tilde{\rho} < \bar{\rho} \leq \rho_i$. Above, we observed that $\frac{\bar{\rho} - \rho_{i+1}}{\bar{\rho}} < 1$.

Applying the same argument as in the proof of [ADR16, Proposition 5.2], we conclude that for any fixed $\delta > 0$, there exists $\hat{h} > 0$ such that for all $h \geq \hat{h}$ it holds

$$\int_0^T \int_{x_{in}}^{x_{out}} \left\{ \mathcal{E}^j(W^h)\partial_t \phi + \mathcal{Q}^j(W^h)\partial_x \phi \right\} \mathrm{dxdt} + \int_{x_{in}}^{x_{out}} \mathcal{E}^j(W_0^h(x))\phi(0, x) \mathrm{dx} \geq -\delta. \quad (1.3.16)$$

Concerning the entropy boundary condition (1.3.3), we observe that it is guaranteed by Proposition 3 for those cases in Proposition 5, where it holds $W^h(t,x_{in}+) \in \mathcal{B}_L^{Rie}(\rho_{in}^h(t),w_{in}^h(t)) \subset \mathcal{B}_L^{Ent}(\rho_{in}^h(t),w_{in}^h(t))$ and $W^h(t,x_{out}-) \in \mathcal{B}_R^{Rie}(\rho_{out}^h(t),w_{out}^h(t)) = \mathcal{B}_R^{Ent}(\rho_{out}^h(t),w_{out}^h(t))$. However, due to the discretization of the domain $\mathcal{W}^h$, in some cases the approximate solution's traces (v^h,w^h) are states that do not belong to the admissible Riemann set, but $|v^h - v_{cr}^h| < \varepsilon$. In these cases, it holds

$$\beta^j(W^h(t,x_{in}+),W_{in}^h(t)) \le C\varepsilon \quad \text{or} \quad \beta^j(W^h(t,x_{out}),W_{out}^h(t)) \ge -C\varepsilon,$$

for some constant $C>0$. We refer to Appendix A for a detailed analysis of these cases. Therefore, for any fixed $\delta>0$, there exists $\hat{h}>0$ such that for all $h \ge \hat{h}$ it holds

$$\operatorname*{ess\,lim}_{x\to x_{in}+} \int_0^T \beta^j(W^h(t,x),W_{in}^h(t))\gamma(t)\mathrm{dt} \le \delta,$$
$$\operatorname*{ess\,lim}_{x\to x_{out}-} \int_0^T \beta^j(W^h(t,x),W_{out}^h(t))\gamma(t)\mathrm{dt} \ge -\delta.$$

Thus, following the proof of [CF99a, Theorem 4.1], the approximate WFT-solution W^h satisfies for any test function $\phi \in \mathbf{C_c^\infty}\Big(]-\infty,T[\times\mathbb{R};\mathbb{R}^{0+}\Big)$ and any $W_2 \in \mathcal{W}$ the inequality

$$\begin{aligned}\int_0^T \int_{x_{in}}^{x_{out}} \Big\{\alpha^j(W^h(t,x),W_2)\partial_t\phi + \beta^j(W^h(t,x),W_2)\partial_x\phi\Big\}\mathrm{dxdt} + \int_{x_{in}}^{x_{out}} \alpha^j(W_0^h(x),W_2)\phi(0,x)\mathrm{dx} \\ + K\left\{\int_0^t \Big|W_{in}^h(t)-W_2\Big|\phi(t,x_{in})\mathrm{dt} + \int_0^t \Big|W_{out}^h(t)-W_2\Big|\phi(t,x_{out})\mathrm{dt}\right\} \ge -3\delta,\end{aligned} \tag{1.3.17}$$

for some $K>0$ and h sufficiently large.
Moreover, since the construction of W^h is based on the Riemann solver (see Definition 1) and the Rankine-Hugoniot conditions hold at rarefaction fronts, the approximate solution is a weak solution in the sense of Definition 5. Therefore, letting $h\to\infty$, we show that W is a weak solution.
Letting now $h\to\infty$ in (1.3.17), due to the $\mathbf{L^1}$ convergence of $\{W^h\}_h$ to W, the equation yields to

$$\begin{aligned}\int_0^T \int_{x_{in}}^{x_{out}} \Big\{\alpha^j(W(t,x),W_2)\partial_t\phi + \beta^j(W(t,x),W_2)\partial_x\phi\Big\}\mathrm{dxdt} + \int_{x_{in}}^{x_{out}} \alpha^j(W_0(x),W_2)\phi(0,x)\mathrm{dx} \\ + K\left\{\int_0^t |W_{in}-W_2|\phi(t,x_{in})\mathrm{dt} + \int_0^t |W_{out}-W_2|\phi(t,x_{out})\mathrm{dt}\right\} \ge 0,\end{aligned}$$

for $j\in\{1,2\}$. Using again [CF99a, Theorem 4.1], we conclude that the limit function W is indeed a entropy weak solution in the sense of Definition 4. □

We emphasize again that, with our choice of the entropy-flux pairs, the entropy weak solution W can include vacuum states which do not belong to the Riemann boundary set.

Remark 15. We remark that our definition of the entropy weak solution is a weaker formulation than the one in [CF99a, Definition 4.2] due to the loss of the $\mathbf{L^1}$ continuity in time. Moreover, our entropies $\mathcal{E}^1$ in (1.2.5a) are not strictly convex. However, [CF99a, Theorem 4.1] still applies, since convexity there is only needed to deal with the strong initial condition [CF99a, equation (4.8)], which we consider in weak form.

Remark 16. The choice of the Riemann solver of Definition 1, Case 8, although inspired by reality, induces some extra difficulties in treating the problem, as the presence of infinite speed waves and the need of "well-prepared" initial data, see Remark 3. We conjecture that a similar existence result could be proved, maybe with less adjustments, using the Riemann solver proposed in Figure 1.2.

Appendix A

Approximate entropy boundary condition

In cases (B.R.1), (C.L.1), (C.L.3), (C.R.2) and (C.R.4) of Proposition 5, we may observe boundary states $W^h_{M'}$ of the discretized solution not belonging to the boundary Riemann set, i.e. $W^h_{M'} \notin B^{Rie}_i, i \in \{R, L\}$. For these particular cases, we prove below that the entropy boundary condition (1.2.7) is satisfied up to an error which vanishes with the discretization grid mesh when passing to the limit in Proposition 7. Again, for notational simplicity, we drop the h-index in the following.
Starting with the left boundary cases ((C.L.1) and (C.L.3)), we define $W_{in} = (v_{in}, w_{in}) = W^+_B$. It holds $\rho_{in} = \mathcal{R}(v_{in}, w_{in}) > \rho_{cr}(w_{in})$, but we may have $\rho_{M'} = \mathcal{R}(v_{M'}, w_{in}) < \rho_{cr}(w_{in})$, which implies $v_{M'} > v_{in}$. Therefore, it suffices to consider in Equation (1.2.8) the case $\bar{v} \in [v_{in}, v_{M'}[$, otherwise we directly obtain that $\beta^1(W_{M'}, W_{in}) = 0$. Since we reach $W_{M'}$ from W_{in} by a negative rarefaction wave, it must hold that $\rho_{M'} v_{M'} \geq \rho_{in} v_{in}$. If $\bar{v} \in [v_{in}, \mathcal{V}(\tau(\rho_{M'}), w_{in})]$, we also have $\rho_{M'} v_{M'} \geq \mathcal{R}(\bar{v}, w_{in})\bar{v} = \bar{\rho}\bar{v}$ which leads to $\beta^1(W_{M'}, W_{in}) \leq 0$ in (1.2.8). However, if $\bar{v} \in]\mathcal{V}(\tau(\rho_{M'}), w_{in}), v_{M'}[$, it holds $\rho_{M'} v_{M'} < \bar{\rho}\bar{v}$ and $\beta^1(W_{M'}, W_{in}) > 0$.
By defining $\varphi_{in}(\rho) := \mathcal{R}(\mathcal{V}(\rho, w_{in})), w_{in})\mathcal{V}(\rho, w_{in})$, we compute

$$\begin{aligned}
\beta^1(W_{M'}, W_{in}) &= \frac{1}{\bar{\rho}}(\varphi_{in}(\bar{\rho}) - \varphi_{in}(\rho_{M'})) \\
&= \frac{1}{\bar{\rho}}\dot{\varphi}_{in}(\hat{\rho})(\bar{\rho} - \rho_{M'}) \\
&= \frac{1}{\bar{\rho}}\dot{\varphi}_{in}(\hat{\rho})(\mathcal{R}(\bar{v}, w_{in}) - \mathcal{R}(v_{M'}, w_{in})) \\
&= \frac{1}{\bar{\rho}}\dot{\varphi}_{in}(\hat{\rho})\mathcal{R}_v(\tilde{v}, w_{in})(\bar{v} - v_{M'}) \\
&\leq \frac{1}{\bar{\rho}} \max_{\rho \in [0, R(w_{max})]} \left|\dot{\varphi}_{in}(\rho)\right| \max_{v \in [0, w_{max}]} \left|\mathcal{R}_v(v, w_{in})\right| (v_{M'} - \bar{v}) \\
&\leq C\varepsilon,
\end{aligned}$$

for some $C > 0$, $\rho_{M'} < \hat{\rho} < \bar{\rho}$ and $\bar{v} < \tilde{v} < v_{M'}$.
Moreover, since $w_{M'} = w_{in}$ and therefore $\operatorname{sgn}\big(\mathcal{R}(v_{in}, w_{in})(\bar{w} - w_{in})\big) = \operatorname{sgn}\big(\mathcal{R}(v_{M'}, w_{M'})(\bar{w} - w_{M'})\big)$ in (1.2.9a), we compute $\beta^2(W_{M'}, W_{in}) = 0$.
Considering now the right boundary cases (B.R.1), (C.R.2) and (C.R.4), we define

$$W_{out} = (v_{out}, w_{out}) = \begin{cases} W_B & \text{if (B.R.1),} \\ W^+_B & \text{if (C.R.2), (C.R.4).} \end{cases}$$

Moreover, we use again the fact that $B^{Rie}_R(\mathcal{R}(v_{out}, w_{out}), w_{out}) = B^{Rie}_R(\mathcal{R}(v_{out}, w), w))$ (see Remark 8).

It holds $\mathcal{R}(v_{out}, w_{M'}) < \rho_{cr}(w_{M'})$, but we may have $\rho_{M'} = \mathcal{R}(v_{M'}, w_{M'}) > \rho_{cr}(w_{M'})$, which implies $v_{M'} < v_{out}$. As before, it suffices to consider the case $\bar{v} \in]v_{M'}, v_{out}]$ in (1.2.8), otherwise we directly obtain that $\beta^1(W_{M'}, W_{out}) = 0$. Since we reach W_{out} from $W_{M'}$ by a positive rarefaction wave, it must hold that $\rho_{M'} v_{M'} \geq \mathcal{R}(v_{out}, w_{M'}) v_{out}$. If $\bar{v} \in [\mathcal{V}(\tau(\rho_{M'}), w_{M'}), v_{out}]$, we also have $\rho_{M'} v_{M'} \geq \mathcal{R}(\bar{v}, w_{M'})\bar{v} = \bar{\rho}\bar{v}$, which leads to $\beta^1(W_{M'}, W_{out}) \geq 0$. However, if $\bar{v} \in]v_{M'}, \mathcal{V}(\tau(\rho_{M'}), w_{M'})[$, we obtain $\rho_{M'} v_{M'} < \bar{\rho}\bar{v}$ and $\beta^1(W_{M'}, W_{out}) < 0$. By defining $\varphi_{out}(\rho) := \mathcal{R}(\mathcal{V}(\rho, w_{M'}), w_{M'})\mathcal{V}(\rho, w_{M'})$, we compute, as in the left boundary case,

$$\begin{aligned}
\beta^1(W_{M'}, W_{out}) &= -\frac{1}{\bar{\rho}}(\varphi_{out}(\bar{\rho}) - \varphi_{out}(\rho_{M'})) \\
&= -\frac{1}{\bar{\rho}}\dot{\varphi}_{out}(\hat{\rho})\mathcal{R}_v(\tilde{v}, w_{M'})(\bar{v} - v_{M'}) \\
&\geq -\frac{1}{\bar{\rho}} \max_{\rho \in [0, R(w_{max})]} \left|\dot{\varphi}_{out}(\rho)\right| \max_{v \in [0, w_{max}]} \left|\mathcal{R}_v(v, w_{M'})\right| (\bar{v} - v_{M'}) \\
&\geq -C\varepsilon,
\end{aligned}$$

for some $C > 0$, $\bar{\rho} < \hat{\rho} < \rho_{M'}$ and $v_{M'} < \tilde{v} < \bar{v}$.
Finally, we have $\beta^2(W_{M'}, W_{out}) \geq 0$, since it holds $w_{M'} = w_{out}$ in (B.R.1) and (C.R.2), and $\rho_{out} = 0$ in (C.R.4).

Chapter 2

Numerical methods

After proving the existence of an entropy solution to the IBVP (1.0.1), we introduce in this chapter some numerical schemes that have been used in [WBG23, WBGG22, WGV23] for computing its approximate solutions.

As typically done when constructing finite volume approximations of hyperbolic systems of conservation laws, we start by discretizing the space-time domain: given a (possibly non-uniform) spatial discretization $\{x_0, \dots, x_M\}$ of the interval $]x_{in}, x_{out}[$ with $x_0 = x_{in}$ and $x_M = x_{out}$, we set the cell sizes $\Delta x_j := x_j - x_{j-1}$ for $j \in \{1, \dots, M\}$ and a time step Δt satisfying a suitable stability condition which will be specified later.
As introduced in Section 1.2.2, we denote by $u = (\rho, y)^\top$ the vector of the conservative variables (where we set $y = \rho w$). Thus, we construct a finite volume [LeV02] approximate solution of (1.0.1) of the form $u^{\Delta x_j}(t,x) = u_j^n = (\rho_j^n, \rho_j^n w_j^n)^\top = (\rho_j^n, y_j^n)^\top$ for $(t,x) \in C_j^n = [t^n, t^{n+1}[\times [x_{j-1}, x_j[$ and $n \in \mathbb{N}$. The approximate traffic speed in section j at time $n\Delta t$ is given by $v_j^n = \mathcal{V}(\rho_j^n, w_j^n)$, where the speed function $\mathcal{V}$ satisfies the assumptions in (II).
To this end, we approximate the initial data with piece-wise constant functions

$$\rho_j^0 = \frac{1}{\Delta x_j} \int_{x_{j-1}}^{x_j} \rho^0(x)\, dx, \qquad y_j^0 = \frac{1}{\Delta x_j} \int_{x_{j-1}}^{x_j} \rho^0(x) w^0(x)\, dx, \qquad \text{for } j \in \{1, \dots, M\},$$

and we iterate in time according to the conservation formulas

$$u_j^{n+1} = u_j^n - \frac{\Delta t}{\Delta x_j} \left(\mathbf{F}_j^n - \mathbf{F}_{j-1}^n \right), \qquad \text{for } j \in \{2, \dots, M-1\}, \tag{2.0.1}$$

where

$$\mathbf{F}_j^n = (F_j^{\rho,n}, F_j^{y,n})^\top = (F_j^{\rho,n}, w_j^n F_j^{\rho,n})^\top \tag{2.0.2}$$

denotes the numerical fluxes at the space position $x = x_j$ and in the time interval $[t^n, t^{n+1}[$. In the following sections, we present different choices for the computation of the flux $F_j^{\rho,n}$ and two different implementation possibilities for the boundary conditions at $j \in \{1, M\}$.

2.1 Godunov scheme

The most widely used numerical scheme for traffic flow macroscopic simulations is the finite volume Godunov scheme [God59] in its Cell Transmission Model (CTM) version [Dag94],

where the fluxes across cell interfaces are given by the minimum of the sending capacity (demand $\mathbf{D}$) of the upstream cell and the receiving capacity (supply $\mathbf{S}$) of the downstream one. This supply-demand formulation of the Godunov scheme, see e.g [LHSM05], allows for sharp approximations since the underlying Riemann problem is solved explicitly for each time step and between each cell [Fan13, PS15].
Thus, the flux $F_j^{\rho,n}$ in Equation (2.0.2) is computed for $j \in \{1, \dots, M-1\}$ by

$$F_j^{\rho,n} = \min\Big\{D^\rho(u_j^n), S^\rho(u_{j+1}^n; w_j^n)\Big\},$$

where the demand $\mathbf{D}$ is defined by $\mathbf{D}(u_j) = \Big(D^\rho(u_j)\ ,\ w_j D^\rho(u_j)\Big)^\top$ with

$$D^\rho(u_j) = \begin{cases} Q(\rho_j, w_j) & \text{if } \rho_j \le \rho_{cr}(w_j), \\ Q(\rho_{cr}(w_j), w_j) & \text{if } \rho_j > \rho_{cr}(w_j), \end{cases}$$

and the supply $\mathbf{S}$ given by $\mathbf{S}(u_{j+1}; w_j) = \Big(S^\rho(u_{j+1}; w_j)\ ,\ w_j S^\rho(u_{j+1}; w_j)\Big)^\top$ with

$$S^\rho(u_{j+1}; w_j) = \begin{cases} Q(\rho_{cr}(w_j), w_j) & \text{if } \rho_{j+\frac{1}{2}} \le \rho_{cr}(w_j), \\ Q(\rho_{j+\frac{1}{2}}, w_j) & \text{if } \rho_{j+\frac{1}{2}} > \rho_{cr}(w_j)\,. \end{cases}$$

The critical density ρ_{cr} is defined in (1.2.2). Moreover, $\rho_{j+\frac{1}{2}}$ corresponds to the density of the intermediate state in the solution of the Riemann problem corresponding to (ρ_j, w_j) and (ρ_{j+1}, w_{j+1}), implicitly defined by $\mathcal{V}(\rho_{j+\frac{1}{2}}, w_j) = \mathcal{V}(\rho_{j+1}, w_{j+1})$ if $\mathcal{V}(\rho_{j+1}, w_{j+1}) < w_j$ and by $\rho_{j+\frac{1}{2}} = 0$ if $\mathcal{V}(\rho_{j+1}, w_{j+1}) \ge w_j$ [LHSM05].
Note that, taking $w_j^n = \textit{constant}$ in the above equations, we recover the first order LWR model in its CTM version. Moreover, to ensure the stability of the numerical solution, in particular $u_j^n \in \tilde{\Omega}$, we consider the following Courant-Friedrichs-Lewy (CFL) condition

$$\Delta t \le \frac{\min\limits_{j\in\{1,\dots,M\}} \Delta x_j}{\max\limits_{(\rho,w)\in\Omega} \big\{\big|\lambda_1(\rho,w)\big|, \big|\lambda_2(\rho,w)\big|\big\}}\,. \tag{2.1.1}$$

2.1.1 Ramp implementation

It is also possible to integrate on- and off-ramp contributions in the second order Godunov scheme implementation by taking the measured on-ramp and off-ramp fluxes, $r_j^{\rho,n}$ and $s_j^{\rho,n}$ respectively, at position x_j and time $n\Delta t$ into account. To this end, the extended discrete GSOM equations read for $j \in \{2, \dots, M-1\}$:
if $r_j^{\rho,n} \ge 0$ and $s_j^{\rho,n} = 0$ (and $r_{j-1}^{\rho,n} = s_{j-1}^{\rho,n} = 0$):

$$\begin{cases} u_j^{n+1} = u_j^n - \dfrac{\Delta t}{\Delta x_j}\Big[\min\Big\{\mathbf{D}(u_j^n), \max\Big\{P_j\mathbf{S}(u_{j+1}^n; w_j^n), \mathbf{S}(u_{j+1}^n; w_j^n) - \mathbf{r}_j^n\Big\}\Big\} - \mathbf{F}_{j-1}^n\Big], \\ u_{j+1}^{n+1} = u_{j+1}^n - \dfrac{\Delta t}{\Delta x_{j+1}}\Big[\mathbf{F}_{j+1}^n - \min\Big\{\mathbf{D}(u_j^n) + \mathbf{r}_j^n, \mathbf{S}(u_{j+1}^n; w_j^n)\Big\}\Big]; \end{cases}$$

if $s_j^{\rho,n} > 0$ and $r_j^{\rho,n} = 0$ (and $r_{j-1}^{\rho,n} = s_{j-1}^{\rho,n} = 0$):

$$\begin{cases} u_j^{n+1} = u_j^n - \dfrac{\Delta t}{\Delta x_j}\Big[\Big(\min\Big\{\max\Big\{\mathbf{D}(u_j^n) - \mathbf{s}_j^n, (0,0)^\top\Big\}, \mathbf{S}(u_{j+1}^n; w_j^n)\Big\} + \\ \qquad\qquad \min\{\mathbf{D}(u_j^n), \mathbf{s}_j^n\}\Big) - \mathbf{F}_{j-1}^n\Big], \\ u_{j+1}^{n+1} = u_{j+1}^n - \dfrac{\Delta t}{\Delta x_{j+1}}\Big[\mathbf{F}_{j+1}^n - \min\Big\{\max\Big\{\mathbf{D}(u_j^n) - \mathbf{s}_j^n, (0,0)^\top\Big\}, \mathbf{S}(u_{j+1}^n; w_j^n)\Big\}\Big], \end{cases}$$

where $\mathbf{r}_j^n := \left(r_j^{\rho,n},\ w_j^n r_j^{\rho,n}\right)^\top$, $\mathbf{s}_j^n := \left(s_j^{\rho,n},\ w_j^n s_j^{\rho,n}\right)^\top$. The priority parameter $P_j \in [0,1]$ is approximated by the number of lanes of cell j divided by the number of lanes of cell j plus the number of lanes of the corresponding on-ramp. Moreover, we choose the discretization in such a way that we cannot have two ramps on subsequent cell interfaces.
Regarding the boundary cell values, they will be implemented as explained in Section (2.4.1) assuming that we cannot have ramps lying on the boundary interfaces.

2.2 Harten-Lax-van-Leer scheme

A cheaper alternative to compute the numerical fluxes in (2.0.1) is to employ the approximate Harten, Lax and van Leer (HLL) [HLvL83] Riemann solver, as done by Fan and Seibold [Fan13, FHS14]. Indeed, the explicit computation of the Riemann solution at every time step can be quite expensive. Instead, the HLL solver approximates the exact Riemann solution by a single constant intermediate state. Although the approximated scheme entails drawbacks due to the averaging over the actual wave structure, it can give good quality solutions in the context of 2×2 hyperbolic systems. Furthermore, the method constructed by the HLL scheme converges to a weak entropy solution which was proven by Harten, Lax and van Leer [HLvL83].

In this case, the numerical flux $F_j^{\rho,n}$ in (2.0.2) is calculated for $j \in \{1, \dots, M-1\}$ by

$$F_j^{\rho,n} = \begin{cases} Q(\rho_j^n, w_j^n) & \text{if } S_{1,j}^n \geq 0, \\ Q_{HLL,j}^n & \text{if } S_{1,j}^n < 0 \leq S_{2,j}^n, \\ Q(\rho_{j+1}^n, w_{j+1}^n) & \text{if } S_{2,j}^n < 0, \end{cases} \tag{2.2.1}$$

where $S_{1,j} < S_{2,j}$ are the approximate wave speeds at cell interface j. In the literature, one can find a variety of approximations for the wave speeds. In this work we refer to [Dav88, Equation 4.5] and we make use of the characteristic speeds (1.1.2) of the 2×2 hyperbolic system, i.e.

$$\begin{aligned} S_{1,j} &= \min\{\lambda_1(\rho_j, w_j), \lambda_1(\rho_{j+1}, w_{j+1})\}, \\ S_{2,j} &= \max\{\lambda_2(\rho_j, w_j), \lambda_2(\rho_{j+1}, w_{j+1})\}. \end{aligned} \tag{2.2.2}$$

Moreover, the HLL-flux $Q_{HLL,j}^n$ is given by

$$Q_{HLL,j} = \frac{S_{2,j}Q(\rho_j, w_j) - S_{1,j}Q(\rho_{j+1}, w_{j+1}) + S_{1,j}S_{2,j}(\rho_{j+1} - \rho_j)}{S_{2,j} - S_{1,j}}.$$

We remark that since $\lambda_2(\rho, w) = \mathcal{V}(\rho, w) \geq 0$ for all $(\rho, w) \in \Omega$, the case $S_{2,j}^n < 0$ in Equation (2.2.1) never occurs. Additionally, in the specific scenario of two subsequent vacuum

states, i.e. $\rho_j^n = 0 = \rho_{j+1}^n$, it holds that $S_{1,j}^n = \min\{w_j^n, w_{j+1}^n\} = \max\{w_j^n, w_{j+1}^n\} = S_{2,j}^n$ and $F_j^{\rho,n} = 0$.
For numerical stability, we impose the same CFL condition (2.1.1) as for the Godunov scheme.

2.3 Hilliges-Weidlich scheme

For the scalar case, i.e. taking $w = constant$, a much easier and cheaper alternative is offered by an upwind type finite volume scheme proposed in [HW95] and more extensively studied in [BGKT08] for multi-class models. In this section, we propose an extension of this scheme to second order models, which we will refer to as Hilliges-Weidlich (HW) scheme [HW95]. Moreover, we prove that the scheme is positivity preserving and obeys a maximum principle under the hypothesis of a unique zero-speed density.

Under the CFL condition

$$\Delta t \leq \frac{\min\limits_{j\in\{1,\dots,M\}} \Delta x_j}{\left\{ \left\| \mathcal{V}(\rho, w) \right\|_{\mathbf{L}^\infty(\Omega)} + R(w_{max}) \left\| \mathcal{V}_\rho(\rho, w) \right\|_{\mathbf{L}^\infty(\Omega)} \right\}}, \tag{2.3.1}$$

the numerical flux in (2.0.2) is chosen to be

$$F_j^{\rho,n} = \rho_j^n \, \mathcal{V}^+(\rho_{j+1}^n, w_{j+1}^n), \tag{2.3.2}$$

where we only consider the non-negative part of the speed function $\mathcal{V}$, thus $\mathcal{V}^+(\rho, w) := \max\{\mathcal{V}(\rho, w), 0\}$. Indeed, since contact discontinuity waves have positive speed and the variable w is advected with ρv, the choice (2.0.2), (2.3.2) gives a good approximation of the flux at the interface, which corresponds to the Riemann problem given by $U_L = (\rho_j^n, w_j^n)$ and $U_M = (\rho_{j+\frac{1}{2}}^n, w_j^n)$. Here, U_M defines the intermediate state of the solution to the Riemann problem corresponding to U_L and $U_R = (\rho_{j+1}^n, w_{j+1}^n)$, where $\rho_{j+\frac{1}{2}}^n$ is implicitly defined by $\mathcal{V}(\rho_{j+\frac{1}{2}}^n, w_j^n) = \mathcal{V}(\rho_{j+1}^n, w_{j+1}^n)$, see Figure 2.1. Therefore we have

$$F_j^{\rho,n} = \rho_j^n \, \mathcal{V}^+(\rho_{j+1}^n, w_{j+1}^n) = \rho_j^n \, \mathcal{V}^+(\rho_{j+\frac{1}{2}}^n, w_j^n),$$

which reduces to the scalar case [BGKT08, HW95].

Proposition 8. *Under the CFL condition* $\Delta t \leq \dfrac{\min\limits_{j\in\{1,\dots,M\}} \Delta x_j}{\left\| \mathcal{V}(\rho, w) \right\|_{\mathbf{L}^\infty(\Omega)}}$, *which is weaker than* (2.3.1), *the numerical scheme* (2.0.1),(2.0.2),(2.3.2) *is positivity preserving.*

Proof. Let us assume that at time $t = t^n$, the approximate solution satisfies $\rho_j^n \geq 0$ for all $j \in \{1, \dots, M\}$. Then we get

$$\begin{aligned}
\rho_j^{n+1} &= \rho_j^n - \frac{\Delta t}{\Delta x_j} \left(\rho_j^n \, \mathcal{V}^+(\rho_{j+1}^n, w_{j+1}^n) - \rho_{j-1}^n \, \mathcal{V}^+(\rho_j^n, w_j^n) \right) \\
&= \rho_j^n \left(1 - \frac{\Delta t}{\Delta x_j} \, \mathcal{V}^+(\rho_{j+1}^n, w_{j+1}^n) \right) + \frac{\Delta t}{\Delta x_j} \, \rho_{j-1}^n \, \mathcal{V}^+(\rho_j^n, w_j^n) \geq 0,
\end{aligned}$$

since $\Delta t \, \mathcal{V}^+(\rho_{j+1}^n, w_{j+1}^n) \leq \Delta x_j$ by assumption. □

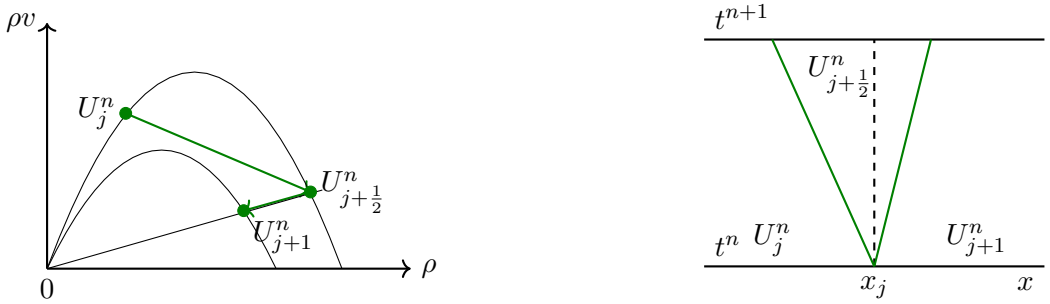

Figure 2.1: Left: Phase-plane representation of an example of solution to the Riemann problem corresponding to $U_L = U_j^n = (\rho_j^n, w_j^n)$ and $U_R = U_{j+1}^n = (\rho_{j+1}^n, w_{j+1}^n)$, consisting of a shock joining U_L to $U_M = U_{j+\frac{1}{2}}^n = (\rho_{j+\frac{1}{2}}^n, w_j^n)$ and a contact discontinuity from U_M to U_R. Right: Space-time representation of the Riemann solution at the corresponding cell interface.

Proposition 9. *Under the CFL condition* (2.3.1) *and if* $R(w) = R_{max}$ *for all* $w \in [w_{min}, w_{max}]$, *the approximate solution constructed by* (2.0.1),(2.0.2),(2.3.2) *satisfies* $\rho_j^n \leq R_{max}$ *for all* $j \in \{1, \dots, M\}$ *and* $n \in \mathbb{N}$. *In particular it holds that* $\mathcal{V}(\rho_j^n, w_j^n) \geq 0$ *for all* $j \in \{1, \dots, M\}$ *and* $n \in \mathbb{N}$.

Proof. We assume that at time $t = t^n$, the approximate solution satisfies $\rho_j^n \leq R_{max}$ for all $j \in \{1, \dots, M\}$. Then we get

$$
\begin{aligned}
\rho_j^{n+1} &= \rho_j^n - \frac{\Delta t}{\Delta x_j}\left[\rho_j^n\, \mathcal{V}^+(\rho_{j+1}^n, w_{j+1}^n) - \rho_{j-1}^n\, \mathcal{V}^+(\rho_j^n, w_j^n)\right] \\
&= \rho_j^n - \frac{\Delta t}{\Delta x_j}\left[\rho_j^n\, \mathcal{V}(\rho_{j+\frac{1}{2}}^n, w_j^n) - \rho_{j-1}^n\, \mathcal{V}(\rho_j^n, w_j^n)\right] \\
&= \rho_j^n - \frac{\Delta t}{\Delta x_j}\left[\rho_j^n\, \mathcal{V}(\rho_{j+\frac{1}{2}}^n, w_j^n) \pm \rho_j^n\, \mathcal{V}(\rho_j^n, w_j^n) - \rho_{j-1}^n\, \mathcal{V}(\rho_j^n, w_j^n)\right] \\
&= \rho_j^n - \frac{\Delta t}{\Delta x_j}\left[\rho_j^n\, \mathcal{V}_\rho(\xi_j^n, w_j^n)\left(\rho_{j+\frac{1}{2}}^n - \rho_j^n\right) + \mathcal{V}(\rho_j^n, w_j^n)\left(\rho_j^n - \rho_{j-1}^n\right)\right] \\
&= \rho_j^n\left[1 - \frac{\Delta t}{\Delta x_j}\left(b_j^n + a_j^n\right)\right] + \rho_{j+\frac{1}{2}}^n \frac{\Delta t}{\Delta x_j} b_j^n + \rho_{j-1}^n \frac{\Delta t}{\Delta x_j} a_j^n,
\end{aligned}
$$

for some $\xi_j^n \in [\min\{\rho_j^n, \rho_{j+\frac{1}{2}}^n\}, \max\{\rho_j^n, \rho_{j+\frac{1}{2}}^n\}]$ and setting $a_j^n := \mathcal{V}(\rho_j^n, w_j^n) \geq 0$ and $b_j^n := -\rho_j^n\, \mathcal{V}_\rho(\xi_j^n, w_j^n) \geq 0$ for all $j \in \{1, \dots, M\}$. Moreover, by (2.3.1), we get $1 - \frac{\Delta t}{\Delta x_j}(a_j^n + b_j^n) \geq 0$ and therefore we conclude

$$
\rho_j^{n+1} \leq R_{max}\left[1 - \frac{\Delta t}{\Delta x_j}\left(b_j^n + a_j^n\right)\right] + R_{max}\frac{\Delta t}{\Delta x_j} b_j^n + R_{max}\frac{\Delta t}{\Delta x_j} a_j^n = R_{max}.
$$

□

We remark that, in the general case where $R(w) \neq R_{max}$ for all $w \in [w_{min}, w_{max}]$, the positivity of the speed cannot be guaranteed. This is why we take $\mathcal{V}^+$ in (2.3.2).

2.4 Boundary cell implementation

In the Godunov scheme, the boundary conditions are typically given in terms of flow. This is motivated by the fact that the traffic flow is usually the most reliable quantity measured by magnetic loop detectors. Consequently, we expect a lower error in our simulation when using better quality data.
In the following, we denote by $q(t, x_{in}) = q_{in}^n$ (resp. $q(t, x_{out}) = q_{out}^n$) the inflow (resp. outflow) for $t \in [t^n, t^{n+1}[$, measured by the left (resp. right) boundary loop detector. Thus, the boundary conditions (1.0.1c) and (1.0.1d) are taken into account by setting

$$\begin{aligned} u_1^{n+1} &= u_1^n - \frac{\Delta t}{\Delta x_1} \left(\mathbf{F}_1^n - \min\left\{ q_{in}^n, S^\rho(\tilde{u}^n; w_{in}^n) \right\} \cdot \begin{pmatrix} 1 \\ w_{in}^n \end{pmatrix} \right), \\ u_M^{n+1} &= u_M^n - \frac{\Delta t}{\Delta x_M} \left(\min\left\{ D^\rho(u_M^n), q_{out}^n \right\} \cdot \begin{pmatrix} 1 \\ w_M^n \end{pmatrix} - \mathbf{F}_{M-1}^n \right), \end{aligned} \tag{2.4.1}$$

where $w_{in}^n = w(t, x_{in})$, $t \in [t^n, t^{n+1}[$ and $\tilde{u}^n = (\tilde{\rho}^n, \tilde{\rho}^n w_{in}^n)^\top$ with $\tilde{\rho}^n = \mathcal{R}(v_1^n, w_{in}^n)$ if $v_1^n < w_{in}^n$ and $\tilde{\rho}^n = 0$ otherwise.
However, since the HLL and HW scheme are not implemented in demand and supply formulation, the boundary data are given in terms of the density ρ and the Lagrangian vehicle property w. Analogously to the initial data, they are approximated by piece-wise constant functions, thus the numerical scheme reads for $j \in \{1, M\}$ as

$$\begin{aligned} u_1^{n+1} &= \frac{1}{\Delta t} \int_{t^n}^{t^{n+1}} u_{in}(t)\, dt, \\ u_M^{n+1} &= \frac{1}{\Delta t} \int_{t^n}^{t^{n+1}} u_{out}(t)\, dt, \end{aligned} \tag{2.4.2}$$

where $u_b = \big(\rho(t, x_b), \rho(t, x_b) w(t, x_b)\big)^\top$ and $b \in \{in, out\}$.
We remark that the implementation of the boundary data can be also done by adding *ghost cells* to the edges of the domain, see e.g. [Fan13, PS15]. However, in our later considered traffic scenarios, the position of the boundary loop detectors will coincide with the boundary cell interfaces, therefore we decide for the implementation as stated in (2.4.2).

Remark 17. The implementation of density boundary conditions is not only restricted to the HLL and HW scheme. It can also be applied to the Godunov scheme and it has an effect on the simulation output. If the application is traffic flow reconstruction, the flow data lead naturally to better results. However, if we are interested in travel time predictions, the density data implementation can be more favorable (see Section 6.1).

2.5 Data projection

Since initial and boundary conditions provided by data can lie outside the domain Ω (1.1.1), we perform a data projection whenever such an outlier occurs. In the data projection Algorithm 1, illustrated in Figure 2.2, we differentiate between the options where the density ρ exceed the maximum density $R(w_{max})$ (see **Case 1**) and where the Lagrangian vehicle property w

exceed w_{max} (see **Case 2** and **Case 3**). In the latter option, the projected data point depends finally on the absolute distance between the original flux ρv and the projected one.

Algorithm 1 Data projection algorithm for IBVP (1.0.1).

Require: Initial or boundary data $U = (\rho, w)$ with corresponding speed v;
  if $\rho > R(w_{max})$ **then**
    Case 1: replace U by $\hat{U} = (\mathcal{R}(v, w_{max}), w_{max})$;
  end if
  if $w > w_{max}$ **then**
    compute $\hat{\rho} = \mathcal{R}(v, w_{max})$ and $\hat{v} = \mathcal{V}(\rho, w_{max})$;
    if $|\hat{\rho}v - \rho v| < |\rho\hat{v} - \rho v|$ **then**
      Case 2: replace U by $\hat{U} = (\hat{\rho}, w_{max})$;
    else
      Case 3: replace U by $\hat{U} = (\rho, w_{max})$ and v by $\hat{v}$.
    end if
  end if

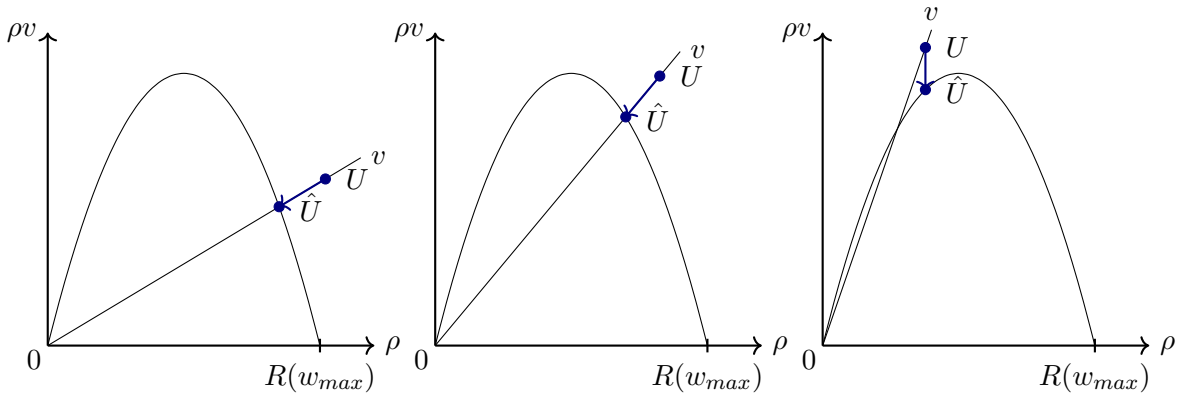

(a) **Case 1.** (b) **Case 2.** (c) **Case 3.**

Figure 2.2: Illustration of the three cases in the data projection algorithm 1.

Remark 18. Due to the fact that the numerical scheme is run by using only initial and boundary data, the data projection is only necessary for outliers in ρ^0, w^0, w_{in} and possibly also ρ_b, $b \in \{in, out\}$, if the boundary data are given in terms of density. Moreover, we remark that the quantity w cannot be directly measured by the loop detectors, instead it is calculated by inverting the velocity function $\mathcal{V}$ whose inverse is well-defined due to the properties stated in (II).

2.6 Numerical tests

In this section, we provide some tests exploring the behavior of solutions to the Riemann problem for (I) with the ARZ speed function $\mathcal{V}(\rho, w) = w - p(\rho)$ with $p(\rho) = \rho$ and initial data of the form $(\rho, w)(0, x) = U_L = (\rho_L, w_L)$ if $x \leq 0.5$ and $(\rho, w)(0, x) = U_R = (\rho_R, w_R)$

if $x > 0$. We compare the solutions at $T = 0.5$ computed on the space interval $[0, 1]$ by the Godunov, HLL and HW schemes with uniform cell sizes $\Delta x_j = \Delta x$ for $j \in \{1, \dots, M\}$ and with absorbing boundary conditions, i.e.

$$u_1^{n+1} = u_1^n - \frac{\Delta t}{\Delta x_1}\left(\mathbf{F}_1^n - \mathbf{F}_0^n\right), \quad u_M^{n+1} = u_M^n - \frac{\Delta t}{\Delta x_M}\left(\mathbf{F}_M^n - \mathbf{F}_{M-1}^n\right),$$

where $\mathbf{F}_0^n = (\rho_1^n v_1^n, w_1^n \rho_1^n v_1^n)^\top$ and $\mathbf{F}_M^n = (\rho_M^n v_M^n, w_M^n \rho_M^n v_M^n)^\top$. The numerical solutions are also compared with the entropy admissible analytical solutions defined in Definition 1 (denoted as Analytical Solution 1 - AS1).
The code is implemented in MATLAB [MAT22] on a laptop with a 4 core 8 thread 2.3 GHz Intel Core i7 processor and 16GB of RAM.

2.6.1 Solutions without vacuum states

In the following, we compare the solutions of the numerical schemes for Riemann problems where vacuum situations do not occur. This analysis refers to Cases 1-5 in Definition 1. Since a shock wave (Case 1), rarefaction wave (Case 3) and a contact discontinuity (Case 5) appear also in Cases 2 and 4, it is sufficient to consider these two.
To compare the performance of the proposed schemes, we consider the $\mathbf{L^1}$-error $\mathbf{L^1}(\Delta x)$ and the numerical order of accuracy $\gamma(\Delta x)$ for different cell sizes $\Delta x \in \left\{\frac{1}{100}, \frac{1}{200}, \frac{1}{400}, \frac{1}{800}, \frac{1}{1600}\right\}$ at time T, defined respectively by

$$\begin{aligned} \mathbf{L^1}(\Delta x) &= \frac{1}{M}\sum_{j=1}^{M}\left\{\left|\rho_j^{\frac{T}{\Delta t}} - \bar{\rho}\right| + \left|y_j^{\frac{T}{\Delta t}} - \bar{y}\right|\right\}, \\ \gamma(\Delta x) &= \log_2\left(\frac{\mathbf{L^1}(2\Delta x)}{\mathbf{L^1}(\Delta x)}\right), \end{aligned} \tag{2.6.1}$$

where $\bar{\rho}$ and $\bar{y}$ denote the cell averages of the exact Riemann solution AS1 at time T. Additionally, we also compare the times t_c (in seconds) which are needed to compute the numerical solutions at T. To this end, we choose the initial data as follows:

- **Test 1:** $U_L = (0.3, 0.5)$, $U_R = (0.7, 0.8)$ (see Figure 2.3 and Table 2.1),
  whose solution corresponds to a shock followed by a contact discontinuity (see Case 2).
- **Test 2:** $U_L = (0.5, 0.7)$, $U_R = (0.3, 0.9)$ (see Figure 2.4 and Table 2.2),
  whose solution corresponds to a rarefaction wave followed by a contact discontinuity (see Case 4).

We observe in Figure 2.3 and 2.4 that all three numerical schemes capture well AS1, however the graphs referring to the HW scheme are slightly more diffusive due to higher numerical viscosity. Therefore, its $\mathbf{L^1}$-error and order of convergence exceed the ones of the other schemes (see Table 2.1 and 2.2). The performance of the Godunov and HLL scheme are very similar noting that the Godunov scheme leads to a lower $\mathbf{L^1}$-error in **Test 1** (except for $\Delta x = \frac{1}{1600}$) and a higher $\mathbf{L^1}$-error in **Test 2**. Moreover we emphasize that, as expected for first order schemes with discontinuous solutions, the order of convergence is about 0.5. Concerning the computation time, we observe for all schemes an increasing time t_c for decreasing mesh sizes

Δx. Moreover, the HW scheme is the cheapest among the schemes, whereas the HLL scheme is slightly more expensive than the Godunov scheme which can be explained by the need to calculate the eigenvalues of the system (see Equations (2.2.2)).

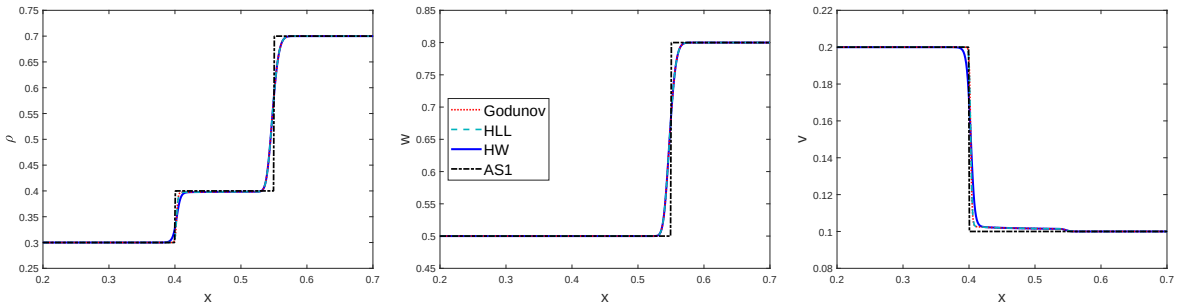

(a) Density ρ. (b) Lagrangian marker w. (c) Speed v.

Figure 2.3: **Test 1**. Solutions of the Riemann problem with $U_L = (0.3, 0.5)$, $U_R = (0.7, 0.8)$, computed by the Godunov, HLL and HW scheme at $T = 0.5$ with $\Delta x = \frac{1}{800}$, compared to the analytical solution.

	Godunov			HLL			HW		
$1/\Delta x$	$\mathbf{L^1}(\Delta x)$	$\gamma(\Delta x)$	t_c	$\mathbf{L^1}(\Delta x)$	$\gamma(\Delta x)$	t_c	$\mathbf{L^1}(\Delta x)$	$\gamma(\Delta x)$	t_c
100	$13.52 \cdot 10^{-3}$	–	0.002	$13.63 \cdot 10^{-3}$	–	0.003	$15.37 \cdot 10^{-3}$	–	0.001
200	$9.46 \cdot 10^{-3}$	0.515	0.007	$9.51 \cdot 10^{-3}$	0.520	0.008	$10.66 \cdot 10^{-3}$	0.528	0.004
400	$6.67 \cdot 10^{-3}$	0.505	0.010	$6.69 \cdot 10^{-3}$	0.508	0.011	$7.32 \cdot 10^{-3}$	0.543	0.005
800	$4.74 \cdot 10^{-3}$	0.495	0.027	$4.74 \cdot 10^{-3}$	0.497	0.048	$5.02 \cdot 10^{-3}$	0.544	0.024
1600	$3.37 \cdot 10^{-3}$	0.490	0.082	$3.37 \cdot 10^{-3}$	0.491	0.117	$3.47 \cdot 10^{-3}$	0.530	0.051

Table 2.1: **Test 1**. $\mathbf{L^1}$-error, numerical order of accuracy and computation time (in seconds) for the Godunov, HLL and HW scheme at $T = 0.5$.

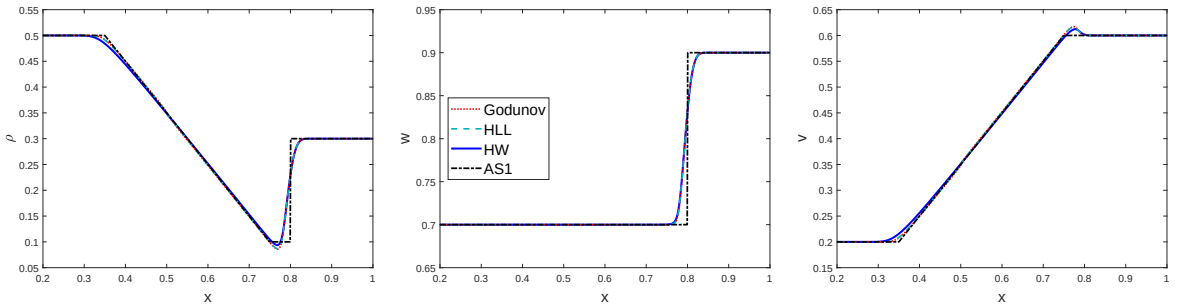

(a) Density ρ. (b) Lagrangian marker w. (c) Speed v.

Figure 2.4: **Test 2**. Solutions of the Riemann problem with $U_L = (0.5, 0.7)$, $U_R = (0.3, 0.9)$, computed by the Godunov, HLL and HW scheme at $T = 0.5$ with $\Delta x = \frac{1}{800}$, compared to the analytical solution.

	Godunov			HLL			HW		
$1/\Delta x$	$\mathbf{L^1}(\Delta x)$	$\gamma(\Delta x)$	t_c	$\mathbf{L^1}(\Delta x)$	$\gamma(\Delta x)$	t_c	$\mathbf{L^1}(\Delta x)$	$\gamma(\Delta x)$	t_c
100	$17.84 \cdot 10^{-3}$	–	0.002	$16.56 \cdot 10^{-3}$	–	0.003	$28.05 \cdot 10^{-3}$	–	0.001
200	$11.64 \cdot 10^{-3}$	0.617	0.003	$10.85 \cdot 10^{-3}$	0.610	0.005	$17.63 \cdot 10^{-3}$	0.670	0.003
400	$8.03 \cdot 10^{-3}$	0.534	0.008	$7.47 \cdot 10^{-3}$	0.539	0.009	$10.77 \cdot 10^{-3}$	0.710	0.005
800	$5.89 \cdot 10^{-3}$	0.447	0.019	$5.58 \cdot 10^{-3}$	0.421	0.039	$6.89 \cdot 10^{-3}$	0.646	0.015
1600	$4.29 \cdot 10^{-3}$	0.458	0.068	$4.12 \cdot 10^{-3}$	0.438	0.095	$4.74 \cdot 10^{-3}$	0.540	0.051

Table 2.2: **Test 2**. $\mathbf{L^1}$-error, numerical order of accuracy and computation time (in seconds) for the Godunov, HLL and HW scheme at $T = 0.5$.

Next, we are also interested in comparing the performances of the schemes when considering smooth initial data which is studied in Test 3:

- **Test 3:** $\rho(0,x) = 0.45 \exp\left(-\frac{(x-0.5)^2}{2 \cdot 0.1^2}\right) + 0.2$, $w(0,x) = 1.12(x-0.5)^2 + 0.7$, whose solution is smooth (see Figure 2.5 and Table 2.3).

This time, the numerical solutions are compared to the cell averages of a reference solution which is computed numerically by the Godunov scheme with a fine cell size $\Delta x = \frac{1}{3200}$. Finally, we can reinforce the observations from **Test 1** and **Test 2**, meaning that we observe again a higher $\mathbf{L^1}$-error for the HW scheme and a similar performance between the Godunov and HLL scheme. This time, the order of convergence is about 1, where HW and HLL showing in general a slightly higher order than Godunov's. Moreover, as expected, the HW scheme is again the fastest performing scheme, followed by the Godunov and finally the HLL one.

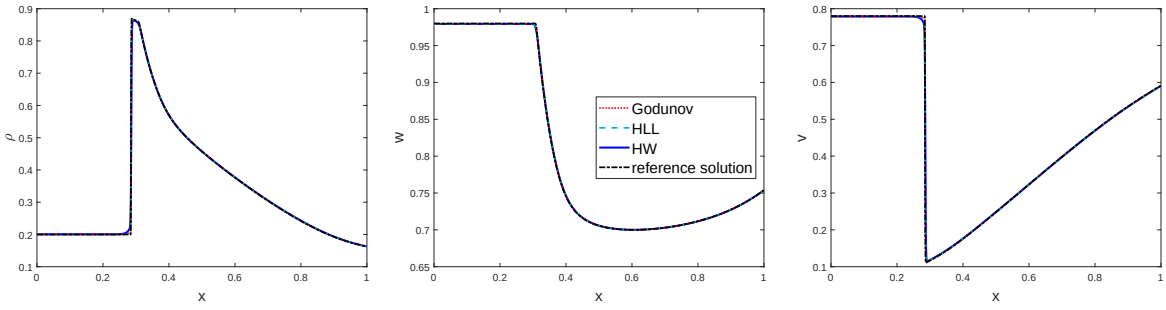

(a) Density ρ. (b) Lagrangian marker w. (c) Speed v.

Figure 2.5: **Test 3**. Solutions of the Riemann problem for smooth initial data computed by the Godunov, HLL and HW scheme at $T = 0.5$ with $\Delta x = \frac{1}{800}$, compared to a reference solution.

Summarizing the results for the numerical tests, we come to similar performances in terms of $\mathbf{L^1}$-error and order of convergences for all proposed numerical schemes. Thus, the quality of the approximation is not significantly impacted by the choice of the numerical scheme since the slightly higher $\mathbf{L^1}$-error in the HW scheme can be neglected. However, if the simulations need to be executed several times, e.g in an optimization algorithm as in [WGV23, Section 4.2], the choice of the HW can be indeed favorable due to a sensibly lower computation time.

	Godunov			HLL			HW		
$1/\Delta x$	$\mathbf{L^1}(\Delta x)$	$\gamma(\Delta x)$	t_c	$\mathbf{L^1}(\Delta x)$	$\gamma(\Delta x)$	t_c	$\mathbf{L^1}(\Delta x)$	$\gamma(\Delta x)$	t_c
100	$10.25 \cdot 10^{-3}$	–	0.007	$10.15 \cdot 10^{-3}$	–	0.011	$20.85 \cdot 10^{-3}$	–	0.005
200	$5.37 \cdot 10^{-3}$	0.932	0.014	$6.72 \cdot 10^{-3}$	0.594	0.014	$12.36 \cdot 10^{-3}$	0.750	0.011
400	$2.76 \cdot 10^{-3}$	0.963	0.020	$3.35 \cdot 10^{-3}$	1.006	0.014	$6.23 \cdot 10^{-3}$	0.988	0.012
800	$1.37 \cdot 10^{-3}$	1.009	0.058	$1.59 \cdot 10^{-3}$	1.074	0.060	$3.06 \cdot 10^{-3}$	1.024	0.036
1600	$0.65 \cdot 10^{-3}$	1.068	0.085	$0.70 \cdot 10^{-3}$	1.185	0.129	$1.44 \cdot 10^{-3}$	1.086	0.056

Table 2.3: **Test 3**. $\mathbf{L^1}$-error, numerical order of accuracy and computation time (in seconds) for the Godunov, HLL and HW scheme at $T = 0.5$.

2.6.2 Solutions involving vacuum states

In the following, we analyse the behavior of the numerical schemes when vacuum states occur. However, as seen in Chapter 1, there is no unique entropy admissible analytical solutions when vacuum is involved. Thus, we compare the numerical solutions not only with AS1 but also with the ones proposed by [Fan13], denoted as AS2.
Since the numerical schemes are expressed in conservative variables $(\rho, y = \rho w)^\top$, the Lagrangian vehicle property w is not defined whenever $\rho = 0$. Therefore, we demonstrate in this section that, whenever $\rho_j^n = 0$, setting

$$w_j^n = \begin{cases} w_k^n \text{ with } k = \max\limits_{i<j}\{i\colon \rho_i^n > 0\} & \text{if } \exists\ i < j \text{ with } \rho_i > 0 \text{ and } j \in \{2, \dots, M\}, \\ w_j^{n-1} & \text{otherwise,} \end{cases}$$

is coherent with the density component of the Riemann solution stated in Cases 6-9 in Definition 1. Notice that, due to numerical viscosity, density at vacuum states may not be exactly zero, affecting the w and $v = \mathcal{V}(\rho, w)$ components.
The results for different initial data are discussed in the following tests:

- **Test 4:** middle vacuum state $\rho_M = 0$ (see Figure 2.6).
  AS1 consists of a rarefaction from $U_L = (0.4, 0.5)$ to $(0, 0.5)$ followed by a contact discontinuity to $U_R = (0.1, 0.9)$ travelling with speed $\mathcal{V}(U_R) = 0.8$ (see Case 6).
  AS2 is composed of a rarefaction wave connecting U_L to $(0, 0.5)$, followed by a vacuum wave and a contact discontinuity between $(0, 0.8)$ and U_R.
  While the ρ component is the same for all solutions, the w and v components of the numerical solutions match AS2, which is $\mathbf{L^1}$-stable in the Riemann invariants.

- **Test 5:** left vacuum state $\rho_L = 0$ (see Figures 2.7 and 2.8).
  (A) Both analytical solutions are the juxtaposition of a shock from $U_L = (0, 0.7)$ to $(0.5, 0.7)$ and a contact discontinuity, moving at the same speed $\mathcal{V}(U_R) = 0.2$ to $U_R = (0.3, 0.5)$ (see Case 7).
  (B) AS1 consists of a discontinuity between $U_L = (0, 0.4)$ and $U_R = (0.2, 0.8)$ travelling with speed $\mathcal{V}(U_R) = 0.6$ (see Case 7).
  AS2 is a vacuum wave from U_L to $(0, 0.6)$ followed by a contact discontinuity.
  We observe that the numerical schemes capture the ρ component, but there is a discrepancy in the Riemann invariants: indeed, due to numerical viscosity, the approximate solutions consist of a stationary vacuum discontinuity followed by a shock from $(0, 0.5)$ (resp. $(0, 0.8)$) to U_R.

- **Test 6:** right vacuum state $\rho_R = 0$ (see Figures 2.9, 2.10 and 2.11).
  (A) AS1 consists of a rarefaction wave from $U_L = (0.3, 0.5)$ to $(0, 0.5)$ (see Case 8 and Figure 1.1b).
  In AS2, the rarefaction is followed by a vacuum wave from $(0, 0.5)$ to $U_R = (0, 0.7)$ (see Figure 1.2b).
  (B) AS1 consists of a rarefaction wave from $U_L = (0.5, 0.7)$ to $(0, 0.7)$ (see Case 8 and Figure 1.1a).
  AS2 is composed of a rarefaction from U_L to $(0.3, 0.7)$, followed by a contact discontinuity to $U_R = (0, 0.4)$ moving with speed $\mathcal{V}(U_R) = 0.4$ (see Figure 1.2a).
  (C) AS1 consists of a rarefaction wave from $U_L = (0.3, 0.8)$ to $(0, 0.8)$ (see Case 8).
  AS2 is composed of a shock from U_L to $(0.5, 0.8)$ with 0 speed, followed by a contact discontinuity to $U_R = (0, 0.3)$ moving with speed $\mathcal{V}(U_R) = 0.3$ (see Figure 1.2d).
  In all the cases, the numerical solutions capture AS1 by construction.

- **Test 7:** two vacuum states $\rho_L = \rho_R = 0$ (see Figures 2.12 and 2.13).
  (A) In AS1, the solution is $U_L = (0, 0.8)$ (see Case 9).
  AS2 is a juxtaposition of a shock shock from U_L to $(0.6, 0.8)$ and a contact discontinuity, moving at the same speed $\mathcal{V}(U_R) = 0.2$ to $U_R = (0, 0.2)$.
  (B) In AS1, the solution is $U_L = (0, 0.2)$ (see Case 9).
  AS2 consists of a vacuum wave from U_L to $U_R = (0, 0.8)$.
  In all the cases, the numerical solutions capture AS1 by construction.

We observe that in all tests the three numerical schemes show the same behavior for the ρ, w and v component, whereas we observe again more diffusive graphs for the HW scheme.

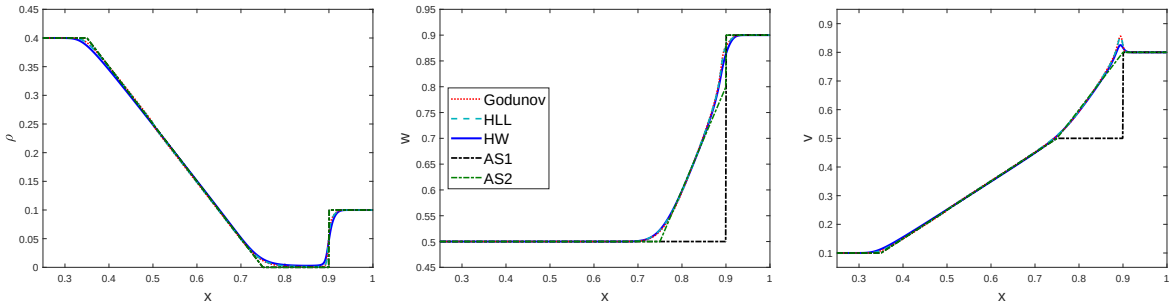

(a) Density ρ. (b) Lagrangian marker w. (c) Speed v.

Figure 2.6: **Test 4**. Solutions of the Riemann problem with $U_L = (0.4, 0.5)$, $U_R = (0.1, 0.9)$, computed by the Godunov, HLL and HW scheme at $T = 0.5$ with $\Delta x = \frac{1}{800}$, compared to the analytical solutions.

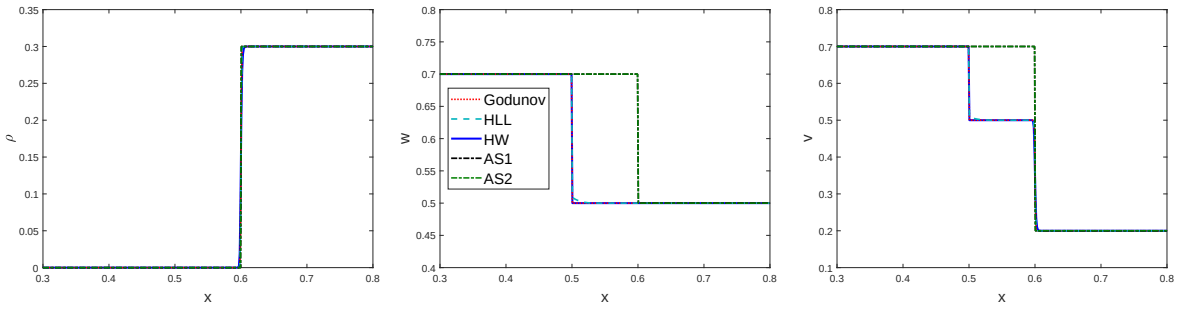

(a) Density ρ. (b) Lagrangian marker w. (c) Speed v.

Figure 2.7: **Test 5** (A). Solutions of the Riemann problem with $U_L = (0, 0.7)$, $U_R = (0.3, 0.5)$, computed by the Godunov, HLL and HW scheme at $T = 0.5$ with $\Delta x = \frac{1}{800}$, compared to the analytical solutions.

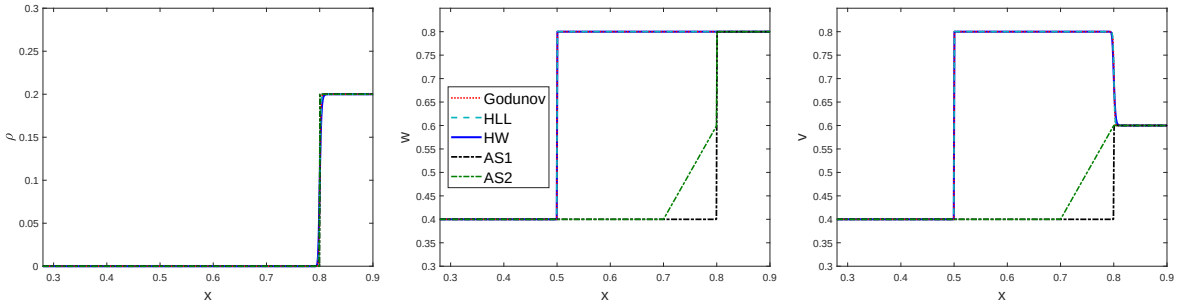

(a) Density ρ. (b) Lagrangian marker w. (c) Speed v.

Figure 2.8: **Test 5** (B). Solutions of the Riemann problem with $U_L = (0, 0.4)$, $U_R = (0.2, 0.8)$, computed by the Godunov, HLL and HW scheme at $T = 0.5$ with $\Delta x = \frac{1}{800}$, compared to the analytical solutions.

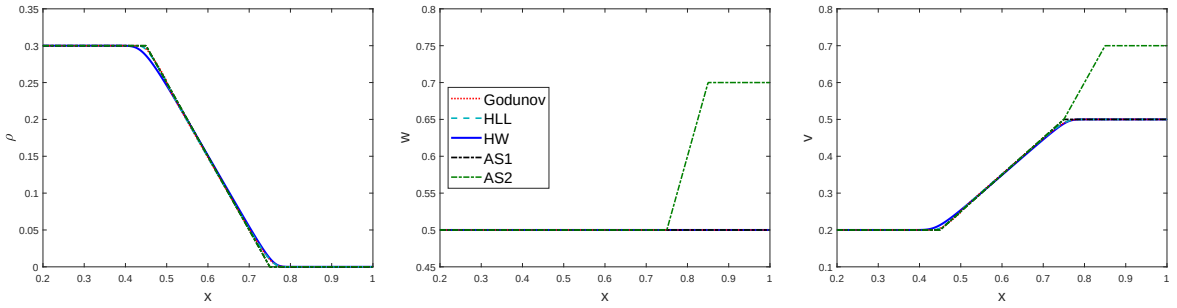

(a) Density ρ. (b) Lagrangian marker w. (c) Speed v.

Figure 2.9: **Test 6** (A). Solutions of the Riemann problem with $U_L = (0.3, 0.5)$, $U_R = (0, 0.7)$, computed by the Godunov, HLL and HW scheme at $T = 0.5$ with $\Delta x = \frac{1}{800}$, compared to the analytical solutions.

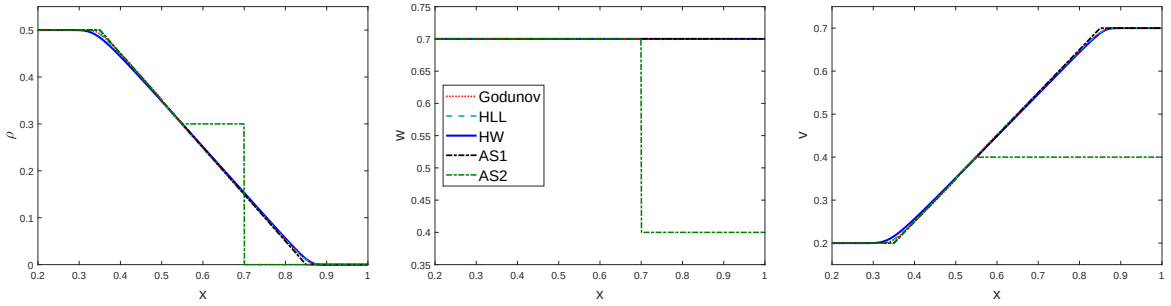

(a) Density ρ. (b) Lagrangian marker w. (c) Speed v.

Figure 2.10: **Test 6** (B). Solutions of the Riemann problem with $U_L = (0.5, 0.7)$, $U_R = (0, 0.4)$, computed by the Godunov, HLL and HW scheme at $T = 0.5$ with $\Delta x = \frac{1}{800}$, compared to the analytical solutions.

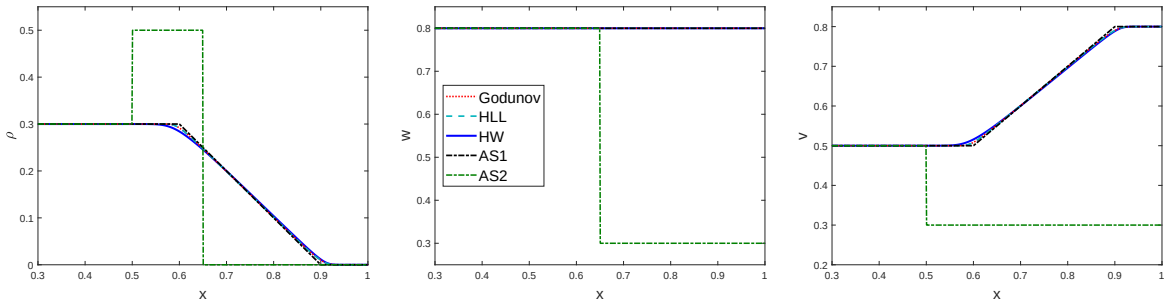

(a) Density ρ. (b) Lagrangian marker w. (c) Speed v.

Figure 2.11: **Test 6** (C). Solutions of the Riemann problem with $U_L = (0.3, 0.8)$, $U_R = (0, 0.3)$,
computed by the Godunov, HLL and HW scheme at $T = 0.5$ with $\Delta x = \frac{1}{800}$, compared to the analytical solutions.

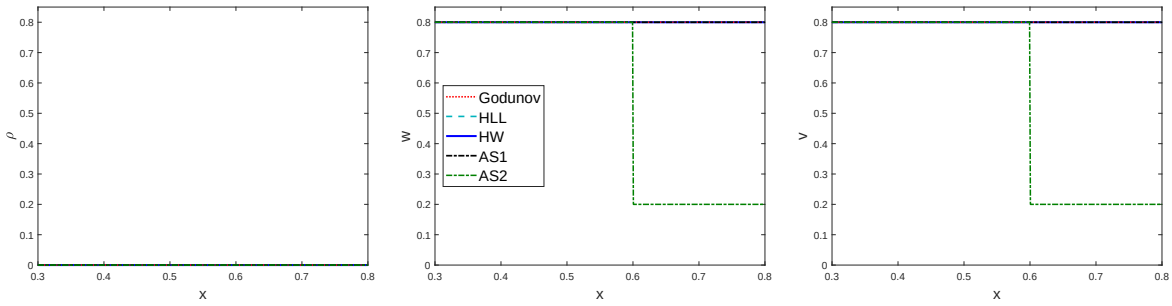

(a) Density ρ. (b) Lagrangian marker w. (c) Speed v.

Figure 2.12: **Test 7** (A). Solutions of the Riemann problem with $U_L = (0, 0.8)$, $U_R = (0, 0.2)$, computed by the Godunov, HLL and HW scheme at $T = 0.5$ with $\Delta x = \frac{1}{800}$, compared to the analytical solutions.

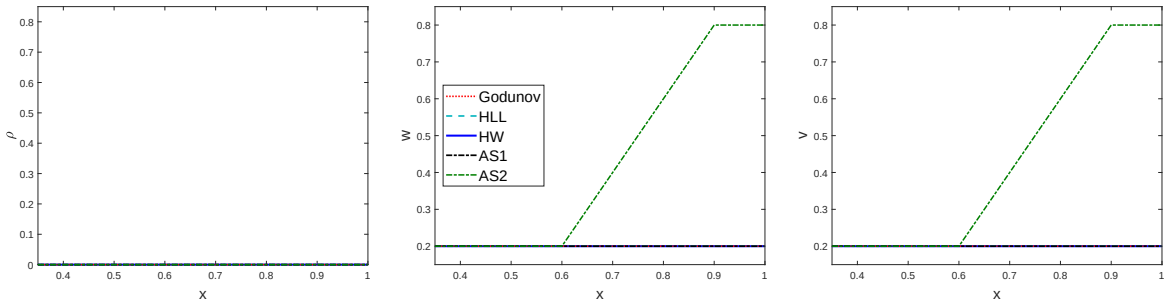

(a) Density ρ. (b) Lagrangian marker w. (c) Speed v.

Figure 2.13: **Test 7** (B). Solutions of the Riemann problem with $U_L = (0, 0.2)$, $U_R = (0, 0.8)$, computed by the Godunov, HLL and HW scheme at $T = 0.5$ with $\Delta x = \frac{1}{800}$, compared to the analytical solutions.

Chapter 3

Calibration approaches

One important ingredient for macroscopic traffic flow models is the fundamental diagram which describes a functional relationship between the traffic density and speed or flow. Therefore, it is necessary to select a suitable speed function $\mathcal{V}$, satisfying the assumptions stated in Equations (II), in order to implement the model. Usually, this function involves some unknown parameters which have to be calibrated. In first order macroscopic traffic flow models a common choice is the triangular flux function, as in [DGK$^+$09, PS15], where the unknown parameters are the critical density, the capacity, i.e. maximum expected flow on a road stretch, and the maximum density. In [FHS14], they consider a smooth speed function, involving again three parameters which are, however, more difficult to interpret from a traffic viewpoint. Thus, we consider the speed function

$$\mathcal{V}(\rho, w) = w \left(1 - \exp\left(\frac{C}{V}\left(1 - \frac{R}{\rho}\right)\right)\right), \tag{3.0.1}$$

which is derived from Newell-Franklin [Fra61, New61] and where the parameters to be identified are summarized in the vector $\theta = (V, C, R)$ with $V > 0$ the maximum speed, $R > 0$ the maximum density and $C > 0$ the wave propagation speed in congestion. Indeed we can prove that for this choice it holds that

$$\mathcal{V}(\rho, w) \geq 0,\ \mathcal{V}(0, w) = \lim_{\rho \to 0} \mathcal{V}(\rho, w) = w,\ \mathcal{V}(R, w) = 0,$$

$$Q_{\rho\rho}(\rho, w) = 2\mathcal{V}_\rho(\rho, w) + \rho \mathcal{V}_{\rho\rho}(\rho, w) = -w \exp\left(\frac{C}{V}\left(1 - \frac{R}{\rho}\right)\right) \frac{C^2}{V^2} \frac{R^2}{\rho^3} < 0 \text{ and}$$

$$\mathcal{V}_w(\rho, w) = 1 - \exp\left(\frac{C}{V}\left(1 - \frac{R}{\rho}\right)\right) > 0.$$

In particular, the condition $\mathcal{V}(0, w) = w$ identifies the Lagrangian marker w as a driver dependent empty road velocity, meaning that the higher w, the more aggressive the driver tends to be. We emphasize that the speed function for the first order LWR model is obtained by fixing $w = V$ in (3.0.1).
The fundamental diagrams, i.e. the density-speed or density-flow mapping described by the model speed function (3.0.1), are illustrated in Figure 3.1, where the lower and upper boundary curves correspond to w_{min} and w_{max} respectively. Note that all curves are equipped with

the same maximum density R and critical density ρ_{cr} since for our choice of $\mathcal{V}$ it holds that $R(w) = R$ and $\rho_{cr}(w) = \rho_{cr}$ for all $w \in [w_{min}, w_{max}]$. We observe that there can occur two cases such that the traffic flow is null: either if the road is empty (density is null) or the road is fully congested (density reaches its maximum value and speed is zero). Moreover, we call the part for densities lower (resp. higher) than the critical one free flow (resp. congested) region. This separation allows the Godunov scheme with its supply-demand formulation to efficiently solve the equations.

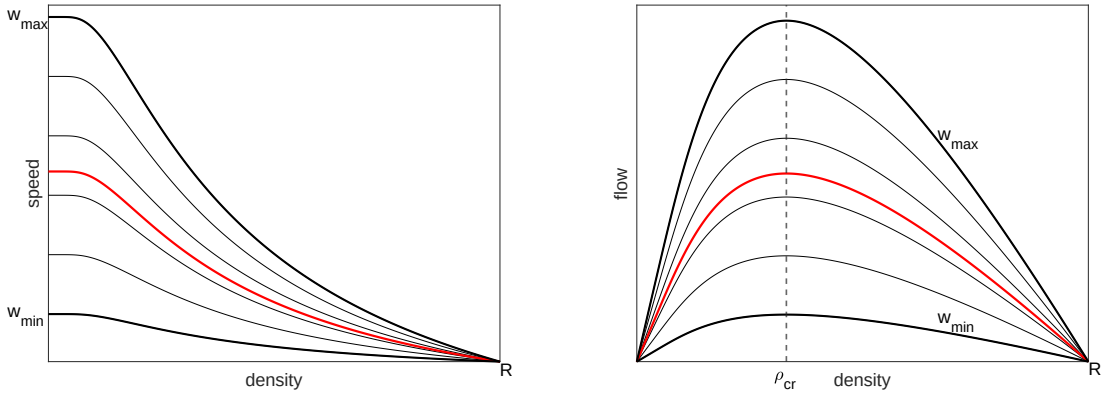

Figure 3.1: Illustration of the fundamental speed and flow diagrams for the GSOM speed function (3.0.1) with $\theta = (80, 30, 300)$. In red: curves corresponding to the choice $w = V$.

A fundamental point for model validation and real world implementation is to calibrate the parameter θ from measured data. The remaining question is now, how to identify the parameter θ from these data. This is why we will focus in the following sections on different deterministic and statistical approaches for parameter calibration, which is often a challenging task due to model limitations and data noise. In general, the idea of calibration is to find a set of suitable parameters such that the modeling result fits well with the real traffic data. Once the parameters are found, a good model can be used for reconstructing and predicting traffic flow. Some of the presented results are detailed in [WBGG22].

Remark 19. We note that, in contrast to [Fan13, FHS14], we do not set a-priori the value of the maximum density R, but we calibrate it along with V and C.
Moreover, we point out that the data projection Algorithm 1 requires the knowledge of the maximum empty road velocity w_{max}, which can be either integrated in the calibration problem or set to a reasonable value beforehand. In this work, we decide for the second option because we did not observe an improvement of the results in preliminary tests when treating w_{max} as unknown. Additionally, this simplification reduces the dimension of the optimization problem.

3.1 Preliminaries

Before presenting the different calibration approaches, we introduce some notation which is used throughout the work. In the following, we denote by P the real process under study, F the so called "field", where P is physically observed, both depending on time t and 1-dimensional space x. The mathematical model, a function of (t, x) and additionally the

calibration parameter θ, is indicated by M. Moreover, $\mathcal{X}_N = \big((t_1, x_1), \dots, (t_N, x_N)\big)$ denotes the set of time-space points where observations have been recorded.
By $y^F(t,x)$ we express the field observations at time t and position x of the real output $y^P(t,x)$. It is generally assumed that the field observations are noisy measurements of the real data, thus P and F are related as

$$y^F(t,x) = y^P(t,x) + \varepsilon,$$

where the observation error ε is assumed to be independent and identically normally distributed (iid) with zero mean, i.e. $\epsilon \sim \mathcal{N}(0, \sigma_\varepsilon^2)$ and $\sigma_\varepsilon^2 > 0$.
Kennedy-O'Hagan (KOH) [KO01] propose to additionally take into account the inadequacy between the mathematical model with optimal parameter $\theta^* = (V^*, C^*, R^*)$ and reality, via an additional discrepancy (or bias) term b, meaning that

$$y^P(t,x) = y^M(t,x,\theta^*) + b(t,x,\theta^*), \tag{3.1.1}$$

where b depends also on the calibration parameter and y^M represents the numerical solution of the macroscopic traffic flow model. We note that the data y^k, $k \in \{F, P, M\}$, can stand for any quantity of interest, typically the flow, speed or density in the traffic context.
Finally, it holds for all $i \in \{1, \dots, N\}$:

$$y^F(t_i, x_i) = y^M(t_i, x_i, \theta^*) + b(t_i, x_i, \theta^*) + \varepsilon.$$

Remark 20. We remark that it is common to have two types of inputs in computer experiments, see for instance [Gra20, Plu17], namely

1. the time and space variables, t and x, which occur in both the mathematical model, the real and field data and
2. the calibration parameter θ which is adjustable for the simulation code but fixed (and mostly unknown) for the real and field observations.

3.2 Gaussian process modeling

To estimate the bias function, introduced in Equation (3.1.1), we rely on a Gaussian process (GP) regression [HKC$^+$04, KO01], which amounts to assume a multivariate normal (MVN) distribution for the discrepancy.

Remark 21. KOH also models y^M with a Gaussian process as y^M is computationally expensive in their setup. This is not necessary here since the mathematical model evaluation is relatively cheap. Therefore, we stick to the simpler framework described in [HKC$^+$04].

Given a set of observations of the field (resp. simulated) data $y^F(\mathcal{X}_N) = \Big(y^F(t_1,x_1), \dots, y^F(t_N,x_N)\Big)$ (resp. $y^M(\mathcal{X}_N, \theta^*) = \Big(y^M(t_1,x_1,\theta^*), \dots, y^M(t_N,x_N,\theta^*)\Big)$) at N observation points $\mathcal{X}_N$, we compute the set of observed (noisy) biases $\mathbf{b}_N$ by

$$\mathbf{b}_N = y^F(\mathcal{X}_N) - y^M(\mathcal{X}_N, \theta^*).$$

The GP assumption considers $\mathbf{b}_N$ as a realization of a (zero-mean) MVN distribution:

$$\mathbf{b}_N \sim \mathcal{N}(\mathbf{0}_N, \mathbf{K}_N) \text{ with } \mathbf{K}_N = \sigma^2 \mathbf{C}_N + \sigma_\varepsilon^2 \mathbf{I}_N = \sigma^2(\mathbf{C}_N + g\mathbf{I}_N) \text{ and } g = \frac{\sigma_\varepsilon^2}{\sigma^2},$$

where $\mathbf{I}_N$ is the $N \times N$ identity matrix. Here, $\mathbf{K}_N$ (resp. $\mathbf{C}_N$) denotes the covariance (resp. correlation) matrix between the observed biases; the hyper-parameter σ^2 stands for the process variance. More precisely, the matrix entries of $\mathbf{C}_N$ are computed by $\mathbb{C}orr\Big(b(t,x), b(t',x')\Big) = c\big((t,x),(t',x')\big)$, where $c(\cdot,\cdot)$ is a positive definite function, typically from a parametric family, such as the Gaussian kernel:

$$c\big((t,x),(t',x')\big) = \exp\left(-\frac{(t-t')^2}{l_1^2}\right) \cdot \exp\left(-\frac{(x-x')^2}{l_2^2}\right), \tag{3.2.1}$$

among others like Matérn kernels, see e.g. [Ste99]. The (hyper-)parameters l_1 and l_2 denote, respectively, the length-scales for the time and space variables. The higher the value of l_i, $i \in \{1,2\}$, the stronger the correlation between two different observed points, whereas a low value of l_i leads to less correlation. Moreover, the parameterization using g instead of σ_ε^2 allows to reduce the number of hyper-parameters. This term accounts for the unknown measurement noise in the bias, assuming an iid Gaussian distribution, as it is typical with physical measurements.

Remark 22. We consider a stationary kernel by the Gaussian covariance function, meaning that it only depends on distances between observed data points. This choice is motivated by the length of the road stretch and the time window considered in the later introduced traffic scenarios (see Chapter 5), where road conditions are supposed to be homogeneous.
Additionally, we note that the correlation between two observation points decreases when their distance increases.

We emphasize that the bias is fully characterized by its covariance structure since the mean is chosen to be zero, which is typically done unless there is some prior knowledge available [BCO21, BG21]. To illustrate the GP dependency on its covariance hyper-parameters, we construct 1-dimensional toy-examples, i.e. considering $c(t,t') = \exp\left(-\frac{(t-t')^2}{l^2}\right)$, with different choices of σ and l on an equally spaced grid in $[0,1]$. The values $b(t_1),\dots,b(t_N)$ are then sampled from $\mathcal{N}(\mathbf{0}_N, \sigma^2\mathbf{C}_N)$, where we set $N = 2001$. Moreover, the diagonal entries of $\mathbf{C}_N$ are equipped with a small term (10^{-6}) in order to improve the condition number of the covariance matrix [Gra20]. In Figure 3.2 we indeed observe that the higher the length-scale l, the more similar the values between close observation points. However, if l is comparatively low as in Figure 3.2a, strong fluctuations exist even between close bias observations. Considering the process variance, the figure emphasizes higher amplitudes for the bias if the variance is high. Thus, for example in Figure 3.2c, the purple line, i.e. $\sigma^2 = 10$, is lying above the other ones which refer to lower values for σ^2. Especially the curve where $\sigma^2 = 0.1$ is quite flat since the variance is relatively low and additionally the length-scale parameter high.
A reason why GPs are widely used in current statistical research, ranging from physics [HKC+04] to engineering [BBK+09, HGBL20] or biology [Plu17], is its predictive power. More precisely, we know from the properties of the MVN distribution, if a $(\hat{N}+N)$-dimensional random multivariate normal vector $Y \sim \mathcal{N}(\mu,\Sigma)$ is partitioned as

$$Y = \begin{pmatrix} Y_1 \\ Y_2 \end{pmatrix} \quad \text{with sizes} \quad \begin{pmatrix} \hat{N} \times 1 \\ N \times 1 \end{pmatrix},$$

and accordingly μ and Σ are partitioned as

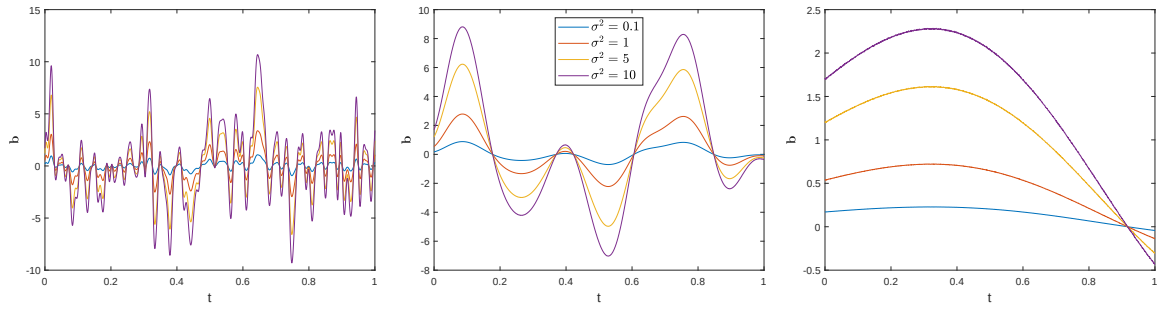

(a) $l = 0.01$ (b) $l = 0.1$ (c) $l = 1$

Figure 3.2: Bias evolution of a 1-dimensional toy-example for different choices of the length-scale hyper-parameter l and process variance σ^2.

$$\mu = \begin{pmatrix} \mu_1 \\ \mu_2 \end{pmatrix} \quad \text{with sizes} \quad \begin{pmatrix} \hat{N} \times 1 \\ N \times 1 \end{pmatrix} \quad \text{and}$$
$$\Sigma = \begin{pmatrix} \Sigma_{11} & \Sigma_{12} \\ \Sigma_{21} & \Sigma_{22} \end{pmatrix} \quad \text{with sizes} \quad \begin{pmatrix} \hat{N} \times \hat{N} & \hat{N} \times N \\ N \times \hat{N} & N \times N \end{pmatrix},$$

that $Y_1 \mid Y_2 \sim \mathcal{N}(\bar{\mu}, \bar{\Sigma})$ [Gra20] where $\bar{\mu} = \mu_1 + \Sigma_{12}\Sigma_{22}^{-1}(Y_2 - \mu_2)$ and $\bar{\Sigma} = \Sigma_{11} - \Sigma_{12}\Sigma_{22}^{-1}\Sigma_{21}$. Thus, the GP prediction of the bias at new locations $\hat{\mathcal{X}}_{\hat{N}} = \left((\hat{t}_1, \hat{x}_1), \dots, (\hat{t}_{\hat{N}}, \hat{x}_{\hat{N}})\right)$, given the observations $\mathbf{b}_N$, is just a particular case of those conditional MVN equations by taking

$$Y_1 = \mathbf{b}(\hat{\mathcal{X}}_{\hat{N}}),\ Y_2 = \mathbf{b}_N,\ \mu = \mathbf{0}_{\hat{N}+N},\ \Sigma_{11} = k(\hat{\mathcal{X}}_{\hat{N}}, \hat{\mathcal{X}}_{\hat{N}}),\ \Sigma_{21} = \Sigma_{12}^\top = \mathbf{k}_N(\hat{\mathcal{X}}_{\hat{N}}),\ \Sigma_{22} = \mathbf{K}_N,$$

where $\mathbf{k}_N(\hat{\mathcal{X}}_{\hat{N}}) := \sigma^2 \mathbf{c}_N(\hat{\mathcal{X}}_{\hat{N}}) := \sigma^2 \left(c\left((t_i, x_i), (\hat{t}_j, \hat{x}_j)\right) \right)_{1 \le i \le N, 1 \le j \le \hat{N}} \in \mathbb{R}^{N \times \hat{N}}$ and $k(\cdot, \cdot) = \sigma^2 c(\cdot, \cdot)$.

To this end, the conditional process $\mathbf{b}(\cdot) \mid \mathbf{b}_N$ is still a GP and the predictive, so called kriging equations are given by

$$\mathbf{b}(\hat{\mathcal{X}}_{\hat{\mathbf{N}}}) \mid \mathbf{b}_N \sim \mathcal{N}\left(m_N(\hat{\mathcal{X}}_{\hat{N}}), s_N^2(\hat{\mathcal{X}}_{\hat{N}}, \hat{\mathcal{X}}_{\hat{N}})\right) \quad \text{with} \tag{3.2.2a}$$
$$m_N(\hat{\mathcal{X}}_{\hat{N}}) := \mathbb{E}[\mathbf{b}(\hat{\mathcal{X}}_{\hat{\mathbf{N}}}) | \mathbf{b}_N] = \mathbf{k}_N(\hat{\mathcal{X}}_{\hat{N}})^\top \mathbf{K}_N^{-1} \mathbf{b}_N, \tag{3.2.2b}$$
$$s_N^2(\hat{\mathcal{X}}_{\hat{N}}, \hat{\mathcal{X}}_{\hat{N}}) := \mathbb{C}ov[\mathbf{b}(\hat{\mathcal{X}}_{\hat{\mathbf{N}}}), \mathbf{b}(\hat{\mathcal{X}}_{\hat{\mathbf{N}}}) | \mathbf{b}_N] = k(\hat{\mathcal{X}}_{\hat{N}}, \hat{\mathcal{X}}_{\hat{N}}) - \mathbf{k}_N(\hat{\mathcal{X}}_{\hat{N}})^\top \mathbf{K}_N^{-1} \mathbf{k}_N(\hat{\mathcal{X}}_{\hat{N}}), \tag{3.2.2c}$$

where the predictive variance are the diagonal elements of $s_N^2(\hat{\mathcal{X}}_{\hat{N}}, \hat{\mathcal{X}}_{\hat{N}})$. Formulas (3.2.2) describe the best linear unbiased predictor (BLUP) [Gra20].

Going back to the 1-dimensional toy-example, we want to illustrate the predictive formulas. For this, we construct bias values by a realization of a GP with fixed $\sigma = 1$, $l = 0.2$ on a fine grid $\mathcal{X}$. This function serves as the underlying ground truth and is assumed to be unknown. Then, we select randomly a small number of bias observations $\mathbf{b}_N$ from the ground truth values on the grid $\mathcal{X}_N \subset \mathcal{X}$ with $N = 7$. In Figure 3.3, we depict the predictive mean and 95% predictive intervals together with some draws of the corresponding conditional multivariate

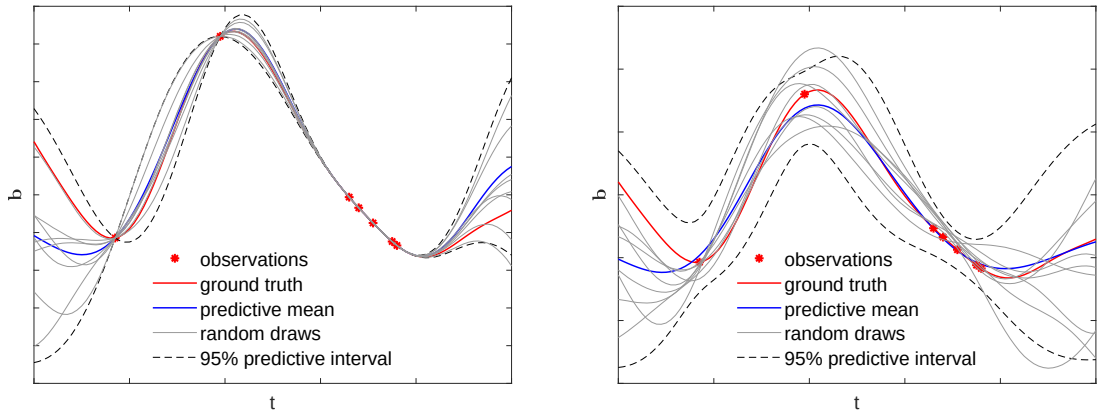

(a) $g = 0$ (b) $g = 0.01$

Figure 3.3: Illustration of bias observations and its predictions for a 1-dimensional toy example with $\sigma = 1$ and $l = 0.2$.

distribution. Moreover, we differentiate between the two cases, namely $g = 0$ and $g > 0$, in order to emphasize the impact of the noise parameter g. In both cases, we observe a wider range for the predictive intervals if we are further away from the observed points due to the increased uncertainty, whereas the predictions are more precise the closer we are to an observation. In the case $g = 0$, the predictive mean and the random draws additionally interpolate the observation points which does not apply for Figure 3.3b since there is a positive noise. The choice $g > 0$ has also a striking effect on the range of the predictive intervals which are visibly larger than the ones in Figure 3.3a.
As typically done in the context of GPs in order to estimate the hyper-parameters of the kernel function, we maximize the likelihood, the probability density of the observations given the parameters: $\mathbb{P}[\mathbf{b}(\mathcal{X}_N) = \mathbf{b}_N]$. As $\mathbf{b}_N \sim \mathcal{N}(0_N, \mathbf{K}_N)$, the likelihood $\mathcal{L}$ is given by the MVN density, i.e.

$$\mathcal{L}(\sigma^2, l_1, l_2, g, \mathbf{b}_N) = \frac{1}{\sqrt{(2\pi)^N |\sigma^2(\mathbf{C}_N + g\mathbf{I}_N)|}} \exp\left(-\frac{1}{2}\mathbf{b}_N^\top \left(\sigma^2(\mathbf{C}_N + g\mathbf{I}_N)\right)^{-1} \mathbf{b}_N\right),$$

where $|\cdot|$ stands for the determinant. Taking the logarithm, this gives

$$\log \mathcal{L}(l_1, l_2, \sigma^2, g, \mathbf{b}_N) = -\frac{N}{2}\log 2\pi - \frac{N}{2}\log \sigma^2 - \frac{1}{2}\log|\mathbf{C}_N + g\mathbf{I}_N| - \frac{1}{2\sigma^2}\mathbf{b}_N^\top(\mathbf{C}_N + g\mathbf{I}_N)^{-1}\mathbf{b}_N. \tag{3.2.3}$$

We can compute the optimal variance $\hat{\sigma}^2$ by differentiating the resulting expression so that

$$\frac{\partial \log \mathcal{L}}{\partial \sigma^2} = -\frac{N}{2\sigma^2} + \frac{1}{2(\sigma^2)^2}\mathbf{b}_N^\top(\mathbf{C}_N + g\mathbf{I}_N)^{-1}\mathbf{b}_N = 0,$$

which gives

$$\hat{\sigma}^2(l_1, l_2, g, \mathbf{b}_N) = \frac{\mathbf{b}_N^\top(\mathbf{C}_N + g\mathbf{I}_N)^{-1}\mathbf{b}_N}{n}. \tag{3.2.4}$$

Plugging $\hat{\sigma}^2$ in (3.2.3), we obtain the concentrated log-likelihood, denoted by $\log \tilde{\mathcal{L}}$:

$$\log \tilde{\mathcal{L}}(l_1, l_2, g, \mathbf{b}_N) = -\frac{N}{2}\log 2\pi - \frac{N}{2}\log \hat{\sigma}^2(l_1, l_2, g, \mathbf{b}_N) - \frac{1}{2}\log|\mathbf{C}_N + g\mathbf{I}_N| - \frac{N}{2}, \quad (3.2.5)$$

where the correlation matrix $\mathbf{C}_N$ also depends on the hyper-parameters l_1, l_2. We note that, in contrast to the process variance $\hat{\sigma}^2$, it is generally not possible to compute the remaining hyper-parameters l_1, l_2 and g explicitly, therefore numerical optimization methods, such as the local MATLAB optimization solver `fmincon`, are mandatory to complete the estimation of the hyper-parameters.

3.2.1 Reduction of computational costs using Kronecker structure

In this section, we describe some possibilities to speed up the computation time in the programming code. If the data are given in a grid structure, i.e. regular measurements at the same loop locations, the computational cost of fitting GPs can be reduced by exploiting the resulting Kronecker structure, see e.g. [CML+17]. Thus, the separable structure of the correlation matrix, i.e. $c\big((t,x),(t',x')\big) = c(t,t')\cdot c(x,x')$, allows us to compute the correlation matrix $\mathbf{C}_N$ by $\mathbf{C}_N = \mathbf{C}_{n_x} \otimes \mathbf{C}_{n_t}$, where $\otimes$ indicates the Kronecker product between $\mathbf{C}_{n_x} = \big(c(x_i, x_j)\big)_{1\le i,j\le n_x}$ and $\mathbf{C}_{n_t} = \big(c(t_i, t_j)\big)_{1\le i,j\le n_t}$. Here, n_x (resp. n_t) denotes the number of loop detectors (resp. time measurement points) satisfying $N = n_x \cdot n_t$. By the properties of Kronecker it holds that

$$\mathbf{C}_N^{-1} = \mathbf{C}_{n_x}^{-1} \otimes \mathbf{C}_{n_t}^{-1} \text{ and } |\mathbf{C}_N| = |\mathbf{C}_{n_x}|^{n_x} \cdot |\mathbf{C}_{n_t}|^{n_t}.$$

Speedups can be significant since these $\mathcal{O}(N^3) = \mathcal{O}\left((n_x \cdot n_t)^3\right)$ operations [Gra20] become $\mathcal{O}(n_x^3 + n_t^3)$. Moreover, due to the positive definiteness and symmetry of the matrices $\mathbf{C}_{n_x}$ and $\mathbf{C}_{n_t}$, they can be decomposed into $\mathbf{U}_{n_x}\mathbf{D}_{n_x}\mathbf{U}_{n_x}^\top$ and $\mathbf{U}_{n_t}\mathbf{D}_{n_t}\mathbf{U}_{n_t}^\top$ respectively. The columns of the orthogonal matrix $\mathbf{U}_k$, i.e. $\mathbf{U}_k^\top\mathbf{U}_k = \mathbf{I}_k$, $k \in \{n_t, n_x\}$, are composed of the eigenvectors of $\mathbf{C}_k$, whereas $\mathbf{D}_k$ is a diagonal matrix with the eigenvalues of $\mathbf{C}_k$ on its diagonal. By applying again the Kronecker properties, we obtain

$$\mathbf{C}_n = \mathbf{C}_{n_x} \otimes \mathbf{C}_{n_t} = (\mathbf{U}_{n_x}\mathbf{D}_{n_x}\mathbf{U}_{n_x}^\top) \otimes (\mathbf{U}_{n_t}\mathbf{D}_{n_t}\mathbf{U}_{n_t}^\top) = (\mathbf{U}_{n_x} \otimes \mathbf{U}_{n_t})(\mathbf{D}_{n_x} \otimes \mathbf{D}_{n_t})(\mathbf{U}_{n_x} \otimes \mathbf{U}_{n_t})^\top,$$

which yields to

$$\mathbf{C}_n + g\mathbf{I}_N = (\mathbf{U}_{n_x} \otimes \mathbf{U}_{n_t})\left((\mathbf{D}_{n_x} \otimes \mathbf{D}_{n_t}) + g\mathbf{I}_N\right)(\mathbf{U}_{n_x} \otimes \mathbf{U}_{n_t})^\top.$$

The inverse and determinant of the matrix $\mathbf{C}_N + g\mathbf{I}_N$ are then respectively given by

$$\begin{aligned}(\mathbf{C}_n + g\mathbf{I}_N)^{-1} &= \left((\mathbf{U}_{n_x} \otimes \mathbf{U}_{n_t})^\top\right)^{-1}\left((\mathbf{D}_{n_x} \otimes \mathbf{D}_{n_t}) + g\mathbf{I}_N\right)^{-1}(\mathbf{U}_{n_x} \otimes \mathbf{U}_{n_t})^{-1} \\ &= (\mathbf{U}_{n_x} \otimes \mathbf{U}_{n_t})\left((\mathbf{D}_{n_x} \otimes \mathbf{D}_{n_t}) + g\mathbf{I}_N\right)^{-1}(\mathbf{U}_{n_x} \otimes \mathbf{U}_{n_t})^\top,\end{aligned} \quad (3.2.6)$$

$$\begin{aligned}\left|\mathbf{C}_n + g\mathbf{I}_N\right| &= \left|(\mathbf{U}_{n_x} \otimes \mathbf{U}_{n_t})\left((\mathbf{D}_{n_x} \otimes \mathbf{D}_{n_t}) + g\mathbf{I}_N\right)(\mathbf{U}_{n_x} \otimes \mathbf{U}_{n_t})^\top\right| \\ &= \left|\mathbf{U}_{n_x} \otimes \mathbf{U}_{n_t}\right|\left|(\mathbf{D}_{n_x} \otimes \mathbf{D}_{n_t}) + g\mathbf{I}_N\right|\left|(\mathbf{U}_{n_x} \otimes \mathbf{U}_{n_t}^\top)\right| \\ &= \left|\mathbf{U}_{n_x}\right|^{n_t}\left|\mathbf{U}_{n_t}\right|^{n_x}\left|(\mathbf{D}_{n_x} \otimes \mathbf{D}_{n_t}) + g\mathbf{I}_N\right|\left|\mathbf{U}_{n_x}\right|^{n_t}\left|\mathbf{U}_{n_t}\right|^{n_x} \\ &= \left|(\mathbf{D}_{n_x} \otimes \mathbf{D}_{n_t}) + g\mathbf{I}_N\right|.\end{aligned} \quad (3.2.7)$$

Both equations are used in the concentrated likelihood formula (3.2.5) and the inverse (3.2.6) additionally in the kriging equations (3.2.2).
In a next step, we state a formula to compute more efficiently the matrix-vector product between $(\mathbf{C}_n+g\mathbf{I}_N)^{-1}$ and $\mathbf{b}_N$ which appears in the process variance (3.2.4) and the predictive mean (3.2.2b), by applying the identity [CML+17]

$$(\mathbf{A}\otimes\mathbf{B})x = \mathrm{vec}(\mathbf{B}\,\mathrm{vec}^{-1}(x)\,\mathbf{A}^\top).$$

The operator $\mathrm{vec}(\cdot)$ stacks the columns of a $m_1\times m_2$ matrix into a m_1m_2-dimensional vector and $\mathrm{vec}(\cdot)^{-1}$ reshapes it back into a matrix of dimension $m_1\times m_2$. Thus, we use this trick three times in the expression $(\mathbf{C}_n+g\mathbf{I}_N)^{-1}\mathbf{b}_N$ since it holds by (3.2.6) that $(\mathbf{C}_n+g\mathbf{I}_N)^{-1}\mathbf{b}_N = M_1\left(M_2\left(M_1^\top\,\mathbf{b}_N\right)\right)$, where $M_1=\mathbf{U}_{n_x}\otimes\mathbf{U}_{n_t}$ and $M_2=\left((\mathbf{D}_{n_x}\otimes\mathbf{D}_{n_t})+g\mathbf{I}_N\right)^{-1}$.
Finally, to calculate the diagonal elements of the predictive covariance (3.2.2c), the diagonal entries of

$$\mathbf{k}_N(\hat{\mathcal{X}}_{\hat{N}})^\top\mathbf{K}_N^{-1}\mathbf{k}_N(\hat{\mathcal{X}}_{\hat{N}}) = \frac{1}{\sigma^2}\left(\mathbf{k}_N(\hat{\mathcal{X}}_{\hat{N}})^\top(\mathbf{U}_{n_x}\otimes\mathbf{U}_{n_t})M_3\right)\left(\mathbf{k}_N(\hat{\mathcal{X}}_{\hat{N}})^\top(\mathbf{U}_{n_x}\otimes\mathbf{U}_{n_t})M_3\right)^\top$$

are obtained by summing up the squared row entries of $\mathbf{k}_N(\hat{\mathcal{X}}_{\hat{N}})^\top(\mathbf{U}_{n_x}\otimes\mathbf{U}_{n_t})M_3$, where the matrix M_3 is given by the square root of the elements of the diagonal matrix $\left((\mathbf{D}_{n_x}\otimes\mathbf{D}_{n_t})+g\mathbf{I}_N\right)^{-1}$. Whereas the diagonal of $k(\hat{\mathcal{X}}_{\hat{N}},\hat{\mathcal{X}}_{\hat{N}})$ is simply given by $\sigma^2\mathbf{1}_{\hat{N}}\in\mathbb{R}^{\hat{N}\times 1}$.

3.2.2 Supporting average observations in the correlation

If the traffic data are recorded by magnetic loop detectors, they are usually aggregated over time, for example the number of vehicles which passed a detector in a certain time interval. In order to take into account in the GP modeling that these are actually average measurements, we extend the proposed Gaussian correlation matrix (3.2.1) by averaging over the observations. Due to the properties of GPs, the integral and also derivative process are still GPs and the resulting processes are jointly Gaussian with the original one [Osb10, WB16]. In formulas, we obtain for the Gaussian kernel

$$\begin{aligned}
&\mathbb{C}orr\left(\frac{1}{\Delta t}\int_t^{t+\Delta t} b(s,x)\mathrm{d}s,\ \frac{1}{\Delta t'}\int_{t'}^{t'+\Delta t'} b(s',x)\mathrm{d}s'\right)\\
&\quad=\left(\frac{1}{\Delta t'}\frac{1}{\Delta t}\int_{t'}^{t'+\Delta t'}\int_{t}^{t+\Delta t}\exp\left(-\frac{(s-s')^2}{l_1^2}\right)\mathrm{d}s\,\mathrm{d}s'\right)\cdot\exp\left(-\frac{(x-x')^2}{l_2^2}\right)\\
&\quad=\frac{1}{\Delta t'}\frac{1}{\Delta t}\frac{\sqrt{\pi}}{2}l_1^2\Bigg(\left(\frac{t'-t+\Delta t}{l_1}\right)\mathrm{erf}\left(\frac{t'-t+\Delta t}{l_1}\right)+\frac{1}{\sqrt{\pi}}\exp\left(-\frac{(t'-t+\Delta t)^2}{l_1^2}\right)\\
&\qquad+\left(\frac{t'-t-\Delta t'}{l_1}\right)\mathrm{erf}\left(\frac{t'-t-\Delta t'}{l_1}\right)+\frac{1}{\sqrt{\pi}}\exp\left(-\frac{(t'-t-\Delta t')^2}{l_1^2}\right)\\
&\qquad-\left(\frac{t'-t+\Delta t-\Delta t'}{l_1}\right)\mathrm{erf}\left(\frac{t'-t+\Delta t-\Delta t'}{l_1}\right)-\frac{1}{\sqrt{\pi}}\exp\left(-\frac{(t'-t+\Delta t-\Delta t')^2}{l_1^2}\right)
\end{aligned}$$

$$-\left(\frac{t'-t}{l_1}\right)\operatorname{erf}\left(\frac{t'-t}{l_1}\right)-\frac{1}{\sqrt{\pi}}\exp\left(-\frac{(t'-t)^2}{l_1^2}\right)\Bigg)\cdot\exp\left(-\frac{(x-x')^2}{l_2^2}\right), \tag{3.2.8}$$

and

$$\begin{aligned}
&\mathbb{C}orr\left(\frac{1}{\Delta t}\int_t^{t+\Delta t} b(s,x)\,\mathrm{ds},\ b(t',x')\right)\\
&\quad=\left(\frac{1}{\Delta t}\int_t^{t+\Delta t}\exp\left(-\frac{(s-t')^2}{l_1^2}\right)\mathrm{ds}\right)\cdot\exp\left(-\frac{(x-x')^2}{l_2^2}\right)\\
&\quad=\frac{1}{\Delta t}\frac{\sqrt{\pi}}{2}l_1\left(\operatorname{erf}\left(\frac{t-t'+\Delta t}{l_1}\right)-\operatorname{erf}\left(\frac{t-t'}{l_1}\right)\right)\cdot\exp\left(-\frac{(x-x')^2}{l_2^2}\right),
\end{aligned} \tag{3.2.9}$$

where equation (3.2.8) is used to calculate $\mathbf{K}_N$ and (3.2.9) to compute $\mathbf{k}_N(\hat{\mathcal{X}}_{\hat{N}})$ in the kriging equations (3.2.2). The function $\operatorname{erf}(\cdot)$ refers to the error function [Wei94] which is defined as $\operatorname{erf}(t)=\frac{2}{\sqrt{\pi}}\int_0^t\exp(-s^2)\,\mathrm{ds}$.
Next, we also state the formulas for the correlations between an average observation and an observation of the derivative at t' or x' which reads as

$$\begin{aligned}
&\mathbb{C}orr\left(\frac{1}{\Delta t}\int_t^{t+\Delta t} b(s,x)\,\mathrm{ds},\ \frac{\mathrm{d}}{\mathrm{dt}'}\,b(t',x')\right)\\
&\quad=\left(\frac{1}{\Delta t}\int_t^{t+\Delta t}\frac{\mathrm{d}}{\mathrm{dt}'}\exp\left(-\frac{(s-t')^2}{l_1^2}\right)\mathrm{ds}\right)\cdot\exp\left(-\frac{(x-x')^2}{l_2^2}\right)\\
&\quad=\frac{1}{\Delta t}\left(\exp\left(-\frac{(t-t')^2}{l_1^2}\right)-\exp\left(-\frac{(t-t'+\Delta t)^2}{l_1^2}\right)\right)\cdot\exp\left(-\frac{(x-x')^2}{l_2^2}\right),
\end{aligned} \tag{3.2.10}$$

and

$$\begin{aligned}
&\mathbb{C}orr\left(\frac{1}{\Delta t}\int_t^{t+\Delta t} b(s,x)\,\mathrm{ds},\ \frac{\mathrm{d}}{\mathrm{dx}'}\,b(t',x')\right)\\
&\quad=\left(\frac{1}{\Delta t}\int_t^{t+\Delta t}\exp\left(-\frac{(s-t')^2}{l_1^2}\right)\mathrm{ds}\right)\cdot\frac{\mathrm{d}}{\mathrm{dx}'}\exp\left(-\frac{(x-x')^2}{l_2^2}\right)\\
&\quad=\frac{1}{\Delta t}\frac{\sqrt{\pi}}{2}l_1\left(\operatorname{erf}\left(\frac{t-t'+\Delta t}{l_1}\right)-\operatorname{erf}\left(\frac{t-t'}{l_1}\right)\right)\cdot\frac{2(x-x')}{l_2^2}\exp\left(-\frac{(x-x')^2}{l_2^2}\right).
\end{aligned} \tag{3.2.11}$$

These correlation matrices will be used later in Chapter 4.

3.2.3 Modeling change in the traffic regime

The traffic community typically differentiates between a free flow and a congested regime. Looking at the fundamental diagram, the free flow regime is defined for the part whenever $\rho \leq \rho_{cr}(w)$, i.e. $v \geq \mathcal{V}(\rho_{cr}(w), w) = v_{cr}(w)$, and the congested situation whenever $\rho > \rho_{cr}(w)$, i.e. $v < v_{cr}(w)$. Such a regime change can easily happen in a traffic scenario, even if the considered time range is short, for example due to bottlenecks. Osborne [Osb10] proposes several options in order to take this change into account in the covariance modeling.
We focus on the following approaches:

1. Adding a second noise hyper-parameter (see Figure 3.5b).
   This turns the covariance matrix into

   $$\mathbf{K}_N = \sigma^2 \left(\mathbf{C}_N + \mathrm{diag}_N(\mathbf{g}) \right),$$

   where the i-th element, $i \in \{1, \ldots, N\}$, of the vector $\mathbf{g}$ is computed by

   $$g(i) = \begin{cases} g^F & \text{if } v(t_i, x_i) \geq v_{cr}\left(w(t_i, x_i)\right), \\ g^C & \text{otherwise.} \end{cases}$$

   The operator $\mathrm{diag}_N(\cdot)$ transforms a N-dimensional vector into a $N \times N$ diagonal matrix. Here, g^F (resp. g^C) denotes the free flow (resp. congestion) noise parameter. Moreover, we point out that the computation of the matrices $\mathbf{k}_N(\hat{\mathcal{X}}_{\hat{N}})$ and $k(\hat{\mathcal{X}}_{\hat{N}}, \hat{\mathcal{X}}_{\hat{N}})$ in the predictive Equations (3.2.2) do not differ from the classical approach due to the fact that the noise parameter g only affects the calculation of the symmetric matrix $\mathbf{K}_N$.

2. Adding a second process variance (see Figure 3.5c).
   Instead of considering two noise parameters and one process variance, as above, we now look at the opposite case which is motivated by [Osb10, Section 4.4.4]. In this case, the two traffic regimes are described by different variances, but they are modeled by the same GP. The covariance is then defined by

   $$\begin{aligned} \mathbf{K}_N = &\sigma_F^2 \left(\mathbf{C}_N \odot \mathbf{Z}_N^F \right) + \sigma_C^2 \left(\mathbf{C}_N \odot \mathbf{Z}_N^C \right) + \sqrt{\sigma_F^2 \sigma_C^2} \left(\mathbf{C}_N \odot \left(\mathbf{1}_{N \times N} - (\mathbf{Z}_N^F + \mathbf{Z}_N^C) \right) \right) + \\ &\sigma_\varepsilon^2 \mathbf{I}_N, \end{aligned}$$

   where $\mathbf{1}_{N \times N}$ denotes the $N \times N$ matrix containing only ones and $\odot$ represents the point-wise matrix product. The matrix entries of the $N \times N$-dimensional matrices $\mathbf{Z}_N^F$ and $\mathbf{Z}_N^C$ are respectively computed by

   $$Z^F\left((t,x),(t',x')\right) = \begin{cases} 1 & \text{if } v(t,x) \geq v_{cr}\left(w(t,x)\right) \text{ and } v(t',x') \geq v_{cr}\left(w(t',x')\right), \\ 0 & \text{otherwise,} \end{cases}$$

   and

   $$Z^C\left((t,x),(t',x')\right) = \begin{cases} 1 & \text{if } v(t,x) < v_{cr}\left(w(t,x)\right) \text{ and } v(t',x') < v_{cr}\left(w(t',x')\right), \\ 0 & \text{otherwise.} \end{cases}$$

Here, σ_F^2 (resp. σ_C^2) describes the variance in the free flow (resp. congested) regime. Regarding the predictive Equations (3.2.2), we define

$$\mathbf{k}_N(\hat{\mathcal{X}}_{\hat{N}}) = \sigma_F^2 \left(\mathbf{c}_N(\hat{\mathcal{X}}_{\hat{N}}) \odot \mathbf{Z}_N^F(\hat{\mathcal{X}}_{\hat{N}})\right) + \sigma_C^2 \left(\mathbf{c}_N(\hat{\mathcal{X}}_{\hat{N}}) \odot \mathbf{Z}_N^C(\hat{\mathcal{X}}_{\hat{N}})\right) + \sqrt{\sigma_F^2\sigma_C^2}\left(\mathbf{c}_N(\hat{\mathcal{X}}_{\hat{N}}) \odot \left(\mathbf{1}_{N\times\hat{N}} - \left(\mathbf{Z}_N^F(\hat{\mathcal{X}}_{\hat{N}}) + \mathbf{Z}_N^C(\hat{\mathcal{X}}_{\hat{N}})\right)\right)\right) \quad \text{and}$$

$$k(\hat{\mathcal{X}}_{\hat{N}}, \hat{\mathcal{X}}_{\hat{N}}) = \sigma_F^2 \left(c(\hat{\mathcal{X}}_{\hat{N}}, \hat{\mathcal{X}}_{\hat{N}}) \odot Z^F(\hat{\mathcal{X}}_{\hat{N}}, \hat{\mathcal{X}}_{\hat{N}})\right) + \sigma_C^2 \left(c(\hat{\mathcal{X}}_{\hat{N}}, \hat{\mathcal{X}}_{\hat{N}}) \odot Z^C(\hat{\mathcal{X}}_{\hat{N}}, \hat{\mathcal{X}}_{\hat{N}})\right) + \sqrt{\sigma_F^2\sigma_C^2}\left(c(\hat{\mathcal{X}}_{\hat{N}}, \hat{\mathcal{X}}_{\hat{N}}) \odot \left(\mathbf{1}_{\hat{N}\times\hat{N}} - \left(Z^F(\hat{\mathcal{X}}_{\hat{N}}, \hat{\mathcal{X}}_{\hat{N}}) + Z^C(\hat{\mathcal{X}}_{\hat{N}}, \hat{\mathcal{X}}_{\hat{N}})\right)\right)\right),$$

where $\mathbf{Z}_N^k(\hat{\mathcal{X}}_{\hat{N}}) := \left(Z^k\left((t_i, x_i), (\hat{t}_j, \hat{x}_j)\right)\right)_{1\le i\le N, 1\le j\le \hat{N}} \in \mathbb{R}^{N\times\hat{N}}$ and $k \in \{F, C\}$.
However, the speed values $v(\hat{\mathcal{X}}_{\hat{N}})$, which are needed to construct $\mathbf{Z}_N^k(\hat{\mathcal{X}}_{\hat{N}})$ and $\mathbf{Z}^k(\hat{\mathcal{X}}_{\hat{N}}, \hat{\mathcal{X}}_{\hat{N}})$, are usually not measured. Thus, they need to be predicted which is done by modeling the observed measurements $v(\mathcal{X}_N)$ by a GP, i.e.

$$v(\mathcal{X}_N) \sim \mathcal{N}(\bar{\mathbf{v}}_N, \mathbf{K}_N^v),$$

where the mean $\bar{\mathbf{v}}_N$ is calculated by taking the average of the observed data. The hyper-parameters of the covariance $\mathbf{K}_N^v$ are obtained by maximizing the concentrated likelihood function (3.2.5), where $\mathbf{b}_N$ is replaced by $v(\mathcal{X}_N)$. Consequently, the predictions $v(\hat{\mathcal{X}}_{\hat{N}})$ follow also a GP and the values are computed by exploiting the predictive mean formula, more precisely

$$v(\hat{\mathcal{X}}_{\hat{N}}) := \bar{\mathbf{v}}_{\hat{N}} + \mathbf{k}_N^v(\hat{\mathcal{X}}_{\hat{N}})^\top (\mathbf{K}_N^v)^{-1}\left(v(\mathcal{X}_N) - \bar{\mathbf{v}}_N\right),$$

where the constant entries of the $\hat{N}$-dimensional vector $\bar{\mathbf{v}}_{\hat{N}}$ coincide with the ones in $\bar{\mathbf{v}}_N$.

3. Adding a second set of hyper-parameters (see Figure 3.5d).
In this approach, based on [Osb10, Section 4.4.1], we consider two distinct sets of hyper-parameters for the two traffic regimes. Unlike the previous approach, we apply this modeling if the two regimes are assumed to be independent and modeled by different GPs. This results in the following covariance matrix:

$$\mathbf{K}_N = \sigma_F^2 \left(\mathbf{C}_N(l_1^F, l_2^F) \odot \mathbf{Z}_N^F\right) + \sigma_C^2 \left(\mathbf{C}_N(l_1^C, l_2^C) \odot \mathbf{Z}_N^C\right) + \sigma_\varepsilon^2 \mathbf{I}_N,$$

where l_1^F, l_2^F (resp. l_1^C, l_2^C) refers to the length-scale parameters in the free flow (resp. congested) regime. Note that, compared to the second approach, we do not assume any correlation between two observations belonging to different regimes. Moreover, the predictive equations are computed analogously as before, namely modeling the observed speed measurements by a GP.

We point out that, except for the first approach, we cannot make use of the Kronecker trick (see Section 3.2.1) to reduce the computation time. This is due to the point-wise matrix products. Moreover, all the proposed methods lead to heteroskedastic GPs, which are typically applied if the underlying scenarios are not stationary [BG21].

Remark 23. The optimal critical speed values v_{cr} depend both on the calibration parameter θ and w. In order to prevent numerical issues in the optimization, we will consider in the following work only one threshold value which is computed by the fundamental diagram where $v_{cr} = v_{cr}(V^*)$ (see Figure 3.4).

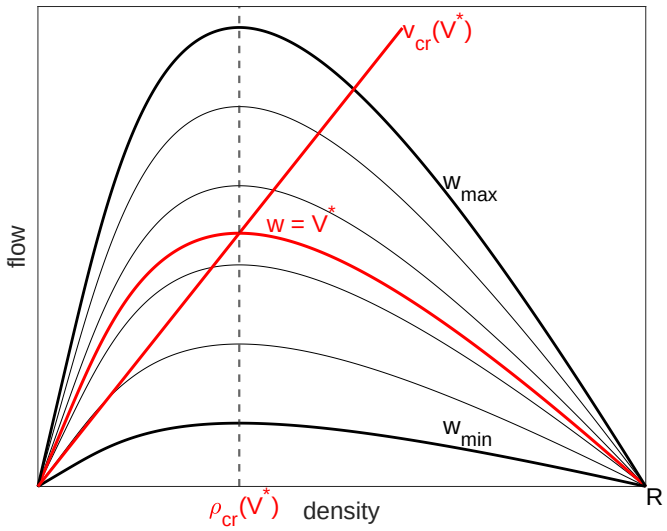

Figure 3.4: Illustration of the flow curve corresponding to $w = V^*$ together with its critical speed value $v_{cr}(V^*)$ and $\theta^* = (80, 30, 300)$.

In Figure 3.5, we compare the performances between the three above presented approaches and the classical one, which considers only the original set of hyper-parameters l_1, l_2 and g. In the illustration, field data are drawn in red and simulated data in gray. After adding the kriging mean to the simulated data, we obtain the so called *corrected data* which are depicted in blue color. We observe that the bias correction in the classical approach does not work well due to a drastic change in the traffic regime. Also, the version with a second g parameter leads almost to the same correction. Next, looking at the approaches proposed by [Osb10], we clearly see that the jump in the data can be captured by the bias, resulting in a clear improvement compared to Figures 3.5a and 3.5b.
However, we need to admit that this 1-dimensional example is a simplification of a realistic road scenario since the space position is fixed. Experimental tests show that adding the location of several loop detectors in the GP modeling, decreases the performance of all approaches but especially the ones illustrated in Figures 3.5c and 3.5d. Further research is needed to accommodate more dimensions, see e.g. [HWN+16]. Thus, our final results presented in Chapter 6, are based on the classical approach since it is computationally much less expensive and the difference in the performances negligible.

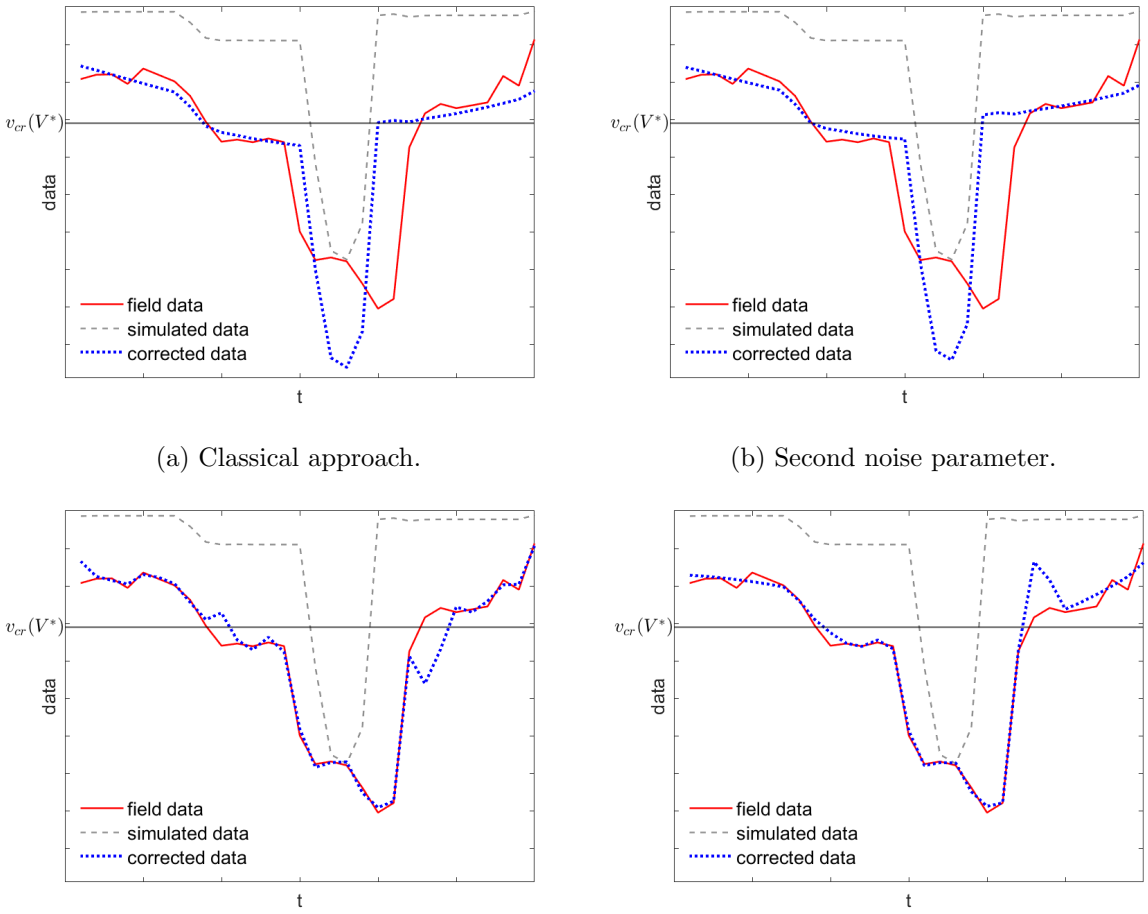

(a) Classical approach.

(b) Second noise parameter.

(c) Second process variance.

(d) Second set of hyper-parameters.

Figure 3.5: Comparison of covariance modeling approaches. The classical approach consists of the three hyper-parameters l_1, l_2 and g. The critical speed $v_{cr}(V^*)$ is drawn by the horizontal black line.

3.3 Fundamental fit approach for calibration

Classically, macroscopic traffic flow models are calibrated by the intuitive approach of fitting data to the fundamental diagram (see e.g. [DGK$^+$09, Fan13, FHS14, FSP$^+$17]). More precisely, given the flow, speed and density observations, denoted by $y_k^F(t_i, x_i)$, $i \in \{1, \dots, N\}$, $k \in \{q, v, \rho\}$ respectively, a least squares method is performed to fit the parameter function to historical measured data. Thus, the calibration parameter θ is obtained by either solving the optimization problem

$$\min_{\theta} \left\{ \sum_{i=1}^{N} \left| y_q^F(t_i, x_i) - Q\left(y_\rho^F(t_i, x_i), w = constant \right) \right|^2 \right\},$$

if we consider the flow as the quantity of interest or by solving

$$\min_{\theta} \Big\{ \sum_{i=1}^{N} \Big| y_v^F(t_i, x_i) - \mathcal{V}\Big(y_\rho^F(t_i, x_i), w = constant\Big)\Big|^2 \Big\},$$

if the speed is the quantity of interest. We point out that in the fundamental fit approach, the fundamental diagram is naturally fit on the key traffic quantities. This is due to the fact that the rather abstract quantity w cannot be measured by the detectors and can be only derived by inserting the density and speed data in the inverted velocity function (see end of Remark 18). Thus, we fix $w = constant$ for fitting the data to the fundamental diagram which leads back to the first order model with only one curve. Typically, w is chosen as the maximum speed resulting in $w = V$.

Next, instead of minimizing over the sum of squares of each measured observation, the data can be grouped first into several bins, which reduces the number of data points to be fitted. Of course, this is only possible if enough (historical) data are available. Then, the minimization is executed using only average values of these bins. This extended approach is especially useful when the amount of historical data is large, because the grouping of the data points reduces the computational cost. The calibration algorithm for the flow quantity of interest is summarized in the following steps [DGK$^+$09]:

1. Order the flow, speed and density observations with respect to increasing density values.
2. Divide the data into bins, each containing x_b data points.
3. For each bin $j \in \{1, \dots, \lceil \frac{N}{x_b} \rceil\}$,
   - compute the mean density $\bar{y}_\rho^{F,j}$ and
   - determine the maximal non-outlier flow $\bar{y}_q^{F,j}$, where the maximum is taken over all flow values within a bin which do not exceed $Q_3 + 1.5(Q3 - Q1)$ and where Q_3 (resp. Q_1) denotes the 75th (resp. 25th) percentile of the bin data points.
4. Solve the optimization problem

$$\min_{\theta} \Big\{ \sum_{j=1}^{\lceil \frac{N}{x_b} \rceil} \Big| \bar{y}_q^{F,j} - Q(\bar{y}_\rho^{F,j}, w = constant)\Big|^2 \Big\}.$$

We point out that this approach proposed by [DGK$^+$09] computes in the second part of step 3 upper flow values which leads to an "upper envelope" instead of a mean curve. However, motivated by experimental tests, if the quantity of interest is the speed, we compute the mean speed $\bar{y}_v^{F,j}$ instead of the maximum non-outlier speed.

Remark 24. In macroscopic traffic flow models, the key traffic quantities are the flow, speed and density. In contrast to flow data, densities cannot be directly measured by the loop detectors but are instead derived by using occupancies. Thus, they are usually not used as a quantity of interest and the optimization is often executed on the flow. However, as stated in the literature [WYG$^+$22], reconstructing the flow seems not as challenging as the speed.

Moreover, depending on the application, an adequate speed matching can be more favorable. This motivates us to consider the equations also for the speed as a quantity of interest, supported by the fact that the flow estimations show mostly a reasonable performance if the speed is reconstructed well.

3.4 Model-driven approaches for calibration

The fundamental fit approach is purely based on measured data and the fundamental diagram. However, in congested regions traffic data do not usually follow closely the shape of this function and are often widely spread (see for example Figure 5.11b). Moreover, data are not necessarily measured on the whole diagram and the number of observations are often imbalanced between the two traffic regimes. All of this complicates the parameter identification process by the fundamental fit approach. Thus, instead of calibrating on the fundamental diagram, one can additionally take the physics into account by integrating the numerical solution y^M in the optimization process. The approaches are detailed in the following sections.

3.4.1 $\mathbf{L^2}$ approach

We denote the first presented method the $\mathbf{L^2}$ approach, which is based on the assumption that the mathematical model can capture perfectly the real dynamics, meaning that

$$y^F(t_i, x_i) = y^M(t_i, x_i) + \varepsilon.$$

Then, the calibration parameters are obtained by minimizing a cost function $C(\theta)$ which is based on the most widely used error metric in parameter estimation [WYG+22], namely the root mean square error (RMSE) between the field and simulated data:

$$\theta^* = \underset{\theta}{\operatorname{argmin}}\, C(\theta) = \underset{\theta}{\operatorname{argmin}} \left\{ \sqrt{\frac{1}{N} \sum_{i=1}^{N} \left| y^F(t_i, x_i) - y^M(t_i, x_i, \theta) \right|^2} \right\}. \tag{3.4.1}$$

Remark 25. Since we do not deal with covariance computations in the $\mathbf{L^2}$ optimization, the critical speed determination is not integrated in the optimization process. Thus, if necessary, it can be computed after obtaining the optimal calibration parameter θ^* by simply inserting $w = V^*$ into $v_{cr}(w)$.

3.4.2 Kennedy O'Hagan approach

However, in reality, models are used to emulate the real system but they are not exact [Plu17]. Even if the true values of the calibration parameters are known, the mathematical model behaves imperfectly [TW15]. Therefore, we adjust the too strong assumption in the $\mathbf{L^2}$ method by applying the statistical framework proposed by [HKC+04, KO01] and refer to it as *KOH approach*. As introduced in Equation (3.1.1), the idea is to correct the simulation error by a discrepancy term. Since this bias depends on the unknown calibration parameter θ, i.e. $\mathbf{b}_N(\theta)$, the process variance $\hat{\sigma}^2$ and finally l_1, l_2 and g also depend on θ. Thus, the optimal calibration parameters are obtained by maximizing the concentrated log-likelihood function (3.2.5):

$$\max_{l_1, l_2, g, \theta} \log \tilde{\mathcal{L}}\left(l_1, l_2, g, \mathbf{b}_N(\theta)\right).$$

Following the principle of modularization [LBB09], we apply a 2-step optimization to isolate the GP fitting and thus preventing confounding effects in the calibration. In the so called *inner-level*, we maximize the concentrated log-likelihood function dependent on θ, thus obtaining the hyper-parameters $l_1(\theta), l_2(\theta), g(\theta)$. These hyper-parameters are then inserted into (3.2.5) and the concentrated likelihood is maximized with respect to θ, giving the optimized calibration parameter θ^*. We call the second step the *higher-level*. Finally, the corresponding bilevel optimization problem writes:

$$\max_{\theta} \left[\max_{l_1,l_2,g} \log \tilde{\mathcal{L}}(l_1, l_2, g, \mathbf{b}_N(\theta)) \right]. \tag{3.4.2}$$

Remark 26. In contrast to the $\mathbf{L^2}$ approach, the optimal calibration parameter θ^* obtained by the KOH approach is not necessarily the one which minimizes the bias. Instead, it is rather chosen jointly together with the bias in order to achieve the best correction of the simulated output [Gra20].

3.4.3 Plumlee approach

As shown in [TW16], the calibration results obtained by the KOH approach can lead to unrealistic parameters since the impact of the bias modeling may be too strong compared to the simulations. Thus, Plumlee proposes in [Plu17] to integrate an orthogonality condition between the bias function and the mathematical model which reduces the influence of the bias and puts more weight on the physical model. The optimization problem reads analogously as the one in (3.4.2) except that the computation of the correlation matrix changes. More precisely, we denote the correlation matrix in the Plumlee approach by $\mathbf{C}_N^{plum}$ reading as

$$\mathbf{C}_N^{plum} = \mathbf{C}_N - \mathbf{C}_N\, \delta y^M \left((\delta y^M)^\top \mathbf{C}_N\, \delta y^M \right)^{-1} (\delta y^M)^\top \mathbf{C}_N, \tag{3.4.3}$$

and the expression $\mathbf{c}_N(\hat{\mathcal{X}}_{\hat{N}})$ and $c(\hat{\mathcal{X}}_{\hat{N}}, \hat{\mathcal{X}}_{\hat{N}})$, appearing in the kriging equations, are computed respectively by

$$\mathbf{c}_N^{plum}(\hat{\mathcal{X}}_{\hat{N}}) = \mathbf{c}_N(\hat{\mathcal{X}}_{\hat{N}}) - \mathbf{C}_N\, \delta y^M \left((\delta y^M)^\top \mathbf{C}_N\, \delta y^M \right)^{-1} (\delta y^M)^\top \mathbf{c}_N(\hat{\mathcal{X}}_{\hat{N}}),$$

and

$$c^{plum}(\hat{\mathcal{X}}_{\hat{N}}, \hat{\mathcal{X}}_{\hat{N}}) = c(\hat{\mathcal{X}}_{\hat{N}}, \hat{\mathcal{X}}_{\hat{N}}) - \mathbf{c}_N(\hat{\mathcal{X}}_{\hat{N}})^\top\, \delta y^M \left((\delta y^M)^\top \mathbf{C}_N\, \delta y^M \right)^{-1} (\delta y^M)^\top \mathbf{c}_N(\hat{\mathcal{X}}_{\hat{N}}).$$

Here, $\delta y^M \in \mathbb{R}^{N \times p}$ represents the derivative matrix of the simulation output y^M, where the p columns refer to the number of calibration parameters (here $p = 3$ since $\theta = (V, C, R)$). If there is no derivative of the simulator available, the quantity δy^M has to be approximated. Choosing the finite difference method as an approximation, the i-th column of $(\delta y^M)^\top$, $i \in \{1, \dots, N\}$, is then computed by

$$\left(\delta y^M(t_i, x_i, \theta) \right)^\top = \frac{1}{h} \begin{pmatrix} y^M(t_i, x_i, \theta + h\vec{e}_1) - y^M(t_i, x_i, \theta) \\ y^M(t_i, x_i, \theta + h\vec{e}_2) - y^M(t_i, x_i, \theta) \\ y^M(t_i, x_i, \theta + h\vec{e}_3) - y^M(t_i, x_i, \theta) \end{pmatrix},$$

where $\vec{e}_j$, $j \in \{1, 2, 3\}$, is a unit vector containing 1 on its j-th row entry.

Remark 27. Due to the more complex structure of the correlation matrix (3.4.3), we cannot make use of the Kronecker tricks presented in Section 3.2. Thus, the computational cost in the Plumlee approach is clearly higher than the one in the KOH approach. This leads more easily to numerical issues, especially if the matrix δy^M has to be approximated. Moreover, the reliability of the computed (approximated) derivative is often questionable, e.g. in the case of highly noisy data [MW14].

3.4.4 Bayesian parameter identification by MCMC

In [KO01], the authors further proposed a Bayesian framework to estimate the best calibration parameter θ^*. Due to the Bayesian estimation procedure, uncertainty quantification is directly available in the form of a posterior distribution on the calibration parameters, rather than scalar values as in the previous sections.
In general, a posterior probability law describes a probability regarding a set of parameters conditioned on given data y^F [CMV15]. It measures our beliefs that θ^* is the true value under y^F. This posterior distribution, denoted by $\pi(\theta^* \mid y^F)$, can be related to the computation of other probabilities [BBS09] which are the likelihood function $L(y^F \mid \theta^*)$, the prior probability $\pi(\theta^*)$ and the marginal likelihood $\pi(y^F)$. The likelihood function quantifies how well the computer model, given the calibration parameter θ, fits to the experimental data, whereas the prior induces uncertainty about the simulated data. The marginal likelihood is a normalizing constant that does not depend on θ. Finally, Bayes' rule expresses the posterior as

$$\pi(\theta^* \mid y^F) = \frac{\mathcal{L}(y^F \mid \theta^*) \cdot \pi(\theta^*)}{\pi(y^F)} .$$

Analytical expressions of posterior distributions are seldom available, leading to a variety of estimation techniques. In this work, we use a standard Markov chain Monte Carlo (MCMC) method, the Metropolis algorithm [HKC$^+$04] stated in Algorithm 2.

Algorithm 2 Metropolis algorithm with symmetric proposal distribution.

Require: Proposal covariance matrix $\mathbf{\Sigma}^p$, prior distribution $\pi(\cdot)$, maximum number of iterations N^{iter};
1: initialize θ_0^* (sample from the prior distribution $\pi(\theta^*)$);
2: initialize l_1^0, l_2^0, g^0 (by maximizing (3.2.5)) and subsequently $\hat{\sigma}_0^2$ (by (3.2.4));
3: **for** each i in $\{1, ..., N^{iter}\}$ **do**
4: generate $\hat{\theta}$ from a symmetric distribution, e.g. $\hat{\theta} \sim \mathcal{N}(\theta_{i-1}^*, \mathbf{\Sigma}^p)$;
5: compute $l_1^i, l_2^i, g^i, \hat{\sigma}_i^2$;
6: compute the ratio $\alpha := \min\left\{1, \frac{\pi(\hat{\theta}|y^F)}{\pi(\theta_{i-1}^*|y^F)}\right\}$;
7: generate a uniform random number $u \sim \mathcal{U}([0,1])$;
8: **if** $u \leq \alpha$ **then**
9: $\theta_i^* = \hat{\theta}$ (acceptance);
10: **else**
11: $\theta_i^* = \theta_{i-1}^*$ (rejection);
12: **end if**
13: **end for**
14: Return $\theta^* = (\theta_1^*, \ldots, \theta_{N^{iter}}^*)$.

In every iteration loop, the algorithm computes a ratio which compares the posterior likelihood $\pi(\cdot \mid y^F)$ between a proposed calibration parameter $\hat{\theta}$ and the previous one θ^*_{i-1}. The proposed parameters are forced to lie close to the current value by using a symmetric proposal distribution centered on θ^*_{i-1}. If the likelihood of the proposal is bigger than the likelihood of the previous parameter, the proposal point will be accepted. Whereas if the likelihood of the proposal is smaller, the acceptance depends on the magnitude of the ratio. The closer it is to 1, the more likely the point will be accepted. Finally, the algorithm generates a sequence $\theta^* = (\theta^*_1, \ldots, \theta^*_{N^{iter}})$ of (optimal) calibration parameters from the unknown posterior distribution $\pi(\theta^* \mid y^F)$. In a next step, the samples are thinned out, keeping only 1 out of p_s samples, to reduce autocorrelation, which is defined as the correlation between two consecutive members of the Markov chain [Hof09]. We note that the number of iterations N^{iter} should be chosen large enough such that the chain can move into higher probability regions and also switch between different regions of higher probability. Moreover, it is not necessary to compute the marginal likelihood in `step 6` of Algorithm 2 since it does not depend on θ and thus it cancels out in the ratio.

Remark 28. We remark that Bayesian calibration via MCMC estimation can be quite time consuming. Usually, several thousands steps are needed to generate properly the posterior. Simplifications have been proposed in the literature, such as relying on particle filtering as in [PS15] or approximate Bayesian computation (ABC) methods as in [Bea19].

Chapter 4

Prediction approaches

In this chapter, we present several statistical approaches for traffic prediction.
First of all, we need to clarify what we mean with the term traffic prediction, because it can be interpreted in various ways. In this work, we are interested in predicting travel times, which are defined as the average time it takes a vehicle to pass a road segment $[x_{in}, x_{out}]$. Thus, our aim is to reconstruct reasonable traffic speeds along a given road stretch and time window by the help of numerical simulations. Once the speed evolution is known, we solve the ordinary differential equation

$$\begin{cases} \frac{\mathrm{dx}}{\mathrm{dt}} = v(t, x(t)), \\ x(t_0) = x_{in}, \end{cases}$$

to determine the travel time which will be given by the first time $\hat{\tau} = \hat{\tau}(t_0) > t_0$ such that $x(\hat{\tau}) = x_{out}$. The whole procedure is summarized in Algorithm 3.

Algorithm 3 Computation of travel times from speed simulation output.

Require: Departure time t_0 of a vehicle starting at position x_{in} and going to position x_{out}, simulated speed $v(t, x)$ at time t and position x, time step size Δt of numerical simulation;

1: initialize space position by $x = x_{in}$;
2: initialize travel time by $\hat{\tau} = 0$;
3: **while** $x < x_{out}$ **do**
4: update space position by $x = x + \Delta t \cdot v(t_0 + \hat{\tau}, x)$;
5: update travel time by $\hat{\tau} = \hat{\tau} + \Delta t$;
6: **end while**
7: return travel time $\hat{\tau}$.

The reconstructed travel time $\hat{\tau}$ is then compared to the real recorded travel time, derived at best from Global Positioning System (GPS) data, probe vehicles or video recordings. However, since these measurements are in reality often not available or accessible [KCB00], aggregated loop detector measurements can serve as an approximation to the ground truth (see Section 4.1.2).
As an error metric we consider the RMSE, comparing the true and reconstructed travel times for the same road stretch at N_τ different departure instants. Thus, the total travel time error

$\mathbf{E}^\tau$ is given by

$$\mathbf{E}^\tau = \sqrt{\frac{1}{N_\tau}\sum_{i=1}^{N_\tau}(\tau_i - \hat{\tau}_i)^2}\,, \tag{4.0.1}$$

where τ_i denotes the real recorded travel time and $\hat{\tau}_i$ the travel times computed by Algorithm 3.

4.1 Reference travel times

In the following two sections, we explain how we compute the reference travel time τ_i in the RMSE (4.0.1), which is not an evident task. In the best case, trajectory data are available and serve as a ground truth (see Section 4.1.1). However, if we do not have access to these data or they simply do not exist, we need to decide how to approximate them by using only the aggregated loop detector measurements (see Section 4.1.2).

4.1.1 A method for trajectory data

In reality, travel times fluctuate a lot during the day due to different traffic situations such as congestion and free flow regimes, due to different driving behaviors or due to external factors such as weather conditions. Even if we compare the travel times for a given road stretch between vehicles starting at a similar or the same time, the results can be very different. This is also due to the existence of various vehicle types, such as trucks or sport cars, which can drive at different speeds. However, in our mathematical model we do not distinguish between vehicle types when feeding the simulations by boundary loop detector data. This is why we obtain average travel times by Algorithm 3, which raises the question how to treat the trajectory data in order to compare the travel times by the RMSE (4.0.1) in a meaningful way.
A simple method is to take the mean travel times over a predefined time window: for computing the average travel time for a vehicle starting at time t, we take the mean over all recorded travel times between $t-\varepsilon$ and $t+\varepsilon$, where $\varepsilon > 0$. Thus, in the case of trajectory data, this average travel time serves from now on as our reference travel time.

Remark 29. Naturally, the value of the reference travel time depend on the size of the chosen time window 2ε. The higher ε, the more smoothed out the fluctuations between the travel times. However, we emphasize that the results in Chapter 6 only depend slightly on the choice of ε, as long as it is reasonably chosen. What is finally important is to use the same reference basis for all approaches.

4.1.2 Methods for aggregated data

If there are no or only a few trajectory data available, it is also possible to approximate travel times by using the aggregated loop detector data, which can indeed serve as a good replacement, as shown in earlier works [KCB00].
The method of N-curves [TK14, Section 19.3] represents one way to do this. It uses accumulated vehicle counts, which are derived by summing up the aggregated flow data measured by loop detectors. Naturally, these counts increase over time and the resulting time dependent

function is called the vehicle's N-curve. Then, in order to estimate the travel time between two loop detectors A and B for a vehicle starting at time t_A at loop detector A, we first compute their N-curves, denoted by N_A and N_B respectively. Second, we calculate the corresponding number of accumulated vehicle counts N^* for loop A at time t_A. Finally, we intersect this number with the N-curve of loop B in order to compute the arrival time t_B. The travel time is then given by the difference of t_A and t_B, i.e. $\tau = t_B - t_A$. The method is visualized in Figure 4.1.
We point out that this approach leads directly to average travel times, due to the usage of aggregated data. Thus, there is no need to apply the smoothing procedure described in Section 4.1.1. Moreover, the finer the aggregation time window of the data, the more accurate the results.

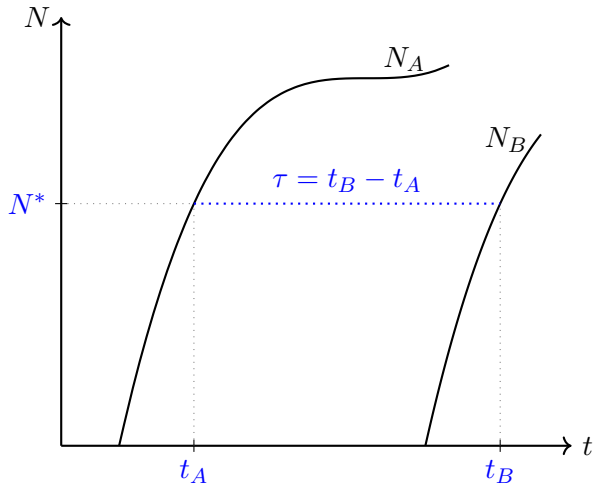

Figure 4.1: Travel time computation by the method of N-curves.

However, a major source of error for the N-curve method is the appearance of intersecting curves. This can be explained by the existence of on- and off-ramps, lane changes and overtaking maneuvers [TK14]. To reduce this error, [TK14] suggest in Section 19.4 a hybrid method which combines the use of floating car and average loop detector data which should be preferably accumulated over all lanes. Of course, this extended approach is only feasible if floating car data are available.
An alternative to reconstruct travel times can be the application of Algorithm 3, where the entries of the field $v(t, x)$ are given by the average speed measurements. Thus, they are constant between the aggregated time intervals and detector mid points. We refer to this as the *baseline method*. Foreshadowing a discussion in Chapter 5, we point out that, compared to the N-curve approach, relying on flow data measurements, the baseline method only uses speed data, which are not obvious to deal with.

4.2 Reconstructed travel times

In order to reconstruct the travel times by Algorithm 3, we need to provide boundary data for running the numerical simulation. For this, it is important to distinguish if we are in the case of travel time estimation or travel time prediction. The first one refers to the computation

of travel times for already realized traffic scenarios [VL04], implying that we have access to the data corresponding to the whole considered time period. Consequently, nothing needs to be predicted and we can simply use the real measured aggregated boundary data in the algorithm. However, in the more interesting and complex case of travel time prediction, some boundary data are not yet available and need to be forecasted. This leads to the question of how to generate the missing data in order to run the simulation also in the future time period. The rest of this chapter will be devoted to answer this question.
Thus, we present in the following several approaches to predict the future (boundary) loop detector data, denoted by $\hat{\mathbf{y}}_B$. The methods can be divided into two categories: the first one is purely data driven, using historical data (see Section 4.2.1); whereas the other one considers only data of a (short) preceding time window (see Section 4.2.2) and which might be additionally model-driven. We remark that the length of the time window for both the preceding and predicted data is variable and has to be fixed before running the approaches. More details for our choices will be given in Chapter 6.
Despite this main distinction between the categories, all approaches follow the same scheme in order to compute the travel times, namely

Step 1 Calibration of $\theta = (V, C, R)$ by one of the approaches detailed in Chapter 3.

Step 2 Determination of predicted boundary data $\hat{\mathbf{y}}_B$ by one of the methods in Section 4.2.

Step 3 Computation of simulated data by one of the numerical schemes proposed in Chapter 2 (using the boundary data from **Step 2**) and possible correction of the simulations by a discrepancy term introduced in Section 3.4.2.

Step 4 Calculation of travel times by Algorithm 3.

We emphasize that after running the above scheme, our travel time prediction result is not only based on measured data but also integrates the physical knowledge by **Step 3** and possibly **Step 2**. This is why we can speak of a *hybrid* travel time prediction method. To the best of our knowledge, this is a new contribution since previous works either deal with average loop detector data prediction (see e.g. [MK18, PS15]) or travel time prediction based on purely data driven methods (see e.g. [KCB00, RVZ04]).
We claim that the integration of the physical knowledge in the prediction process improves the results. This will be shown later in Chapter 6.

4.2.1 Loop detector data prediction from historical data

In the literature, we can find several prediction methods which use historical traffic data such as in [KCB00, RVZ04], where they rely on linear regression. However, we focus on two approaches which we consider as the most intuitive ones (see Section 4.2.1.1) or a nowadays frequently used one (see Section 4.2.1.2).
In the following, the historical traffic data form the *train data* set which is scaled by first subtracting its mean and then dividing by its standard deviation. This normalization is done for each loop detector separately. Moreover, we deal with multi-dimensional data, where the dimension represents the number of loop detectors.

4.2.1.1 Dynamic Time Warping approach

The Dynamic Time Warping (DTW) approach aims to find a time series in the train data set which behaves similarly to the data which immediately precede the prediction time slot. We will call these data *test data*, also normalized by the mean and standard deviation of the train data. To measure the similarity between two sequences, we follow [All08] and use the DTW-metric `DTW` from MATLAB, which computes a predefined distance, such as the Euclidean one, between aligned time series [RG21]. This alignment allows to find also similarities between time series with shifted patterns or which evolve differently in time. A comparison with the non-aligned version is illustrated in Figure 4.2. The DTW approach leads to a good match between the two depicted time series TS_1 and TS_2 which follow clearly the same pattern. However, the non-aligned version, presented in Figure 4.2a, does not detect this shift and leads therefore to higher distances compared to the ones in the right graphic in Figure 4.2b.

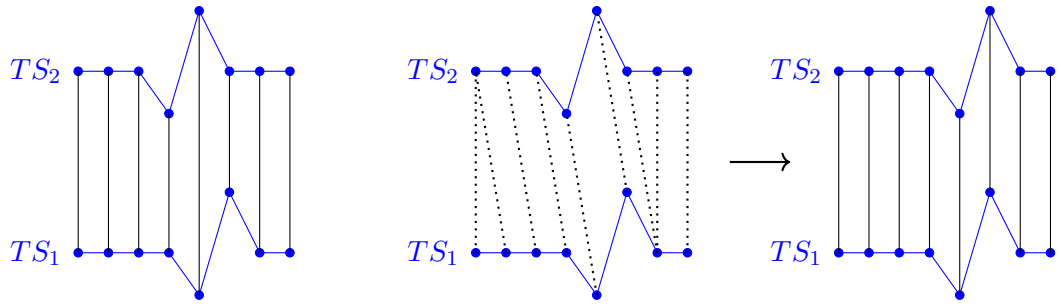

(a) Non-aligned approach. (b) DTW approach.

Figure 4.2: Comparison of the distance between two time series TS_1 and TS_2 by the non-aligned and DTW approach. Solid lines: distances between the time series; dotted lines: illustration of similar pattern detection by the DTW approach.

To conclude, the reference time series in the train data set is the one with the smallest DTW-distance with respect to the test data. Once it is found, we perform a linear least square regression between the reference and test data, leading to the 2-dimensional parameter $\hat{\boldsymbol{\beta}} = (\hat{\beta}_1, \hat{\beta}_2)^\top$. Then, the succeeding observations of the reference time series, adapted by the regression parameter $\hat{\boldsymbol{\beta}}$, form the predicted data in **Step 2**. The complete predicting procedure is summarized in Algorithm 4.
We remark that in `step 5` of the algorithm, we create the 1-dimensional version of the time series by stacking them along their time dimension.

Remark 30. We point out that Algorithm 4 compares time series with the same number of observations, which is not necessarily required for applying the DTW-metric. However, the execution of a least square regression compensate this simplification. Indeed, as observed in experimental tests, the simpler version proposed above does not lead to significant differences in the results.

Algorithm 4 Dynamic Time Warping approach.

Require: Normalized (multi-dimensional) test time series $d^{test} = (d_1^{test}, d_2^{test} \ldots, d_{n_t}^{test})$ with n_t observations, set of m (multi-dimensional) normalized train time series $d^{i,train} = (d_1^{i,train}, d_2^{i,train} \ldots, d_{n_t}^{i,train})$, $i \in \{1, \ldots, m\}$;

1: **for** each i in $\{1, ..., m\}$ **do**

2: compute the Euclidean DTW-distance: $\text{dist}^{\,i} = \texttt{DTW}(d^{test}, d^{i,train})$;

3: **end for**

4: find index $*$ of reference time series: $* = find\,\big(\text{dist} == \min(\text{dist})\big)$;

5: perform an ordinary least square fit: $\hat{\boldsymbol{\beta}} = \underset{\boldsymbol{\beta}=(\beta_1,\beta_2)^\top}{\operatorname{argmin}} (Y - X\beta)^\top (Y - X\beta)$, where

$$X = \begin{pmatrix} 1, 1, \ldots, 1 \\ \text{vec}(d^{test}) \end{pmatrix}^\top,\ Y = \text{vec}(d^{*,train})^\top;$$

6: return the predicted time series $\hat{d}$ with $\hat{n}_{\hat{t}}$ future observations:

$\hat{d} = (d_{n_t+1}^{*,train}, d_{n_t+2}^{*,train}, \ldots, d_{n_t+\hat{n}_{\hat{t}}}^{*,train}) \cdot \hat{\beta}_2 + \hat{\beta}_1$.

4.2.1.2 LSTM approach

After presenting a rather intuitive approach in Section 4.2.1.1, we now focus on a machine learning (ML) algorithm belonging to the class of recurrent neural networks (RNN). In the literature, the long short-term memory RNN (LSTM) turns out to be the most frequently used neural network since it is proven to be effective in the context of time series analysis [BCO23]. Moreover, it is capable to detect long-term dependencies between time series. In order to create a LSTM regression network, we follow the example taken from MATLAB[1].
First, we need to define the LSTM architecture, where the size of the sequence input layer coincides with the number of considered loop detectors. The number of hidden units of the LSTM layer is set to 128. Indeed, we observe in experimental tests that taking a higher number of hidden units increases the computation time and does not improve the performance during the training. For the output time series, we consider a fully connected layer with the same size as the input layer and finally we include a regression layer.
Second, we specify the training options, where the `adam`-optimizer is used with 400 epochs and a learning rate of 0.001. Moreover, the `SequencePaddingDirection` (resp. `Shuffle`) specification is set to *left* (resp. *every-epoch*).
Then, taking the train data set, the network is trained on the above defined architecture with the training options. Once it is carried out, we use the trained network to predict future time steps. Here, we need to differentiate between open and closed loop forecasting. The first one predicts only one time step ahead. Thus, when we want to predict subsequent steps, we wait until the data are available and we use them for the next prediction. However, in order to do *ad hoc* travel time predictions, we need to consider the closed loop forecasting algorithm, meaning that we predict several time steps in the future without updating the predictions by true values. Thus, we predict the data by iteratively transmitting the non-updated predicted values to the `predictAndUpdateState` function from MATLAB.

[1] See `https://fr.mathworks.com/help/deeplearning/ug/time-series-forecasting-using-deep-learning.html`. Accessed on 06/13/2023.

Remark 31. In Physics-informed neural networks (PINNs), which have recently gained more attention in the literature (see e.g. [RPK17, SMD21]), the physics model is typically injected during the training process of the network. However, we emphasize that by applying the LSTM framework we decouple the two parts, meaning that the physics are injected after the ML approach (see separation of **Step 2** and **Step 3** above), as it is also done in [BCO23].

4.2.2 Loop detector data prediction without historical data

Assuming that historical data are not available, we present in the following several options to predict the future boundary data $\hat{\mathbf{y}}_B$ based on a (short) preceding time window. The simplest idea that comes to mind is to keep the data constant which is also considered by [BCO23] as a comparative method. As a choice for this constant, one could set it to the last recorded measurement or an average of the last observed data. Later in Chapter 6, we will see that this rather naive approach, which obviously takes no information about the traffic evolution into account, does not lead to convincing results. This motivates us to develop approaches which exploit better the traffic dynamics of the available past data.

4.2.2.1 A pure GP approach

The pure GP approach belongs to the class of data driven approaches, where we model the measured traffic data by a GP. This reads in formulas as

$$y^F(\mathcal{X}_N) \sim \mathcal{N}(\bar{\mathbf{y}}_N, \mathbf{K}_N) \text{ with } \mathbf{K}_N = \sigma^2(\mathbf{C}_N + g\mathbf{I}_N),$$

where the mean $\bar{\mathbf{y}}_N$ is computed by taking the average of all the observed data. The hyper-parameters, needed to construct the covariance, are obtained by maximizing the likelihood function and differ naturally in their values from those of the KOH approach presented in Section 3.4.2.

Remark 32. We point out that the choice of the mean is not evident. Since predicted data reverts typically to its prior mean [LO18], we believe that $\bar{\mathbf{y}}_N$ is a reasonable and especially simple-to-implement choice. A more advanced suggestion can be found in [LO18], where they propose the so called Single Nugget Kriging method in order to reduce the influence of the prior mean on the predictions.

Then, as elaborated in Section 3.2, the predicted data still follow a GP, meaning that

$$y^F(\hat{\mathcal{X}}_{\hat{N}}) \mid y^F(\mathcal{X}_N) \sim \mathcal{N}\left(m_N^y(\hat{\mathcal{X}}_{\hat{N}}), (s_N^y)^2(\hat{\mathcal{X}}_{\hat{N}}, \hat{\mathcal{X}}_{\hat{N}})\right),$$

whose predictive equations are given by

$$\begin{aligned} m_N^y(\hat{\mathcal{X}}_{\hat{N}}) &= \bar{\mathbf{y}}_{\hat{N}} + \mathbf{k}_N(\hat{\mathcal{X}}_{\hat{N}})^\top \mathbf{K}_N^{-1}\left(y^F(\mathcal{X}_N) - \bar{\mathbf{y}}_N\right), \\ (s_N^y)^2(\hat{\mathcal{X}}_{\hat{N}}, \hat{\mathcal{X}}_{\hat{N}}) &:= k(\hat{\mathcal{X}}_{\hat{N}}, \hat{\mathcal{X}}_{\hat{N}}) - \mathbf{k}_N(\hat{\mathcal{X}}_{\hat{N}})^\top \mathbf{K}_N^{-1}\mathbf{k}_N(\hat{\mathcal{X}}_{\hat{N}}), \end{aligned} \tag{4.2.1}$$

and the constant entries of the $\hat{N}$-dimensional vector $\bar{\mathbf{y}}_{\hat{N}}$ coincide with the ones in $\bar{\mathbf{y}}_N$.
Then, denoting by $\hat{\mathcal{X}}_{\hat{N}_B}$ the set of observation points in the future time slot and at boundary loop detector positions, x_{in} and x_{out}, the desired boundary data $\hat{\mathbf{y}}_B$ are extracted from Equation (4.2.1), resulting in

$$\hat{\mathbf{y}}_B = m_N^y(\hat{\mathcal{X}}_{\hat{N}_B}).$$

We note that we do not make use of the predictive covariance $(s_N^y)^2$, but it can be also included in the analysis, e.g. for uncertainty quantification purposes.

Remark 33. As discussed in Section 2.4, the boundary data in the numerical scheme for the GSOM are either given in terms of the density $\rho(t, x_B)$ or the flow $q(t, x_B)$, together with the Lagrangian vehicle property $w(t, x_B)$. In any case, two traffic quantities have to be predicted, which increases tremendously the uncertainty of the results. This is why a consideration of the first order LWR model in the prediction part seems more convincing because only one quantity (density or flow) needs to be determined.

4.2.2.2 Hybrid GP approaches

Motivated by our conviction that the physical model provides useful information helping to improve the prediction results, we now consider methods that integrate the PDE into the GP modeling. This is the reason why we call them hybrid GP approaches.
In [CCZW22], they propose a method to create points, where the PDE has to be satisfied. This can be only applied to non-linear PDEs taking a specific form (see [CCZW22, Equation 2.16]): the non-linear term consists only in products of derivatives which is not satisfied in our case due to the choice of a non-linear speed function. Moreover, in [CHOS21] they suggest another method in order to force the PDE to be satisfied at a finite set of points. This idea requires the strong existence of the solution for their convergence proof. However, as proven in Theorem 1, our IBVP admits entropy solutions in a weak sense (see Definition 4). A more general approach is suggested in [LWK$^+$22], which has no restrictions on the form of the PDE or its solution. The idea is to construct two likelihoods, a data and a virtual one. The first likelihood serves to fit the observations and the second one to fulfil the PDE equation at so called virtual points. Since there is no closed form for the posterior distribution available, they end up with a variational posterior expression. Finally, this results in solving a high dimensional optimization problem, where the number of parameters depends on the number of observations and virtual points. Thus, the approach is not very practical in real world scenarios. Additionally, it is not clear how their algorithm performs in true prediction cases because the optimal set of hyper-parameters are based on a RMSE computed by considering also the (unavailable) prediction data.
This motivates us to create our own hybrid approach in order to overcome the shortcomings of the previous ones: it applies to all kind of differential equations and the set of hyper-parameters do not increase compared to the pure GP modeling. The method is based on multi-objective optimization (MOO) and it is detailed in the following.

MOO approach
In the MOO appoach, we require two objective functions to be minimized.
First, we again model the data by a GP resulting in the minimization of the negative concentrated log-likelihood function which reads as

$$\min_{l_1,l_2,g} f_1^{obj}(l_1, l_2, g) = \min_{l_1,l_2,g} \left(-\log \tilde{\mathcal{L}} \left(l_1, l_2, g, y^F(\mathcal{X}_N) \right) \right),$$

where the function $\log \tilde{\mathcal{L}}$ is defined in Equation (3.2.5). Then, we additionally want the system of PDEs to be satisfied at virtual points, denoted by $\tilde{X}_{\tilde{N}} = \left((\tilde{t}_1, \tilde{x}_1), \ldots, (\tilde{t}_{\tilde{N}}, \tilde{x}_{\tilde{N}}) \right)$.

This leads to the formulation of the second objective, namely to minimize the PDE residuals at $\tilde{X}_{\tilde{N}}$:

$$\min_{l_1,l_2,g} f_2^{obj}(l_1,l_2,g) = \min_{l_1,l_2,g} \left| \partial_t\, y^F(\tilde{X}_{\tilde{N}}) + \partial_x\, f\left(y^F(\tilde{X}_{\tilde{N}})\right)\right|,$$

where $y^F(\tilde{X}_{\tilde{N}}) = m_N^y(\tilde{X}_{\tilde{N}})$ and f defined in Equation (1.2.3). The derivative expressions are computed by deriving the kernels, thus it holds

$$\partial_t\, y^F(\tilde{X}_{\tilde{N}}) = \partial_t\, m_N^y(\tilde{X}_{\tilde{N}}) = \partial_t \left(\mathbf{k}_N(\tilde{X}_{\tilde{N}})\right)^\top \mathbf{K}_N^{-1}\left(y^F(\mathcal{X}_N) - \bar{\mathbf{y}}_N\right),$$
$$\partial_x\, y^F(\tilde{X}_{\tilde{N}}) = \partial_x\, m_N^y(\tilde{X}_{\tilde{N}}) = \partial_x \left(\mathbf{k}_N(\tilde{X}_{\tilde{N}})\right)^\top \mathbf{K}_N^{-1}\left(y^F(\mathcal{X}_N) - \bar{\mathbf{y}}_N\right),$$

where $\partial_z\left(\mathbf{k}_N(\tilde{X}_{\tilde{N}})\right) = \sigma^2\left(\mathbb{C}orr\left(b(t_i,x_i),\ \frac{\mathrm{d}}{\mathrm{dz}}\, b(\tilde{t}_j,\tilde{x}_j)\right)\right)_{1\le i\le N, 1\le j\le \tilde{N}}$ and $z\in\{t,x\}$,
or in case of the integral extension (see Section 3.2.2),
where $\partial_z\left(\mathbf{k}_N(\tilde{X}_{\tilde{N}})\right) = \sigma^2\left(\mathbb{C}orr\left(\frac{1}{\Delta t}\int_{t_i}^{t_i+\Delta t} b(s,x_i)\,\mathrm{ds},\ \frac{\mathrm{d}}{\mathrm{dz}}\, b(\tilde{t}_j,\tilde{x}_j)\right)\right)_{1\le i\le N, 1\le j\le \tilde{N}}$.

Remark 34. The choice of virtual points is not evident and it has an influence on the prediction. In our application, we generate uniformly distributed random numbers which seems to deliver reasonable results. However, we cannot deny that improvements might be achieved by considering more involved methods, as the "active PDE-informed Kriging" (APIK) approach proposed in [CCZW22].

As already pointed out in Remark 33, the consideration of the GSOM would imply to predict two traffic quantities. Moreover, we have to conform to a system of PDEs, which also increases the number of objective functions. As observed in our tests, the LWR model turns out to perform better compared to the GSOM since less traffic quantities have to be predicted. Then, by considering this first order model, the second objective is expressed only in terms of the density. Consequently, it is natural to implement density boundary conditions in the numerical scheme. This is why we consider

$$y^F(\mathcal{X}_N) = \Big(\rho(t_1,x_1),\dots,\rho(t_N,x_N)\Big),$$

in the case of the MOO approach which implies $f\left(y^F(\mathcal{X}_N)\right) = y^F(\mathcal{X}_N)\cdot\mathcal{V}\left(y^F(\mathcal{X}_N)\right)$.
Finally, to complete this section, we need to deal with the question of how to compute the optimal hyper-parameters, since we obtain a set of non-dominated optimal solutions rather than a single one. This set represents the Pareto front meaning that there exists no solution which is better in at least one of the objectives and not worse in any of them [Mie99].
We rely on the simple knee-point method which allows us to determine a solution on the Pareto front without any prior knowledge [SNI15]. For this, we connect the extreme points of the Pareto front by a line (in the 2-dimensional case). Then, the knee-point is the one which maximizes the Euclidean distance among all points on the front and this line. It is considered as a reasonable solution since moving on the Pareto front would lead to a large deterioration in one of the objectives. The method is illustrated in Figure 4.3.
After the knee-point is determined, the optimal hyper-parameters l_1, l_2 and g, are known. This enables us to compute the desired boundary loop detector data, again by exploiting the predictive mean formula, namely $\hat{\mathbf{y}}_B = m_N^y(\hat{\mathcal{X}}_{\hat{N}_B})$.

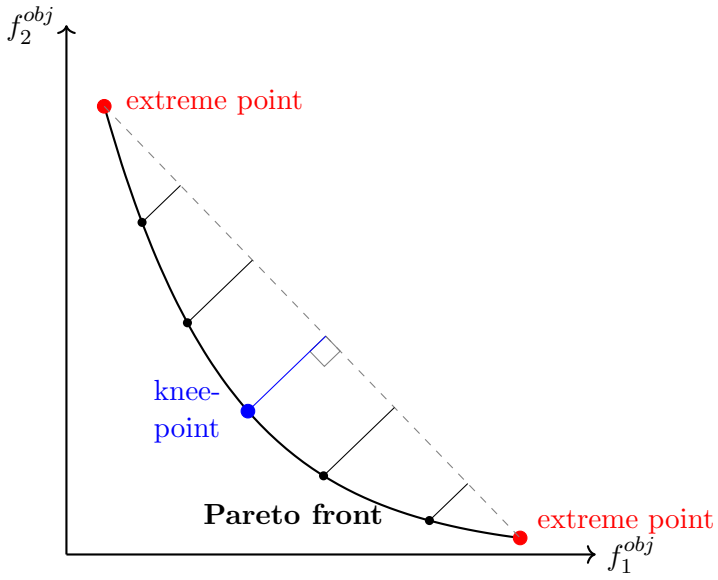

Figure 4.3: Illustration of the knee-point method for a 2-dimensional MOO problem.

Remark 35. The second objective function f_2^{obj} reminds of the residual function in the PINNs approach, where the traffic state variable is approximated by a neural network. More precisely, the approximate solution of the PDE is obtained by training a loss function consisting of both a data and a residual error, where the second one typically has to be calculated by using a large amount of so called auxiliary points. However, in our case, we use the GP predictive equations, which are computational less expensive.
Moreover, analogously to [LWK+22], we consider two terms in the MOO approach, where one refers to the observations and the other one to the PDE equation. Unlike them, we keep the two terms separated in the multi-objective optimization, instead of modeling both by a likelihood function and combine them via multiplication.

Chapter 5

Description of traffic data sets

In order to validate our proposed models and statistical approaches, we need to introduce some traffic data. Thus, this chapter is devoted to the description of two data sets: one is composed of purely synthetic data (see Section 5.1) and the other one of real world traffic data (see Section 5.2).
In any case, we consider data which are recorded by loop detectors providing aggregated information over time. Therefore, we have access to temporal data averages, typically the traffic flow q and the occupancy O, which is defined as the percentage of time a detector is occupied by a vehicle [PS15]. From the occupancy measurement, we can then derive the traffic density ρ by using the formula

$$\rho = \frac{O}{l}, \tag{5.0.1}$$

where l denotes the average vehicle length. Obviously, this formula gives only an approximation for the density due to the estimation of l.
If two detectors are installed in very close succession, the traffic speed v can be also directly computed. In this case, the measurements provide the temporal (also called arithmetic) mean speed which is the average speed of the vehicles passing a road section during the aggregated time interval [TK14]. In reality however, the speed is mostly not measured and must be derived, which can be done by using the fundamental diagram equation

$$v = \frac{q}{\rho}, \tag{5.0.2}$$

leading finally to a spatial rather than a temporal average value. We point out that contrary to the flow (resp. density) which belongs to the class of temporal (resp. spatial) traffic data, the speed can be defined as both a temporal and a spatial quantity. However, these two definitions differ from each other, thus they naturally lead to different results in applications such as travel time predictions [TK14].

Remark 36. If the detectors provide flow and speed traffic data (and not occupancy data), we point out that the density can be only approximated by $\rho = \frac{q}{v}$ which leads to an error since v is measured by its temporal mean and the density is a spatial quantity. In any case, the flow data are the most reliable ones, since there is no need of deriving them by a formula.

Next, if we consider scenarios with several lanes, the overall flow at a fixed detector position is calculated by summing the measured flow values of the individual lanes. The computation

of the overall density is done in the same way, assuming that the occupancy is given. The derivation of the overall speed is detailed in Section 5.1.

We remark that all the presented scenarios will have homogeneous road conditions. This means that both the number of lanes and the speed limit do not change. If we considered more complex scenarios, the proposed models and approaches would need to be adapted, e.g. by generalizing the model and increasing the number of parameters, since they do not account for changing conditions along the road stretch [KCB00].
Moreover, every considered scenario, regardless if it is an artificial or real one, covers a period of 3 hours and includes congestion phases. Since the calibration and prediction process is more difficult and interesting for dense traffic situations, we are particularly interested in the performance of our models for such congested situations.

5.1 Synthetic microscopic traffic data

The quality of the data coming from real world traffic situations is often questionable. This may be due to non-functioning sensors or measurement errors. Thus, before testing our approaches on real world scenarios, we want to validate them on synthetic data. We focus on data generated by microscopic simulations created by the open source package *Simulation of Urban MObility* (in short SUMO) [LBBW$^+$18]. In contrast to data derived by simulations based on a macroscopic traffic flow model, the microscopic simulator models each vehicle individually. This enables us to have access to trajectory data, from which we can then directly derive the travel times, as explained in Section 4.1.

Remark 37. In [WBG23], we propose a method to generate data by numerical simulations based on macroscopic traffic flow models. This paper is a first approach to validate our proposed statistical methods. After having obtained satisfactory results, we are now interested in considering a microscopic simulator, assuming that it can create more realistic road scenarios.

In the following, we describe three traffic scenarios created by SUMO. All of them simulate a highway traffic situation for a 10km road stretch with three lanes and a constant speed limit of 100km/h. The traffic flow consists of three different vehicle types which differ in their desired maximum speed. The length of all vehicles is set to 5m. Next, we equip the road with 30 loop detectors, one for each lane at ten different, non-equidistant locations. Moreover, the sensor data are aggregated every 6 minute.
Thanks to SUMO, we have access to all possible measurable traffic quantities: the flow, occupancy and speed. Thus, the density needs to be derived by applying Equation (5.0.1) and setting $l = 0.005$km. Moreover, the speed is given in two versions: the arithmetic and harmonic mean speed, where the second one can be seen as an approximation for the spatial average of the speed at a fixed loop detector position [TK14]. In order to compute the average speed over the three lanes, we use the space mean formula

$$v = \frac{\sum_{i=1}^{3} \rho_i v_i}{\rho}, \tag{5.1.1}$$

where the sum is taken over each lane speed v_i and density ρ_i, $i \in \{1, 2, 3\}$.
The remaining question is now how to choose v_i. If the raw traffic data are not available,

which is often the case, the harmonic mean speed cannot be computed. This is why we exclude its consideration for the determination of v_i. However, if we use the arithmetic speed, which always exceeds the harmonic one [TK14], travel times will be usually underestimated. Thus, computing v_i by the fundamental diagram formula $v_i = \frac{q_i}{\rho_i}$, where q_i denotes the flow on lane i, is the most reasonable choice. This finally leads back to equation (5.0.2).
A schematic representation of the road is illustrated in Figure 5.1, where the blue vertical lines indicate the coarse segmentation used in the numerical schemes. In order to avoid confounding effects, each segment contains at most one global loop detector which includes the data of the corresponding lane detectors.

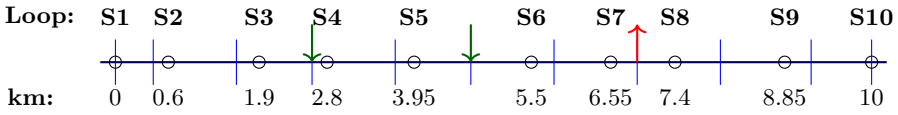

Figure 5.1: Schematic representation of the 10km road stretch generated by SUMO.
Loop detectors are illustrated by black circles, the on- (resp. off-) ramps by green (resp. red) vertical arrows and the coarse segmentation of the numerical scheme by blue vertical lines.

5.1.1 SUMO scenarios

In a next step, we give more details on the three considered SUMO scenarios:

1A) SUMO-1A:

The first one does not consider the ramps depicted in Figure 5.1. It deals with a highly congested traffic situation generated by reducing gradually the speed limit on the last 0.01km of the road stretch. By this, vehicles are forced to slow down at the downstream boundary inducing a backward moving congestion wave, which dissipates after the considered time window of 3 hours. In Figure 5.2a we depict the speed values measured by the loop detectors for the 6 minute aggregated time intervals. We point out that the first three loop detectors are not affected by the congestion wave. The distribution of all the data points is visualized by the fundamental diagrams in Figure 5.2b. By the peak of the flow diagram at the critical density, it is well visible that data are lying in both traffic regimes: the free flow and congested one. Additionally, in contrast to the lower density region, the data in the congested part are more widely spread, which is typical of real traffic scenarios [Fan13, FHS14].

1B) SUMO-1B:

Keeping exactly the same left boundary inflow and speed reduction as before, we equip **SUMO-1A** additionally with two on-ramps and one off-ramp located after 2.6km, 4.7km and 6.9km respectively. In Figure 5.3a we observe that the contribution of the on-ramp inflows increases traffic congestion tremendously, especially in the first half of the road stretch. Now, the congestion spills back until the very first loop detector, which was not the case in the rampless version. Moreover, the fundamental diagrams in Figure 5.3b emphasize the denser situation because more data points are lying in the congested region. This time, the maximum density almost reaches a value of 450veh/km which is indeed higher than in **SUMO-1A**, where it does not exceed 280veh/km.

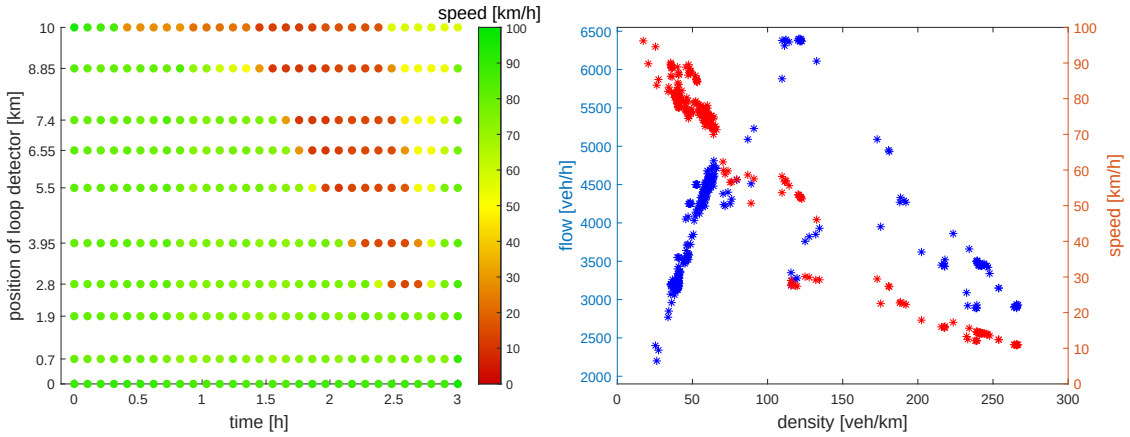

(a) Speed evolution. (b) Fundamental diagrams.

Figure 5.2: Traffic scenario **SUMO-1A**.

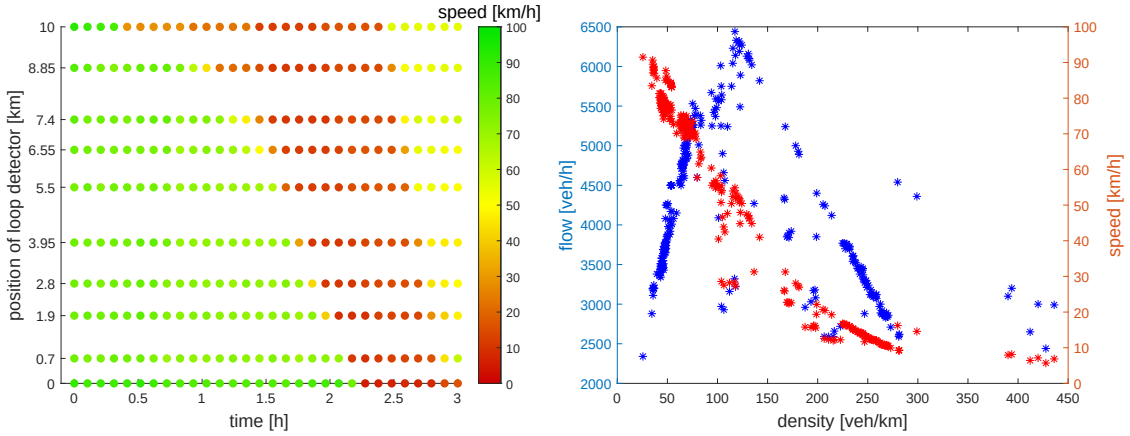

(a) Speed evolution. (b) Fundamental diagrams.

Figure 5.3: Traffic scenario **SUMO-1B**.

2.) SUMO-2:

The second constructed rampless scenario simulates an accident. We implement this in SUMO by closing the rightmost lane after 1 hour between kilometer 6 and 9 for a duration of 80 minutes. In contrast to **SUMO-1A** and **SUMO-1B**, we observe in Figure 5.4a that the congestion is less present. Consequently, there are only a few data points in the congested region in Figure 5.4b and the maximum density does not exceed 200veh/km. However, we observe a sudden change in the traffic regime, especially for the loop detector which is placed after 5.5km, right before the lane closure. This drastic jump is emphasized by the speed profile of loop detector S6 in Figure 5.5. From a modeling point of view, such scenarios are interesting to analyze since these sudden changes are often difficult to capture. Additionally, the numerical schemes, as proposed in Chapter 2, can struggle to reconstruct the scenario appropriately since the last boundary detector is not affected by this lane closure.

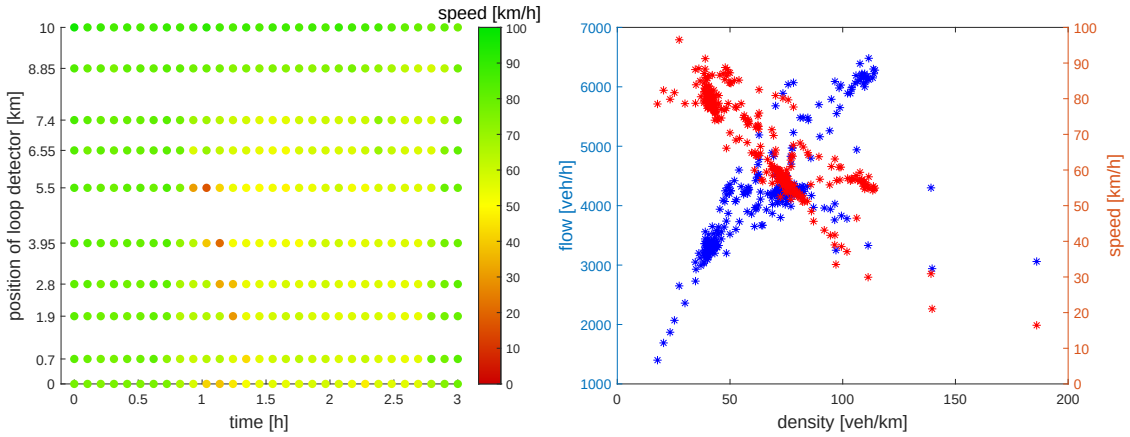

(a) Speed evolution. (b) Fundamental diagrams.

Figure 5.4: Traffic scenario **SUMO-2**.

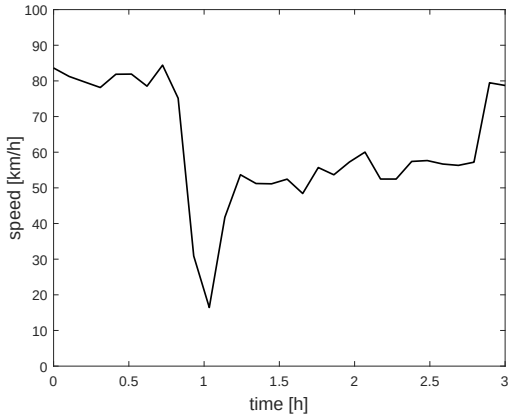

Figure 5.5: **SUMO-2**. Sudden change in speed profile for loop detector S6.

In the last part of this synthetic data section, we illustrate the evolution of the travel times for the artificially created scenarios. Thanks to SUMO, we have access to the exact travel times for each individually modeled vehicle.
We are interested in the average time taken by a vehicle to pass the 10km long road stretch. As explained in Section 4.1.1, we compute this mean travel time for a vehicle starting at time t by averaging over the recorded times in the interval $]t-\varepsilon, t+\varepsilon[$, where we choose $\varepsilon = 10$s. Then, these travel times serve as our reference values and they will be compared with the two methods for aggregated data, introduced in Section 4.1.2. We note that, due to a later implemented initialization period, we look at travel times for cars which departs after the first 6 minutes. The last considered departure time is after 2 hours and 30 minutes which finally results in the consideration of 865 vehicle trajectories.

Starting with **SUMO-1A**, we observe in Figure 5.6a a steadily increasing travel time up to $\tau = 27$min due to the artificially created congestion. The results for the method of N-curves (resp. baseline method) is depicted in black (resp. blue) color. It is clearly visible that the

black dashed line reflects better the ground truth than the blue dotted one which is also confirmed by the RMSEs (in minutes): $\mathbf{E}^{\tau}_{\text{N-curve}} = 0.43 < \mathbf{E}^{\tau}_{\text{baseline}} = 0.84$. Thus, the method of N-curve outperforms the baseline approach, certainly due to the consideration of flow data which are directly given by the detectors. Instead, the baseline approach uses piece-wise constant speed data to approximate the travel times. As already pointed out, the speed data are not unique and not directly measurable which leads finally to worse approximations.
Additionally, by Figure 5.6b, we emphasize the worse performance of the baseline method when using the arithmetic mean speed in Equation (5.1.1). As expected, the travel times are clearly underestimated and the RMSE exceeds the one in the fundamental diagram version.

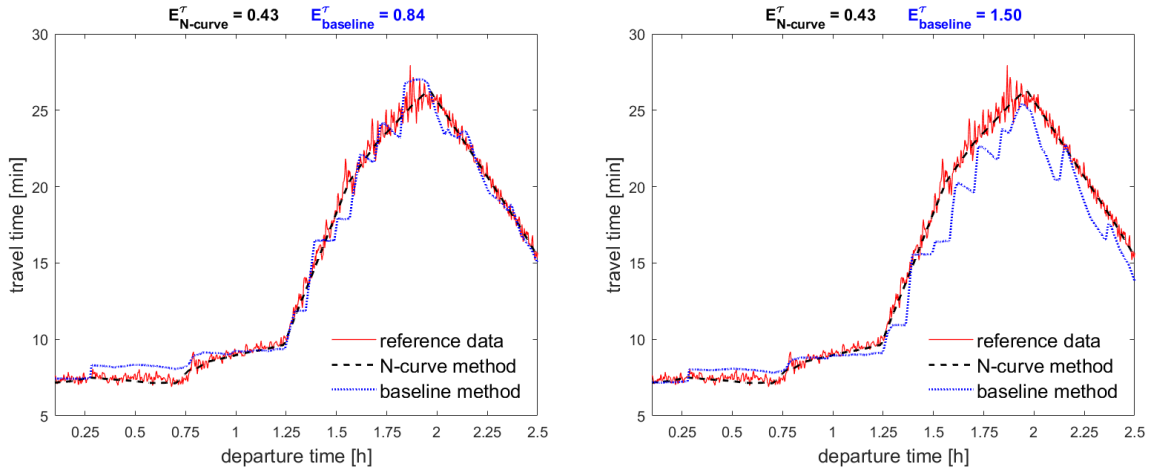

(a) Speed by fundamental relation.

(b) Speed by arithmetic mean.

Figure 5.6: **SUMO-1A**. Comparison of travel times derived by trajectory and aggregated data. Left (resp. right) column: baseline method is based on speed values given by the fundamental equation (resp. arithmetic mean speed).

Next, analyzing the travel times of **SUMO-1B** in Figure 5.7, we come to the same conclusion as before:

1. The method of N-curve outperforms the baseline approach.
2. The use of the arithmetic mean speed in Equation (5.1.1) underestimates the travel times compared to the fundamental Equation.

Moreover, due to the presence of ramps and the denser traffic situation, the average duration of travelling through the road is now higher than in **SUMO-1A**. This time the travel time can exceed $\tau = 30$min. Additionally, all the RMSEs are higher than the corresponding ones of the rampless scenario. However, it is remarkable that the method of N-curve still leads to a good approximation ($\mathbf{E}^{\tau}_{\text{N-curve}} = 0.54$). Thus, assuming good quality data, this approach could serve as a reasonable travel time approximation for real world scenarios when trajectory data are not available.

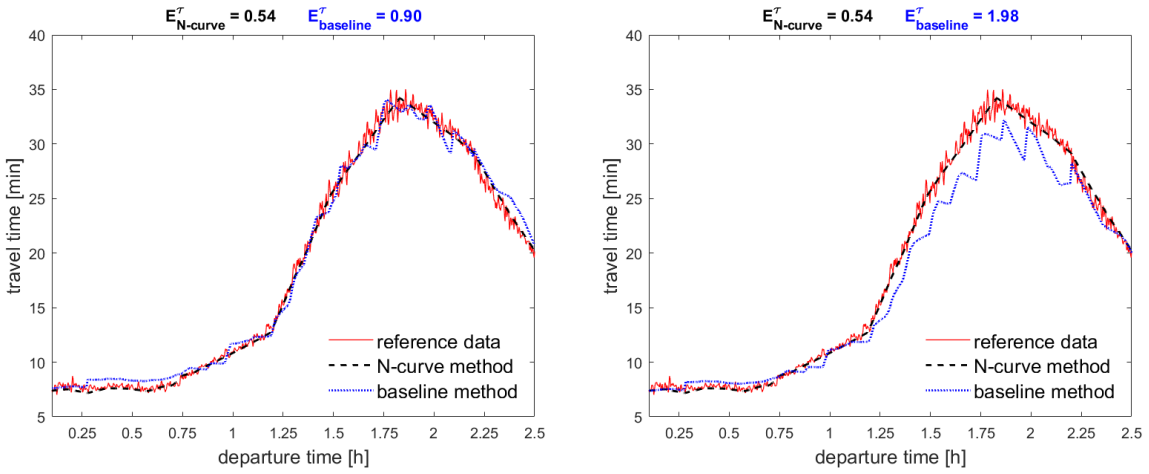

(a) Speed by fundamental relation.

(b) Speed by arithmetic mean.

Figure 5.7: **SUMO-1B**. Comparison of travel times derived by trajectory and aggregated data. Left (resp. right) column: baseline method is based on speed values given by the fundamental equation (resp. arithmetic mean speed).

It remains to consider the travel time results for **SUMO-2**, illustrated in Figure 5.8. Due to less congestion, the travel times are in a lower range than in the two previously presented cases. The jump of the traffic regime is well reflected by the sudden increase of the travel time which has its peak approximately after 1 hour. This is exactly the time instant when the rightmost lane is getting closed. Finally, for this scenario the RMSE of the baseline method lies closer to the one of the N-curve approach. However, it still performs worse, especially if we consider the arithmetic mean, emphasized by Figure 5.8b.

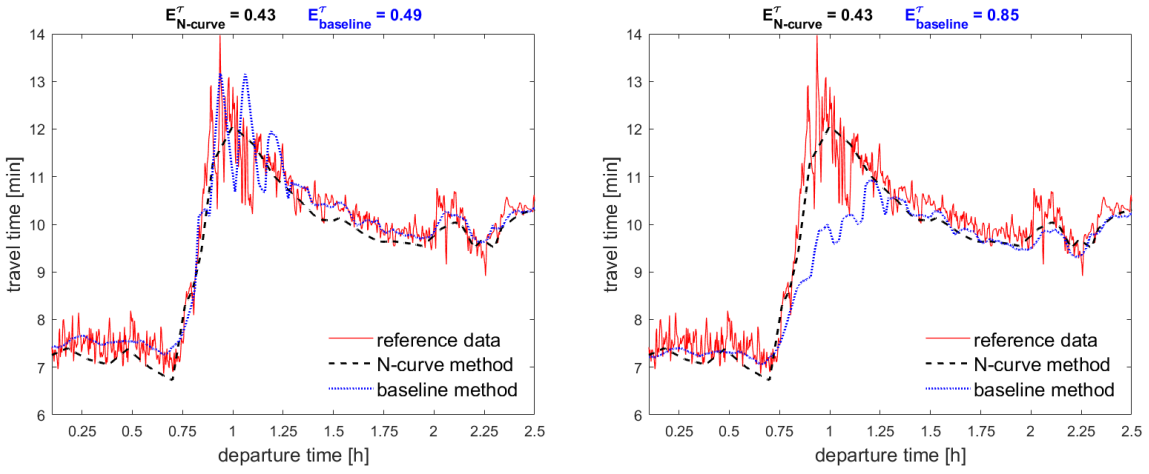

(a) Speed by fundamental relation.

(b) Speed by arithmetic mean.

Figure 5.8: **SUMO-2**. Comparison of travel times derived by trajectory and aggregated data. Left (resp. right) column: baseline method is based on speed values given by the fundamental equation (resp. arithmetic mean speed).

Remark 38. Although the method of N-curve seems to perform well in every considered scenario, it remains a questionable choice for travel time reconstructions. More complex scenarios, as longer road stretches including more ramps, lane changes and overtaking maneuvers, will decrease the reliability on the N-curve approach [TK14]. This is why traffic flow models, as proposed in this work, can be seen as a replacement.

5.2 Real traffic data

We continue now by considering a real world data set which is referred to as the RTMC data set [Min], provided by the Minnesota Department of Transportation (MnDOT). Analogously to the artificial SUMO data, the RTMC data are 6 minute averages obtained by single loop detectors measuring the traffic flow and the occupancy. Moreover, the MnDOT transforms the recorded occupancy values into densities by using the so called average field length[1] of the traffic sensor which consists of the average vehicle length and the sensitivity of a sensor. For the tests, we consider a 4.85km long road stretch on the northbound direction of the interstate highway I-35W equipped with 8 sensors on the mainlane (IDs: S54, S1706, S56, S57, S1707, S59, S60, S61), 2 at on-ramps (IDs: 129, 130) and 3 at off-ramps (IDs: 169, 170, 171). The road stretch has in total five lanes and the speed limit is 55miles/hour ($\approx$ 90km/h). To visualize the position of the sensors along the road, we refer to Figure 5.9.

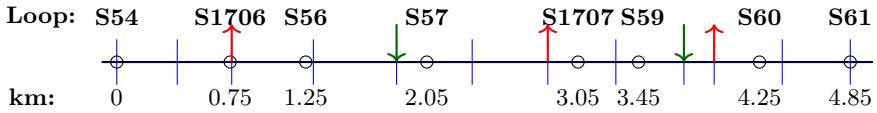

Figure 5.9: Schematic representation of a section of highway I-35W in Minnesota.
Loop detectors are illustrated by black circles, the on- (resp. off-) ramps by green (resp. red) vertical arrows and the coarse segmentation of the numerical scheme by blue vertical lines.

5.2.1 Data pre-processing

We extract all the sensor data measured in the year 2013, serving as the historical train data, and some selected days in 2014. Instead of extracting single lane data, we consider directly the accumulated measurements over the five lanes which are also provided by the MnDOT. For our later analysis, however, we need to pre-process these raw-data in order to remove abnormalities [LMLR06].
In a first step, we detect missing data which are indicated by negative values. In this case, we note that the detectors did not work properly for several hours. Thus, we decided to discard the following eight days completely from our analysis: 06/21/2013-06/24/2013, 08/25/2013-08/26/2013 and 09/08/2013-09/09/2013. Next, motivated by the fundamental diagram, we replace all measured flow (resp. density) values by zero if the corresponding density (flow) is zero. Naturally, a zero flow could also correspond to a fully congested road, however this is never the case for our extracted RTMC data, which can be easily verified by comparing the data measured by nearby loop detectors. Then, we compute the average speed values by the fundamental Equation (5.0.2) and they are set to 200km/h in the case of $\rho = q = 0$.

[1] See `http://data.dot.state.mn.us/datatools/Density.html`. Accessed on 09/15/2023.

Moreover, we verify that the computed speeds never exceed the threshold of 200km/h, which is true except for two ramp observations due to very low measured density (and flow) values. In those two rare cases we set $v = 200$km/h.

5.2.2 Data clustering

To get more insight into the historical data, we perform a clustering technique which is based on the well-known K-means method [Llo82]. Here, we measure the distance between the centroids and train time series again by the DTW-metric. In general, the clustering can be performed on any of the traffic quantities. However, as previously pointed out, we are interested in a good speed reconstruction, therefore we consider the historical speed data in the algorithm. Moreover, the results of the clustering will be later used in Chapter 6 when testing the fundamental fit approach, introduced in Section 3.3.
The complete procedure is summarized in Algorithm 5, where we set $N^{iter} = 30$ (number of iterations per random initialization), $\varepsilon = 10^{-6}$ (stopping criteria), $m = 365-8 = 357$ (number of days in the training set) and $n_t = 24 \cdot \frac{60}{6} = 240$ (number of daily time observations).

Algorithm 5 K-means clustering with DTW-distance.

Require: Set of m normalized (multi-dimensional) train time series $d^{i,train} = (d_1^{i,train}, d_2^{i,train} \dots, d_{n_t}^{i,train})$ with n_t observations, $i \in \{1, \dots, m\}$, number of clusters K, maximum number of iterations N^{iter}, stopping criteria ε;

1: initialize iteration counter $p = 1$ and error $E = 1$;
2: initialize K centroid time series $c^{k,p} = (c_1^{k,p}, c_2^{k,p}, \dots, c_{n_t}^{k,p})$, $k \in \{1, \dots, K\}$, by choosing randomly K time series from the training set;
3: **while** $E > \varepsilon$ and $p \leq N^{iter}$ **do**
4: **for** each i in $\{1, ..., m\}$ **do**
5: **for** each k in $\{1, ..., K\}$ **do**
6: compute the Euclidean DTW-distance by $\text{dist}^k = \texttt{DTW}(c^{k,p}, d^{i,train})$;
7: **end for**
8: assign time series $d^{i,train}$ to cluster k by $k = \underset{k \in \{1,\dots,K\}}{\text{argmin}} \ \text{dist}^k$;
9: **end for**
10: **for** each k in $\{1, ..., K\}$ **do**
11: update centroids by taking the mean over the set of N_k time series, denoted by $d^{j,k}$, $j \in \{1, \dots, N_k\}$, belonging to cluster k: $c^{k,p+1} = \frac{1}{N_k} \sum_{j=1}^{N_k} d^{j,k}$;
12: **end for**
13: $E = \sum_{k=1}^{K} \|c^{k,p+1} - c^{k,p}\|_F$;
14: $p = p + 1$;
15: **end while**
16: return $\texttt{inertia} = \sum_{k=1}^{K} \sum_{j=1}^{N_k} \|c^{k,p} - d^{j,k}\|_F^2$.

Since we deal with 8-dimensional time series, where each dimension corresponds to a loop detector, we consider the Frobenius norm in `step 14` and `17`. Moreover, in order to compute the updated centroid in `step 12`, the mean is calculated for each loop detector and each time

point separately such that the dimensions of $c^{k,p+1}$ and $d^{j,k}$ coincide.
This algorithm is executed 50 times since the result depends on the random initialization in `step 3`. Finally, we pick the initialization which leads to the lowest inertia, defined as the Frobenius norm between every train time series and its corresponding cluster centroid. Of course, the number of optimal clusters K is not known in advance. Thus, the whole procedure has to be repeated for different choices of K. In Figure 5.10a, we plot the inertia value against the number of clusters. Typically, one tries to find the "elbow" of this curve, which in this case could correspond to $K = 2$ or $K = 3$. Comparing the daily time series for these two options, we decide for $K = 2$ since a third cluster shows no behavior that has not already been captured by the other two. Finally, we illustrate all the 357 daily time series from 2013 recorded by loop detector S59 in Figure 5.10b, where the time series belonging to cluster 1 (resp. cluster 2) are drawn in red (resp. black). In total, 201 (resp. 156) out of 357 time series are assigned to cluster 1 (resp. cluster 2).

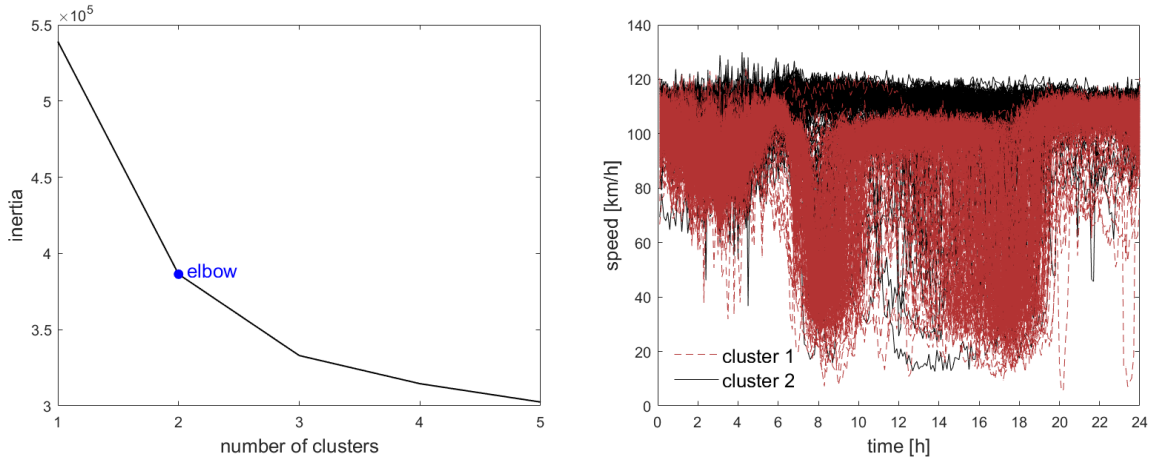

(a) Elbow plot.

(b) Daily time series.

Figure 5.10: Illustration of clustering results by Algorithm 5. Left column: inertia dependent on the number of clusters. Right column: daily time series for loop detector S59 and $K = 2$.

Generally speaking, the data belonging to cluster 1 exhibit two rush hour periods, one in the morning and the other one in the afternoon. In contrast, the second cluster captures a more steady traffic situation with only a few cases with peaks. Thus, it is not surpising that the first (resp. second) cluster is mainly represented by weekdays (resp. Saturdays and Sundays), where the traffic is typically more dense (resp. less dense).

5.2.3 RTMC scenarios

In the following section, we describe two sample scenarios for the RTMC data set which will be later used to test our models and statistical approaches. The data are chosen from the year 2014, so they are not integrated in the clustering procedure. We pick the scenarios in a way such that they belong to the two different clusters.

Remark 39. In order to determine which cluster a test day belongs to, we compare the DTW-distance between the two centroids and the test time series. Then, we pick the cluster which leads to the lowest value of the DTW-metric. Moreover, we point out that the time

slot between 8am-9am will later be considered as the prediction time slot, so all the data after 8am are treated as unknown. This is why the cluster assignment and also the DTW Algorithm 4 involves only the data of the first 8 hours of the test and centroid time series.

1.) RTMC-1:

The first scenario belongs to cluster 1 and covers the morning time slot from 6am to 9am of Wednesday, 11/05/2014. In the speed evolution depicted in Figure 5.11a, a free flow situation is well recognizable in the first 30 minutes. Then, the traffic is getting more dense almost until the end of the considered time period. In particular, the fundamental flow diagram in Figure 5.11b emphasizes these two traffic regimes since data are present for both lower and higher densities. Moreover, the congested part is well recognizable due to the larger spread of the data for densities higher than 110veh/km.

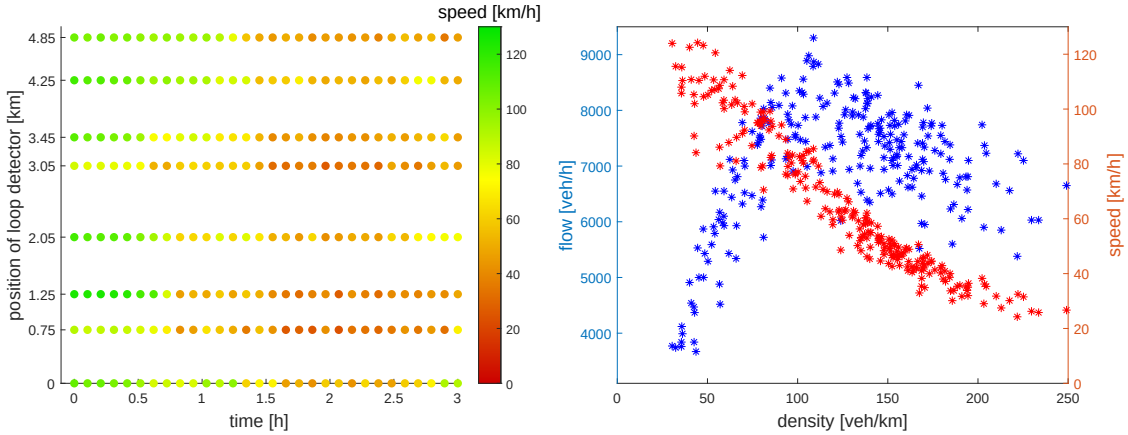

(a) Speed evolution.

(b) Fundamental diagrams.

Figure 5.11: Traffic scenario **RTMC-1**.

2.) RTMC-2:

In contrast, the second scenario which belongs to cluster 2, refers to a much less intense traffic situation. The data are recorded on Monday, 02/10/2014, again from 6am-9am and they belong most of the time to the free flow regime which is pointed out by the two graphics in Figure 5.12: first, in the left column, there are only a few points drawn in darker orange or red color; second, in the right column, the measured flow data are mainly distributed around the increasing part of the fundamental flow diagram. Consequently, the maximum measured density is lower than in **RTMC-1** and does not exceed 200veh/km.

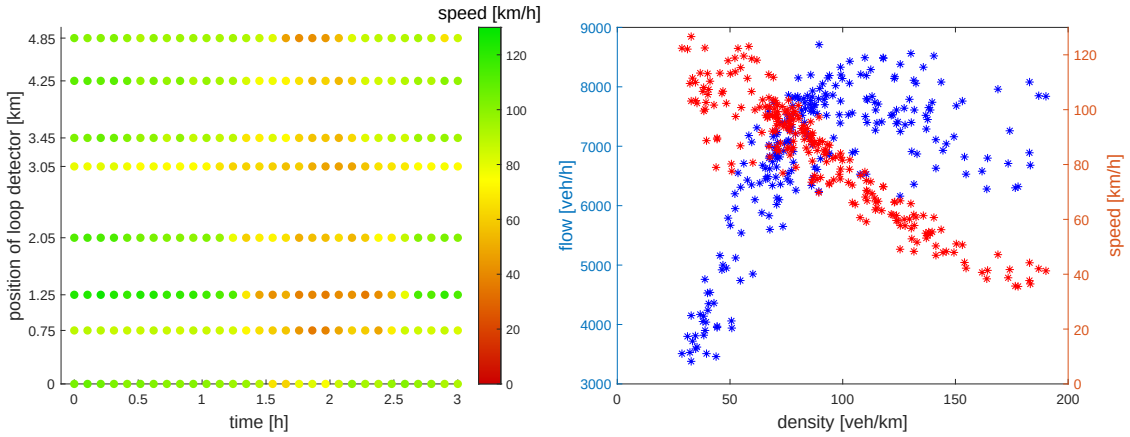

(a) Speed evolution.

(b) Fundamental diagrams.

Figure 5.12: Traffic scenario **RTMC-2**.

Analogously to the SUMO data, we study the travel times for the presented RTMC scenarios in a final part of this section. However, this time we do not have access to trajectory data, so the reference travel time can be only estimated by using the aggregated loop detector data. As before, we compare the method of N-curves and the baseline approach.
The initialization of the N-curves belonging to the first and last loop detector are based on a free flow assumption at 6am. Thus, we shift the N-curve for sensor S61 by a fictive computed travel time towards the future. This time is computed by dividing the length of the road stretch (4.85km) by the mean of the speeds, measured by the eight sensors, at 6am. We point out that in the artificial data case, the execution of this shift was not necessary because it was known at the beginning of the time slot how many cars have already passed the first loop and not reached the last one. In Figure 5.13, we illustrate the results of the two approaches for vehicles departing during the first 2 hours. In both scenarios, the method of N-curve fails since the travel time decreases constantly, which will finally result in negative values. Indeed, we observe intersecting N-curves after more than 2 hours which is a typical drawback of this approach when dealing with real world data (see Remark 38). Instead, the baseline approach shows an increasing behavior in the travel time, which seems to be realistic due to lower measured speeds for both scenarios in the second part of the time slot. However, it is not clear how much we can rely on this simple method because in **RTMC-2** the two approaches produces different results already in the very beginning. Moreover, for the SUMO data, the difference in the travel times between the two methods is in a much lower range, where we finally observe a worse performance for the baseline method. Thus, in case of the RTMC data, it is hard to know which of the two methods actually gives more reasonable results in the first period.

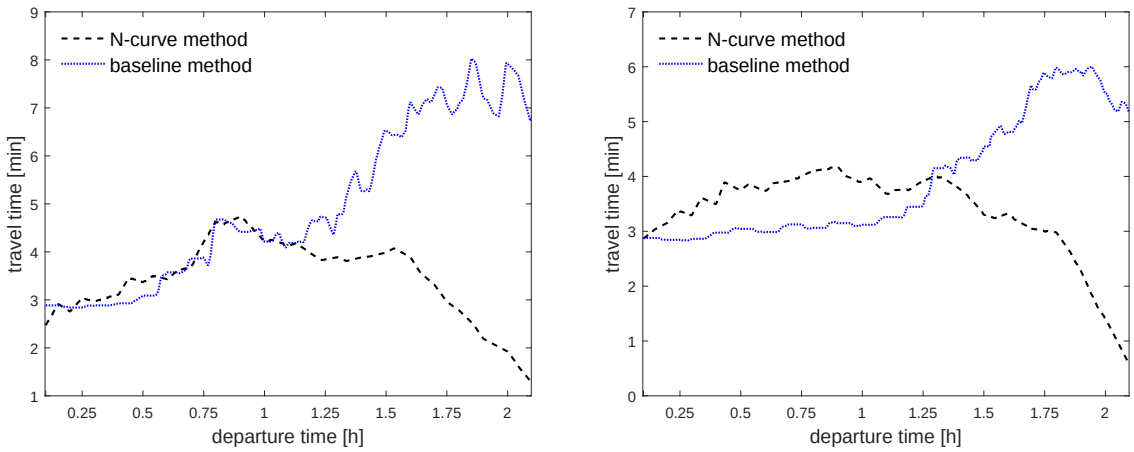

(a) **RTMC-1**. (b) **RTMC-2**.

Figure 5.13: **RTMC** data. Comparison of travel times between N-curve and baseline method.

Due to the uncertainty in the latest observations, we decided not to carry out further investigations on the reconstruction of travel times for the RTMC data in Chapter 6. However, we will still evaluate the goodness of our approaches for the prediction of aggregated data at loop detector positions, since these are the data which are actually available.

Chapter 6

Validation of calibration and prediction approaches

In this chapter, we validate the calibration and prediction approaches presented in Chapter 3 and Chapter 4. The whole analysis is carried out on both synthetic (SUMO) and real (RTMC) traffic data scenarios, which have been described in Chapter 5. Moreover, we also compare the performance of the different numerical methods introduced in Chapter 2.
Throughout the following study, we consider the homoskedastic approach, meaning that we do not differentiate in the noise hyper-parameter modeling between the two traffic regimes (see Section 3.2.3). Additionally, we apply the classical Gaussian kernel (see Equation (3.2.1)) without the integral extension presented in Section 3.2.2. Both choices are based on preliminary experimental tests, which showed a negligible performance gain for the advanced methods and the strikingly lower computational cost of the original approaches.
In all the experiments, we fix the maximum empty road velocity to $w_{max} = 200$km/h, thus reducing the number of calibration parameters, as pointed out in Remark 19.

6.1 Traffic calibration results

The calibration parameter $\theta = (V, C, R)$ appearing in the speed function (3.0.1) is not only dependent on the traffic scenario [PS15] but also on the choice of the traffic flow model, the numerical scheme and the statistical approach. As a short reminder, we compactly list in the following all the proposed possibilities which can be taken into account during the calibration. First, we need to decide for the macroscopic traffic flow model (LWR model (1^{st}) or GSOM (2^{nd})), for the numerical scheme (Godunov (Godu), HLL, HW) and, in the case of the Godunov scheme, the way to implement the boundary data (by density ρ or flux q). A summarized overview of all the options is given in Diagram 6.1.
Next, we have to decide between one of the below stated calibration approaches:

fundamental fit (FF), $\mathbf{L^2}$, KOH, Plumlee or MCMC.

As emphasized in the previous chapters, our final application are travel time reconstructions, thus it seems natural to us to consider the speed as our quantity of interest in the optimization. As a solver we use the local optimizer `fmincon` provided by MATLAB together with its default option *interior-point*. This solver aims to find a minimum of a non-linear multivariable

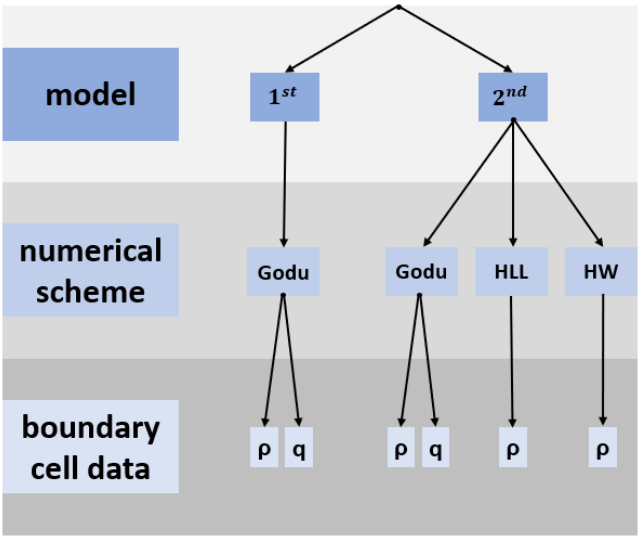

Figure 6.1: Overview of setting combinations defined in Chapter 2.

function. For applying `fmincon`, we need to specify admissible intervals for the parameters which are listed in Table 6.1.

	V	C	R	l_1	l_2	g
lower bound	55	10	150	10^{-3}	10^{-3}	10^{-3}
upper bound	150	100	600	3	L	5

Table 6.1: Upper and lower bounds for the calibration and hyper-parameters used in the calibration approaches. The upper bound for l_2 is given by the length of the road stretch L.

Moreover, we have to provide an initial guess, whose choice is typically crucial for the result of a local solver. Thus, in order to reduce the probability of being stuck in a local minimum, we compute the objective function beforehand for 200 randomly chosen θ values. Then, we decide for the parameter combination which leads to the best objective. Analogously, we do the same for GP the hyper-parameter determination. Since the computation time of the likelihood is strikingly faster (for a fixed θ) than the execution of the simulation code, we can easily propose here 500 randomly chosen values for the initial guess procedure. We point out that considering a global solver, for example `pso` (particle swarm optimization), does not lead to better results but to more computational effort. Finally, we remind that in the KOH and Plumlee approaches, we follow the principle of modularization [LBB09] by applying the 2-step optimization detailed in Section 3.4.2.
The optimization code is executed on the first 2 hours for each presented 3 hour scenario. The last hour will be only considered in Section 6.3 for the prediction tests. The piece-wise constant initial condition in the numerical scheme is taken from traffic data. However, to overcome the difficulty of precisely reconstructing the initial condition from loop measurements, we run the traffic model through an initialization phase of 6 minutes (see [FHS14]).
Next, in order to compare numerically the predictive accuracy of the results between the different proposed models with and without statistical approaches, we define an error metric

E which is given by the RMSE between the field and simulated speed data:

$$\mathbf{E} = \sqrt{\frac{1}{N}\sum_{i=1}^{N}\left|y^F(t_i,x_i) - y^M(t_i,x_i,\theta^*)\right|^2}. \tag{6.1.1}$$

Additionally, we are also interested in the performance between the field data and the kriging mean corrected simulated data y_c^M, defined as

$$y_c^M(t,x,\theta^*) = y^M(t,x,\theta^*) + m_N(t,x).$$

The related error is denoted by $\mathbf{E}_c$ which is obtained by replacing y^M with y_c^M in Equation (6.1.1).

Remark 40. Since the direct simulation output of the numerical schemes from Chapter 2 are the density ρ and w, we compute the average speed by the fundamental function (5.0.2), where the flow is given by $q = Q(\rho, w)$. This is also coherent with the speed data treatment for the field data.

Finally, in order to underline the benefit coming from the physical model, we define a third error, $\mathbf{E}_{GP}$, where this time the simulation y^M is completely replaced by the kriging mean of $y^F(\mathcal{X}_N) \sim \mathcal{N}(\bar{\mathbf{y}}_N, \mathbf{K}_N)$ with $\mathbf{K}_N = \sigma^2(\mathbf{C}_N + g\mathbf{I}_N)$ (see notation in Section 4.2.2.1). By this, the speed data are directly modeled by a GP without taking the physical model and its calibration parameter into account. We will see later that $\mathbf{E}_c$ always outperforms $\mathbf{E}_{GP}$.

Now, we are ready to present the calibration results for each traffic scenario:

SUMO-1A:

The calibration parameters computed by the $\mathbf{L^2}$, KOH and FF approach are summarized in Table 6.2, where we indicate in blue the parameter which will lead later to the best performance (see Table 6.3) and which will be referred to as the *best approach*.

	$\mathbf{L^2}$			KOH		
	V	C	R	V	C	R
$1^{st} - Godu - q$	71	78	315	78	33	357
$1^{st} - Godu - \rho$	**96**	**24**	**344**	96	22	356
$2^{nd} - Godu - q$	77	88	309	115	32	413
$2^{nd} - Godu - \rho$	140	40	344	146	40	352
$2^{nd} - HLL$	131	25	383	117	32	353
$2^{nd} - HW$	146	27	390	95	21	373

Table 6.2: **SUMO-1A**. Calibration results.
Fundamental fit approach: $\theta^* = (89, 34, 326)$. In blue: best approach.

First, we observe that we obtain different outcomes for the statistical approaches. Moreover, the two traffic flow models lead to parameters lying in completely different ranges. Especially the second order models with density boundary cell implementation lead to high V values. Additionally, comparing the second order Godunov, HLL and HW results, the parameters are

not necessarily close to each other although the schemes are considered to perform similarly. Indeed, in [WGV23] they lead to almost the same parameters, however the underlying traffic scenario was less congested and the road stretch only 1.1km long.
At this stage, the only possible statement which can be given is that there might exist an anti-correlated behavior between C and R, meaning that a calibration approach with higher C values tends to have a lower R value and vice-versa.
In order to emphasize the different ranges of the calibration parameters obtained by the approaches, we illustrate the fundamental diagrams for the $1^{st} - Godu - \rho$ and $2^{nd} - HW$ parameters in Figure 6.2 which reports the same data as Figure 5.2b. For the first order model, many flow data points are lying above the curve, whereas the speed data are following the shape better. In contrast, in the second order model the representation of the flow curve corresponding to $w = V^*$ is more convincing, whereas the maximum speed $V = 146$km/h is clearly overestimated. We point out that the first order model cannot capture the whole spread of the data in the congested regime due to its single curve. Thus, in order to come to a meaningful conclusion about the best performance, it will be necessary to compare the error metrics.

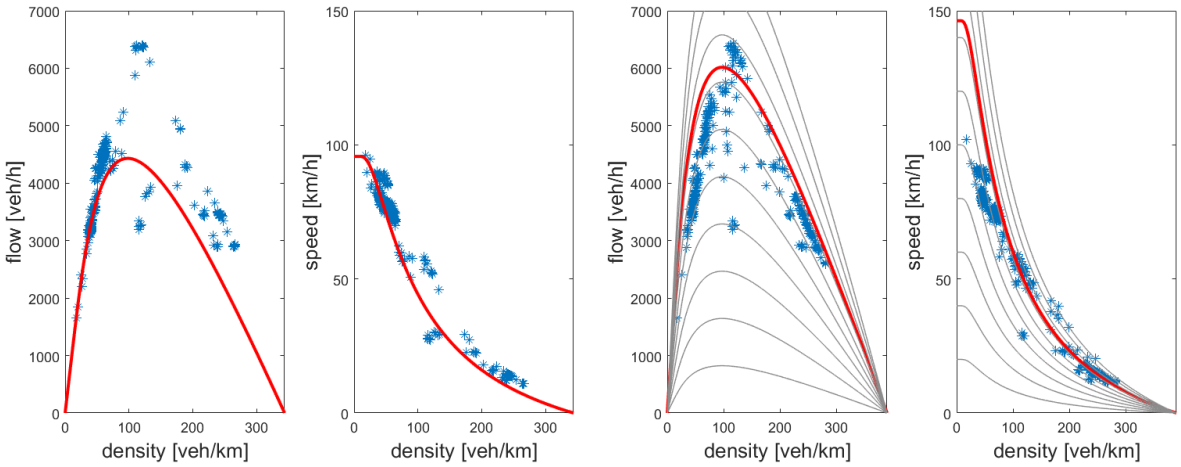

(a) $1^{st} - Godu - \rho : \theta^* = (96, 24, 344)$. (b) $2^{nd} - HW : \theta^* = (146, 27, 390)$.

Figure 6.2: **SUMO-1A**. Fundamental flow and speed diagrams. $\mathbf{L^2}$ approach.
In red: curves corresponding to $w = V^*$. Parameter in blue: best approach.

Next, we also apply the MCMC sampling approach to obtain a posterior probability distribution of the model parameters. In the following, we introduce the formulas used in the Metropolis Algorithm 2:
The prior $\pi(\theta)$ for $\theta = (V, C, R)$ is given by a multivariate normal distribution, thus it holds

$$\pi(\theta) \propto \frac{1}{\sqrt{|\Sigma_\theta|}} \exp\Big\{-0.5\,(\theta - \mu_\theta)^\top\, \mathbf{\Sigma}_\theta^{-1}\,(\theta - \mu_\theta)\Big\},$$

with mean $\mu_\theta = (96, 24, 344)$ and covariance matrix $\mathbf{\Sigma}_\theta = \mathrm{diag}(10^3, 10^3, 10^4)$.
The proposal distribution for $\hat{\theta}$ is also defined as a multivariate normal distribution, $\hat{\theta} \sim \mathcal{N}(\theta^*_{i-1}, \mathbf{\Sigma}^p)$, with covariance matrix $\mathbf{\Sigma}^p = \mathrm{diag}(5, 2, 15)$. To run the algorithm, we set the number of iterations to $N^{iter} = 6 \cdot 10^4$. It is a common approach to remove the first MCMC

outputs in order to reduce the dependence of the proposal distribution on the initial guess. We set this *burn-in phase* to $\frac{100}{6}\%$ of the N^{iter}-iterations. Then, in order to minimize autocorrelations, we reduce the sample chain to $\hat{N}_{ESS} = 103$ computed by using the multivariate effective sample size (ESS) function `multiESS` in the R package `mcmcse` [FHVD20]. For a graphical representation of the results, we consider in Figure 6.3 both the histograms and the 2-dimensional density contour plots, which are smoothed by a kernel density estimator. In the histogram graphics, we additionally add the probability density of the prior distribution for the calibration parameters (green line) and the kernel smoothed posterior distribution which is computed by the MATLAB command `fitdist` (red line). This operator fits a kernel probability distribution object to the sample data. The parameters for the kernel distribution object in MATLAB are chosen to be *normal* by default. Now, the previously assumed negative correlation between C and R becomes more evident, due to the clear diagonal shape of the $C - R$ contours. Moreover, it gets obvious that the $1^{st} - Godu - \rho$ KOH approach leads to completely different results in terms of C and R parameters. This is emphasized by the black vertical line which indicates the KOH optimization result and which lies out of the range of the MCMC samples. Indeed, the mode parameter of the MCMC approach is $\theta^m = (91, 17, 443)$. Finally, for all parameters we can conclude that the mostly flat prior distributions always differ from the more peaked or shifted posteriors.

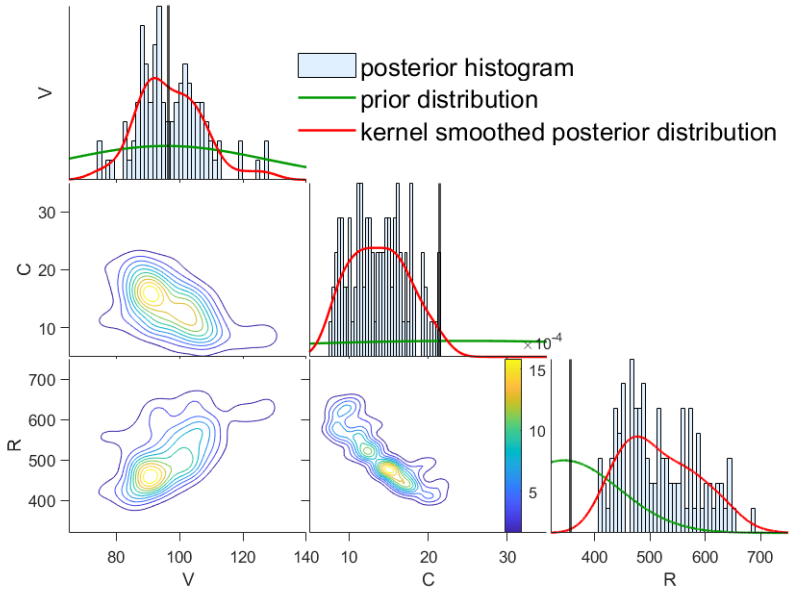

Figure 6.3: **SUMO-1A**. $1^{st} - Godu - \rho$. MCMC approach. Histograms and 2-dimensional density contour plots. Black vertical line: parameter estimate obtained by KOH approach.

Remark 41. We expect that the posterior probability depends mainly on the likelihood function because we assume that the given data are representative and the parameter boundaries are chosen properly [CMV15]. In other words, the choice of the prior distribution should not affect the posterior distribution in a sensitive way. In practice, the prior is often chosen for reasons of computational convenience [Hof09].

After dealing with the calibration parameters, it is now time to analyse the results of the

above defined error metrics in order to come to a well-founded decision for the best approach. In Table 6.3, we state the RMSEs for all possible combinations.

	FF		$\mathbf{L^2}$		KOH	
	$\mathbf{E}$	$\mathbf{E}_c$	$\mathbf{E}$	$\mathbf{E}_c$	$\mathbf{E}$	$\mathbf{E}_c$
$1^{st} - Godu - q$	12.53	5.33	11.76	4.47	13.41	3.46
$1^{st} - Godu - \rho$	10.99	5.41	**5.46**	**2.46**	6.05	2.93
$2^{nd} - Godu - q$	15.40	4.93	13.68	5.37	14.06	4.29
$2^{nd} - Godu - \rho$	10.92	4.91	9.40	2.82	9.77	3.76
$2^{nd} - HLL$	10.89	4.77	9.16	3.13	9.77	3.59
$2^{nd} - HW$	9.96	3.41	8.90	2.80	9.07	2.57

Table 6.3: **SUMO-1A** with $\theta^* = (96, 24, 344)$. $\mathbf{E}_{GP} = 4.53$.
Comparison of speed RMSE between calibration approaches. In blue: best approach.

First, we point out that all the values listed in the FF column rely on the same calibration parameter since the fundamental fit approach does not involve the mathematical model. Comparing its errors with the corresponding ones of the $\mathbf{L^2}$ and KOH approach, we detect almost everywhere a worse performance, which emphasizes the advantage of using the solution of the physical model. Therefore, we will discard the fundamental fit approach in the following analysis.
Second, we conclude that both errors $\mathbf{E}$ and $\mathbf{E}_c$ are noticeably worse when the implementation of the numerical schemes is done by flow boundary conditions instead of density ones.
Focusing now on the comparison between the $\mathbf{L^2}$ and KOH approach, we observe in all cases a lower simulation error for the former one. This is indeed not surprising, since the objective of this method is to minimize exactly the RMSE $\mathbf{E}$ (see Equation (3.4.1)). However, what is much more astonishing is that also after the bias correction the $\mathbf{L^2}$ corrected error $\mathbf{E}_c$ is often lower. Intuitively, one would have assumed a better performance for the KOH approach because it takes into account the bias in its modeling. This rather disappointing behavior of the KOH approach was also observed in [TW15]. They point out that the KOH modeling might lead to unreasonable estimates in contrast to the consistent and computationally more efficient $\mathbf{L^2}$ method. Also Gramacy remarks in [Gra20] that the flexibility in the KOH method could be even too high and the coupling of the bias and the mathematical model with θ might not work properly. This induces unrealistic results in the parameter identification process. Consequently, we are curious to see if the Plumlee approach for $1^{st} - Godu - \rho$ works better because the idea is to put more emphasis on the model in order to reduce confounding effects. We obtain $\theta^*_{plum} = (91, 29, 329)$, $\mathbf{E} = 5.30$ and $\mathbf{E}_c = 3.13$. Thus, it provides even a smaller simulation error than the $\mathbf{L^2}$ approach, whereas $\mathbf{E}_c$ is higher. As pointed out in Remark 27, the possible performance gain by the Plumlee approach comes together with much more computational effort, since we cannot exploit the Kronecker structure in the covariance modeling. Moreover, it often suffers from a bad approximation of the derivative of the simulator. Although it seems promising in this particular case, we will discard the approach later because the results are inconclusive. Additionally, also the MCMC mode parameter does not lead to a better performance ($\mathbf{E} = 15.67$, $\mathbf{E}_c = 3.02$), thus it should not be considered as a replacement for the other approaches. Instead, it can be seen as an additional source of information that provides insights into the posterior distribution of the

calibration parameters.
Next, we compare also the performance between the first and second order models, observing that the first order ones lead usually to lower errors. This observation was also made in [PHF+15, SMD21, WBG23], but it is in contrast with [WBGG22]. Intuitively, the second order model should reconstruct the speed better, at least before the bias correction, because it is equipped with more information. However, the lack of information on the additional w parameter and the increase in the dimension seem to have negative effects on the calibration process.
Finally, we want to point out that the performance of the second order schemes (Godu, HLL, HW) with density boundary conditions is very similar. Although the calibration parameters differ, the resulting errors are close to each other. However, the HW-scheme, seen as the cheapest and easiest-to-implement scheme among them, provides slightly better results.
As a conclusion, the simplest model $1^{st} - Godu - \rho$ together with the $\mathbf{L^2}$ approach seems to work best in this case. Before proceeding in the analysis for the other traffic scenarios, we also compare the parameters and error metrics when removing some loop detectors in the calibration process. More precisely, we choose

$$\text{loop} = \begin{cases} \text{S1, S6, S10} & \text{if } n_x = 3, \\ \text{S1, S4, S6, S8, S10} & \text{if } n_x = 5, \\ \text{S1, S2, S4, S6, S7, S9, S10} & \text{if } n_x = 7, \end{cases}$$

where n_x denotes the number of detectors. In Table 6.4 we observe a convergent behavior for θ when increasing the number of loops. Regarding the errors, an improvement of $\mathbf{E}_c$ and $\mathbf{E}_{GP}$ is clearly detectable, where the first one always beats largely the second one. In contrast, the simulation error $\mathbf{E}$ seems rather stable, thus it does not really benefit from the additional data information (except in the change from $n_x = 3$ to $n_x = 5$). Moreover, it is outperformed by $\mathbf{E}_{GP}$ when considering $n_x = 10$ detectors, which is not surprising since the model alone is not able to describe the traffic dynamics.

n_x	V	C	R	$\mathbf{E}$	$\mathbf{E}_c$	$\mathbf{E}_{GP}$
3	103	24	355	6.78	5.69	14.88
5	90	34	317	5.41	4.66	8.23
7	96	24	345	5.48	3.94	6.02
10	96	24	344	5.46	2.46	4.53

Table 6.4: **SUMO-1A**. $1^{st} - Godu - \rho$, $\mathbf{L^2}$ approach.
Calibration and speed RMSE results for different number of loop detectors $n_x \in \{3, 5, 7, 10\}$.

SUMO-1B:

We remind that in the construction of the artificial scenario **SUMO-1B** we include the ramps, which increases further the congestion with respect to **SUMO-1A**. Thus, we test two settings in the calibration: one where we run the code considering the ramp data and the other without this additional information. Table 6.5 provides the results for the calibration parameters. We remind that in the case of ramp consideration, there are no results available for $2^{nd} - HLL$ and $2^{nd} - HW$ since the ramp implementation in its demand and supply

notation (see Section 2.1.1) is only applicable for the Godunov scheme.
The $1^{st} - Godu - \rho$ seems to perform similarly in the two settings, however in all other cases no obvious pattern can be derived.

	$\mathbf{L^2}$			KOH		
	V	C	R	V	C	R
$1^{st} - Godu - q$	75	100	315	61	96	315
$1^{st} - Godu - \rho$	86	37	281	89	13	546
$2^{nd} - Godu - q$	109	15	441	68	15	405
$2^{nd} - Godu - \rho$	138	38	326	139	40	326
$2^{nd} - HLL$	-	-	-	-	-	-
$2^{nd} - HW$	-	-	-	-	-	-

(a) With ramp consideration.

	$\mathbf{L^2}$			KOH		
	V	C	R	V	C	R
$1^{st} - Godu - q$	75	100	274	73	42	310
$1^{st} - Godu - \rho$	**89**	**33**	**277**	105	24	301
$2^{nd} - Godu - q$	60	66	278	137	14	188
$2^{nd} - Godu - \rho$	74	11	345	123	21	337
$2^{nd} - HLL$	75	14	330	122	23	330
$2^{nd} - HW$	111	27	310	121	27	322

(b) Without ramp consideration.

Table 6.5: **SUMO-1B**. Calibration results.
Fundamental fit approach: $\theta^* = (90, 34, 330)$. In blue: best approach.

We thus focus on the error metrics in Table 6.6, getting to the same conclusion as for **SUMO-1A**: the fundamental fit approach is outperformed by $\mathbf{L^2}$ and KOH, the density boundary implementation leads mostly to a lower $\mathbf{E}$ and $\mathbf{E}_c$, and the $\mathbf{L^2}$ method delivers always (resp. often) a better simulation (resp. corrected simulation) error than the KOH one. Moreover, the performance between the second order models is similar, with sightly better results for the HW numerical method but still worse compared to the first order ones.
Next, comparing additionally the two versions (with and without ramp consideration), it seems that the second order schemes lead to lower errors when including the ramp data. However, the best $\mathbf{E}$ is provided by the rampless $\mathbf{L^2}$ setting with $1^{st} - Godu - \rho$, which delivers also a convincing $\mathbf{E}_c = 3.47$ value. We remark that the value $\mathbf{E}_c = 3.30$ of the version with ramps is almost 5% lower than the rampless one, however the simulation error $\mathbf{E} = 7.91$ is 29% higher. This justifies the blue highlighted version as our choice for the best approach.
In order to point out the slightly distinct performance between the two versions, we visualize in Figure 6.4 their space-time speed evolution and also their difference. In fact, there is only one striking deviation: at the border of the congested regime, indicated by the yellow color in Figure 6.4c. Otherwise, it is remarkable that the simpler implementation without ramps can capture the dynamics so well (or even better).

	FF		$\mathbf{L^2}$		KOH	
	E	$\mathbf{E}_c$	**E**	$\mathbf{E}_c$	**E**	$\mathbf{E}_c$
$1^{st} - Godu - q$	15.59	4.42	11.73	4.70	15.81	4.47
$1^{st} - Godu - \rho$	21.10	3.88	7.91	3.30	18.89	2.93
$2^{nd} - Godu - q$	16.78	4.43	13.32	4.00	13.51	4.16
$2^{nd} - Godu - \rho$	17.78	3.80	8.49	2.78	8.70	3.40
$2^{nd} - HLL$	-	-	-	-	-	-
$2^{nd} - HW$	-	-	-	-	-	-

(a) With ramp consideration.

	FF		$\mathbf{L^2}$		KOH	
	E	$\mathbf{E}_c$	**E**	$\mathbf{E}_c$	**E**	$\mathbf{E}_c$
$1^{st} - Godu - q$	12.21	3.92	11.29	4.52	13.36	4.15
$1^{st} - Godu - \rho$	24.24	3.59	**6.13**	**3.47**	6.73	4.24
$2^{nd} - Godu - q$	15.25	4.43	14.33	4.52	29.47	3.73
$2^{nd} - Godu - \rho$	23.18	3.98	9.77	4.49	10.01	4.59
$2^{nd} - HLL$	23.56	3.66	9.91	4.22	10.01	4.48
$2^{nd} - HW$	22.30	3.46	9.61	3.29	9.65	3.50

(b) Without ramp consideration.

Table 6.6: **SUMO-1B** with $\theta^* = (89, 33, 277)$. $\mathbf{E}_{GP} = 4.02$.
Comparison of speed RMSE between calibration approaches. In blue: best approach.

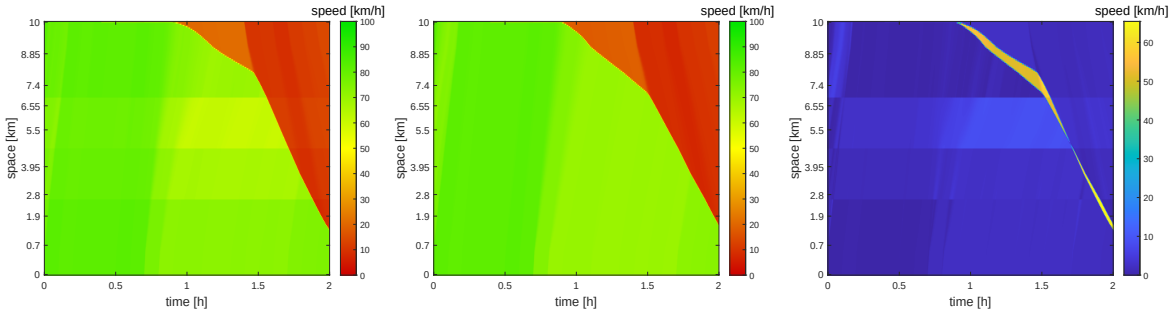

(a) With ramps. $\mathbf{E} = 7.91$. (b) Without ramps. $\mathbf{E} = 6.13$. (c) Speed difference.

Figure 6.4: **SUMO-1B**. $1^{st} - Godu - \rho$, $\mathbf{L^2}$ approach. Real data: see Figure 5.3.
Space-time speed visualization of the simulated speeds and their difference.

Remark 42. We point out that in contrast to the measured loop detector data, the numerical solution enables us to reconstruct the traffic quantities along a finer space-time dimension. This is also of interest from an application point of view, such as travel time estimation (see Section 6.2), since we obtain detailed information on traffic dynamics, illustrated as in Figure 6.4, compared to the coarse version as in Figure 5.3a.

SUMO-2:

The last synthetic scenario which remains to analyze is **SUMO-2**, characterized by a sudden change of the traffic regime due to a lane closure. In general, we observe for this case lower maximum densities R, which is reasonable due to less congestion. We refer to Table 6.19 in Appendix B for a summary of the obtained calibration parameters.
By Table 6.7, we detect the same behavior as for the two previous scenarios. Moreover we remark that this time the values for $\mathbf{E}_c$ are lying in a lower range compared to the two more congested situations. However, the simulation error of the best approach, $\mathbf{E} = 8.17$, is remarkably higher than before. Indeed, in this traffic scenario, the simulation cannot reflect the traffic dynamics properly since the model is not designed to capture the lane closure. Thus, **SUMO-2** represents a good toy example to emphasize the benefit of the bias modeling.

	FF		$\mathbf{L^2}$		KOH	
	E	$\mathbf{E}_c$	**E**	$\mathbf{E}_c$	**E**	$\mathbf{E}_c$
$1^{st} - Godu - q$	21.32	4.85	12.89	2.76	13.46	2.84
$1^{st} - Godu - \rho$	8.32	2.61	**8.17**	**2.34**	8.29	2.41
$2^{nd} - Godu - q$	22.18	4.06	15.09	3.94	13.46	3.00
$2^{nd} - Godu - \rho$	9.05	2.34	8.60	3.77	8.70	2.30
$2^{nd} - HLL$	9.02	2.31	8.65	2.30	9.39	2.46
$2^{nd} - HW$	8.92	2.34	8.65	2.32	9.22	2.43

Table 6.7: **SUMO-2** with $\theta^* = (93, 31, 300)$. $\mathbf{E}_{GP} = 5.76$.
Comparison of speed RMSE between calibration approaches. In blue: best approach.

This is also emphasized by the space-time speed illustration in the left and middle graphics of Figure 6.5. Indeed, in the corrected version we recognize the traffic jam created around loop detector S6, which is not visible in the pure simulation. Additionally, the speed profile for sensor S6 in the right column reinforces this last statement: the blue line (y^M) does not capture the sudden change in the traffic regime, however the green one (y_c^M) convinces, although we consider the homoskedastic modeling.

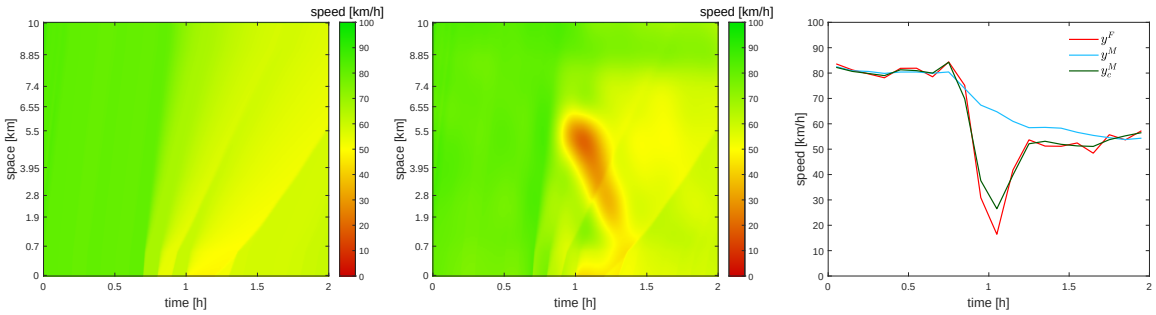

(a) Simulation. $\mathbf{E} = 8.17$. (b) Corrected simulation. $\mathbf{E_c} = 2.34$. (c) Speed profile.

Figure 6.5: **SUMO-2**. $1^{st} - Godu - \rho$, $\mathbf{L^2}$ approach. Real data: see Figure 5.4.
Space-time speed visualization and speed profile for loop detector S6.

Now, we continue our analysis by considering the real world highway traffic scenarios which include naturally on- and off-ramps. First, we present the results of the fundamental fit approach applied on the historical data of the year 2013. We remark that compared to the synthetic data, the resulting parameters do not depend only on the data of the considered day. Instead, we obtain a set of parameters for a whole traffic cluster. In Figure 6.6, we illustrate the shape of the fundamental curves for the two clusters, together with the historical RTMC data measured by detector S59. It seems that this approach leads to curves lying in the middle of the data cloud which can be explained by considering the mean speeds for each bin of the algorithm. We refer to Section 3.3 for a more detailed explanation of the fundamental fit approach applied on historical data. Additionally, cluster 1 is presented by a lower maximum speed V and higher maximum density R which is natural since it consists of the more congested scenarios. In a next step, we describe the results in more detail for the RTMC scenarios introduced in Section 5.2.

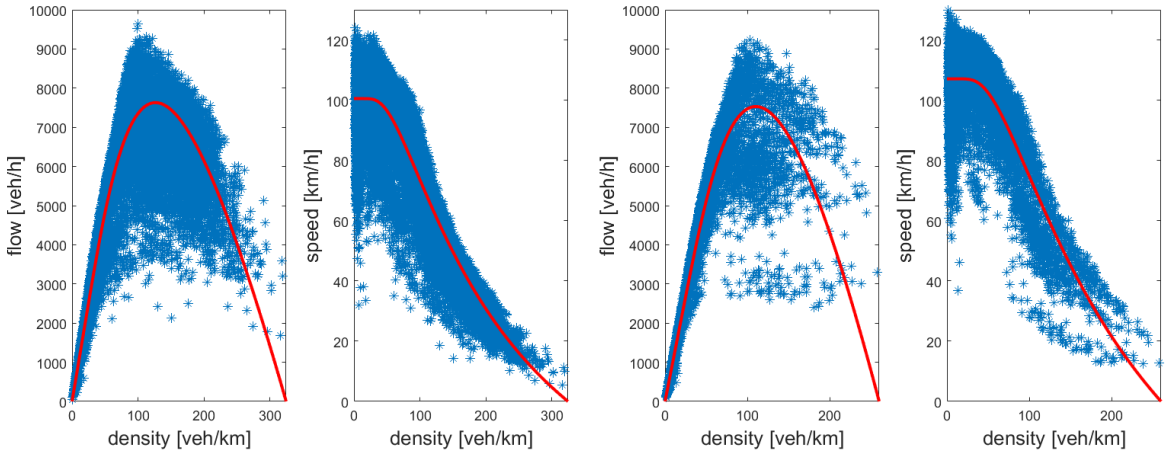

(a) Cluster 1: $\theta^* = (101, 59, 324)$. (b) Cluster 2: $\theta^* = (107, 80, 260)$.

Figure 6.6: Fundamental flow and speed diagrams with historical RTMC data measured by loop detector $S59$. Parameters obtained by fundamental fit approach based on [DGK+09]. In red: curves corresponding to $w = V^*$.

RTMC-1:

For **RTMC-1**, belonging to the first cluster, we state the calibration parameters in Table 6.8 in order to see if we observe differences compared to the synthetic scenarios. However, the parameter ranges still depend crucially on the choice of the model and calibration approach. This time, even the $\mathbf{L^2}$ calibration with $1^{st} - Godu - \rho$ leads to completely different results for the options with and without ramps.
By illustrating the fundamental flow and speed curves together with the measured data in Figure 6.7, we recognize again a good fit of the data on the speed curve for the $\mathbf{L^2}$ approach with $1^{st} - Godu - \rho$. However, the flow data lie mostly above the line which was also the case for **SUMO-1A** (see Figure 6.2). Moreover, the curves corresponding to $w = V^*$ for the second order model are again disappointing, since both the speed and flow data are completely underestimated, also in the free flow region. Even if considering the whole family of curves,

	$\mathbf{L^2}$			KOH		
	V	C	R	V	C	R
$1^{st} - Godu - q$	104	100	261	81	60	345
$1^{st} - Godu - \rho$	107	86	290	109	100	237
$2^{nd} - Godu - q$	79	91	260	69	24	355
$2^{nd} - Godu - \rho$	64	98	203	122	89	280
$2^{nd} - HLL$	-	-	-	-	-	-
$2^{nd} - HW$	-	-	-	-	-	-

(a) With ramp consideration.

	$\mathbf{L^2}$			KOH		
	V	C	R	V	C	R
$1^{st} - Godu - q$	127	32	379	150	34	212
$1^{st} - Godu - \rho$	**120**	**54**	**291**	111	59	272
$2^{nd} - Godu - q$	138	11	378	103	15	171
$2^{nd} - Godu - \rho$	78	56	221	90	17	510
$2^{nd} - HLL$	76	58	221	75	38	275
$2^{nd} - HW$	95	72	224	134	50	306

(b) Without ramp consideration.

Table 6.8: **RTMC-1**. Calibration results.
Fundamental fit approach (cluster 1): $\theta^* = (101, 59, 324)$. In blue: best approach.

several data points are not captured well in the congested regime.

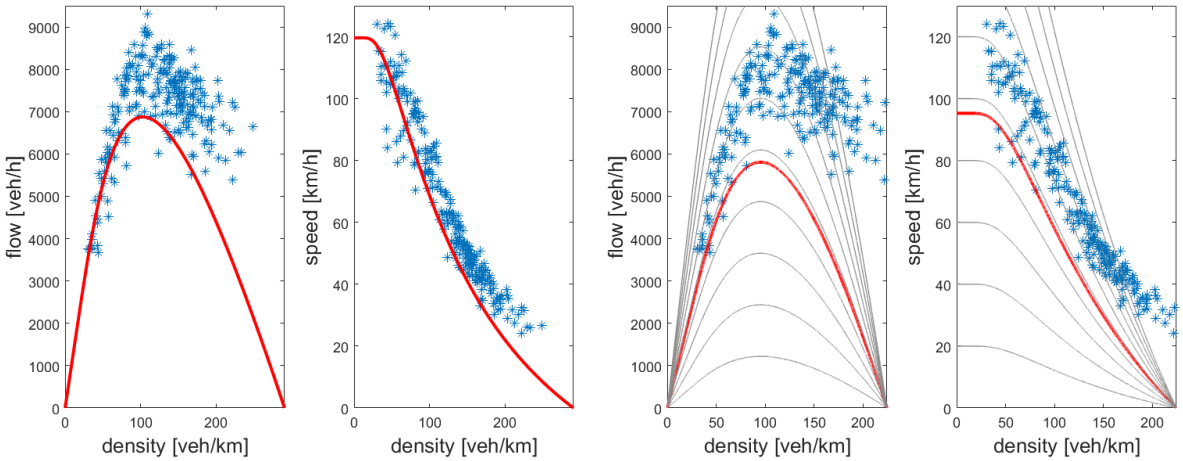

(a) $1^{st} - Godu - \rho : \theta^* = (120, 54, 291)$.

(b) $2^{nd} - HW : \theta^* = (95, 72, 224)$.

Figure 6.7: **RTMC-1** without ramp consideration. Fundamental flow and speed diagrams. $\mathbf{L^2}$ approach. In red: curves corresponding to $w = V^*$. Parameter in blue: best approach.

As before, we also verify if the MCMC calibration gives us more insight. For the multivariate normal distributed prior we pick $\mu_\theta = (120, 54, 291)$ and covariance matrix $\mathbf{\Sigma}_\theta = \text{diag}(10^3, 10^3, 10^4)$, whereas the proposal covariance matrix is given by $\mathbf{\Sigma}^p = \text{diag}(12, 5, 30)$. Then, after determining the effective sample size by `multiESS`, $\hat{N}_{ESS} = 436$ samples remain in the reduced chain. For this scenario, we can conclude that the $1^{st} - Godu - \rho$ KOH calibration parameter (without ramp consideration) coincides more with the mode parameter $\theta^m = (106, 65, 260)$ since the black vertical lines in the histograms in Figure 6.8 are closer to the peak of the posterior distributions. Moreover, the anti-correlated behavior between C and R appears again, underlined by the diagonal shape of their contour plots. Indeed, the thinned chain consists of quite high C values compared to relatively low maximum densities R. Finally, due to the nicely peaked red curves, we conclude that the posterior distribution gives us a clear indication which θ values explain the data best.

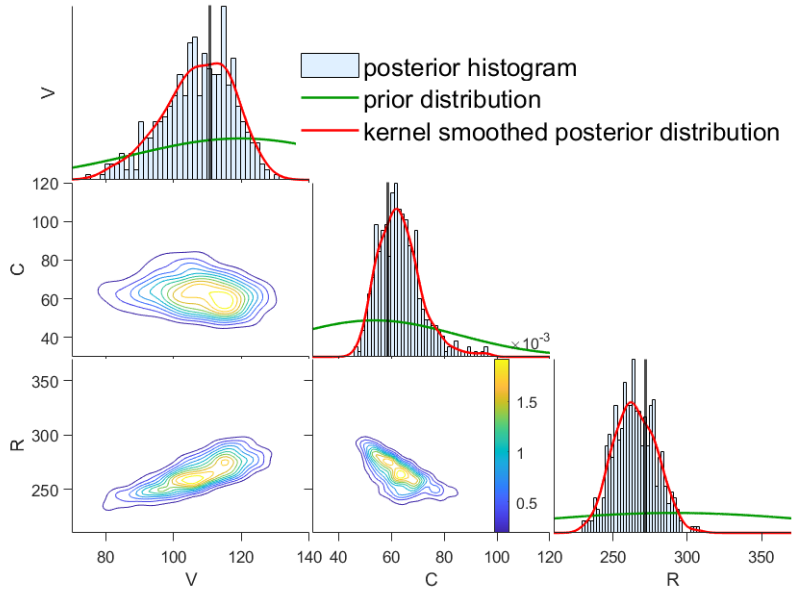

Figure 6.8: **RTMC-1**. $1^{st} - Godu - \rho$, MCMC approach. Histograms and 2-dimensional density contour plots. Black vertical line: parameter estimate obtained by KOH approach.

Next, looking at the more easily interpretable results of the error metric computations in Table 6.9, we detect first a bad performance of the simulation error of the fundamental fit approach, where we used the historical data. This result is not very surprising because the approach provides rather an average calibration parameter, suitable for all the scenarios in the cluster, but it does not emphasize specifically the dynamics of **RTMC-1**. Second, the error $\mathbf{E}_{GP} = 8.77$ is higher than any other corrected error $\mathbf{E}_c$ in the table. Consequently, there is indeed a benefit in the calibration process induced by the consideration of the solution of the physical model. Third, the bias correction seems to work better in the KOH approach compared to the results for the synthetic data. However, our aim is not to find an approach which leads only to a good corrected error, because this does not mean at the same time that the simulation code works reasonably. Indeed, the KOH approach gives almost everywhere a strikingly worse simulator error $\mathbf{E}$ compared to the $\mathbf{L^2}$ method. Thus, as already observed in **SUMO-1A** and in [TW15], the influence of the bias can be too large in the KOH modeling, leading to confounding effects. Moreover, also the Plumlee calibration ($\theta^*_{plum} = (81, 45, 434)$) fails to improve the results, since $\mathbf{E} = 19.65$ and $\mathbf{E_c} = 5.71$ ($1^{st} - Godu - \rho$ without ramp consideration) are visibly higher than the corresponding values in the $\mathbf{L^2}$ and KOH columns. This seems to be an example, where the Plumlee optimization suffers from the derivative approximations and from possible numerical issues in the covariance calculations.

Remark 43. For reconstructing traffic scenarios at loop detector positions and aggregated time intervals, a good working bias suffices to produce convincing results. However, a poorly working simulation typically causes problems when dealing with travel time predictions (in the future). This is why one should always choose an approach where both errors, $\mathbf{E}$ and $\mathbf{E}_c$, perform reasonably.

Next, we observe that the two errors are generally lying in higher ranges than the ones for the synthetic data. This can be an indication that measurement errors always remain when

	FF		$\mathbf{L^2}$		KOH	
	E	$\mathbf{E}_c$	**E**	$\mathbf{E}_c$	**E**	$\mathbf{E}_c$
$1^{st} - Godu - q$	25.64	6.44	21.40	7.90	30.19	6.26
$1^{st} - Godu - \rho$	17.62	6.62	15.61	4.86	14.46	5.56
$2^{nd} - Godu - q$	23.93	7.42	22.07	6.67	26.57	6.83
$2^{nd} - Godu - \rho$	15.21	5.47	11.54	6.11	14.04	5.37
$2^{nd} - HLL$	-	-	-	-	-	-
$2^{nd} - HW$	-	-	-	-	-	-

(a) With ramp consideration.

	FF		$\mathbf{L^2}$		KOH	
	E	$\mathbf{E}_c$	**E**	$\mathbf{E}_c$	**E**	$\mathbf{E}_c$
$1^{st} - Godu - q$	24.80	5.29	20.86	4.74	22.67	5.76
$1^{st} - Godu - \rho$	17.22	3.74	**15.58**	**4.71**	16.02	4.69
$2^{nd} - Godu - q$	28.46	7.45	21.41	5.83	26.07	5.80
$2^{nd} - Godu - \rho$	19.85	5.55	16.22	6.70	20.82	5.23
$2^{nd} - HLL$	19.75	5.56	16.81	6.77	17.90	5.73
$2^{nd} - HW$	18.99	5.50	16.77	6.58	17.68	5.57

(b) Without ramp consideration.

Table 6.9: **RTMC-1** with $\theta^* = (120, 54, 291)$. $\mathbf{E}_{GP} = 8.77$.
Comparison of speed RMSE between calibration approaches. In blue: best approach.

dealing with real traffic scenarios, also despite data pre-processing. In contrast, we expect the SUMO data to be perfect; still, an error persists since the macroscopic model cannot fit them perfectly. Moreover, it is remarkable again that the errors are rather similar for the second order model with density boundary conditions, although the calibration parameters do not coincide. By the space-time speed evolution illustrations in Figure 6.9, we aim to emphasize the slightly different performances between the $2^{nd} - Godu - \rho$ and $2^{nd} - HW$ simulation applied on the same calibration parameter.

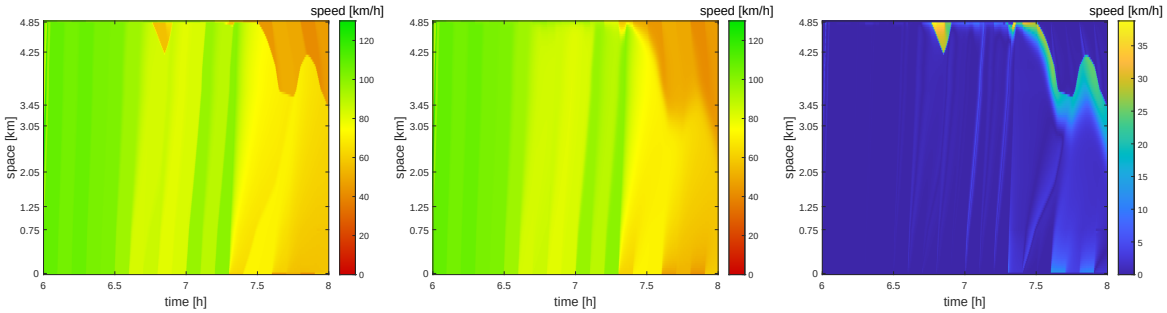

(a) $2^{nd} - Godu - \rho$. $\mathbf{E} = 19.85$. (b) $2^{nd} - HW$. $\mathbf{E} = 18.99$. (c) Speed difference.

Figure 6.9: **RTMC-1** without ramp consideration. Real data: see Figure 5.11.
Space-time speed visualization of the simulated data and their difference. Calibration parameter chosen from fundamental fit approach: $\theta^* = (101, 59, 324)$.

The behavior is similar but the HW scheme is more diffusive along the transition between the two traffic regimes. Additionally, the Godunov method creates a slight congestion at the end of the road stretch after 45 minutes, which is not observed in reality (see Figure 5.11a). Finally, we conclude that the best approach is again the simplest combination, namely the $\mathbf{L^2}$ approach without ramp consideration and with $1^{st} - Godu - \rho$. Thus, also in this scenario, the additional information provided by ramps does not seem necessary to improve the simulations.

In a very last step, we conduct the same experimental test as for **SUMO-1A** by reducing the number of loop detectors. We consider

$$\text{loop} = \begin{cases} \text{S54, S57, S61} & \text{if } n_x = 3, \\ \text{S54, S56, S59, S61} & \text{if } n_x = 4, \\ \text{S54, S1706, S57, S1707, S60, S61} & \text{if } n_x = 6. \end{cases}$$

Analysing Table 6.10, we cannot observe a convergence for the parameters this time. Even if we consider 6 or 8 loops, the parameters do not lie in the same ranges. However, for the error metrics, we make a similar observation as before: the more information we use in the calibration, the lower the errors. Again, especially $\mathbf{E}_c$ and $\mathbf{E}_{GP}$ benefit from the augmentation of the amount of data, whereas the simulation error $\mathbf{E}$ remains more stable. Finally, we point out that $\mathbf{E}_c$ outperforms $\mathbf{E}_{GP}$ except in the case $n_x = 3$.

n_x	V	C	R	$\mathbf{E}$	$\mathbf{E}_c$	$\mathbf{E}_{GP}$
3	118	46	369	18.58	16.16	15.25
4	127	53	303	16.18	13.08	13.41
6	101	83	259	15.77	9.62	10.93
8	120	54	291	15.58	4.71	8.77

Table 6.10: **RTMC-1**. $1^{st} - Godu - \rho$, $\mathbf{L^2}$ approach without ramp consideration.
Calibration and speed RMSE results for different number of loop detectors $n_x \in \{3, 4, 6, 8\}$.

RTMC-2:

To complete this section, it remains to consider **RTMC-2**. The list of calibration parameters can be found in Table 6.19 in Appendix B. It is surprising that the values of maximum density R are often higher than the ones in the previous scenario, although this case belongs to the cluster with less congestion. This time however, the second order model with the implementation of density boundary conditions leads in the $\mathbf{L^2}$ approach to almost the same parameters, which has never been observed before.
Next, the error Table 6.11 does not provide many new insights except that we notice a very bad behavior of the KOH simulation in the first order model with ramp consideration. In contrast, the $1^{st} - Godu - \rho$ $\mathbf{L^2}$ approach with ramps performs nicely, also compared to the version without ramps. This shows again that the KOH calibration method is more error-prone and less reliable. Additionally, we remark that **RTMC-2** is the only scenario where the best approach takes the ramp information in the simulation into account. It seems that the additional data provided by the ramp detectors have a positive impact on scenarios with less dense traffic occurrences, while in congested situations the loop detector measurements on the

main road seem to be sufficient. Indeed, the simulation error $\mathbf{E} = 12.74$ in the $2^{nd} - Godu - \rho$ $\mathbf{L^2}$ approach with ramps is lower than any other one computed in a rampless version.

	FF		$\mathbf{L^2}$		KOH	
	E	$\mathbf{E}_c$	**E**	$\mathbf{E}_c$	**E**	$\mathbf{E}_c$
$1^{st} - Godu - q$	32.43	4.94	21.68	10.17	51.64	5.30
$1^{st} - Godu - \rho$	18.66	5.00	**13.76**	**2.62**	51.65	5.00
$2^{nd} - Godu - q$	24.13	7.93	22.03	8.17	23.08	4.90
$2^{nd} - Godu - \rho$	14.21	5.52	12.74	4.44	15.26	2.53
$2^{nd} - HLL$	-	-	-	-	-	-
$2^{nd} - HW$	-	-	-	-	-	-

(a) With ramp consideration.

	FF		$\mathbf{L^2}$		KOH	
	E	$\mathbf{E}_c$	**E**	$\mathbf{E}_c$	**E**	$\mathbf{E}_c$
$1^{st} - Godu - q$	26.19	3.80	21.92	3.48	21.97	4.91
$1^{st} - Godu - \rho$	15.83	4.47	15.10	5.24	26.90	4.80
$2^{nd} - Godu - q$	29.37	3.62	20.47	4.05	22.20	4.88
$2^{nd} - Godu - \rho$	16.63	4.61	14.75	4.17	18.89	4.52
$2^{nd} - HLL$	16.52	4.56	14.75	4.15	18.71	4.48
$2^{nd} - HW$	16.18	4.67	14.74	4.17	17.41	2.44

(b) Without ramp consideration.

Table 6.11: **RTMC-2**. $1^{st} - Godu - \rho$ with $\theta^* = (99, 92, 298)$. $\mathbf{E}_{GP} = 5.35$.
Comparison of speed RMSE between calibration approaches. In blue: best approach.

To conclude, we summarize the main observations obtained by the analysis of all traffic scenarios above:

1. The calibration parameters are highly scenario dependent.

2. The implementation of density boundary conditions leads in general to lower speed simulation errors.

3. The first order model is sufficient for a reasonable traffic speed reconstruction.
   Possible but rare performance gains by second order models can be mostly compensated by the bias modeling.

4. The $\mathbf{L^2}$ approach is not only the most efficient but also the most consistently performing one among scenarios.

5. The contribution of ramp data remains unclear. In congested cases it seems sufficient to use only main loop detector measurements.

6. The solution of the physical model improves the speed reconstruction results.

6.2 Traffic estimation results

After having presented the calibration results on traffic reconstruction for every single scenario in detail, we continue by analyzing the traffic estimation outcomes. As explained in Chapter 4, by traffic estimation we denote the reconstruction of travel times for vehicles which ended their trip in the past. This "past" period consists of the 2 hours during which the calibration methods are executed. To this end, we consider 505 fictive trajectories, starting every 10 seconds after an initialization period of 6 minutes. The last vehicle departs after 90 minutes, such that the reconstruction time window covers its whole trip. Then, in order to compare the simulated travel times with the real ones, we use the travel time error metric, stated in Equation (4.0.1). Following the previous section, we also define a corrected travel time error, denoted by $\mathbf{E}_c^\tau$, which is obtained by replacing $\hat{\tau}$ with the result of Algorithm 3 when considering the corrected simulation as an input. In the same way, by using the pure GP constructed data, we define the error $\mathbf{E}_{GP}^\tau$.
In the following, we detail the results for the best approach of each SUMO scenario. We point out that we cannot give insights in the RTMC traffic estimation performances since there are no reasonable reference data available.

SUMO-1A:

In Figure 6.10 we compare the travel time profiles computed by the simulation, corrected simulation and N-curve method with the reference data.

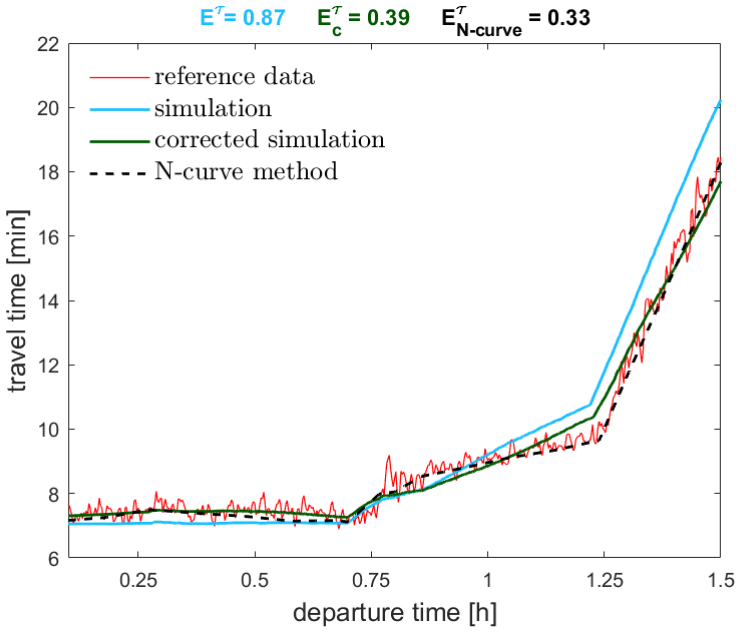

Figure 6.10: **SUMO-1A**. $1^{st} - Godu - \rho$, $\mathbf{L^2}$ approach. $\mathbf{E}_{GP}^\tau = 0.70$, $\mathbf{E}_{\text{baseline}}^\tau = 0.66$. Travel time estimation results.

As concluded in Chapter 5, the N-curve method delivers convincing results in the synthetic data cases. Indeed, it performs slightly better than our approach since $\mathbf{E}_{\text{N-curve}}^\tau = 0.33 < 0.39 = \mathbf{E}_c^\tau$. However, we have also seen before that this approach can fail, especially when

dealing with real world data (see Figure 5.13). Considering now the pure simulation result, we observe an underestimation of the speed towards the end of the considered time window. However, the bias corrected version adjusts this deviation. This better performance goes along with the previous observations where also $\mathbf{E}_c$ outperformed $\mathbf{E}$. Moreover, we point out that the results for both the pure GP and baseline method are beaten by the corrected simulation since $\mathbf{E}^{\tau}_{GP} = 0.70 > \mathbf{E}^{\tau}_{\text{baseline}} = 0.66 > \mathbf{E}^{\tau}_{c} = 0.39$. This observation will hold also for the following SUMO scenarios, which justifies again the consideration of the physical model.
Next, we conduct the same experimental test as in the calibration section, namely we reduce the number of loop detectors and compare the performance between the corrected simulation, the GP and baseline method. Figure 6.11 emphasizes that the corrected simulation is able to reconstruct reasonable travel times even when only a few data are available, while the baseline and pure data based GP method clearly suffer from this. The exact values of the travel time errors are given in Table 6.12.

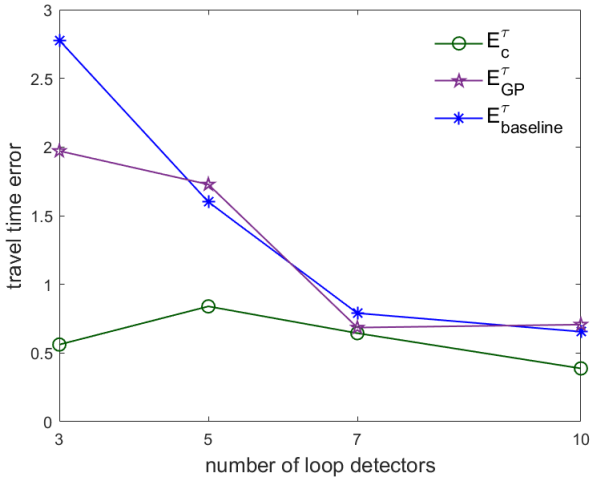

Figure 6.11: **SUMO-1A**. $1^{st} - Godu - \rho$, $\mathbf{L^2}$ approach. Travel time estimation results.

n_x	$\mathbf{E}^{\tau}_{c}$	$\mathbf{E}^{\tau}_{GP}$	$\mathbf{E}^{\tau}_{\text{baseline}}$
3	0.56	1.97	2.78
5	0.84	1.73	1.60
7	0.64	0.69	0.79
10	0.39	0.70	0.66

Table 6.12: Travel time errors illustrated in Figure 6.11.

SUMO-1B:

The travel time profiles in Figure 6.12 for **SUMO-1B** resemble the ones of **SUMO-1A**, except that the travel time is in average higher due to the ramp contribution. Additionally, we observe that all the illustrated approaches perform worse than before, especially the pure simulation whose error increases by 150%. Again, the N-curve approach provides the lowest travel time error.

SUMO-2:

The last scenario to present is the one with the sudden change in the traffic regime which is well visible in Figure 6.13. As already emphasized before, the simulation fails to capture this jump, therefore it is not surprising that the travel time profile does not follow the red curve of the reference data. We remark that the scale of the y-axis (travel time in minutes) is

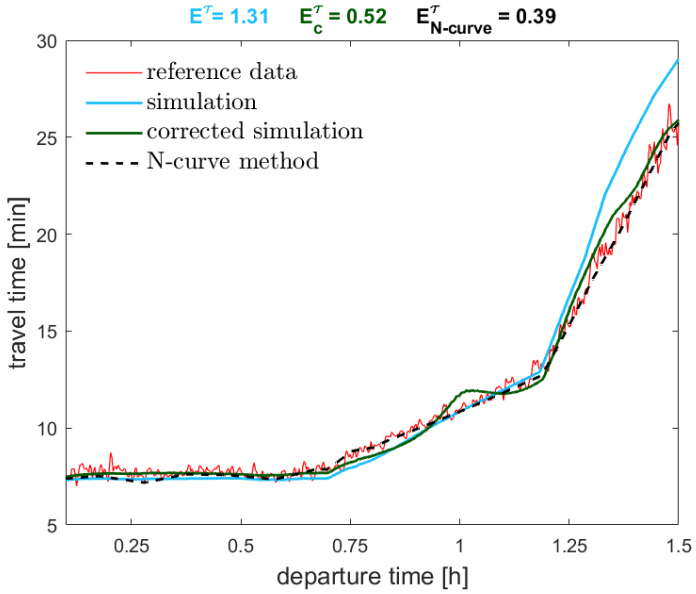

Figure 6.12: **SUMO-1B**. $1^{st} - Godu - \rho$, $\mathbf{L^2}$ approach. $\mathbf{E}^{\tau}_{GP} = 0.53$, $\mathbf{E}^{\tau}_{\text{baseline}} = 0.67$. Travel time estimation results.

much lower than in the previous cases, therefore an error of $\mathbf{E} = 1.05$ is comparatively high. Finally, we point out that **SUMO-2** is the only scenario where the corrected simulated version outperforms slightly the N-curve method which mostly underestimates the travel times in this particular case.

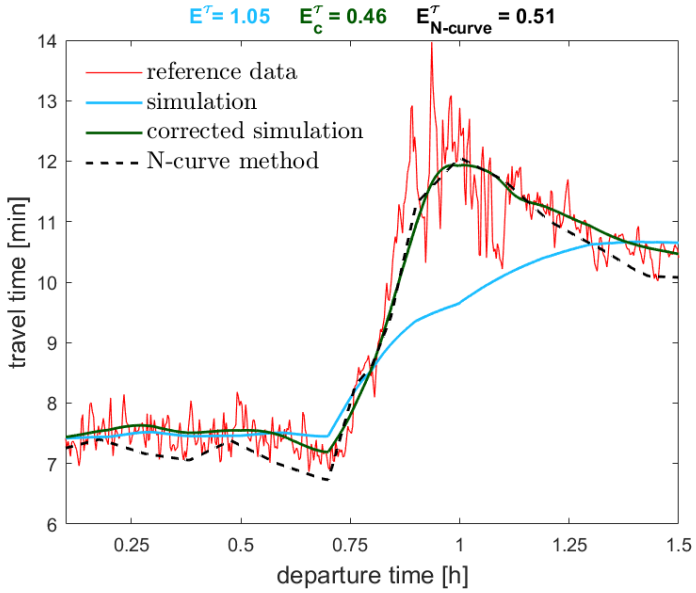

Figure 6.13: **SUMO-2**. $1^{st} - Godu - \rho$, $\mathbf{L^2}$ approach. $\mathbf{E}^{\tau}_{GP} = 0.81$, $\mathbf{E}^{\tau}_{\text{baseline}} = 0.62$. Travel time estimation results.

6.3 Traffic prediction results

In the last part of this chapter, we present the traffic prediction results which can be divided in two parts:

1. The prediction of future boundary loop detector data for running the simulation code.
2. The computation of predicted travel times for comparison with the reference data.

Again, the second part is only possible for the synthetic data set. In the first part, we have the option between the following approaches:

DTW, LSTM, pure GP, MOO and constant boundary data,

where the DTW and LSTM method can only be applied if historical data are available, namely in the RTMC data setting. In the rather naive case of treating the boundary conditions as constant, we fix the value to the last recorded measurement before the beginning of the prediction window.
Due to the results obtained in Section 6.1, we focus in the numerical schemes on the implementation of density boundary conditions. Therefore, it is natural to predict density data by the above listed prediction approaches. Moreover, we point out that they lead to exactly the same bias correction within a scenario because the computation of the (future) bias kriging mean is based only on the data in the past (2 hours) and not the choice of the prediction method. However, the methods naturally differ in their predicted (corrected) simulations, due to the difference in their boundary data. We will see that it is indeed important to define the best approach as the one with a low $\mathbf{E}$ and not only $\mathbf{E}_c$ value, because the prediction results rely heavily on the goodness of the simulation (see Remark 43).
Next, we provide more details for the MOO approach, which is executed by the MATLAB function `paretosearch` considering 100 points on the Pareto front. For the determination of the number of virtual time points which are used in the second objective function, we differentiate between the time and space dimension: for the first one, we double the size of the 6 minute aggregated data in the 3 hours, thus sampling $\frac{180}{6} \cdot 2 = 60$ points from the uniform distribution. The virtual space points however are not sampled, instead they match exactly the position of the main loop detectors. We observe that sampling the space points lead to worse results in our case. As pointed out in Remark 34, it is certainly possible to improve the choice of these virtual points, however for our purpose the simple and easy-to-implement proposed version above seems to perform sufficiently well.
Next, we also want to point out that in the pure GP and MOO approaches, the kriging mean formula can lead to negative or too high densities. Such unrealistic cases can be prevented by choosing suitable hyper-parameter bounds, which is often a challenging task [BG21]. Instead, in the MOO method we can ensure reasonable densities by penalizing the second objective f_2^{obj} whenever $m_N^y(\tilde{t}, \tilde{x}) < 0$ or $m_N^y(\tilde{t}, \tilde{x}) > R$.

As a last prerequisite before presenting the prediction results, we define the error metrics that we need to compare numerically the above listed approaches. First, we are interested in the goodness of the predicted density boundary data, thus the error is defined as

$$\hat{\mathbf{E}}_B^\rho = \frac{1}{2\hat{n}_{\hat{t}}} \left\| y_\rho^F(\hat{\mathcal{X}}_{\hat{N}_B}) - \hat{\mathbf{y}}_\mathbf{B} \right\|_F,$$

where $y_\rho^F(\hat{\mathcal{X}}_{\hat{N}_B})$ (resp. $\hat{\mathbf{y}}_\mathbf{B}$) denotes the aggregated measured (resp. predicted) density data at $2\hat{n}_{\hat{t}}$ predicted boundary observation points. We remind that the future time window consists of 1 hour, thus $\hat{n}_{\hat{t}} = 10$ in our case of 6 minute aggregated data. Next, after the simulation has been performed, we also compare the simulated speed with the available coarse field data at loop detector positions and aggregated future times which leads to the metric $\hat{\mathbf{E}}$, given by

$$\hat{\mathbf{E}} = \sqrt{\frac{1}{\hat{n}_{\hat{t}} \cdot n_x} \sum_{i=1}^{\hat{n}_{\hat{t}} \cdot n_x} \left| y^F(\hat{t}_i, \hat{x}_i) - y^M(\hat{t}_i, \hat{x}_i, \theta^*) \right|^2},$$

where n_x denotes the number of loop detectors. Again, replacing y^M by y_c^M, we obtain the corrected version of this error, denoted by $\hat{\mathbf{E}}_c$. These metrics should give us an indication for a good travel time prediction, because we assume that the lower $\hat{\mathbf{E}}$ or $\hat{\mathbf{E}}_\mathbf{c}$ the better the predictions. As another comparison, we compute the two speed metrics using real measured boundary data $y_\rho^F(\hat{\mathcal{X}}_{\hat{N}_B})$ in the simulation. This will be referred to as the *oracle boundary case*.
Finally, in the SUMO data case, we will also compare the travel time metrics $\mathbf{E}^\tau$ and $\mathbf{E}_c^\tau$ with the reference data. This time the metric considers the vehicles departing between $t = 90$min and $t = 150$min which leads to 361 trajectories.

SUMO-1A:

Starting with the first SUMO scenario, we highlight in Table 6.13 the lowest value for each considered error metric in bold. First, we observe that, compared to the previous estimation section, the difference between the predicted speed errors $\mathbf{E}$ and $\mathbf{E}_c$ are negligible, meaning that the bias correction in the future time slot has almost no or even a negative impact. Second, the MOO density boundary RMSE $\hat{\mathbf{E}}_B^\rho$ outperforms clearly the other ones. We remind that this value is obtained by the knee-point heuristic, illustrated in Figure 6.14a. Although the heuristic does not lead to the lowest possible value (see right column of the Figure), the performance is acceptable since only a few points on the Pareto front undercut this point. Third, unlike expectations, a good density boundary prediction does not necessarily lead to the lowest speed $\hat{\mathbf{E}}$ value, which is emphasized by the oracle boundary case. Here it holds $\hat{\mathbf{E}}_B^\rho = 0$ but $\hat{\mathbf{E}}$ is outperformed by the one of the pure GP method. This underlines the difficulty when dealing with different traffic quantities. Since the numerical scheme is written in terms of densities, a good reconstruction of the density does not necessarily result in a good speed estimation. Similarly, if using the flow boundary conditions, we can nicely reconstruct the traffic flow but, as seen in Section 6.1, it performs poorly for our case, namely when the speed is the quantity of interest. However in contrast to our assumption, the lowest $\hat{\mathbf{E}}$ value is no indication for the best travel time prediction result: the MOO approach outperforms the other cases although its coarse speed reconstruction is worse. As a final remark, we point out that the naive approach keeping the boundary values constant fails completely. Every error metric is largely beaten by the other strategies.

	pure GP	MOO	constant boundary	oracle boundary
$\hat{\mathbf{E}}_B^\rho$	41.88	**31.41**	62.30	0
$\hat{\mathbf{E}}$	20.68	23.87	33.06	22.14
$\hat{\mathbf{E}}_c$	**20.28**	23.39	32.58	21.25
$\mathbf{E}^\tau$	2.30	**1.75**	8.81	3.50
$\mathbf{E}_c^\tau$	2.48	1.83	8.59	3.26

Table 6.13: **SUMO-1A**. $1^{st} - Godu - \rho$, $\mathbf{L^2}$ approach.
Prediction RMSE and travel time results for different prediction approaches.

Next, in order to understand the rather disappointing performance of the oracle boundary case, we illustrate in Figure 6.14b the profiles for the results of the MOO and oracle boundary method, where $\mathbf{E}^\tau_{\text{oracle}}$ represents the corrected version of the oracle boundary case error. By the black vertical line, we highlight the starting point of the 361 considered trajectories, used in the travel time error computation. Naturally, the oracle boundary curve and corrected simulated curve coincide in the past because the simulation is executed with the same boundary data. Towards the future, the oracle boundary case starts to overestimate the travel times, thus it shows exactly the same behavior as the simulation in Figure 6.10. In contrast, the (corrected) simulation both under- and overestimates the speed which leads therefore in average to a lower RMSE. Due to the increasing uncertainty, it is clear that the correction tends to go back to the pure simulation, which in turn explains the behavior of the oracle boundary curve. The graphic depicts nicely this convergent behavior, thus also the two errors $\mathbf{E}^\tau$ and $\mathbf{E}_c^\tau$ are quite similar and they would get even closer if we moved the first considered vehicle trajectory more towards the future.

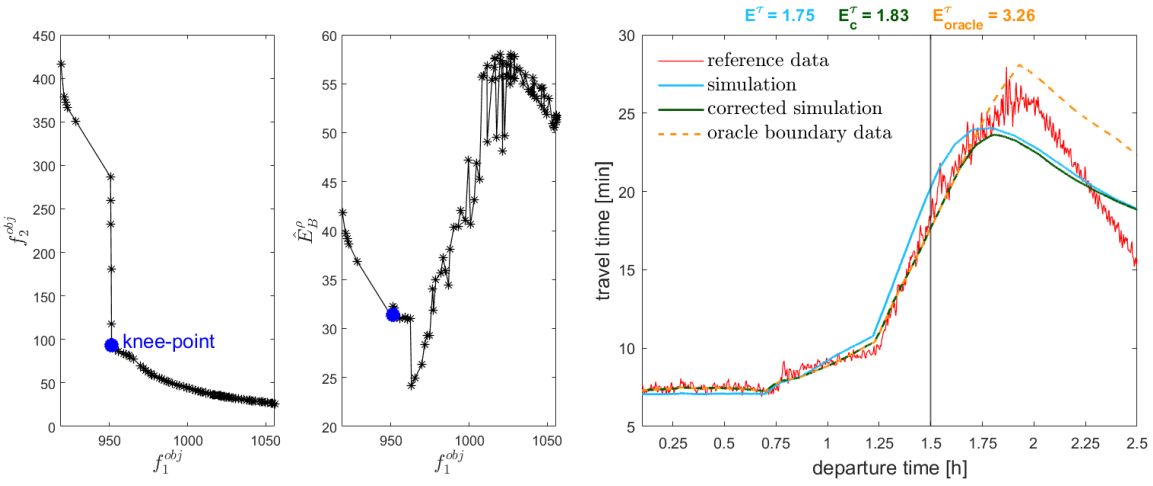

(a) Knee-point. (b) Predicted travel time.

Figure 6.14: **SUMO-1A**. $1^{st} - Godu - \rho$, $\mathbf{L^2}$ and MOO-approach.
Travel time prediction results.

Remark 44. We point out that in practice, the right graph in Figure 6.14a is not available because the metric $\hat{\mathbf{E}}_B^{\rho}$ involves the (unknown) future boundary density data. The illustration serves to showcase the knee-point heuristic's performance.

SUMO-1B:

SUMO-1B represents our most involved case because the ramp contributions increase the traffic volume tremendously. This scenario is especially difficult to predict because the occurrence of the congestion in the left boundary loop detector starts in the prediction window (see Figure 5.3a), which is impossible to forecast. Figure 6.15b emphasizes this by several underestimated future travel times for the converging blue and green curves. Thus, it is not surprising that the predicted boundary values in Table 6.14 are lying in a higher range than in the previous case. We observe that the pure GP and MOO approaches lead almost to the same error, also regarding the speed RMSE. Moreover, this is the only scenario where the pure GP gives the best performance for the travel time prediction errors $\mathbf{E}^{\tau}$ and $\mathbf{E}_c^{\tau}$. Since this artificial scenario represents an extreme case, it remains unclear if these results are very meaningful. Besides, an average error of $\mathbf{E}^{\tau} = 1.71$ minutes, obtained by the MOO approach, is still acceptable in situations of very dense traffic.
Regarding the case of constant boundary data, we come to exactly the same conclusion as before: it delivers clearly the worst results. Moreover, for the oracle boundary case, we obtain this time very good speed predictions, but again not satisfying travel time errors. As before, this can be traced back to the convergence towards the pure simulation, which underestimates the speed (see Figure 6.12). Thus, the travel times are overestimated, which finally leads to this comparatively high errors. Of course, the question remains why the simulation tends to show this behavior. One possible answer might be the overall speed quantity problem which is detailed in the beginning of Chapter 5: calculating the speed by the fundamental equation $v = \frac{q}{\rho}$ certainly also induces errors. However, using the arithmetic or even the harmonic versions do not lead in general to better results.

	pure GP	MOO	constant boundary	oracle boundary
$\hat{\mathbf{E}}_B^{\rho}$	192.53	**192.50**	220.50	0
$\hat{\mathbf{E}}$	16.45	16.20	29.92	10.04
$\hat{\mathbf{E}}_c$	16.28	16.02	29.90	**9.92**
$\mathbf{E}^{\tau}$	1.55	1.71	10.78	3.50
$\mathbf{E}_c^{\tau}$	**1.31**	1.89	10.12	2.89

Table 6.14: **SUMO-1B**. $1^{st} - Godu - \rho$, $\mathbf{L^2}$ approach.
Prediction RMSE and travel time results for different prediction approaches.

To conclude, we mention the graphical results for the knee-point algorithm in Figure 6.15a. The heuristic convinces also in this setting, it leads almost to the best possible option.

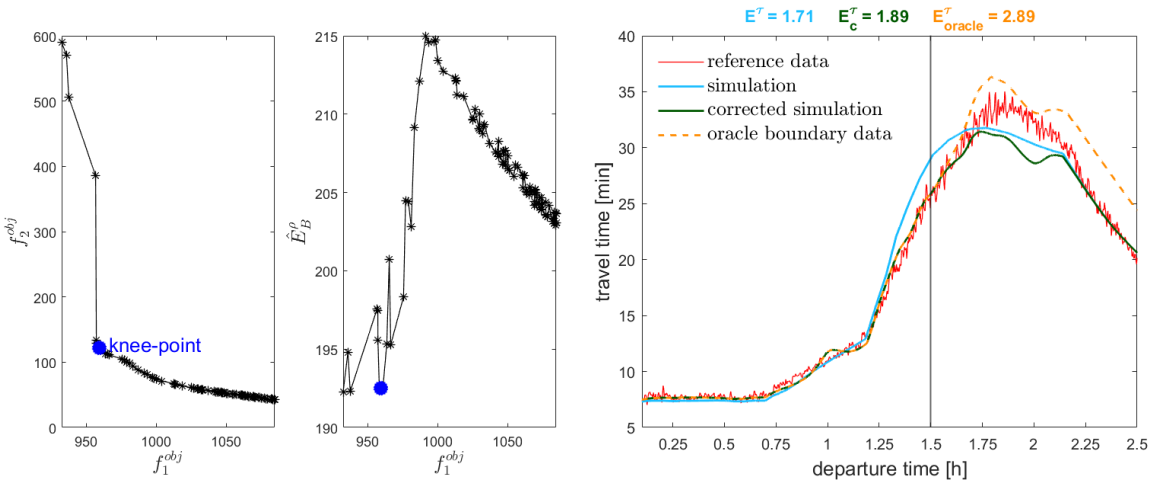

(a) Knee-point. (b) Predicted travel time.

Figure 6.15: **SUMO-1B**. $1^{st} - Godu - \rho$, $\mathbf{L^2}$ and MOO-approach.
Travel time prediction results.

SUMO-2:

Comparing the previous results of the congested scenarios with **SUMO-2**, we come to different observations. Now, all four proposed methods perform very similarly in terms of travel time prediction. The oracle boundary case shows a slight outperformance, although its speed RMSEs are worse than the other ones. Looking at the traffic volume in the prediction hour (see Figure 5.4a), the good results are easily explainable: the congestion induced by the lane closure has almost no impact on the future, consequently it is easier to predict the boundary data. The scenario stays almost all the time in the free flow regime, therefore also the naive case of constant boundary data delivers reasonable results: indeed $\mathbf{E}^{\tau}$ and $\mathbf{E}_c^{\tau}$ are even lower than in the pure GP approach.

	pure GP	MOO	constant boundary	oracle boundary
$\hat{\mathbf{E}}_B^{\rho}$	23.52	**23.20**	25.21	0
$\hat{\mathbf{E}}$	8.88	8.16	9.56	10.20
$\hat{\mathbf{E}}_c$	8.51	**7.75**	9.21	9.68
$\mathbf{E}^{\tau}$	0.56	0.54	0.54	0.52
$\mathbf{E}_c^{\tau}$	0.37	0.34	0.34	**0.31**

Table 6.15: **SUMO-2**. $1^{st} - Godu - \rho$, $\mathbf{L^2}$ approach without ramp consideration.
Prediction RMSE and travel time results for different prediction approaches.

Next, in Figure 6.16a we demonstrate that also in light traffic situations the knee-point algorithm proposes a good candidate point, whose value lies closely to the minimum. Finally, Figure 6.16b underlines nicely the typical convergent behavior of the corrected simulation. Additionally, the already well-known overestimation of the travel time when using real boundary data (oracle boundary case) is visible for the last trajectories. In contrast, the MOO method

rather underestimates the trip duration, because it fails to forecast the slightly lower speeds in the left boundary loop detector.

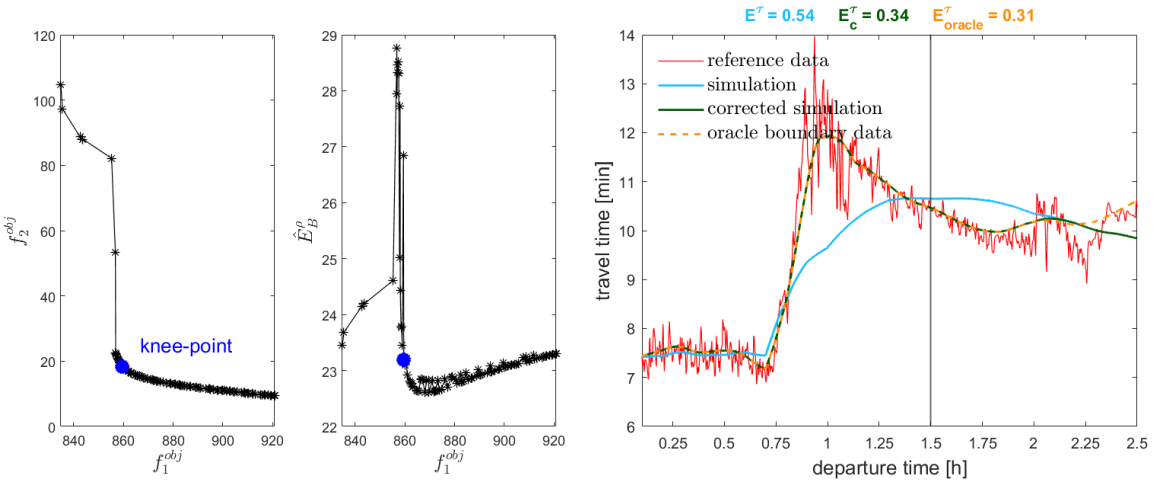

(a) Knee-point. (b) Predicted travel time.

Figure 6.16: **SUMO-2**. $1^{st} - Godu - \rho$, $\mathbf{L^2}$ and MOO-approach.
Travel time prediction results.

In the following, we continue by discussing the real data results, where we do not have access to the travel times. Instead, we can analyze additionally the DTW and LSTM method.

RTMC-1:

By looking at Table 6.16, the results are more difficult to interpret: the DTW approach, which provides clearly the lowest $\hat{\mathbf{E}}_B^{\rho}$, performs the worst in terms of speed RMSE. In contrast, although the boundary predictions obtained by the LSTM network are disappointing, its speed prediction power is convincing. The different boundary profile reconstructions corresponding to these two approaches is depicted in Figure 6.17b. Here, the DTW algorithm creates a time series which tries to match the reality and which performs well for the left boundary loop detector. However, the LSTM network predicts almost a flat line, leading finally to the bad observed error.

	pure GP	MOO	DTW	LSTM	constant boundary	oracle boundary
$\hat{\mathbf{E}}_B^{\rho}$	37.16	30.29	**22.79**	38.96	24.78	0
$\hat{\mathbf{E}}$	17.48	**11.21**	20.31	12.85	18.91	16.95
$\hat{\mathbf{E}}_c$	17.72	11.67	20.16	14.53	18.77	16.39

Table 6.16: **RTMC-1**. $1^{st} - Godu - \rho$, $\mathbf{L^2}$ approach without ramp consideration.
Prediction RMSE for different prediction approaches.

Going back to Table 6.16, we also emphasize that the MOO approach leads to the best performance in terms of speed RMSE. Its knee-point heuristic provides again almost the lowest possible $\hat{\mathbf{E}}_B^{\rho}$ value (see Figure 6.17a). Furthermore, the oracle boundary case takes

this time an average ranking: it performs better than the pure GP, DTW and constant boundary approach, but worse than the MOO and LSTM method.
Finally, we also underline in this scenario the similar performance of $\mathbf{E}^{\tau}$ and $\mathbf{E}_c^{\tau}$, which reinforces again that the additional information provided by the bias vanishes as we predict further into the future.

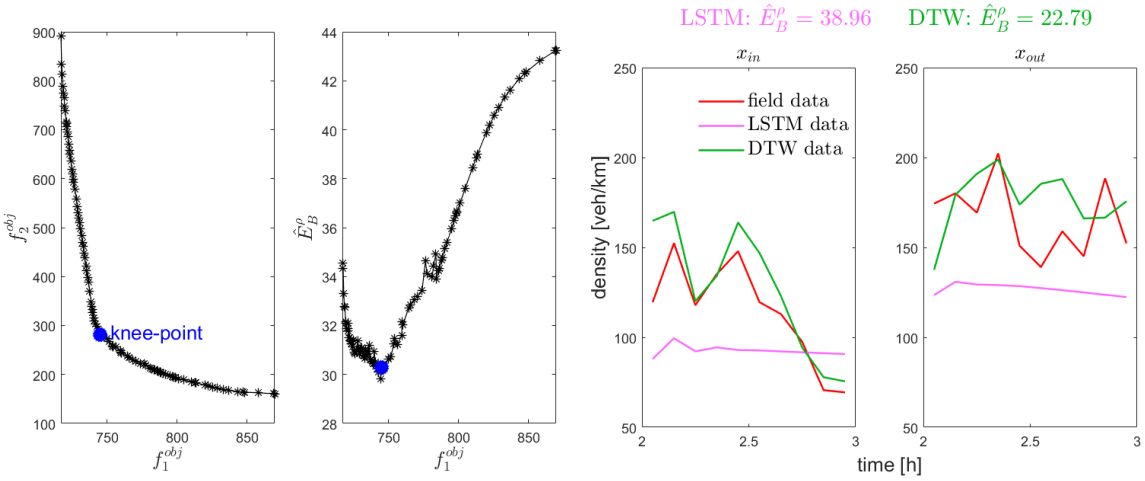

(a) Knee-point.

(b) Density boundary profiles.

Figure 6.17: **RTMC-1**. $1^{st} - Godu - \rho$, $\mathbf{L^2}$ approach.
Left column: MOO-approach. Right column: LSTM and DTW approach.

RTMC-2:

At first, we remind that **RTMC-2** is the only scenario where we integrate the measured ramp detector data in the calibration process. However, due to their questionable impact, we set the ramp data to zero in the prediction time slot. This avoids to forecast the ramp data by one of the proposed methods.
Looking at Table 6.17, we obtain similar results as for **RTMC-1**. Thus, the MOO approach leads again to the lowest $\mathbf{E}^{\tau}$ and $\mathbf{E}_c^{\tau}$ errors. Moreover, the DTW method clearly outperforms the LSTM network with respect to $\hat{\mathbf{E}}_B^{\rho}$, but it underperforms in terms of speed RMSE.

	pure GP	MOO	DTW	LSTM	constant boundary	oracle boundary
$\hat{\mathbf{E}}_B^{\rho}$	29.37	18.97	**9.06**	29.66	66.09	0
$\hat{\mathbf{E}}$	18.24	**14.23**	17.80	15.60	35.81	17.53
$\hat{\mathbf{E}}_c$	18.05	14.67	18.46	16.05	35.53	18.30

Table 6.17: **RTMC-2**. $1^{st} - Godu - \rho$, $\mathbf{L^2}$ approach with ramp consideration.
Prediction RMSE for different prediction approaches.

The profiles in Figure 6.18b show the same behavior as before: a more realistic DTW prediction and a flat LSTM forecast. Also the oracle boundary case executes analogously, namely it can be ranked after the MOO and LSTM results. The only striking difference is the great

failure of the constant boundary data method.
Considering finally Figure 6.18a, we see for the first time a fluctuating behavior of the $\hat{\mathbf{E}}_B^\rho$ value in the knee-point algorithm. However, the heuristic still achieves to propose an acceptable point.

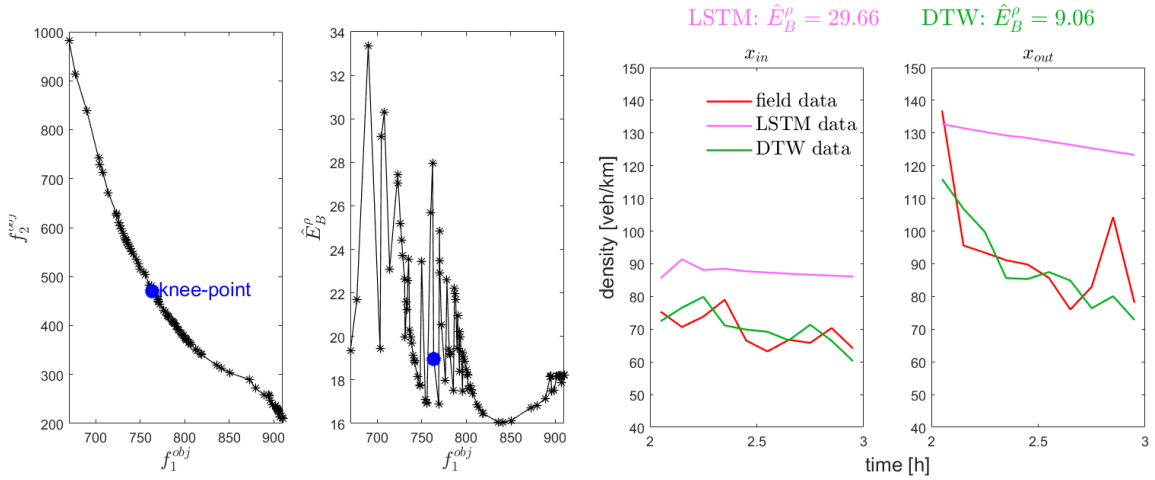

(a) Knee-point. (b) Density boundary profiles.

Figure 6.18: **RTMC-2**. $1^{st} - Godu - \rho$, $\mathbf{L^2}$ approach.
Left column: MOO-approach. Right column: LSTM and DTW approach.

From the last observations of the RTMC scenarios, we conclude that, without additional information on travel times, the results are quite hard to explain. However, it seems that this non-logical anti-correlated behavior of the metrics $\hat{\mathbf{E}}_B^\rho$ and $\hat{\mathbf{E}}$ can be traced back to the speed quantity problem, as already pointed out in the discussion of **SUMO-1B**. It seems that in the real world data case this strange behavior is even more pronounced, probably induced by measurement errors from loop detectors, which are not assumed to occur in the synthetic data scenarios.

As an overall conclusion of this section, we get to the following summary:

1. The correction of the bias in the future can be neglected due to its convergence behavior towards the pure simulation.

2. The MOO method delivers in general the most robust results. Indeed, in every test it convinces by its competitive $\hat{\mathbf{E}}_B^\rho$, $\mathbf{E}^\tau$ and $\mathbf{E}_c^\tau$ values.

3. The choice of the speed data treatment has an impact on the error metrics. By applying the fundamental equation $v = \dfrac{q}{\rho}$, travel times are mostly overestimated.

Remark 45. We point out that the difficulty of predicting the speed is a frequently mentioned problem (see for example [LLW+23, TK14, WYG+22]). Instead, convincing flow predictions seem to be much easier to obtain, as shown by various results found in the literature (see for example [MK18, PS15, SLY+16]). This can be supported by the following two arguments: the usually better flow data quality and the implementation of flow boundary conditions in the Godunov scheme.

Appendix B

Calibration results for selected scenarios

	$\mathbf{L^2}$			KOH		
	V	C	R	V	C	R
$1^{st} - Godu - q$	118	40	158	141	23	200
$1^{st} - Godu - \rho$	**93**	**31**	**300**	89	49	222
$2^{nd} - Godu - q$	145	21	180	136	15	186
$2^{nd} - Godu - \rho$	69	25	182	84	84	169
$2^{nd} - HLL$	80	88	167	86	73	166
$2^{nd} - HW$	83	85	170	116	100	166

Table 6.18: **SUMO-2**. Calibration results.
Fundamental fit approach: $\theta^* = (92, 47, 221)$. In blue: best approach.

	$\mathbf{L^2}$			KOH		
	V	C	R	V	C	R
$1^{st} - Godu - q$	99	95	283	60	81	202
$1^{st} - Godu - \rho$	**99**	**92**	**298**	62	14	410
$2^{nd} - Godu - q$	60	100	185	81	76	240
$2^{nd} - Godu - \rho$	76	81	231	124	68	347
$2^{nd} - HLL$	-	-	-	-	-	-
$2^{nd} - HW$	-	-	-	-	-	-

(a) With ramp consideration.

	$\mathbf{L^2}$			KOH		
	V	C	R	V	C	R
$1^{st} - Godu - q$	137	56	169	137	52	150
$1^{st} - Godu - \rho$	116	28	486	90	20	468
$2^{nd} - Godu - q$	107	15	221	119	18	156
$2^{nd} - Godu - \rho$	60	123	209	123	16	536
$2^{nd} - HLL$	60	129	209	140	15	581
$2^{nd} - HW$	59	129	209	141	26	479

(b) Without ramp consideration.

Table 6.19: **RTMC-2**. Calibration results.
Fundamental fit approach: $\theta^* = (107, 80, 260)$. In blue: best approach.

Conclusion and perspectives

In this thesis, we compared various calibration and prediction approaches for parameter identification and traffic reconstruction in macroscopic traffic flow models, exploiting synthetic and real world loop detector data sets. We started from a mathematical viewpoint by studying the underlying traffic flow model in order to build the theoretical foundation for the subsequent, more applied chapters considering real data.
Regarding the calibration techniques, we applied a modularized version of KOH calibration [LBB09, TW16], alleviating some of the shortcomings of the original approach. However, due to the strong flexibility of this framework, we observed that a simple least square optimization usually performs better. Additionally, our results pointed to the benefit of correcting the simulation output by a bias in order to compensate model limitations in reproducing real data. Moreover, the obtained calibration parameters are highly scenario dependent, thus the calibration procedure has to be performed on each individual traffic case.
Regarding traffic reconstruction, we were interested in a good performance of the speed quantity, since our aim is to provide travel time predictions. However, trajectory data are rarely available, therefore reference travel times are typically approximated by methods considering average loop detector data. In the synthetic data case, the N-curve approximation delivered the best results, while it failed in more complex (real) traffic situations. Thus, we proposed the MOO method, which belongs to the class of hybrid approaches and which combines physical knowledge and GPs. More precisely, we force the PDE to be satisfied at virtually created points, whereas the observed measurements are modeled by a GP. Although the approach does not achieve to completely satisfy the PDE by its knee-point heuristic (see for example Figure 6.14a), we could forecast reasonable boundary data in the prediction window, which are necessary to simulate the speed data at a finer scale in order to do travel time predictions. The study has highlighted that the method we propose delivers the most robust results. Finally, we also compared the performance of different numerical methods, coming to the conclusion that the Godunov scheme, implemented for the LWR model and with density boundary conditions, leads to the most convincing results in terms of speed reconstruction.

This thesis opens several perspectives for future research. Since we could only perform our travel time analysis on synthetic data, a natural next step is to validate the obtained results in real world situations. This requires both loop detector and trajectory data for the same traffic scenario.
From the traffic modeling point of view, further investigations should consider more complex situations including the presence of road junctions and traffic lights. Moreover, a generalization of the numerical methods and statistical approaches to road networks and multi-class models are certainly worth to analyze. In particular, it could be also interesting to consider a time or space dependency for some parameters [PBKL22], as well as local variations of the

bias on the road.
Obviously, GP improvements are possible, as the extension of current physics based GPs to our setup. Moreover, modeling the prior mean by more advanced methods [LO18] could reduce the influence of the prior information on the predictions. Additionally, the choice of virtual points in the MOO approach can be improved by considering for example the "active PDE-informed Kriging" (APIK) approach proposed in [CCZW22]. Another extension is to index the GP by graphs as proposed in [EGL14], which would allow to integrate more involved network situations while avoiding the numerical scheme to become too complex. Also, as pointed out in Section 3.2.3, further research is needed to accommodate more dimensions in the heteroscedastic GP modeling (see e.g. [HWN$^+$16]) in order to take better into account the different traffic regimes.
Last but not least, it would be also interesting to compare the performance of our proposed MOO approach with the PINNs method.

Bibliography

[AC97] D. Amadori and R. M. Colombo. Continuous dependence for 2 x 2 conservation laws with boundary. *Journal of Differential Equations*, 138(2):229–266, 1997.

[ADR16] B. Andreianov, C. Donadello, and M. D. Rosini. A second-order model for vehicular traffics with local point constraints on the flow. *Math. Models Methods Appl. Sci.*, 26(4):751–802, 2016.

[AEG+16] A. Allström, Jo. Ekström, D. Gundlegård, R. Ringdahl, C. Rydergren, A. M. Bayen, and A. D. Patire. Hybrid approach for short-term traffic state and travel time prediction on highways. *Transportation Research Record*, 2554(1):60–68, 2016.

[AG02] F. Ancona and P. Goatin. Uniqueness and stability of L^∞ solutions for Temple class systems with boundary and properties of the attainable sets. *SIAM J. Math. Anal.*, 34(1):28–63, 2002.

[All08] G. Allain. *Prévision et analyse du trafic routier par des méthodes statistiques.* PhD thesis, Université Toulouse III, 2008.

[Ama97] D. Amadori. Initial-boundary value problems for nonlinear systems of conservation laws. *NoDEA Nonlinear Differential Equations Appl.*, 4(1):1–42, 1997.

[AR00] A. Aw and M. Rascle. Resurrection of "second order" models of traffic flow. *SIAM J. Appl. Math.*, 60(3):916–938, 2000.

[BB97] P. Baiti and A. Bressan. The semigroup generated by a Temple class system with large data. *Differential Integral Equations*, 10(3):401–418, 1997.

[BBK+09] M. J. Bayarri, J. O. Berger, M. C. Kennedy, A. Kottas, R. Paulo, J. Sacks, J. A. Cafeo, C.-H. Lin, and J. Tu. Predicting vehicle crashworthiness: Validation of computer models for functional and hierarchical data. *Journal of the American Statistical Association*, 104(487):929–943, 2009.

[BBS09] J. O. Berger, J. M. Bernardo, and D. Sun. The formal definition of reference priors. *Ann. Statist.*, 37(2):905–938, 2009.

[BCO21] M. Binois, N. Collier, and J. Ozik. A portfolio approach to massively parallel Bayesian optimization. *arXiv preprint arXiv:2110.09334*, 2021.

[BCO23] M. Briani, E. Cristiani, and E. Onofri. Inverting the fundamental diagram and forecasting boundary conditions: How machine learning can improve macroscopic models for traffic flow. *arXiv preprint arXiv:2303.12740*, 2023.

[Bea19] M. A. Beaumont. Approximate Bayesian computation. *Annual Review of Statistics and Its Application*, 6:379–403, 2019.

[Ben86] A. Benabdallah. Le "p système" dans un intervalle. *C. R. Acad. Sci. Paris Sér. I Math.*, 303(4):123–126, 1986.

[BG21] M. Binois and R. B. Gramacy. hetgp: Heteroskedastic Gaussian process modeling and sequential design in R. *Journal of Statistical Software*, 98(13):1–44, 2021.

[BGKT08] R. Bürger, A. E. García, K. H. Karlsen, and J. D. Towers. A family of numerical schemes for kinematic flows with discontinuous flux. *J. Engrg. Math.*, 60(3-4):387–425, 2008.

[BGR15] M. Binois, D. Ginsbourger, and O. Roustant. Quantifying uncertainty on pareto fronts with Gaussian process conditional simulations. *European Journal of Operational Research*, 243(2):386–394, 2015.

[Bia00] S. Bianchini. The semigroup generated by a Temple class system with non-convex flux function. *Differential and Integral Equations*, 13(10-12):1529–1550, 2000.

[BlRN79] C. Bardos, A. Y. le Roux, and J.-C. Nédélec. First order quasilinear equations with boundary conditions. *Comm. Partial Differential Equations*, 4(9):1017–1034, 1979.

[BO14] J. Brynjarsdóttir and A. O'Hagan. Learning about physical parameters: The importance of model discrepancy. *Inverse problems*, 30(11):114007, 2014.

[BR03] P. Bagnerini and M. Rascle. A multiclass homogenized hyperbolic model of traffic flow. *SIAM J. Math. Anal.*, 35(4):949–973, 2003.

[Bre00] A. Bressan. *Hyperbolic systems of conservation laws: the one-dimensional Cauchy problem*, volume 20. Oxford Lecture Series in Mathematics and its Applications, Oxford University Press, 2000.

[BS87] A. Benabdallah and D. Serre. Problèmes aux limites pour des systèmes hyperboliques non linéaires de deux équations à une dimension d'espace. *C. R. Acad. Sci. Paris Sér. I Math.*, 305(15):677–680, 1987.

[BWG+11] S. Blandin, D. Work, P. Goatin, B. Piccoli, and A. Bayen. A general phase transition model for vehicular traffic. *SIAM J. Appl. Math.*, 71(1):107–127, 2011.

[CB11] C. G. Claudel and A. M. Bayen. Convex formulations of data assimilation problems for a class of hamilton–jacobi equations. *SIAM Journal on Control and Optimization*, 49(2):383–402, 2011.

[CBC+19] M. Carmassi, P. Barbillon, M. Chiodetti, M. Keller, and E. Parent. Bayesian calibration of a numerical code for prediction. *Journal de la société française de statistique*, 160(1):1–30, 2019.

[CCZW22] J. Chen, Z. Chen, C. Zhang, and C. F. J. Wu. APIK: Active physics-informed kriging model with partial differential equations. *SIAM/ASA Journal on Uncertainty Quantification*, 10(1):481–506, 2022.

[CF99a] G.-Q. Chen and H. Frid. Divergence-measure fields and hyperbolic conservation laws. *Archive for Rational Mechanics and Analysis*, 147:89–118, 1999.

[CF99b] G.-Q. Chen and H. Frid. Vanishing viscosity limit for initial-boundary value problems for conservation laws. *Contemporary Mathematics*, 238:35–51, 1999.

[CFGG20] F. A. Chiarello, J. Friedrich, P. Goatin, and S. Göttlich. Micro-macro limit of a nonlocal generalized Aw-Rascle type model. *SIAM J. Appl. Math.*, 80(4):1841–1861, 2020.

[CG04] R. M. Colombo and A. Groli. On the initial boundary value problem for Temple systems. *Nonlinear Anal.*, 56(4):569–589, 2004.

[CG07] C. Chalons and P. Goatin. Transport-equilibrium schemes for computing contact discontinuities in traffic flow modeling. *Commun. Math. Sci.*, 5(3):533–551, 2007.

[CGP07] R. M. Colombo, P. Goatin, and F. S. Priuli. Global well posedness of traffic flow models with phase transitions. *Nonlinear Anal.*, 66(11):2413–2426, 2007.

[CHOS21] Y. Chen, B. Hosseini, H. Owhadi, and A. M. Stuart. Solving and learning nonlinear PDEs with Gaussian processes. *Journal of Computational Physics*, 447:110668, 2021.

[CML+17] I. Crandell, A. J. Millican, S. Leman, E. Smith, W. N. Alexander, W. J. Devenport, R. Vasta, R. B. Gramacy, and M. Binois. Anomaly detection in large-scale wind tunnel tests using Gaussian processes. In *33rd AIAA Aerodynamic Measurement Technology and Ground Testing Conference*, page 4131, 2017.

[CMV15] A. Corbetta, A. Muntean, and K. Vafayi. Parameter estimation of social forces in pedestrian dynamics models via a probabilistic method. *Math. Biosci. Eng.*, 12(2):337–356, 2015.

[Col02] R. M. Colombo. Hyperbolic phase transitions in traffic flow. *SIAM J. Appl. Math.*, 63(2):708–721, 2002.

[CR05] R. M. Colombo and M. D. Rosini. Well posedness of balance laws with boundary. *Mathematical Models and Methods in Applied Sciences*, 311(2):683–702, 2005.

[Daf72] C. M. Dafermos. Polygonal approximations of solutions of the initial value problem for a conservation law. *J. Math. Anal. Appl.*, 38:33–41, 1972.

[Daf05] C. M. Dafermos. *Hyperbolic conservation laws in continuum physics*, volume 3. Springer-Verlag, 2005.

[Dag94] C. F. Daganzo. The cell transmission model: A dynamic representation of highway traffic consistent with the hydrodynamic theory. *Transportation Research Part B: Methodological*, 28(4):269–287, 1994.

[Dag95] C. F. Daganzo. Requiem for second-order fluid approximations of traffic flow. *Transportation Research Part B: Methodological*, 29(4):277–286, 1995.

[Dav88] S. F. Davis. Simplified second-order Godunov-type methods. *SIAM J. Sci. Statist. Comput.*, 9(3):445–473, 1988.

[DGDMF22] C. Daini, P. Goatin, M. L. Delle Monache, and A. Ferrara. Centralized traffic control via small fleets of connected and automated vehicles. In *2022 European Control Conference (ECC)*, pages 371–376. IEEE, 2022.

[DGK+09] G. Dervisoglu, G. Gomes, J. Kwon, R. Horowitz, and P. Varaiya. Automatic calibration of the fundamental diagram and empirical observations on capacity. In *Transportation Research Board 88th Annual Meeting*, volume 15, pages 31–59. Citeseer, 2009.

[DLF88] F. Dubois and P. Le Floch. Boundary conditions for nonlinear hyperbolic systems of conservation laws. *J. Differential Equations*, 71(1):93–122, 1988.

[DMCC+21] M. L. Delle Monache, K. Chi, Y. Chen, P. Goatin, K. Han, J.-M. Qiu, and B. Piccoli. A three-phase fundamental diagram from three-dimensional traffic data. *Axioms*, 10(1):17, 2021.

[EGH00] R. Eymard, T. Gallouët, and R. Herbin. *Finite volume methods*, volume 7 of *Handbook of Numerical Analysis*. Elsevier, 2000.

[EGL14] T. Espinasse, F. Gamboa, and J.-M. Loubes. Parametric estimation for Gaussian fields indexed by graphs. *Probability Theory and Related Fields*, 159:117–155, 2014.

[Fan13] S. Fan. *Data-fitted generic second order macroscopic traffic flow models*. Phd thesis, ProQuest LLC, Ann Arbor, MI, 2013.

[FHS14] S. Fan, M. Herty, and B. Seibold. Comparative model accuracy of a data-fitted generalized Aw-Rascle-Zhang model. *Netw. Heterog. Media*, 9(2):239–268, 2014.

[FHVD20] J. M. Flegal, J. Hughes, D. Vats, and N. Dai. mcmcse: Monte carlo standard errors for MCMC. Riverside, CA, Denver, CO, Coventry, UK, and Minneapolis, MN, R package version 1.4-1, 2020.

[Fra61] R. Franklin. The structure of a traffic shock wave. *Civil Engineering Pulb. Wks. Rev*, 56:1186–1188, 1961.

[FSP+17] S. Fan, Y. Sun, B. Piccoli, B. Seibold, and D. B. Work. A collapsed generalized Aw-Rascle-Zhang model and its model accuracy. eprint 1702.03624, physics.soc-ph, 2017.

[FSS18] A. Ferrara, S. Sacone, and S. Siri. *Freeway traffic modelling and control*, volume 585. Springer-Verlag, 2018.

[GHO08] M. Godvik and H. Hanche-Olsen. Existence of solutions for the Aw-Rascle traffic flow model with vacuum. *J. Hyperbolic Differ. Equ.*, 5(1):45–63, 2008.

[GHO10] M. Godvik and H. Hanche-Olsen. Car-following and the macroscopic Aw-Rascle traffic flow model. *Discrete Contin. Dyn. Syst. Ser. B*, 13(2):279–303, 2010.

[GK20] S. Göttlich and S. Knapp. Artificial neural networks for the estimation of pedestrian interaction forces. In Livio Gibelli, editor, *Crowd Dynamics, Volume 2: Theory, Models, and Applications*, pages 11–32. Springer International Publishing, Cham, 2020.

[Goa06] P. Goatin. The Aw-Rascle vehicular traffic flow model with phase transitions. *Math. Comput. Modelling*, 44(3-4):287–303, 2006.

[God59] S. K. Godunov. A difference method for numerical calculation of discontinuous solutions of the equations of hydrodynamics. *Mat. Sb. (N.S.)*, 47 (89):271–306, 1959.

[GP06] M. Garavello and B. Piccoli. Traffic flow on a road network using the Aw-Rascle model. *Communications in Partial Differential Equations*, 31(2):243–275, 2006.

[Gra20] R. B. Gramacy. *Surrogates: Gaussian process modeling, design, and optimization for the applied sciences*. CRC press, 2020.

[GSW19] S. N. Gomes, A. M. Stuart, and M.-T. Wolfram. Parameter estimation for macroscopic pedestrian dynamics models from microscopic data. *SIAM J. Appl. Math.*, 79(4):1475–1500, 2019.

[GT21] S. Göttlich and C. Totzeck. Optimal control for interacting particle systems driven by neural networks. *arXiv preprint arXiv:2101.12657*, 2021.

[GW23] P. Goatin and A. Würth. The initial boundary value problem for second order traffic flow models with vacuum: existence of entropy weak solutions. *Nonlinear Analysis*, 233:113295, 2023.

[HB07] B. Haut and G. Bastin. A second order model of road junctions in fluid models of traffic networks. *Netw. Heterog. Media*, 2(2):227–253, 2007.

[Hei94] A. Heibig. Existence and uniqueness of solutions for some hyperbolic systems of conservation laws. *Arch. Rational Mech. Anal.*, 126(1):79–101, 1994.

[HFV18] M. Herty, A. Fazekas, and G. Visconti. A two-dimensional data-driven model for traffic flow on highways. *Netw. Heterog. Media*, 13(2):217–240, 2018.

[HGBL20] J. Huang, R. B. Gramacy, M. Binois, and M. Libraschi. On-site surrogates for large-scale calibration. *Applied Stochastic Models in Business and Industry*, 36(2):283–304, 2020.

[HKC+04] D. Higdon, M. Kennedy, J. C. Cavendish, J. A. Cafeo, and R. D. Ryne. Combining field data and computer simulations for calibration and prediction. *SIAM Journal on Scientific Computing*, 26(2):448–466, 2004.

[HLvL83] A. Harten, P. D. Lax, and B. van Leer. On upstream differencing and Godunov-type schemes for hyperbolic conservation laws. *SIAM Rev.*, 25(1):35–61, 1983.

[HMR06] M. Herty, S. Moutari, and M. Rascle. Optimization criteria for modelling intersections of vehicular traffic flow. *Netw. Heterog. Media*, 1(2):275–294, 2006.

[Hof09] P. D. Hoff. *A first course in Bayesian statistical methods*, volume 580. Springer-Verlag, 2009.

[HS97] S. Hochreiter and J. Schmidhuber. Long short-term memory. *Neural computation*, 9(8):1735–1780, 1997.

[HW95] M. Hilliges and W. Weidlich. A phenomenological model for dynamic traffic flow in networks. *Transportation Research Part B: Methodological*, 29(6):407–431, 1995.

[HWN+16] W. Herlands, A. Wilson, H. Nickisch, S. Flaxman, D. Neill, W. Van Panhuis, and E. Xing. Scalable Gaussian processes for characterizing multidimensional change surfaces. In *Artificial intelligence and statistics*, pages 1013–1021. PMLR, 2016.

[IK09] T. Idé and S. Kato. Travel-time prediction using Gaussian process regression: A trajectory-based approach. In *Proceedings of the 2009 SIAM International Conference on Data Mining*, pages 1185–1196. SIAM, 2009.

[KCB00] J. Kwon, B. Coifman, and P. Bickel. Day-to-day travel-time trends and travel-time prediction from loop-detector data. *Transportation Research Record*, 1717(1):120–129, 2000.

[KGG17] O. Kolb, S. Göttlich, and P. Goatin. Capacity drop and traffic control for a second order traffic model. *Networks and Heterogeneous Media*, 12(4):663–681, 2017.

[KO01] M. C. Kennedy and A. O'Hagan. Bayesian calibration of computer models. *Journal of the Royal Statistical Society: Series B (Statistical Methodology)*, 63(3):425–464, 2001.

[Lax57] P. D. Lax. Hyperbolic systems of conservation laws II. *Communications on pure and applied mathematics*, 10(4):537–566, 1957.

[LBB09] F. Liu, M. J. Bayarri, and J. O. Berger. Modularization in Bayesian analysis, with emphasis on analysis of computer models. *Bayesian Analysis*, 4(1):119–150, 2009.

[LBBW+18] P. A. Lopez, M. Behrisch, L. Bieker-Walz, J. Erdmann, Y.-P. Flötteröd, R. Hilbrich, L. Lücken, J. Rummel, P. Wagner, and E. Wießner. Microscopic traffic simulation using SUMO. In *The 21st IEEE International Conference on Intelligent Transportation Systems*. IEEE, 2018.

[LeV02] R. J. LeVeque. *Finite volume methods for hyperbolic problems*, volume 31. Cambridge University press, 2002.

[LHSM05] J.-P. Lebacque, H. Haj-Salem, and S. Mammar. Second order traffic flow modeling: supply-demand analysis of the inhomogeneous Riemann problem and of boundary conditions. *Proceedings of the 10th Euro Working Group on Transportation (EWGT)*, 3(3), 2005.

[Llo82] S. Lloyd. Least squares quantization in pcm. *IEEE Transactions on Information Theory*, 28(2):129–137, 1982.

[LLW+23] Z. Liu, C. Lyu, Z. Wang, S. Wang, P. Liu, and Q. Meng. A Gaussian-process-based data-driven traffic flow model and its application in road capacity analysis. *IEEE Transactions on Intelligent Transportation Systems*, 2023.

[LMHS07a] J.-P. Lebacque, S. Mammar, and H. Haj-Salem. The Aw-Rascle and Zhang's model: Vacuum problems, existence and regularity of the solutions of the Riemann problem. *Transportation Research Part B: Methodological*, 41(7):710–721, 2007.

[LMHS07b] J.-P. Lebacque, S. Mammar, and H. Haj-Salem. Generic second order traffic flow modelling. In *Transportation and Traffic Theory 2007*, 2007.

[LMLR06] J.-M. Loubes, É. Maza, M. Lavielle, and L. Rodriguez. Road trafficking description and short term travel time forecasting, with a classification method. *Canadian Journal of Statistics*, 34(3):475–491, 2006.

[LO18] M. R. Lee and A. B. Owen. Single nugget kriging. *Statistica Sinica*, pages 649–669, 2018.

[LW55] M. J. Lighthill and G. B. Whitham. On kinematic waves. II. A theory of traffic flow on long crowded roads. *Proc. Roy. Soc. London Ser. A*, 229:317–345, 1955.

[LWK+22] D. Long, Z. Wang, A. Krishnapriyan, R. Kirby, S. Zhe, and M. Mahoney. AutoIP: A united framework to integrate physics into Gaussian processes. In *International Conference on Machine Learning*, pages 14210–14222. PMLR, 2022.

[MAT22] MATLAB. The MathWorks Inc., Natick, Massachusetts, United States, version: 9.12.0 (R2022a). Website: `https://www.mathworks.com`, 2022. Accessed on 09/13/2023.

[MDdWS19] S. Mollier, M. L. Delle Monache, C. Canudas de Wit, and B. Seibold. Two-dimensional macroscopic model for large scale traffic networks. *Transportation Research Part B: Methodological*, 122:309–326, 2019.

[MHG21] I. Marsh, P.-L. Hsu, and C. Ghandeharioon. Data-driven traffic flow: A state-of-the-art report, 2021.

[Mie99] K. Miettinen. *Nonlinear multiobjective optimization*, volume 12. Springer Science & Business Media, 1999.

[Min] Minnesota Departement of Transportation. Mn/Dot Traffic Data. Website: `http://data.dot.state.mn.us/datatools/`. Accessed on 09/13/2023.

[MK18] O. Mohammed and J. Kianfar. A machine learning approach to short-term traffic flow prediction: A case study of interstate 64 in Missouri. In *2018 IEEE International Smart Cities Conference (ISC2)*, pages 1–7. IEEE, 2018.

[MW14] J. J. Moré and S. M. Wild. Do you trust derivatives or differences? *Journal of Computational Physics*, 273:268–277, 2014.

[New61] G. Newell. A theory of traffic flow in tunnels. *Theory of Traffic Flow*, pages 193–206, 1961.

[NH03] D. Ngoduy and S. P. Hoogendoorn. An automated calibration procedure for macroscopic traffic flow models. *IFAC Proceedings Volumes*, 36(14):263–268, 2003. 10th IFAC Symposium on Control in Transportation Systems 2003, Tokyo, Japan, 4-6 August 2003.

[Osb10] M. A. Osborne. *Bayesian Gaussian processes for sequential prediction, optimisation and quadrature.* PhD thesis, Oxford University, UK, 2010.

[Pay71] H. J. Payne. Model of freeway traffic and control. *Mathematical Model of Public System*, pages 51–61, 1971.

[PBKL22] M. Pereira, P. B. Baykas, B. Kulcsár, and A. Lang. Parameter and density estimation from real-world traffic data: A kinetic compartmental approach. *Transportation Research Part B: Methodological*, 155:210–239, 2022.

[PG06] B. Piccoli and M. Garavello. *Traffic flow on networks*, volume 1. American Institute of Mathematical Sciences (AIMS), Springfield, MO, 2006.

[PH13] L. Pan and X. Han. The Aw-Rascle traffic model with Chaplygin pressure. *J. Math. Anal. Appl.*, 401(1):379–387, 2013.

[PHF+15] B. Piccoli, K. Han, T. L. Friesz, T. Yao, and J. Tang. Second-order models and traffic data from mobile sensors. *Transportation Research Part C: Emerging Technologies*, 52:32–56, 2015.

[Plu17] M. Plumlee. Bayesian calibration of inexact computer models. *Journal of the American Statistical Association*, 112(519):1274–1285, 2017.

[PS15] N. Polson and V. Sokolov. Bayesian analysis of traffic flow on interstate I-55: The LWR model. *The Annals of Applied Statistics*, 9(4):1864 – 1888, 2015.

[PVG+11] F. Pedregosa, G. Varoquaux, A. Gramfort, V. Michel, B. Thirion, O. Grisel, M. Blondel, P. Prettenhofer, R. Weiss, V. Dubourg, et al. Scikit-learn: Machine learning in python. *The Journal of Machine Learning Research*, 12:2825–2830, 2011.

[RG21] N. Ronzoni and P. Goatin. *Road Traffic Data analysis: Clustering and Prediction.* Université Côte d'Azur, Inria, Research Report. Weblink: `https://inria.hal.science/hal-03370282/file/RR-9426.pdf`, 2021. Accessed on 09/13/2023.

[Ric56] P. I. Richards. Shock waves on the highway. *Operations Res.*, 4:42–51, 1956.

[Ris93] N. H. Risebro. A front-tracking alternative to the random choice method. *Proc. Amer. Math. Soc.*, 117(4):1125–1139, 1993.

[RPK17] M. Raissi, P. Perdikaris, and G. E. Karniadakis. Physics informed deep learning (part I): Data-driven solutions of nonlinear partial differential equations. *arXiv preprint arXiv:1711.10561*, 2017.

[RVZ04] J. Rice and E. Van Zwet. A simple and effective method for predicting travel times on freeways. *IEEE Transactions on Intelligent Transportation Systems*, 5(3):200–207, 2004.

[RW06] C. E. Rasmussen and C. Williams. *Gaussian processes for machine learning*, volume 2. MIT press Cambridge, MA, 2006.

[Ser96] D. Serre. *Systemes de lois de conservation*, volume 1. Diderot Paris, 1996.

[SLY+16] Q. Shang, C. Lin, Z. Yang, Q. Bing, and X. Zhou. A hybrid short-term traffic flow prediction model based on singular spectrum analysis and kernel extreme learning machine. *PLoS one*, 11(8):e0161259, 2016.

[SMD21] R. Shi, Z. Mo, and X. Di. Physics-informed deep learning for traffic state estimation: A hybrid paradigm informed by second-order traffic models. In *Proceedings of the AAAI Conference on Artificial Intelligence*, volume 35, pages 540–547, 2021.

[SNI15] Y. Setoguchi, K. Narukawa, and H. Ishibuchi. A knee-based EMO algorithm with an efficient method to update mobile reference points. In *EMO (1)*, pages 202–217, 2015.

[SPN+18] G. A. Strofylas, K. N. Porfyri, I. K. Nikolos, A. I. Delis, and M. Papageorgiou. Using synchronous and asynchronous parallel differential evolution for calibrating a second-order traffic flow model. *Advances in Engineering Software*, 125:1–18, 2018.

[SPP+17] A. Spiliopoulou, I. Papamichail, M. Papageorgiou, Y. Tyrinopoulos, and J. Chrysoulakis. Macroscopic traffic flow model calibration using different optimization algorithms. *Operational Research*, 17:145–164, 2017.

[Ste99] M. L. Stein. *Interpolation of spatial data: some theory for kriging*. Springer Science & Business Media, 1999.

[Tem83] B. Temple. Systems of conservation laws with invariant submanifolds. *Trans. Amer. Math. Soc.*, 280(2):781–795, 1983.

[TK14] M. Treiber and A. Kesting. Traffic flow dynamics: data, models and simulation. *Physics Today*, Vol. 67(3), 2014.

[TW15] R. Tuo and C. F. J. Wu. Efficient calibration for imperfect computer models. *The Annals of Statistics*, 43(6):2331–2352, 2015.

[TW16] R. Tuo and C. F. J. Wu. A theoretical framework for calibration in computer models: Parametrization, estimation and convergence properties. *SIAM/ASA Journal on Uncertainty Quantification*, 4(1):767–795, 2016.

[VL04] J. W. C. Van Lint. Reliable travel time prediction for freeways. *Netherlands TRAIL Research School Jaffalaan*, 2004.

[Wag10] P. Wagner. Fluid-dynamical and microscopic description of traffic flow: a data-driven comparison. *Philos. Trans. R. Soc. Lond. Ser. A Math. Phys. Eng. Sci.*, 368(1928):4481–4495, 2010.

[WB16] X. Wang and J. O. Berger. Estimating shape constrained functions using Gaussian processes. *SIAM/ASA Journal on Uncertainty Quantification*, 4(1):1–25, 2016.

[WBG23] A. Würth, M. Binois, and P. Goatin. Validation of calibration strategies for macroscopic traffic flow models on synthetic data. In *2023 8th International Conference on Models and Technologies for Intelligent Transportation Systems (MT-ITS)*, pages 1–6. IEEE, 2023.

[WBGG22] A. Würth, M. Binois, P. Goatin, and S. Göttlich. Data-driven uncertainty quantification in macroscopic traffic flow models. *Advances in Computational Mathematics*, 48(6):1–26, 2022.

[WBT+10] D. B. Work, S. Blandin, O.-P. Tossavainen, B. Piccoli, and A. M. Bayen. A traffic model for velocity data assimilation. *Appl. Math. Res. Express. AMRX*, pages 1–35, 2010.

[Wei94] J. A. C. Weideman. Computation of the complex error function. *SIAM Journal on Numerical Analysis*, 31(5):1497–1518, 1994.

[WGV23] A. Würth, P. Goatin, and L. M. Villada. A cheap and easy-to-implement upwind scheme for second order traffic flow models. *HYP2023 Proceedings*. Weblink: `https://hal.science/hal-03957121v1`, 2023. Accessed on 09/13/2023.

[Whi74] G. B. Whitham. *Linear and nonlinear waves*. Pure and Applied Mathematics, Wiley, 1974.

[WP05] Y. Wang and M. Papageorgiou. Real-time freeway traffic state estimation based on extended Kalman filter: a general approach. *Transportation Research Part B: Methodological*, 39(2):141–167, 2005.

[WYG+22] Y. Wang, X. Yu, J. Guo, I. Papamichail, M. Papageorgiou, L. Zhang, S. Hu, Y. Li, and J. Sun. Macroscopic traffic flow modelling of large-scale freeway networks with field data verification: State-of-the-art review, benchmarking framework, and case studies using metanet. *Transportation Research Part C: Emerging Technologies*, 145:103904, 2022.

[Zha02] H. M. Zhang. A non-equilibrium traffic model devoid of gas-like behavior. *Transportation Res. Part B*, 36(3):275–290, 2002.